Top pair production in the dilepton decay channel with a tau lepton

Matteo Corbo

Université Pierre et Marie Curie

Top Pair Production in the Dilepton Decay Channel with a τ Lepton

Candidat
Matteo Corbo

Directeurs de thèse
Mme Aurore Savoy-Navarro
M. Stephan Lammel

Rapporteurs
M. Oscar Eboli
M. Ian Shipsey

Examinateurs
Mme Cinzia Da Via
M. Bertrand Laforge
M. Matteo Cacciari

19 Septembre 2012

Contents

Résumé

La production de paires de quarks top se désintégrant en deux leptons dont au moins un lepton τ est étudiée dans le cadre de l'expérience CDF auprès du collisionneur proton-antiproton, Tevatron, a FNAL aux USA. La sélection exige un électron ou un muon produit par désintégration du lepton τ ou par désintégration d'un W. L'analyse utilise toutes les données enregistrées, 9 fb^{-1}, avec un déclenchement basé sur un électron ou muon à faible moment transverse et une trace chargée isolée. La section efficace de production de paires de top a cette énergie (1.96 TeV dans c.m.) obtenue est de $8,2 \pm 1.7^{+1.2}_{-1.1} \pm 0,5$ pb, et le rapport de branchement en leptons τ est de $0,120 \pm 0,027^{+0,022}_{-0,019} \pm 0,007$ avec erreur statistique, systématique et sur la luminosité respectivement. Ce sont à jour les résultats les plus précis dans ce canal de désintégration du top, en bon accord avec les résultats obtenus au Tevatron avec tous les autres canaux de désintégration du top. Le rapport de branchement est aussi mesuré en séparant les événements τ plus lepton et avec deux leptons τ avec une méthode de maximum de vraisemblance. C'est la première fois que ces modes de désintégration sont identifiés séparément. Par une méthode de maximum de vraisemblance appliquée pour séparer ces deux canaux une mesure alternative du rapport de branchement du top en lepton τ de $0,098 \pm 0,022(stat.) \pm 0,014(syst.)$ est obtenue, en bon accord avec les prédictions du Modèle Standard (universalité). Une limite supérieure de 0,159 pour ce rapport de branchement, avec 95% de niveau de confiance est extraite donnant un indice de Physique au delà du Modèle Standard en particulier un possible boson de Higgs chargé.

Abstract

The top quark pair production and decay into leptons with at least one being a τ lepton is studied in the framework of the CDF experiment at the Tevatron proton antiproton collider at Fermilab (USA). The selection requires an electron or a muon produced either by the τ lepton decay or by a W decay. The analysis uses the complete Run II data set i.e. 9.0 fb^{-1}, selected by one trigger based on a low transverse momentum electron or muon plus one isolated charged track. The top quark pair production cross section at 1.96 TeV is measured at $8.2 \pm 1.7^{+1.2}_{-1.1} \pm 0.5$ pb, and the top branching ratio into τ lepton is measured at $0.120 \pm 0.027^{+0.022}_{-0.019} \pm 0.007$ with statistical, systematics and luminosity uncertainties. These are up to date the most accurate results in this top decay channel and are in good agreement with the results obtained using other decay channels of the top at the Tevatron. The branching ratio is also measured separating the single τ lepton from the two τ leptons events with a log likelihood method. This is the first time these two signatures are separately identified. With a fit to data along the log-likelihood variable an alternative measurement of the branching ratio is made: $0.098 \pm 0.022(stat.) \pm 0.014(syst.)$; it is in good agreement with the expectations of the Standard Model (with lepton universality) within the experimental uncertainties. The branching ratio is constrained to be less than 0.159 at 95% confidence level. This limit translates into a limit of a top branching ratio into a potential charged Higgs boson.

Résumé de Thèse

Introduction

Le Modèle Standard (SM) représente depuis quelques décennies la synthèse théorique et expérimentale la plus réussie de la seconde moitié du 20 siècle. Ce modèle avec quelques légères améliorations (introduction du mélange des neutrinos par exemple) a été confirmé jusqu'à présent par l'ensemble des expériences, à un très grand niveau de précision. Malgré son succès, le SM contient des incohérences et la théorie cherche depuis également des décennies des nouvelles voies qui permettent de palier aux insuffisances et même incohérences du Modèle Standard. Tout ce travail théorique a ouvert le champ de ce qui est appelé la "Physique au delà du Modelé Standard" ou Physique Nouvelle et donc de possible nouveaux processus ou interactions. Ces interactions peuvent par exemple être une conséquence de doublets de Champs de Higgs, qui génèrent des représentations physiques, comme le boson de Higgs chargé. Ces bosons sont la déduction directe des extensions du secteur de Higgs du SM.

La production de paires de top avec la désintégration en tau lepton et un état final contenant un tau qui se désintègre hadroniquement est l'un des processus les moins exploré. Une mesure précise du rapport de branchement du quark top en tau représente un outil important pour examiner les propriétés du SM et rechercher les médiateurs qui peuvent intervenir dans cette désintégration du top en lepton tau plus un quark b autres que le boson W; le boson chargé de Higgs serait suivant certains de ces développements théoriques au delà du MS, un autre candidat médiateur possible.

Le processus de désintégration que nous voulons observer est: $t\bar{t} \rightarrow b\bar{\tau}\nu + \bar{b}\tau\bar{\nu}$, où l'un des leptons tau se désintègre leptoniquement en un électron ou en un muon, et l'autre se désintègre hadroniquement en un jet de hadrons. L'analyse présentée dans cette thèse cherche l'existence d'un boson de Higgs chargé comme direct produit de la désintégration du quark top.

Cette thèse est basée sur les données recueillies par le Collider Detector à Fermilab (CDF), expérience située auprès du collisionneur proton-antiproton, le Tevatron, au Laboratoire National, "Fermi National Accelerator Laboratory" (FNAL), en Illinois, aux États Unis. Les données ont été acquises au cours du Run II du Tevatron, qui a duré de 2002 à l'été 2011, avec plus de 10,0 fb^{-1} de luminosité intégrée.

Le cadre expérimental

Le détecteur CDFII [22] est un spectromètre magnétique de symétrie approximativement cylindrique conçu pour effectuer un large spectre de mesures permettant d'étudier un très large éventail de processus physiques. Le détecteur est constitué de plusieurs sous-systèmes spécialisés disposés en couches concentriques.

La partie la plus interne intérieure de CDF est le détecteur de traces chargées, composé du détecteur au silicium et du "Central Outer Tracker" (COT). Le détecteur au silicium est composé de trois sous-unités: le "Layer 00" (L00) [23], le "Silicon Vertex Detector" (SVXII) [24] et le "Intermediate Silicon Layers" (ISL) [25], couvrant la région $|\eta| < 4$ à une distance du tube du faisceau allant respectivement de 1.35 cm à 28 cm. Après les détecteurs en Silicium, se trouve la chambre à dérive, COT, qui permet; la reconstruction précise de la trace correspondant au passage des particules chargées, et la mesure précise de leur impulsion grâce au champ magnétique. Le COT contient 96 couches de fils de détection, qui sont regroupés radialement en groupe de huit *Supercouches*

Les calorimètres de CDF [22] couvre la région $|\eta| < 3.6$. Le secteur central du calorimètre comprend le calorimètre électromagnétique central (CEM) et le calorimètre hadronique central (CHA). Les calorimètres bouchons sont placés dans la région avec $1.1 < \eta < 3.6$ et ils sont composés du "Plug Electronic Calorimeter" (PEM), et du "Plug Hadronic Calorimeter" (PHA). Un calorimètre supplémentaire, le "Wall Hadronic Calorimeter" (WHA), est situé derrière le système CEM/CHA au-dessus des bouchons.

Les détecteurs à muons [26] ont une couverture de $0.03 \lesssim |\eta| \lesssim 1.5$. Le système est divisé dans le "Central MUon detector" (CMU), le "Central Muon uPgrade" (CMP), le 'Central Muon eXtension" (CMX), et le "Intermediate MUon system" (IMU).

Les détecteurs Cerenkov de Luminosité, CLC [28], mesurent la luminosité instantanée et ils sont situés dans la région avant du détecteur.

L'identification des particules

La signature des processus que nous voulons sélectionner contient un électron ou un muon, un jet de hadrons produit par une désintégration du tau et deux jets de hadrons produits par la désintégration du quark b. Les neutrinos représentent une partie invisible des produits de désintégration et leur nombre est de trois, si l'électron (muon) provient directement de la désintégration du boson W, ou cinq si l'électron (muon) provient de la désintégration du tau.

Nous utilisons une classe de déclenchements qui sont généralement désignés comme *lepton plus isolated track*. Cette classe sélectionne un muon CMX ou CMUP avec impulsion transverse $p_T \geq 8$ GeV ou un électron avec un dépôt d'énergie transverse dans le calorimètre $E_T \geq 8$ GeV, avec une trace isolée de $p_T \geq 5$ GeV. La condition d'isolement impose qu'il n'y ait pas de traces avec $p_T \geq 1.5$ GeV dans un anneau d'isolation allant de 10° à 30°,

autour de la trace dite isolée. La luminosité totale est 9.0 fb^{-1}.

Les électrons centraux sont caractérisés par un dépôt d'énergie très étroite ("cluster") dans le calorimètre électromagnétique central, et doit correspondre à une trace provenant du point d'interaction primaire. La fraction électromagnétique du dépôt d'énergie et les informations de la forme de gerbe dans le calorimètre est utilisée pour discriminer le fond. Les candidats électrons sont sélectionnés par un ensemble de conditions caractéristiques constituant désormais leurs critères standards d'identification dans CDF.

Deux catégories différentes de muons sont utilisées dans l'analyse: les muons centraux reconstruits dans le CMU+CMP et dans les détecteurs CMX. L'identification nécessite un dépôt d'énergie dans le calorimètre et une bonne adéquation entre la trace reconstruite par le COT et le passage dans la chambre à muons.

Les particules dites au minimum d'ionisation (MIP), permettent d'exclure le fond. Cette classe de particules peut être des muons qui ne passent pas l'identification standard des muons CMUP ou CMX en raison de l'inefficacité du détecteur ou des zones mortes de détection entre les éléments des systèmes des détecteur de muons. Ils doivent avoir le même dépôt d'énergie dans le calorimètre que les muons.

Pour ce qui concerne la reconstruction et l'identification de tau, nous commençons par le sélection de une tour du calorimètre avec énergie transverse $E_T^{seedtwr} > 6$ GeV. Les tours latérales avec l'énergie $E_T^{shtwr} > 1$ GeV sont ajoutées pour former un cluster calorimètre. Le nombre de tours qui contribuent au cluster devrait être faible, $N^{twr} \leq 6$.

Une trace avec $p_T^{seedtrk} > 4.5$ GeV/c doit être liée à la tour principale. La direction de la trace est ensuite utilisée comme direction pour la sélection off-line des produits de la désintégration du tau.

Un cône qui contient les produits de désintégration du tau est défini avec une amplitude variable $\theta_{sig} = min(0.17, 5.0/E^{cluster}[\text{GeV}])$ rad (cône de signalisation). Les traces et les pions neutres dans le cône sont ensuite utilisés pour calculer le quadri-moment de la désintégration hadronique du tau. C'est ce qu'on appelle le moment visible. Un anneau d'isolation de 30 degrés, entourant le cône de signal, est utilisé pour rejeter les object identifiés par erreur comme tau.

Pour obtenir une bonne reconstruction du moment, nous exigeons que l'intersection de la trace principale ne coïncide pas avec les fissures du calorimètre, $9.0 <\mid Z_{CES} \mid < 230.0$ cm. La reconstruction du moment du tau est ensuite utilisée pour calculer la masse du jet de tau, M^{vis}, qui doit être inférieure à 1.8 GeV/c^2. En outre, une condition est ajoutée afin d'éliminer la contamination des muons mal identifiés, $E/P > 0.4$, où E représente l'énergie du cluster et P est la somme des moments des traces de signal.

La variable ξ' est définie pour supprimer des électrons ou des muons libérant une grande partie de l'énergie électromagnétique dans le calorimètre. Il est défini comme suit:

$$\xi' = \frac{E_{tot}}{\Sigma \mid \vec{p}_i \mid} \left(0.95 - \frac{E_{EM}}{E_{tot}}\right); \tag{1}$$

Les conditions pour sélectionner les candidats tau sont résumées dans le Tableau 1.

Variable	Condition
$E_T^{SeedTwr}$	≥ 6.0 GeV
$p_T^{SeedTrk}$	≥ 6.0 GeV/c ou ≥ 8.0 GeV/c sur l'échantillon avec muon candidates
$E_T^{Cluster}$	≥ 10.0 GeV pour taus avec une trace ou ≥ 15.0 GeV avec trois traces
p_T^{Vis}	≥ 15.0 GeV/c pour taus avec une trace ou ≥ 20.0 GeV/c avec trois traces
$\mid Z_{CES} \mid$	$9 \leq \mid Z_{CES} \mid \leq 230$ cm
Σp_T^{iso}	≤ 2.0 GeV/c
$\Sigma E_T^{\pi^0\ iso}$	≤ 1.0 GeV
p_T^{iso}	≤ 1.5 GeV/c
N^{twr}	≤ 6
ξ'	≤ 0.1
E_{tot}/p	≥ 0.4
M^{vis}	≤ 1.8 GeV/c^2
N^{trk}	$= 1, 3$
Charge	± 1

Table 1: Les conditions pour l'identification des leptons tau.

Il a été démontré que l'efficacité des leptons dans le "lepton plus isolated track" est compatible avec celle mesurée par le "high-p_T" déclenchement [46, 47], qui est fourni par la collaboration CDF.

Pour le tau (le déclenchement de l'objet appelé "trace isolée") nous effectuons une étude sur l'efficacité de déclenchement qui est rapportée dans ce qui suit.

Nous définissons d'abord les jets de hadrons qui passent les conditions d'identification du tau (*objets satisfaisant aux conditions du déclenchement*), qui appartiennent à un échantillon qui n'a pas de biais de déclenchement. Leur nombre est le dénominateur de la mesure d'efficacité. Pour chaque événement enregistré CDF conserve la trace de tous les déclenchements qui sont déclenchés. Si un événement contient des objets satisfaisant aux conditions du déclenchement il est compté dans le numérateur.

Les conditions sur les "traces isolées" ont peu de différences entre les différents types de déclenchement avec un électron ou un muon. Comme conséquence naturelle, nous avons étudié séparément l'efficacité de déclenchement pour la composante du tau dans l'échantillon avec un objet électron et dans l'échantillon avec un objet muon.

Nous avons utilisé deux classes d'échantillons: l'"échantillon d'étalonnage", qui contient les événements avec des électrons ou muons ayant une énergie transverse supérieure à 8 GeV; l'échantillon de "hauts Pt", qui contient les événements avec des électrons ou muons ayant l'énergie transverse ou le moment supérieur à 18 GeV. Nous sélectionnons des événements pour un tel échantillon qui contient les candidats leptons pour la mesure de l'efficacité. Ces événements doivent passer les conditions du déclenchement "lepton plus isolated track". Le Tableau 2 résume la mesure de l'efficacité de déclenchement de niveau

1 à 3 pour la branche tau en utilisant les électrons de haut Pt. Le Tableau 3 présente les résultats obtenus en utilisant des échantillons CMUP, pour respectivement les muons d'étalonnage et les muons de haut Pt.

Échantillons	**Multiplicité des Traces**	**Périodes 0-14**	**Périodes 15-30**	**Périodes 31-35**
haute-p_T	1 trace	0.901 ± 0.009	0.790 ± 0.009	0.864 ± 0.013
	3 traces	0.876 ± 0.008	0.801 ± 0.008	0.867 ± 0.011
étalonnage	1 trace	0.944 ± 0.010	0.819 ± 0.019	0.901 ± 0.023
	3 traces	0.898 ± 0.011	0.856 ± 0.014	0.900 ± 0.018

Table 2: Efficacité de déclenchement de la composante tau, mesurée avec les électrons d'étalonnage et de hauts Pt.

Échantillons	**Multiplicité des Traces**	**Périodes 0-10**	**Périodes 11-35**
high-p_T	1 trace	0.972 ± 0.010	0.929 ± 0.006
	3 traces	0.955 ± 0.010	0.943 ± 0.007
calibration	1 trace	0.973 ± 0.006	0.888 ± 0.006
	3 traces	0.952 ± 0.006	0.907 ± 0.005

Table 3: Efficacité de déclenchement de la composante tau, mesurée avec les muons CMUP d'étalonnage et de hauts Pt.

Les résultats de la mesure de l'efficacité de déclenchement obtenus avec l'étalonnage et l'échantillon à haut p_T sont pour la plupart en accord à l'intérieur de l'incertitude statistique. Dans l'analyse, nous utilisons la valeur moyenne et les écarts sont considérés comme l'incertitude systématique (3%).

Les quarks top devraient toujours se désintégrer en quarks W et b dans le cadre du SM. La masse des hadrons b est petite comparée à l'impulsion, de sorte que les produits de sa désintégration sont émis sous forme de jets. L'énergie attribué à ces jets, "énergie brute" est multipliée par un ensemble de corrections standards dans CDF. Dans notre analyse, nous appliquons la sélection suivante sur les jets:

- $\eta \leq 2.0$
- $E_T > 20$ GeV pour le premier jet, 15 GeV pour le second.
- $E_{EM}/E < 0.9$

où E_{EM}/E représente la fraction de l'énergie électromagnétique du cluster jet et E_T l'énergie transverse corrigée du jet.

On exploite la longue durée de vie du quark de saveur lourde, b, pour identifier les jets provenant de sa désintégration qui sont caractérisés par un vertex secondaire déplacé par rapport au vertex primaire de l'interaction. L'algorithme SECVTX fonctionne séparément par jet. Un vertex déplacé exige au moins deux traces, qui satisfont aux conditions de

qualité des traces chargées et ont un paramètre d'impact non négligeable par rapport au vertex primaire.

L'énergie transverse totale manquante de l'évènement, en dehors de l'erreur de mesure instrumentale, indique la présence de particules qui n'interagissent pas avec la matière du calorimètre comme les neutrinos. Elle correspond à une estimation de la somme des moments des neutrinos. Nous corrigeons l'énergie transverse manquante en tenant compte de:

- les corrections de CDF de l'énergie des jets;
- l'impulsion transverse des muons identifiés et des particules au minimum de ionisation;
- la position du vertex primaire au lieu du centre géométrique du détecteur.

Événements du Signal et de Fond

Nous décrivons dans cette section l'échantillon d'événements simulés les événements de signal et, avant de décrire la sélection des événements nous voulons présenter les processus qui peuvent simuler la signature du signal:

- événements avec les mêmes particules dans l'état final que le signal, à savoir *fond physique* ou *fond irréductible*;
- événements avec différentes particules dans l'état final, mais où l'une des particules est mal identifiée de telle manière que la signature finale se confond avec le signal, à savoir *fond avec des particules mal identifiées.*

Nous estimons le fond physique en utilisant des échantillons de données simulées Nous comptons sur la simulation pour décrire l'acceptance de la sélection globale, mais nous appliquons les facteurs d'échelle pour tenir compte des défauts ou imperfections de la modélisation.

Les événements où les jets induits par la QCD sont identifiés à tort comme les produits de la désintégration du tau sont la principale source de fond. Nous avons développé une technique pour évaluer le fond des jets de hadrons semblables aux produits de désintégration des leptons tau en hadrons: "jet-tau". Il est basé sur le calcul de la probabilité de jets ("fake rate") de passer l'identification du tau. Nous tenons à souligner que cette méthode est complètement basée sur les données. La composante du fond due à des électrons ou à des muons mal identifiés comme taus est évaluée au moyen de données simulées.

Pour guider notre sélection des événements $t\bar{t}$ avec un ou les deux quarks top se désintégrant en tau, nous avons préparé un échantillon d'événements $t\bar{t}$. Ces événements sont générés dans le cadre du Modéle Standard, par la technique de Monte Carlo en utilisant le générateur d'évènements PYTHIA. Pour accroître l'efficacité de la génération nous avons

configuré PYTHIA pour avoir la désintégration du top en leptons, neutrinos et b, avec un rapport d'un tiers pour chacun des trois leptons.

La condition d'un électron ou d'un muon isolé, plus un tau se désintégrant en hadrons permet de sélectionner le fond physique explicite ci-dessous:

- la production de Drell-Yan avec désintégration de Z/γ^* en deux taus, avec une section efficace $\sigma_{Z/\gamma} = 355$ pb^{-1}, $M_{Z/\gamma} \geq 20$ GeV;
- la production de WW avec de deux bosons se désintégrant en leptons, avec une section efficace de: $\sigma_{WW} = 11.3$ pb^{-1};
- la production de bosons comme WZ et ZZ avec le Z (ou W) boson se désintégrant en tau, avec une section efficace de respectivement $\sigma_{WW} = 3.2$ pb^{-1} et $\sigma_{WW} = 3.6$ pb^{-1}.

La condition de deux jets supplémentaires supprime les deux premières sources énumérées ci-dessus, mais les sections efficaces de production du processus de Drell Yan sont telles que ce processus constitue le fond majeur. Nous avons choisi de modéliser cette classe de processus à l'aide du générateur Alpgen car il fournit une bonne description des événements avec une haute multiplicité en jets. La production de deux bosons, WW, WZ et ZZ, est plutôt modélisée à l'aide du générateur PYTHIA.

Le taux de faux ("fake rate") tau a été calculé en utilisant différents échantillons avec des données de jets. Ces données sont collectées avec des déclenchements qui exigent que l'évènement ait au moins un cluster dans le calorimètre avec une énergie au-dessus d'un certain seuil. Le seuil requis sur l'énergie transverse du cluster dans le calorimètre est respectivement de: 20, 50, 70 et 100 GeV (ou une seule tour avec 5 GeV). Les échantillons appartiennent à 4 ensembles de périodes de données, correspondant aux périodes de prise de données de 1 à 4, 9 et 10, de 11 à 13, et de 18 à 28. Ces groupes de périodes ont été choisis parce qu'ils sont correspondent à des différentes régimes de luminosité. Comme la luminosité instantanée du Tevatron n'a pas changé dans les dernières périodes de prise de données, nous avons étendu le résultat obtenu pour des périodes de 18 à 28 à la dernière phase de prise de données correspondant aux périodes 29 à 38.

Nous supprimons l'influence du déclenchement. Nous exigeons que les particules satisfassent les conditions de déclenchement "jets", puis nous rejetons les événements qui ne contiennent qu'un seul des objets qui passent les conditions de ces déclenchements. La suppression de l'influence de déclenchement est appliquée séparément à chacun des trois niveaux du déclenchement.

Nous partons de la sélection des jets sélectionnés avec des conditions relaxées, que nous appelons "fakable tau object". Le jet doit être reconstruit comme un tau et doit passer les conditions définis dans le Tableau 1, sans les conditions sur l'isolement et sur la masse invariante des produits de désintégration du tau.

Les jets de plus haute énergie transverse ont en moyenne un taux, le fake rate, plus élevé que les deuxième jets en énergie transverse. Il peut être souligné que cette propriété

est liée à la fraction de jets de gluons rayonnés dans les deux catégories de jets. Dans cette représentation de l'incertitude systématique est relié à la hiérarchie de l'énergie transverse des jets. Afin de réduire l'incertitude systématique, nous avons paramétré le taux de faux jets tau en fonction de l'énergie transverse, de la pseudorapidité et $|\eta|$ du jet et sur la multiplicité de traces.

Les résultats correspondant à des ensembles de données des périodes 18 à 28 sont présentés dans la figure 1, pour les jets les plus énergétiques et les deuxièmes jets les plus énergétiques. Les résultats, liés au lepton tau avec une seule trace, sont paramétrés en fonction de E_T. Il peut être remarqué que les résultats obtenus avec des échantillons différents de jets sont généralement en accord à l'intérieur de l'incertitude statistique (comme commenté ci-dessus). Le fake rate pour les jets les plus énergétiques et les deuxièmes les

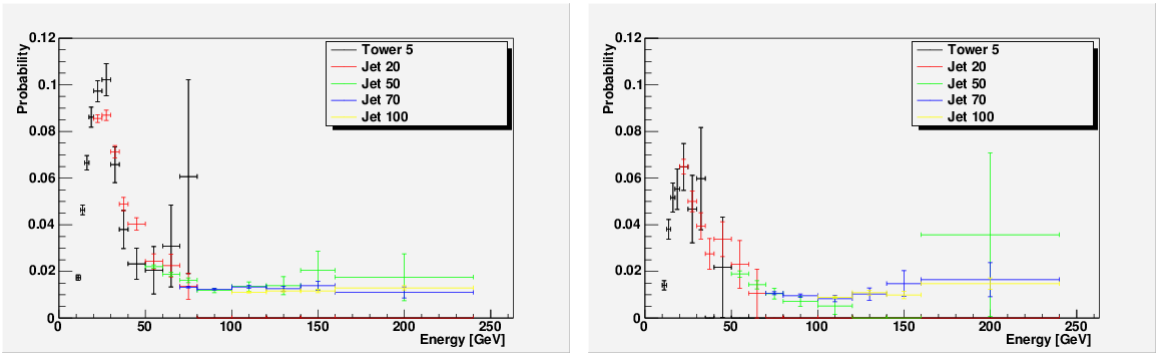

Figure 1: Le taux de faux jets tau pour des périodes de 18 à 28 pour le cas du jet le plus énergétique (à gauche) et le deuxième jet le plus énergétique (à droite). Résultats pour taus avec une trace.

plus énergétiques est obtenu en collectant les valeurs sur chaque échantillon de jet. Les gammes d'énergie considérées sont les suivantes:

- de 10 GeV (ou 15 GeV pour le tau avec 1 trace) à 20 GeV en utilisant l'échantillon base sur les tours de 5 GeV;
- de 20 GeV à 50 GeV en utilisant l'echantillon "Jet 20";
- de 50 GeV à 70 GeV en utilisant l'echantillon "Jet 50";
- de 70 GeV à 100 GeV en utilisant l'echantillon "Jet 70";
- de 100 GeV à 240 GeV en utilisant l'echantillon "Jet 100".

Le fake rate que nous allons utiliser dans notre analyse est la moyenne des résultats obtenus avec les jets les plus énergétiques et les deuxièmes jets les plus énergétiques. La Figure 2 donne la distribution de ces valeurs moyennes. On compare le fake rate du tau dans

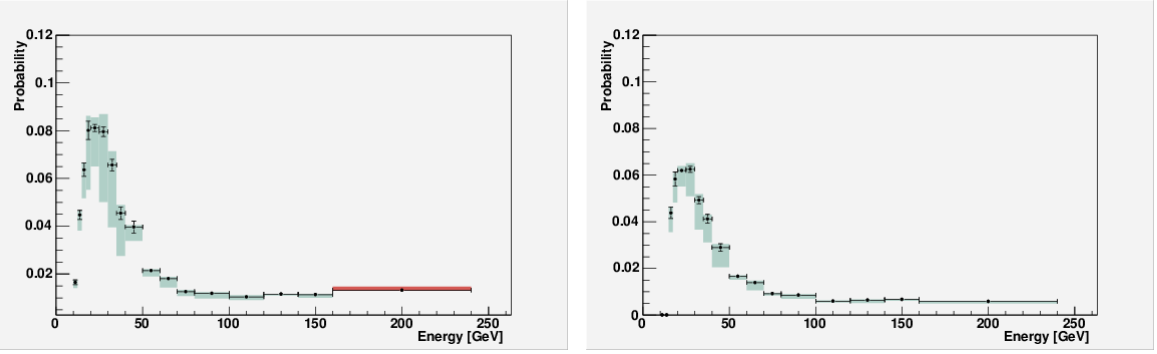

Figure 2: La valeur moyenne du fake pour les périodes de 18 à 28. Sur la gauche, le résultat pour les taus avec une trace, et sur la droite, avec trois traces. La valeur moyenne est calculée à partir du resultat du premier et du deuxième jet.

les différentes périodes de données calculant le rapport entre les mesures correspondant au même échantillon de jet. Le rapport entre les périodes de données n'est souvent pas compatible avec l'unité. Il peut être remarqué que le fake rate à partir des périodes de 18 à 28 est généralement plus élevé que les autres. Nous pouvons en déduire que la luminosité instantanée peut affecter sensiblement la mesure du fake rate de tau.

Nous mesurons le fond en raison de jets mal identifiés comme tau dans les échantillons de leptons d'étalonnage, "Etalonnage électron", "Etalonnage Muon", et l'échantillon "Lepton plus Track". Les premiers deux déclenchements ont déjà été décrits, et l'échantillon "Lepton Plus Track" contient des événements avec des électrons ou muons ayant $p_T \geq 8$ GeV, plus une trace de COT avec $p_T \geq 8$ GeV. L'objet tau dans les échantillons de muons doit avoir $p_T^{seedtrk} \geq 8$ GeV pour se conformer aux conditions de déclenchement de l'échantillon "Lepton Plus Track".

Pour estimer les événements avec des faux leptons tau, nous recueillons des événements avec un électron ou un muon jumelé avec au moins un objet similaire aux leptons tau. Chaque objet est alors considéré comme un possible événement sélectionné pondéré par le taux de faux lepton tau.

La moyenne du fake rate calculé pendant périodes de 1 à 4, 9 et 10, 11 à 13 est utilisé pour des événements appartenant aux périodes de prise de données de 0 à 13, le fake rate calculé dans les périodes 18 à 28 est utilisé pour des événements appartenant aux périodes de prise de données de 18 à 38.

La production d'un boson Z, avec la désintégration $Z \rightarrow ee/\mu\mu$, représente une source possible de fond. Cela se produit lorsque l'un des leptons passe les conditions d'identification tau. Nous estimons le nombre d'événements attendus de fond de cette source à travers des échantillons générés avec ALPGEN.

Nous demandons alors:

- 1 candidat tau et 1 candidat électron ou muon (charges opposées);
- 2 jets;
- $\not\!\!E_T \geq 10$ GeV;
- $H_T \geq 150$ GeV pour d'événements avec des leptons tau à une trace, $H_T \geq 155$ GeV pour d'événements avec des leptons tau à trois traces, ou $H_T = \not\!\!E_T + E_T^{tau} + \sum_i E_T^{jet_i}$, E_T^{tau} est le E_T du cluster du tau, $E_T^{jet_i}$ est le E_T des jets passant les conditions de sélection.

Nous rejetons les processus Drell-Yan. Nous rejetons les événements de l'échantillon d'électrons lorsque des jets avec une fraction de l'énergie électromagnétique égal à 90%, a une masse invariante avec les électrons candidats compatible avec la masse de la résonance Z, $86 \leq M_{inv} \leq 96$ GeV. On rejette les événements de l'échantillon muons lorsque une particule au minimum de ionisation a une masse invariante avec le muon candidat dans les gammes en masse invariante de $76 \leq M_{inv} \leq 106$ GeV et $M_{inv} \leq 15$ GeV.

Résultats de la Sélection

Nous appliquons la sélection décrite dans la section précédente sur tous les échantillons MC. Nous avons évalué le fond avec des particules mal identifiées avec un échantillon d'événements contenants au moins un électron et un jet tau. Les événements qui passent la sélection sont pondérés par la probabilité du jet d'être identifié comme un tau.

Figure 3 montre les caractéristiques des distributions cinématiques des processus de signal, en sommant sur tous les échantillons. Les caractéristiques des événements observées et celles des événements attendues sont en accord dans l'incertitude statistique. Les événements sélectionnés contiennent encore une forte contamination des événements avec faux taus et le fond irréductible du processus Drell-Yan en deux taus. Pour supprimer la contamination nous requérons un vertex secondaire reconstruit par l'algorithme SECVTX.

Après l'application de cette sélection nous obtenons le résultat résumés dans le Tableau 4. On peut remarquer dans la Table 4 que la plupart du fond irréductible est rejeté, et seule reste une petite fraction de Drell-Yan dans les processus avec lepton tau. Après l'application de la condition d'un vertex SECVTX nous observons encore une non négligeable quantité d'événements avec des faux leptons tau. Cela nous a incité à rechercher quelle est la source de ce fond.

Avant de regarder la cinématique des événements pour rechercher les variables qui nous permettent de distinguer le signal et le fond, nous avons besoin de comprendre un peu plus l'origine des événements avec taus mal identifiés. Pour étudier plus en détail les contributions dominantes dans le fond de jets mal identifiés comme lepton tau, nous avons utilisé des échantillons de Monte Carlo de $t\bar{t}$ et de $W + b\bar{b}$. L'étude nous a montré que la contribution la plus importante dans le fond de jets mal identifiés vient de la production de $t\bar{t}$ avec la désintégration d'un W en électrons ou muons et de l'autre W en hadrons.

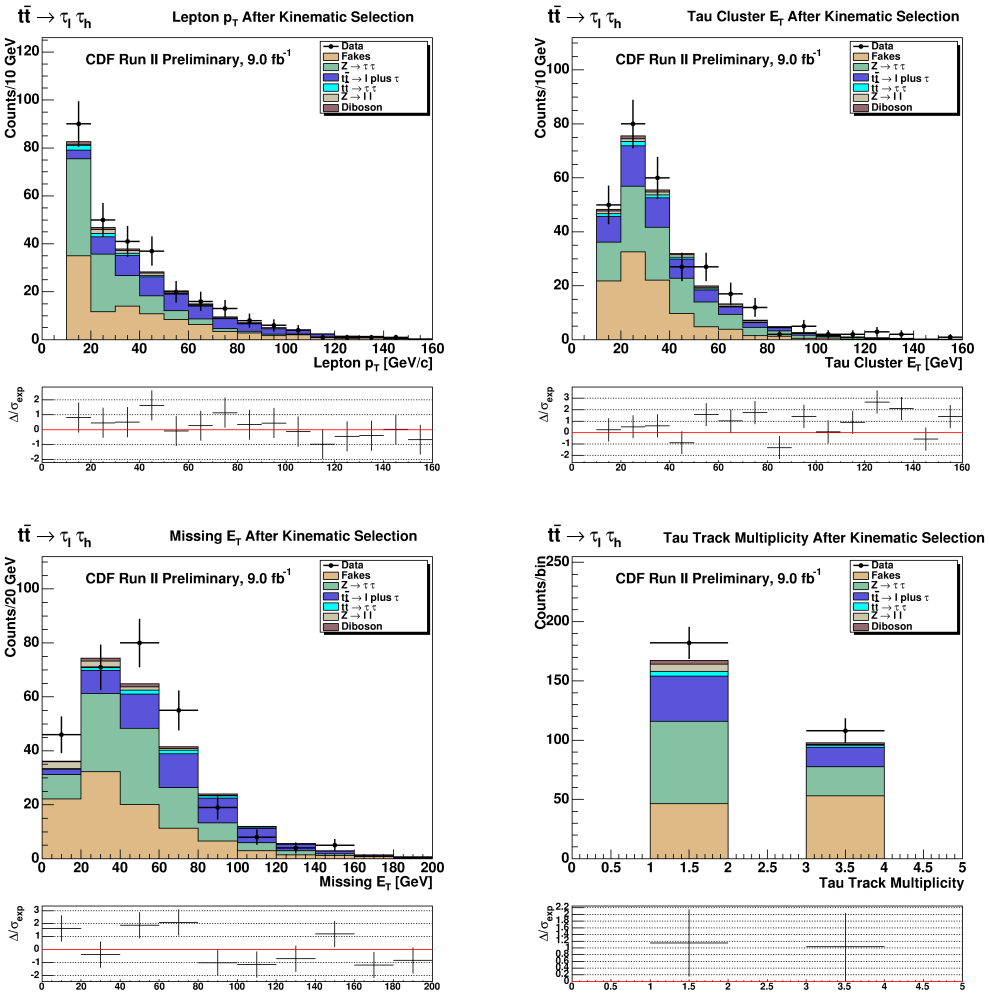

Figure 3: Distribution du E_T des électrons et p_T des muons (en haut à gauche), de cluster E_T des leptons tau (en haut à droite), $\not\!\!E_T$ (en bas à gauche), et la multiplicité des traces des leptons tau (en bas à droite).

Pour séparer la production de $t\bar{t}$ dans le canal de désintégration dilepton avec tau, du fond principal de taus mal identifiés, nous cherchons des variables qui distinguent les deux sources. Les deux variables d'identification du tau plus sensibles aux taus mal identifiés sont le rapport de l'énergie du cluster et le moment des traces et l'isolement du tau, Σp_T^{iso}.

Nous avons également examiné dans la cinématique des événements $t\bar{t}$ désintégrés en un seul lepton et jets et identifié les variables pour les distinguer de nos événements de signal. Nous avons trouvé que variables les plus importantes sont:

Processus	**Échantillon de Muons**	**Échantillon Electron**	**Total**
Faux	5.47 ± 0.59	10.78 ± 1.63	16.25 ± 1.74
$Z/\gamma^* \to \tau\tau$	1.70 ± 0.09	2.17 ± 0.10	3.87 ± 0.14
$Z/\gamma^* \to \ell\ell$	0.15 ± 0.03	0.12 ± 0.01	0.26 ± 0.03
Diboson	0.11 ± 0.02	0.13 ± 0.03	0.24 ± 0.03
$t\bar{t} \to \tau\ell + X$	13.50 ± 0.10	17.46 ± 0.11	30.96 ± 0.15
$t\bar{t} \to \tau\tau + X$	1.44 ± 0.03	1.83 ± 0.04	3.27 ± 0.05
Total Attendu	22.4 ± 0.6	32.5 ± 1.6	54.9 ± 1.7
Observé	18	40	58

Table 4: Événements attendus et données qui passent la sélection cinématique et la condition d'un vertex SECVTX.

- le module de l'énergie manquante transverse,
- la masse transverse du système de l'électron plus $\not\!\!E_T$, $M_T(e, \not\!\!E_T)$,
- l'énergie transverse du troisième jet E_T,

Nous avons intégré dans notre analyse une sélection basée sur la probabilité. La méthode que nous avons mis en oeuvre est connue sous le nom de méthode discriminante du *logarithme de rapport de vraisemblance* (*LLR*): l'outil est facilement obtenu en combinant les modèles de distribution à une dimension de fond et des événements de signal.

Les résultats obtenus avec la sélection de vraisemblance sont résumés dans la Figure 4. Il est possible de constater une réduction significative du fond avec des jets mal identifiés.

L'expérience CDF mesure la luminosité avec les compteurs de luminosité Cherenkov, CLC. L'acceptance des compteurs et la mesure de la section efficace inélastique $p\bar{p}$ sont les incertitudes dominantes dans la mesure de luminosité. L'incertitude totale est $5,9\%$.

Une source d'incertitude systématique est l'incertitude attribuée à la section efficace de chaque processus physique estimé avec des échantillons MC. Le programme MCFM [68] a été utilisé pour calculer les sections efficaces des processus de production de deux bosons (WW, WZ et ZZ) [69]. Il a une incertitude de 6%. L'incertitude expérimentale des événements Drell-Yan est obtenue à partir d'un résultat récent de CDF [64]: 15%.

La gerbe de parton est modélisée différemment dans la simulation MC de PYTHIA et HERWIG. Les différences sont simplement évalués en comparant les efficacités obtenues avec chacun des deux générateurs. Nous avons mesuré l'incertitude systématique de reconnexion de couleur en remplaçant l'échantillon $t\bar{t}$ standard avec deux autres échantillons obtenu avec PYTHIA: Apro et ACRpro. Nous avons également estimé l'effet de deux échantillons $t\bar{t}$ généré par PYTHIA ayant plus de Radiation sur l'État Initial (ISR) et moins de Radiation sur l'État Final (FSR).

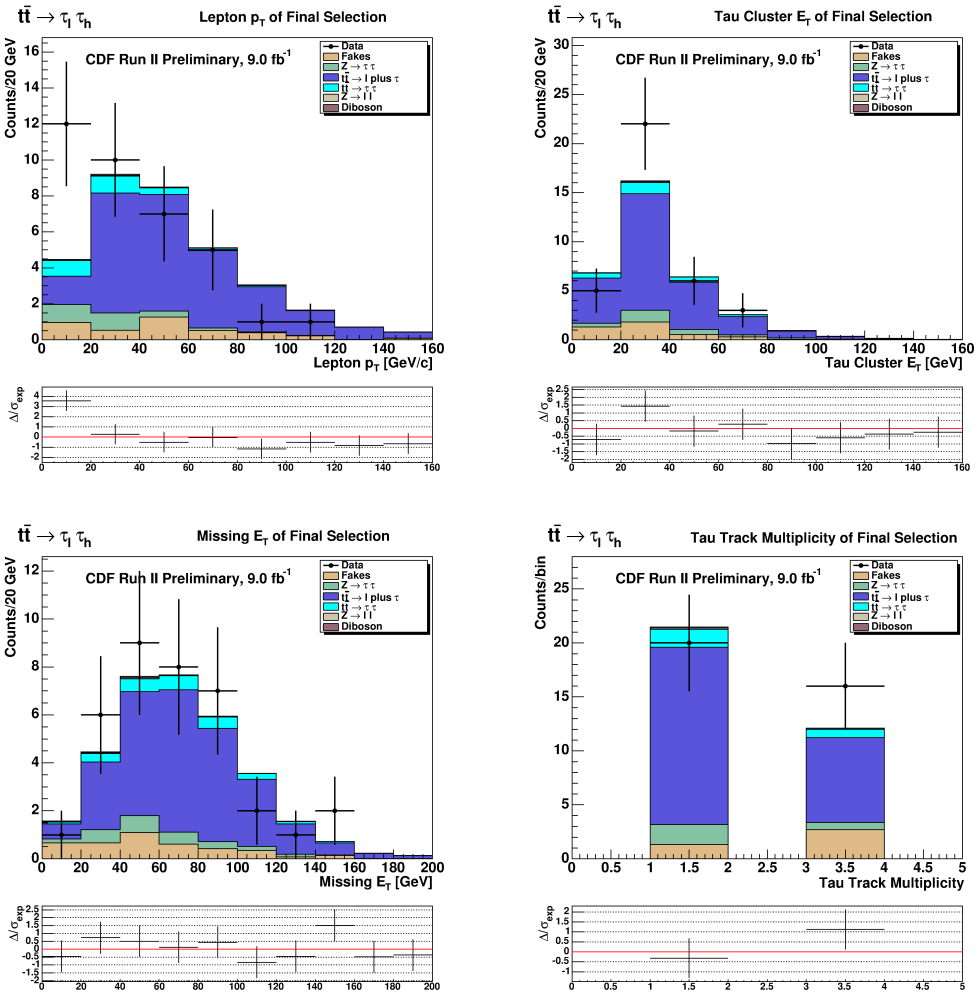

Figure 4: Distribution en E_T des électrons ou p_T des muons (à gauche vers le haut), de E_T du cluster des leptons tau (à droite vers le haut), $\not\!\!E_T$ (à gauche vers le bas), la multiplicité des traces dans le tau (à droite vers le bas). Les résultats obtenus avec la sélection cinématique, un vertex SECVTX et de la variable discriminante LLR.

Nous déterminons l'incertitude systématique due à l'incertitude dans la Fonction de Distribution de Particules (PDF). Les résultats obtenus à partir de l'ensemble de PDF sont contenues dans une variation de $0,5\%$ autour de la valeur nominale.

Les événements avec une vertex secondaire SECVTX doivent être pondérés par $96,0\%$ avec une incertitude systématique égal à 5%. Le nombre de vertex secondaires qui sont mal identifiés sont calculé à partir de la probabilité des jets de être mal identifiés. Dans ce cas l'incertitude systématique est égal à 20%.

Nous appliquons une correction à l'énergie des jets (JEC) dans les données et les échantillons MC. Nous calculons la propagation de l'incertitude en appliquant des changements de $\pm 1\sigma$ à l'échelle de l'énergie. Nous observons de légères fluctuations du nombre d'événements attendu. Les fluctuations ne sont pas statistiquement en accord avec la valeur nominale en le cas des processus Drell-Yan en deux tau et dans échantillons de paires de top. Nous observons une incertitude systématique de 9% pour $Z/\gamma^* \to \tau\tau$, 20% pour $Z/\gamma^* \to \ell\ell$ et les processus de production de dibosons; nous observons une incertitude de 2% et 3%, pour le signal correspondant aux processus respectivement avec lepton plus tau et avec deux taus.

L'évaluation de l'incertitude de l'efficacité de la sélection a été faite en pondérant l'Événements MC sur la base de la multiplicité des vertex primaires. Nous avons généré une distribution de multiplicité de vertex de l'échantillon $t\bar{t}$ MC et deux distributions de multiplicité de vertex des données en correspondance avec régimes de luminosité instantanée haut et basse. Nous avons ponderé chaque événement par le rapport de la distribution du MC e des données. Nous obtenons $\pm 2\%$ d'incertitude pour le processus avec lepton et tau, et $\pm 3\%$ pour le processus ditau.

Les incertitudes systématiques que nous considérons pour la sélection du lepton tau sont trois. La première est relative à la mesure du fake rate et sa propagation dans le nombre attendu d'événements avec des faux lepton tau: $2.20 \pm 0.64^{+0.18}_{-0.48}$, pour l'échantillon avec électrons; $1.80 \pm 0.31^{+0.13}_{-0.31}$, pour l'échantillon avec muons. La seconde est liée à l'incertitude sur les facteurs avec lesquels doit être multipliée l'efficacité de la sélection des événement simulé. Les facteurs d'échelle que nous appliquons sur la sélection MC sont obtenus à partir des études antérieures [47].

La dernière incertitude systématique est l'incertitude dans l'échelle d'énergie de l'énergie hadronique des leptons tau. On change l'échelle par $\pm 5\%$ et les résultats sont compatibles avec celles de la valeur nominale. Puis nous utilisons l'incertitude statistique comme estimation de l'effet sur cette incertitude systématique.

Nous avons analysé la propagation des incertitudes systématiques sur le nombre d'événements attendus après la sélection avec *LLR*. Les événements attendus de fond et des processus de signal sont résumées dans le Tableau 5, où est rapporté l'erreur induite par toutes les incertitudes systématiques.

Résultats

La section efficace de production $t\bar{t}$ multipliée par le rapport de branchement est définie comme suit:

$$\sigma_{t\bar{t}} = \frac{N_{sel} - \sum N^i_{bg}}{\sum_{CMX,\ CMUP,\ CEM} [(BR_{\ell\tau}\epsilon_{\ell\tau} + BR_{\tau\tau}\epsilon_{\tau\tau}) \int \mathcal{L}dt]} \tag{2}$$

où N_{sel} est le nombre d'événements de signal sélectionnés dans le canal lepton plus tau et ditau; N_{bg} est le nombre d'événements attendus de fond; la somme est calculée sur

Processus	**Échantillon de Muons**	**Échantillon de Electrons**	**Total**
Faux	$1.80 \pm 0.31^{+0.13}_{-0.31}$	$2.20 \pm 0.64^{+0.18}_{-0.48}$	$4.01 \pm 0.71^{+0.31}_{-0.80}$
$Z/\gamma^* \to \tau\tau$	$1.12 \pm 0.07 \pm 0.25$	$1.41 \pm 0.08 \pm 0.29$	$2.53 \pm 0.11 \pm 0.53$
$Z/\gamma^* \to \ell\ell$	$0.10 \pm 0.03 \pm 0.03$	$0.03 \pm 0.01 \pm 0.01$	$0.13 \pm 0.03 \pm 0.04$
Diboson	$0.09 \pm 0.02 \pm 0.03$	$0.09 \pm 0.02 \pm 0.03$	$0.17 \pm 0.03 \pm 0.05$
$t\bar{t} \to \tau\ell + X$	$10.56 \pm 0.08 \pm 1.34$	$13.73 \pm 0.10 \pm 1.75$	$24.29 \pm 0.13 \pm 3.09$
$t\bar{t} \to \tau\tau + X$	$1.07 \pm 0.03 \pm 0.14$	$1.37 \pm 0.03 \pm 0.18$	$2.44 \pm 0.04 \pm 0.32$
Total Attendu	$14.7 \pm 0.3^{+1.6}_{-1.7}$	$18.8 \pm 0.6^{+2.1}_{-2.1}$	$33.6 \pm 0.7^{+3.7}_{-3.8}$
Observé	12	24	36

Table 5: Événements attendus et événements de données qui passent la sélection cinématique ainsi que les conditions d'un vertex secondaire SECVTX et $\ln(LR) > 0$.

les catégories de leptons utilisés dans notre analyse, à savoir l'électron reconstruit avec le détecteur CEM et le muon avec les chambres à muons CMUP et CMX; $BR_{\ell\tau}$ représente le produit combinatoire de rapport de branchement de la désintégration du quark top en électrons ou muons, $BR(t \to \ell\nu b)$, et la désintégration du quark top en tau hadronique $BR(t \to \tau\nu b) \cdot BR(\tau \to \text{jet}\nu)$; $BR_{\tau\tau}$ est le rapport de branchement de la désintégration du quark top en tau leptonique et tau hadronique; $\epsilon_{\ell\tau}$ et $\epsilon_{\tau\tau}$ sont les efficacités global de sélection pour les canaux ditau et lepton tau.

Pour obtenir la mesure de la section efficace de production de paires de quarks top, $t\bar{t}$, nous supposons que le rapport de branchement de top en W et b est égal à 100% et utilisons les rapport de branchement du tau en électrons ou muons comme indiqué dans le PDG [7]. Nous obtenons un section efficace de

$$\sigma_{t\bar{t}} = 8.2 \pm 1.7(stat.)^{+1.2}_{-1.1}(syst.) \pm 0.5(lum.) \text{ pb}. \tag{3}$$

Notre mesure de la section efficace du $t\bar{t}$ est en bon accord avec d'autres combinaisons de tous les canaux leptonique et dileptonique de CDF, $\sigma_{t\bar{t}} = 7,5 \pm 0,5$ pb, et DØ, $\sigma_{t\bar{t}} = 7,6 \pm 0,6$ pb.

La mesure du rapport de branchement de la désintégration du $t \to \tau\nu b$ est obtenu en utilisant comme signal la catégorie d'événements avec un lepton et un tau. Le rapport de branchement est donné par l'équation suivante:

$$BR(t \to \tau\nu b) = \frac{1}{2BR(W \to \ell\nu)} \frac{N_{sel} - \sum_i N^i_{bg}}{\sigma_{t\bar{t}} \sum_{CMX,\ CMUP,\ CEM} \epsilon_{\ell\tau} \int \mathcal{L}dt}. \tag{4}$$

Nous avons considéré aussi l'incertitude de la section efficace de production de paire de top expérimentale. Nous utilisons la plus récente combinaison de CDF, $7,5 \pm 0,5$ [70]. Nous avons calculé la propagation de l'incertitude systématique dans le rapport de branchement: $BR(t \to \tau\nu b)$. Le résultat est

$$\sigma_{t\bar{t}} \times (BR_{\ell\tau} + BR_{\tau\tau}) = 0.145 \pm 0.030(stat)^{+0.022}_{-0.019}(syst.) \pm 0.008 \text{ pb}, \tag{5}$$

en bon accord avec les prévisions théoriques sur le processus de désintégration $t \to Wb$ et les valeurs du rapport de branchement de désintégration du boson W [7]:

$$BR(t \to \tau\nu b) = 0.120 \pm 0.027(stat.)^{+0.022}_{-0.019}(syst.) \pm 0.007(lum.), \tag{6}$$

Notre mesure du rapport de branchement $BR(t \to \tau\nu b)$ indique que nous pouvons limiter le rapport de branchement $BR(t \to H^{\pm}b)$, car dans le MSSM le processus $H^{\pm} \to \tau\nu$ est le favori pour $\tan(\beta) > 1$ et $M_{H^{\pm}} < M_t$. Notre analyse nous permettra d'estimer les limites des paramètres du boson de Higgs chargé.

Pour discriminer la signature de la désintégration lepton tau de processus ditau et effectuer une mesure du rapport de branchement de la désintégration du quark top en tau, nous avons construit une autre discrimination basé sur le logarithme du rapport de vraisemblance (défini par LLR') pour séparer les deux processus. Nous utilisons la distribution de la masse transversale de l'électron (ou muon) et de l'énergie transverse manquante, l'angle azimutal entre l'électron et l'énergie transverse manquante, énergie transverse (impulsion transverse) de l'électron (ou du muon).

Les modèles utilisés sont obtenus avec l'échantillon d'événements de la simulation MC. Nous demandons la sélection cinématique, un vertex secondaire SECVTX et $\ln(LR) > 0$. Nous représentons dans la Figure 5 la distribution des événements de données par rapport aux données simulées en fonction de la variable $\ln(LR)$.

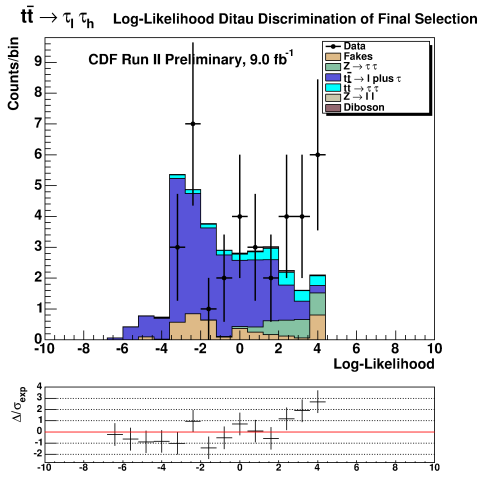

Figure 5: La comparaison des données et des événements attendus en fonction de la variable $\ln(LR)$ en utilisant des échantillons de données avec des électrons et des muons.

Avec un ajustement aux données des distributions de $\ln(LR)$ nous obtenons

$$BR(t \to \tau\nu b) = 0.098 \pm 0.022(stat.) \pm 0.014(syst.) \tag{7}$$

L'étude rapportée dans ce travail de thèse est motivé par un double objectif. En premier lieu une mesure du processus de production de paires de top en lepton plus tau, canal très peu étudie jusqu'à présent car très difficile à misurer expérimentalement. L'étude de ce processus dans cette voie de désintégration du top, a été limitée jusqu'ici, par le faible rapport de branchement, la difficulté de la sélection de cette signature et le fond élevé dû aux jets mal identifiés qui passent la sélection du lepton tau. En second lieu ce processus donne une ouverture sur la recherche de phénomènes au delà du Modèle Standard, par son étude sur une signature caractéristiques de tels processus nouveaux dans la troisième génération de fermions.

Avec l'échantillon complet des données, on obtient la mesure la plus précise de la production de paires de top dans le canal de désintégration en deux leptons charges avec un lepton tau. Le résultat de cette mesure est en bon accord avec celles effectuées dans d'autres voies de désintégration des paires de top au Tevatron. De plus le résultat est compatible avec les prévisions théoriques du Modèle Standard, dans la limite des incertitudes expérimentales.

Nous utilisons la distribution des événements dans la variable logarithme de vraisemblance pour extraire une mesure du rapport de branchement $BR(t \to \tau\nu b)$. De cette façon nous obtenons une mesure indépendant de l'hypothèse sur le rapport de branchement de la désintégration du quark top en électrons ou muons.

Introduction

The discovery of the top quark is one of the great achievements of the CDF and DØ experiments. It was made possible using the $p\bar{p}$ collisions of the Tevatron Collider located at the Fermi National Accelerator Laboratory, in the United States. The Tevatron Run I and Run II research projects allowed the measurement of several properties of the top quark such as the production cross section, mass and decay branching ratios.

The mass of the top quark is over two orders of magnitude higher than any other known constituent of matter. Its dominant production at hadron colliders is through QCD processes that emit top pairs, $q\bar{q} \to t\bar{t}$ and $gg \to t\bar{t}$. The consequence is that the production cross section of top quarks is extremelly small and some of its properties are still not fully explored.

Measurement of top production and decay have been in good agreement with the present model universally accepted for describing particle interactions. This model, known as "Standard Model" (SM), has been the most successful synthesis of theoretical and experimental studies of the second half of the 20th century.

Despite its success, the SM contains an inconsistency in the term describing the longitudinal WW scattering. The cross section of this process grows with the momentum exchanged and the unitary of the SM is violated at the energy scale of the order of TeV. The recently observed Higgs boson will fix this. Several beyond the Standard Model theories incorporate in addition to this Higgs boson new particles and interactions. The interactions may be a consequence of doublets of Higgs fields, that generate physical representations like the charged Higgs boson. These boson states are a direct deduction of SM extensions like supersymmetric models. The minimal formulation of these models, the Minimal Supersymmetric Standard Model (MSSM), requires at least two Higgs doublets that imply the existence of a pair of charged Higgs bosons.

Top pair production with decay into tau and a final state containing a hadronic tau decay is one of the least explored processes. A precise measurement of the branching ratio of top quark into tau represents one important tool to test the properties of the SM and search for unobserved mediators that interact with both the top and the tau fields. The charged Higgs boson is one possible candidate.

The decay process we want to observe is $t\bar{t} \to b\bar{\tau}\nu + \bar{b}\tau\bar{\nu}$, where one of the tau decays leptonically in an electron or a muon, and the other decays hadronically into a jet of

hadrons. We select lepton plus tau events which contain missing transverse energy, due to the emission of the neutrinos, and at least 2 hadronic jets from the b quark decays. The analysis presented in this thesis investigats the existence of a charged Higgs boson as a direct product of the top quark decay.

This thesis is based on the data collected by the Collider Detector at Fermilab (CDF) experiment, located in the Fermi National Accelerator Laboratory, Batavia, Illinois. The data was acquired during Run II, that extended from 2002 through the summer 2011, corresponding to 10.0 fb^{-1} of integrated luminosity.

Chapter 1

Theoretical Motivations

The "Standard Model" (SM) has represented so far the most elegant synthesis of the work made by theoretical and experimental particle physicists in the past half century. It brings together the human understanding of three forces of nature: the Weak, the Electromagnetic and the Strong interaction. We are going to describe it focusing our attention to the Electroweak part and the Spontaneous Symmetry Breaking. We are then going to briefly illustrate the open problems of the SM and the possible solutions obtained with supersymmetric models.

1.1 The Standard Model

The SM is a quantum field theory and describes the dynamics of the fundamental constituents of the Universe, the elementary particles. The model describes the particles as quantized fields and their interactions are expressed in terms of Lagrangian density. The basic concept in its formulation is that the dynamics derive from the symmetry principle, as proven by the theorem of Noether.

The Lagrangian of the SM is set so that the corresponding action does not change under local gauge transformations of the fields. The gauge symmetry group of the model is $\mathrm{SU}(3)_C \times \mathrm{SU}(2)_L \times \mathrm{U}(1)_Y$ where the terms indicate the irreducible subgroups associated to the color charge, the weak isospin and the hypercharge.

The model accomodates three generations of fermion fields, which are the constituents of the matter. These particle are summarized in Table 1.1.

All the fermions are subject to the electro-weak dynamics described by the so called Glashow-Salam-Weinberg Model [1]. They are divided in two groups "leptons" and "quarks"; the latter group of particles interacts also through the strong interaction.

The interaction are mediated by $8 \oplus 3 \oplus 1$ gauge bosons and a scalar field (the Higgs boson) necessary to motivate the phenomenon known as Spontaneous Symmetry Breaking at the Fermi scale.

	Electric Charge	1st generation	2nd generation	3rd generation
quarks	+2/3	u	c	t
	-1/3	d	s	b
leptons	0	ν_e	ν_μ	ν_τ
	-1	e	μ	τ

Table 1.1: Table summarizing the physical states of the fermion fields in the SM.

1.1.1 The Lagrangian of Quantum Electrodynamics

The general Lagrangian of a Dirac free fermion field ψ is expressed by

$$\mathcal{L} = i\bar{\psi}\gamma_\mu\partial^\mu\psi - m\bar{\psi}\psi, \tag{1.1}$$

where the first is the kinetic term the second the mass term. The requirement of invariance of the Lagrangian under a global trasformation imply that the action does not change under the trasformation of the fields $\psi(x) \rightarrow e^{iq\alpha}\psi(x)$. This kind of invariance results in a charge conservation, without interaction terms.

The interactions in the SM are generated requiring the Lagrangian to be invariant under local gauge trasformations, for example the U(1) trasformation $\psi(x) \rightarrow e^{iq\alpha(x)}\psi(x)$, where now the phase *alpha* depends on the time-space coordinates. If we insert the trasformed fields in the Dirac Lagrangian 1.1 we obtain

$$\mathcal{L} = i\bar{\psi}\gamma_\mu(\partial^\mu + iq\partial^\mu\alpha)\psi - m\bar{\psi}\psi. \tag{1.2}$$

So the Lagrangian 1.1 is not invariant. If we intend to obtain a Lagrangian invariant under local gauge trasformation we have to modify the standard derivative introducing the so called covariant derivative, which should transform like *phi*: $D^\mu\psi(x) \rightarrow e^{iq\alpha(x)}D^\mu\psi(x)$. This is accomplished with

$$D^\mu \equiv \partial^\mu + igA^\mu, A^\mu \rightarrow A^\mu + \frac{1}{q}\alpha(x). \tag{1.3}$$

The new Lagrangian we obtain with the covariant derivative is

$$\mathcal{L} = \bar{\psi}(i\gamma_\mu\partial^\mu - m)\psi + q\bar{\psi}\gamma_\mu\psi A^\mu, \tag{1.4}$$

which is now invariant under local gauge transformation. The vector field A^μ introduced by demand of a local phase invariance in called gauge field. As we anticipated the request of local gauge symmetry introduce an interaction term $q\bar{\psi}\gamma_\mu\psi A^\mu$ which can be regarded as the electromagnetic interaction of the electron field with the vector photon field. From

this point of view, the Lagrangian 1.4 is still incomplete because a new term corresponding to the photon kinetic term should be added. We need a term that is invariant under the trasformation in 1.3 and the only available term is the gauge invariant field tensor: $F^{\mu\nu} \equiv \partial^\mu A^\nu - \partial^\nu A^\mu$.

We obtain the local U(1) invariant Lagrangian in the following form:

$$\mathcal{L} = \bar{\psi}(i\gamma_\mu \partial^\mu - m)\psi + q\bar{\psi}\gamma_\mu \psi A^\mu - \frac{1}{4}F^{\mu\nu}F_{\mu\nu}, \tag{1.5}$$

We modified the free Dirac Lagrangian to be invariant under the request of a U(1) local symmetry and we obtained the Lagrangian describing the electromagentic interactions. The request of other local gauge trasformations imply the introduction of other interaction terms. Introduction of other group of trasformation of the fields we can accomodate in a single Lagrangian the interactions of the weak and strong interaction. This is one of the fundamental aspects of the SM Lagrangian formulation and we are going to introduce this property in the next sections.

1.1.2 Electro-weak Theory

The first efforts to explain the weak interaction brought the introduction of a symmetry group $SU(2)_L$; where the index L reminds that the weak interaction couples only to left handed fermions. We know that parity is maximally violated in weak interactions since only left-handed particles participate in charged weak interactions. The left-handed fields transform as doublets under $SU(2)_L$, the right-handed fermions as singlets. The left-handed fermions of the first generation are usually represented in the following way:

$$q_L = \begin{pmatrix} u_L \\ d_L \end{pmatrix}, \quad l_L = \begin{pmatrix} \nu_L \\ e_L \end{pmatrix}. \tag{1.6}$$

The right-handed fermions are instead

$$e_R, \quad u_R, \quad d_R. \tag{1.7}$$

The invariance under local trasformation generates the interaction of a triplet of weak gauge bosons with a triplet of fermion currents defined by

$$J^i_\mu(x) = \bar{\chi}_L \gamma_\mu \frac{1}{2}\sigma^i \chi_L \tag{1.8}$$

where σ_i are the usual Pauli matrices and χ_L is the doublet of left handed fermions (leptons in this case):

$$\chi_L = \begin{pmatrix} \nu_\ell \\ \ell \end{pmatrix}. \tag{1.9}$$

The current $J^3_\mu(x)$ represents the neutral current, while $J^1_\mu(x)$ and $J^2_\mu(x)$ are the linear combinations of the positive and negative charged currents. The gauge bosons associated to the $SU(2)_L$ symmetry are expressed as W^i_μ. For each current we can associate a charge obtained integrating the 0 component over the space:

$$T^i = \int J^i_0(x) d^3x \tag{1.10}$$

and it can be shown that the charges satisfy the anticommutation property $[T^i, T^j] = i\epsilon_{ijk}T^k$. The linear combination of the currents $J^1_\mu(x)$ and $J^2_\mu(x)$ well describe the charged weak interaction, but what is experimentally known that the electromagnetic current J^{em}_μ does not have the properties of the neutral current J^3_μ.

This problem is solved once a weak hypercharge is postulated, introducing the symmetry group $U(1)_Y$. With this new interaction the electromagnetic interaction can be described as the exchange of the combination between the W^3_μ and the B_μ boson associated with the $U(1)_Y$. Together with the electromagnetic current a new kind of physics processes were assumed between the neutral current J^{NC}_μ and a new vector boson.

For what concern the electromagnetic charge and current, we have:

$$Q = T^3 + \frac{Y}{2}, \text{ and} \tag{1.11}$$

$$J^{em}_\mu = J^3_\mu + \frac{1}{2}J^Y_\mu. \tag{1.12}$$

Since the J^Y_μ represent a singlet under $SU(2)_L$ group the entire symmetry group of the electro-weak interaction is given by $SU(2)_L \otimes U(1)_Y$ and the $U(1)_q$ group of the electroweak interaction is contained in it.

The interaction term of the fermions with the gauge bosons in the electro-weak Lagrangian is

$$\mathcal{L} = gJ_\mu W^\mu + \frac{g'}{2}J^Y_\mu B^\mu. \tag{1.13}$$

If we substitute the gauge bosons with their physical states

$$W^\pm_\mu = \frac{1}{\sqrt{2}}(W^1_\mu \pm iW^2_\mu), \tag{1.14}$$

$$Z_\mu = cos(\theta_w)W^3_\mu - sin(\theta_w)B_\mu, \tag{1.15}$$

$$A_\mu = sin(\theta_w)W^3_\mu + cos(\theta_w)B_\mu, \tag{1.16}$$

where θ_W is defined such that $\tan(\theta_W) = g'/g$; and we define the currents as

$$J_\mu^\pm = \bar{\phi}_L \gamma_\mu \sigma^\pm \phi_L \quad (1.17)$$
$$J_\mu^3 = \bar{\phi}_L \gamma_\mu \sigma^3 \phi_L \quad (1.18)$$
$$J_\mu^{em} = \bar{\phi} \gamma_\mu Q \phi \quad (1.19)$$

we can rewrite the Lagrangian 1.13 in the following way:

$$\mathcal{L} = \frac{g}{\sqrt{2}}(J_\mu^- W^{\mu-} + J_\mu^+ W^{\mu+}) + \frac{g}{\sqrt{\cos(\theta_W)}}(J_\mu^3 - \sin^2(\theta_W) J_\mu^{em}) Z^\mu + g \sin(\theta_W) J_\mu^{em} A^\mu. \quad (1.20)$$

The last term in the Lagrangian 1.20 gives the photon coupling to the electromagnetic currents and we can recognize the electric charge $e = g\sin(\theta_W)$ Moreover if we interpret the weak interaction in the context of the Fermi coupling, in which four fermions directly interact with one another at one vertex, we obtain a prediction on the W and Z boson masses:

$$m_W = \left(\frac{g^2\sqrt{2}}{8G_F}\right)^{1/2} = \left(\frac{e^2\sqrt{2}}{8G_F \sin(\theta_W)}\right)^{1/2} \quad (1.21)$$
$$m_Z = \frac{m_W}{\cos(\theta_W)} \quad (1.22)$$

After the formulation of the Glashow-Salam-Weinberg theory (GSW) of the electroweak interaction, many experimental results confirmed and measured the parameters of the model. First, in 1973, the neutral current interactions was observed with the Gargamelle bubble chamber [2]. It photographed the tracks of a few electrons after the interaction with neutrinos. Few years later a first relatively precise measurement of the $\sin(\theta_W)$ was available, 0.24 ± 0.02 [3], which allowed to predict the $W^\pm$ and Z^0 boson masses. The electro-weak bosons were first directly produced by the collisions at the Super Proton Synchrotron, at CERN. The signals of W bosons were seen in January 1983 and the Z boson was discovered a few months later, in May 1983, with the experiments UA1 [4] and UA2 [5].

1.2 The Lagrangian of the Quantum Chromodynamics

The strong interaction is based on the invariance under the $SU(3)_C$ symmetry group. The conserved charge of this force is called color and there are three possible values of this charge (three degrees of freedom). The QCD Lagrangian can be written in the form:

$$\mathcal{L}_{\mathrm{QCD}} = i \sum_{i,j} \bar{q^i}(\gamma^\mu D_\mu - m_q) q^j - \frac{1}{4} F_{\mu\nu}^\alpha F_\alpha^{\mu\nu}, \quad (1.23)$$

where the quark fields are represented by triplets. The covariant derivative to be embended in the Lagrangian is given by

$$D_\mu = \left(\partial_\mu - ig_s \frac{\lambda_\alpha}{a} A_\mu^\alpha\right). \tag{1.24}$$

The terms λ_α are the generators of the SU(3)$_C$ group, which are 3×3 traceless Hermitian matrices. The gauge fields A_μ^α represent the 8 gluon fields ($\alpha = 1, ..., 8$). The field strength tensor of the gluon is

$$F_{\mu\nu}^\alpha \equiv \partial_\mu A_\nu^\alpha - \partial_\nu A_\mu^\alpha + g_s f^{\alpha\beta\gamma} A_{\mu\beta} A_{\nu\gamma} \tag{1.25}$$

The strong interaction differs from the electro-weak for the term $g_s f^{\alpha\beta\gamma} A_{\mu\beta} A_{\nu\gamma}$, which arises from the coupling among gluons.

The peculiar property of the QCD is that neither quarks nor gluons are observed as free particles ("confinement"). Hadrons are color singlet combinations of quarks and antiquarks.

1.2.1 The Higgs Field

We have seen that the gauge boson have a mass that should be considered in the SM Lagrangian. Any non-null term of the form $m_W W^\mu W_\mu$ would destroy the invariance under the group SU(2)$_L$⊗U(1)$_Y$. This means that without any mechanism that could explain the gauge boson mass, the GSW model is in clear contradiction with the experimental evidence. The direct insertion of the boson mass terms would indeed cause unrenormalizable divergencies that would spoil the agreement between theory and observation.

Peter Higgs et al. [6] found a solution to this unconsistency postulating a scalar field ϕ, doublet under SU(2)$_L$, with non-vanishing vacuum expectation value. This mechanism, introduced in the SM, is known as the Higgs mechanism of the Spontaneous Symmetry Breaking. It can introduce the observed mass terms of the $W^\pm$ and Z^0 bosons without violating the gauge invariance.

We can add to the Lagrangian the kinetic and potential term of the form

$$\mathcal{L}_H = (D_\mu \phi)^\dagger (D^\mu \phi) - V(\phi), \tag{1.26}$$

where the simplest renomalizable potential is of the form $V(\phi) = \mu \phi^\dagger \phi + \lambda (\phi^\dagger \phi)^2$ and ϕ is doublet of scalar fields, known as Higgs field, with hypercharge $Y = 1$

$$\phi = \begin{pmatrix} \phi^+ \\ \phi^0 \end{pmatrix}. \tag{1.27}$$

If $\mu^2 < 0$ and $\lambda > 0$ the potential shows a minimum where the field has a non-zero vacuum expectation value (VEV):

$$\langle \phi_0 \rangle = \langle 0|\phi|0\rangle = \frac{v}{\sqrt{2}} \tag{1.28}$$

To obtain a theory in which the $W^{\pm}$ and Z^0 bosons have mass while the electromagnetic field is massless we have to choose a ground state of the field such that:

$$\phi = \frac{1}{\sqrt{2}} \begin{pmatrix} 0 \\ v \end{pmatrix} \tag{1.29}$$

In order to preserve the invariance under $\mathrm{SU}(2)_L \otimes \mathrm{U}(1)_Y$ the covariant derivative D_μ must be

$$D^\mu = \partial_\mu + igT \cdot W_\mu + \frac{g'}{2} Y B_\mu. \tag{1.30}$$

Expanding the field ϕ around its vacuum expectation value and substituting the covariant derivative in the Lagrangian 1.26 we finally obtain tree level masses for the gauge bosons:

$$(D_\mu \phi)^\dagger D^\mu \phi = \frac{g^2 v^2}{4} W_\mu^+ W^{-\mu} + \frac{(g^2 + g'^2) v^2}{8} Z_\mu Z^\mu + ... \tag{1.31}$$

while the the Higgs field itself gets a mass from the potential $V(\phi)$, which becomes $V(\phi) = 2\mu^2 H^2 + ...$ It could be noticed that while the value of the parameter v can be obtained from the $W^{\pm}$ and the Z^0 boson masses, the mass of the Higgs boson, depending on λ, remains unconstraint from other measurements.

We can now insert terms in the Lagrangian that describe the interaction of fermion fields with the Higgs field. The terms are scalars under the gauge group of the SM and can be written as

$$\mathcal{L}_Y = \sum_{generations} \bar{Q}_L^i \lambda_u^{ij} \phi^\dagger u_R^j + \bar{Q}_L^i \lambda_d^{ij} \phi d_R^j + \bar{L}_L^i \lambda_e^i j \phi e_R^j + \bar{L}_L^i \lambda_\nu^i j \phi \nu_R^j \tag{1.32}$$

where λ_u^{ij}, λ_d^{ij}, λ_e^{ij}, λ_ν^{ij} are arbitrary matrices 3×3. The interactions we wrote are mass terms and we have written the Lagrangian $\mathcal{L}_Y$ in such a way that neutrino masses are included. The λ matrices can be diagonalized with the use of biunitary transformations

$$U_L^\dagger \lambda_{u,d,e} U_R = \lambda_{u,d,e}^{Diag.}, \tag{1.33}$$

to make the mass terms of quarks and lepton explicit. It is important to notice that such transformations should be applied also on the kinetic term, which contains the fermion interaction with the vector bosons. The neutral and the electro-magnetic currents remain flavor diagonal also in the mass eigenbasis. The charged current, instead, is no longer diagonal and can be expressed as

$$J^{\mu} = \bar{d}'_L \gamma_\mu U_L^{d\dagger} U_L^u u'_L + \bar{e}'_L \gamma_\mu U_L^{e\dagger} U_L^\nu \nu'_L \tag{1.34}$$

where the primed fields are the rotated one. The unitary matrices $U_L^{d\dagger}U_L^u$ and $U_L^{e\dagger}U_L^\nu$ are not generally diagonal and induce interactions of the charged vector bosons with a fermion current that interchange the generations. The matrix $U_L^{d\dagger}U_L^u$, in particular, interchanges the quark generations and is known as Cabibbo, Kobayashi and Maskawa matrix, V_{CKM} [8, 9].

The V_{CKM} is a 3×3 unitary matrix where the terms are generally indicated by

$$\begin{pmatrix} V_{ud} & V_{us} & V_{ub} \\ V_{cd} & V_{cs} & V_{cb} \\ V_{td} & V_{ts} & V_{tb} \end{pmatrix}. \tag{1.35}$$

It is experimentally known that elements in the diagonal are close to 1. The off diagonal elements V_{cd} and V_{us} are about $sin(\theta_C)$ where $\theta_C \simeq 13^\circ$ is the called Cabibbo angle and the remaining ones are of the order of few percent or less.

1.2.2 Top Quark

The top quark belongs to the heaviest generation of quarks and is the member of a weak-isospin multiplet with quantum numbers $Q = 2/3$ and $T^3 = +1/2$. At the Tevatron top quarks are produced dominantly in pairs trough QCD processes $q\bar{q} \rightarrow t\bar{t}$ and $gg \rightarrow t\bar{t}$, whose diagrams at tree level are showed in Figure 1.2.2.

At the Tevatron about 85% of top pairs are produced by $q\bar{q}$ annihilation and the remaining by gluon-gluon fusion. Figure 1.2 shows the results of the production cross section calculation as function of top quark mass. The results are obtained at second order interaction diagrams and use different parton distribution functions (PDF).

Top decay with Ws and Wd final states are expected to be suppressed. The decay brancing ratios are respectivelly of the order of $(V_{ts})^2$ and $(V_{td})^2$ where V_{ts} and V_{td} are the element of the CKM matrix. The unitary condition of the matrix together with the direct measurement of some elements implies that the diagonal term $V_{tb} > 0.999$. In the SM picture, and the mass of the top quark higher than the mass of the W boson plus b quark, the decay width is dominated by the two body decay $t \rightarrow Wb$ and is

$$\Gamma_t \simeq \frac{G_F m_t^3}{8\pi\sqrt{2}} \left(1 - \frac{M_W^2}{m_t^2}\right)^2 \left(1 + 2\frac{M_W^2}{m_t^2}\right) \left[1 - \frac{2\alpha_2}{3\pi}\left(\frac{2\pi^2}{3} - \frac{5}{2}\right)\right], \tag{1.36}$$

where m_t and M_W refer respectivelly to the top quark mass and W boson mass, G_F and α_s to the Fermi constant and the strong interaction coupling constant. The width Γ_t is 1.32 GeV/c^2 for a top mass $m_t = 172.5$ GeV/c^2 and corresponds to a lifetime of $\approx 10^{-24}$ s. The decay width implies that the top quark decays even before top flavored hadrons can form.

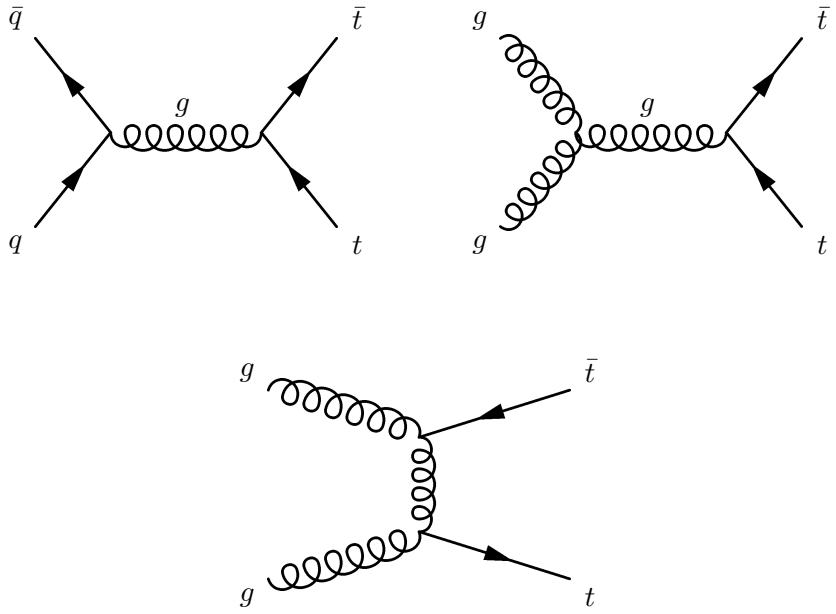

Figure 1.1: Top pair production diagrams at tree level.

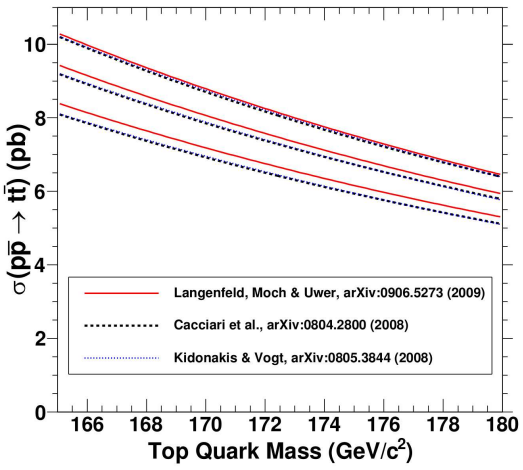

Figure 1.2: NLO calculation of the $t\bar{t}$ cross section as function of top quark mass.

The final states for top pair production can be divided into three classes:

1. $t\bar{t} \to W^+bW^-\bar{b} \to q\bar{q}'bq''\bar{q}'''\bar{b}$, (46.2%)
2. $t\bar{t} \to W^+bW^-\bar{b} \to q\bar{q}'b\ell\bar{\nu}_\ell\bar{b}$, or $\bar{\ell}\nu_\ell bq\bar{q}'\bar{b}$, (43.5%)
3. $t\bar{t} \to W^+bW^-\bar{b} \to \bar{\ell}\nu_\ell b\ell\bar{\nu}_\ell\bar{b}$. (10.3%)

The decay channels 1, 2 and 3 are respectivelly referred to as all-jets, lepton plus jets and dilepton channels. The ℓ in the processes above refers to e, μ or τ. Most of the studies in the lepton plus jets and dilepton channel are based, up to date, on e and μ leptons.

The tau lepton belongs to the isospin doublet of the third generation of leptons. Its mass is the highest among the leptons and is higher than the mass of light and strange flavored mesons (admixture of u, d, s quarks). The main tau decay modes are

1. $\tau \to \mu\bar{\nu}_\mu\nu_\tau$, (17.4%)
2. $\tau \to e\bar{\nu}_e\nu_\tau$, (17.8%)
3. $\tau \to \pi^- + \nu_\tau + n\pi^0 \quad (n = 0, 1, 2...)$, (46.7%)
4. $\tau \to \pi^- + \pi^+ + \pi^- + \nu_\tau + n\pi^0 \quad (n = 0, 1, 2...)$, (11.9%)

We reported in the list the decay branching ratios. The other tau decay channels account for 6.2% and involve strange flavored mesons or more than 3 charged pions.

The quarks from the top quark decay in the final states (q, b and their antiparticles) evolve into jets of hadrons. The b quarks commonly form mesons or baryons that have lifetimes of the order 10^{-12} s and the distance the particles cover before decaying is on average 400-500 μm. Products of B hadron decay originate from a point that can be discriminated from the interaction point through sophisticated tracking detectors with silicon technology.

1.3 Two Higgs Doublet Model

The SM presented in the previous sections is generally known as the minimal SM. This means that it includes a minimal formulation of the Higgs sector because it comprises only one complex Higgs doublet. The choice of a minimal Higgs sector is arbitrary, so there is no a priori limit to the number of Higgs doublets. The are only two major constraints coming from the experimental measurements.

The first constraint concerns the value of $\rho = m_W^2/(m_z\cos(\theta_W))^2$ which is really close to 1. In the SM the value of the parameter ρ is automaticaly obtained without any tuning of the parameters of the model. In more general representations with multiple Higgs fields the condition $\rho = 1$ is obtained with fine tuning of the paramenters.

The second constraint comes from the severe experimental limit on the existence of flavor changing neutral currents (FCNC). In the minimal Higgs model this kind of processes are automaticaly forbidden, but this property generaly ceases to be true in non-minimal Higgs Models. A theorem formulated by Glashow and Weinberg [10] demonstrated that the FCNC is absent in models where fermions with given electric charge couple to no more than one doublet. A second possible picture could explain the unobserved FCNC: the Higgs masses are large (of the order of 1 TeV) so that the tree level FCNC mediated by the Higgs is sufficiently suppressed to be consistent with the experimental data.

We want to underline that despite some experimental constraint there is still room for larger and alternative representations of Higgs sector in the Standard Model. The two Higgs doublet model (2HDM) is particularly actractive for several reasons. This extension adds some new interesting phenomena to the SM and at the same time adds few new paramenters. It may satisfy the costraint $\rho \approx 1$ and conply with the absence of FCNC.

1.3.1 Outline of the 2HDM

The 2HDM assumes two complex $\mathrm{SU}(2)_L$ doublets of scalar fields ϕ_1 and ϕ_2 with hypercharge $Y = 1$. The most general potential is expressed in terms of 14 parameters. After imposing the invariance under the trasformation of the fields $\phi \to -\phi$, which guarantees the absence of FCNC at tree-level the number of free paramenters is 7 [11]:

$$
\begin{aligned}
V(\phi_1, \phi_2) &= \lambda_1(\phi_1^\dagger\phi_1 - v_1^2)^2 + \lambda_2(\phi_2^\dagger\phi_2 - v_2^2)^2 && (1.37)\\
&+ \lambda_3[(\phi_1^\dagger\phi_1 - v_1^2) + (\phi_2^\dagger\phi_2 - v_2^2]^2 && (1.38)\\
&+ \lambda_4[(\phi_1^\dagger\phi_1)(\phi_2^\dagger\phi_2) - (\phi_1^\dagger\phi_2)(\phi_2^\dagger\phi_1)] && (1.39)\\
&+ \lambda_5[\mathrm{Re}(phi_1^\dagger\phi_2) - v_1 v_2\cos(\xi)]^2 && (1.40)\\
&+ \lambda_6[\mathrm{Im}(phi_1^\dagger\phi_2) - v_1 v_2\cos(\xi)]^2 && (1.41)
\end{aligned}
$$

The parameters $\lambda_1, ..., \lambda_6$ are all real paramenters by the hermiticity of the potential. If all the parameters $\lambda_1, ..., \lambda_6$ are not negative the minimum of the potentials is

$$
\langle\phi_1\rangle = \begin{pmatrix} 0 \\ v_1 \end{pmatrix}, \quad \text{and} \quad \langle\phi_2\rangle = \begin{pmatrix} 0 \\ v_2 e^{i\xi} \end{pmatrix}, \tag{1.42}
$$

which properly breaks the $\mathrm{SU}(2)_L \otimes \mathrm{U}(1)_Y$ down to $\mathrm{U}(1)_{em}$ as desired. We assume in this discussion that the potential is invariant under CP trasformation so the value of the parameter ξ is set to zero.

In this model a key parameter is the ratio of the vacuum expectation values of the two Higgs doublets:

$$
\tan(\beta) = v_2/v_1. \tag{1.43}
$$

The masses of the physical Higgs states are obtained diagonalizing the Higgs boson mass matrix $M^2_{ij} = \frac{\partial^2 V}{\partial\phi_i \partial\phi_j}$. This model contains two physical charged Higgs bosons:

$$H^{\pm} = -\phi_1^{\pm}\sin(\beta) + \phi_2^{\pm}\cos(\beta), \tag{1.44}$$

with mass $m^2_{H^{\pm}} = \lambda_4(v_1^2 + v_2^2)$. One $CP-$odd physical state is present:

$$A^0 = \sqrt{2}[-\mathrm{Im}(\phi_1^0)\sin(\beta) + \mathrm{Im}(\phi_2^0)\cos(\beta)], \tag{1.45}$$

with mass $m^2_{A^0} = \lambda_6(v_1^2 + v_2^2)$, and two $CP-$even states:

$$\begin{aligned} H^0 &= \sqrt{2}[-\mathrm{Re}(\phi_1^0 - v_1)\cos(\alpha) + \mathrm{Re}(\phi_2^0 - v_2)\sin(\alpha)], & (1.46)\\ h^0 &= \sqrt{2}[\mathrm{Re}(\phi_1^0 - v_1)\sin(\alpha) + \mathrm{Re}(\phi_2^0 - v_2)\cos(\alpha)], & (1.47) \end{aligned}$$

with mass

$$m^2_{H^0,h^0} = \frac{1}{2}[M_{11} + M_{22} \pm \sqrt{(M_{11} - M_{22})^2 + 4M_{12}^2}], \tag{1.48}$$

where the terms α and M_{ij} are defined as

$$\begin{aligned} \sin(2\alpha) &= \frac{2M_{12}}{\sqrt{(M_{11} - M_{22})^2 + 4M_{12}^2}}, & (1.49)\\ \cos(2\alpha) &= \frac{M_{11} - M_{22}}{\sqrt{(M_{11} - M_{22})^2 + 4M_{12}^2}}, & (1.50)\\ M_{11} &= 4v_1^2(\lambda_1 + \lambda_3) + v_2^2\lambda_5, & (1.51)\\ M_{22} &= 4v_2^2(\lambda_2 + \lambda_3) + v_1^2\lambda_5, & (1.52)\\ M_{12} &= (4\lambda_3 + \lambda_5) + v_1 v_2. & (1.53) \end{aligned}$$

To summarize, this model possesses five physical Higgs boson states. The free parameters of this Higgs model are 6: four Higgs masses, the ratio of the vacuum expectation values, and a Higgs mixing angle, α. The mass of the H^0 boson is by definition greater than the one of the h^0 and the quantity $v_1^2 + v_2^2$ is fixed by the mass of the W boson through the equation $v_1^2 + v_2^2 = \frac{2m_W}{g}$.

The coupling of the Higgs boson to gauge bosons can be expressed in terms of the SM Higgs couplings, but rescaled by factors that tend in general to suppress the process:

$$\frac{g_{h^0VV}}{h_{\phi^0VV}} = \sin(\beta - \alpha), \quad \frac{g_{H^0VV}}{h_{\phi^0VV}} = \cos(\beta - \alpha). \tag{1.54}$$

The coupling of the Higgs bosons to the fermion sector depends on the choice of model for the Higgs sector. The so called Model I assumes that quarks and leptons do not couple to the first Higgs doublet. Model II assumes that the ϕ_1 couples only to down-type quarks and leptons (electron, muon, tau) and the ϕ_2 couples only to up-type quarks and neutrinos. In this chapter we focus on the Model II since it provides a phenomenology that could enhance the processes we select in our analysis. Indeed, the couplings of the charged

Higgs boson to fermions depend on different functions of $\tan(\beta)$. Model I, on the contrary, suppresses or enhances uniformly all the couplings to fermions at the variation of $\tan(\beta)$.

In the 2HDM II the couplings of the neutral Higgs bosons to fermions are functions of α and β and with different choices of those parameters the coupling could be highly enhanced or suppressed. The ratios of the couplings of the 2HDM II and the ones provided by the minimal SM Higgs formulation are

$$\frac{g_{H^0u\bar{u}}}{h_{\phi^0u\bar{u}}} = \frac{\sin(\alpha)}{\sin(\beta)}, \qquad \frac{g_{H^0d\bar{d}}}{h_{\phi^0d\bar{d}}} = \frac{\cos(\alpha)}{\cos(\beta)}, \tag{1.55}$$

$$\frac{g_{h^0u\bar{u}}}{h_{\phi^0u\bar{u}}} = \frac{\cos(\alpha)}{\sin(\beta)}, \qquad \frac{g_{h^0d\bar{d}}}{h_{\phi^0d\bar{d}}} = \frac{-\sin(\alpha)}{\cos(\beta)}, \tag{1.56}$$

$$\frac{g_{A^0u\bar{u}}}{h_{\phi^0u\bar{u}}} = \cot(\beta), \qquad \frac{g_{A^0d\bar{d}}}{h_{\phi^0d\bar{d}}} = \tan(\beta). \tag{1.57}$$

$$\tag{1.58}$$

The charged Higgs boson in the 2HDM II couples to the up and down type quarks with

$$g_{H^-t\bar{b}} = \frac{g}{2\sqrt{2}m_W}[m_t\cot(\beta)(1+\gamma_5) + m_b\tan(\beta)(1-\gamma_5)], \tag{1.59}$$

where we have explicitly written the top and b quark masses m_t and m_b, in the charged Higgs decay channel into $t\bar{b}$. It could be noticed that the coupling costant is proportial to the mass of the b and top quark mass for large and small values of $tan(\beta)$, regions where the b mass and top mass terms are respectively enhanced.

The condition $m_t > m_{H^\pm} + m_b$ would allow the top quark to decay in the channel $t \to H^+b$.

$$\frac{BR(t\to H^+b)}{BR(t\to W^+b)} \approx \frac{P_{H^+}}{P_{W^+}} \times \frac{(m_b^2 + m_t^2 - m_{H^+}^2)(m_b^2\tan^2(\beta) + m_t^2\cot^2(\beta) + 4m_b^2m_t^2\tan(\beta)\cot(\beta)}{m_{W^+}^2(m_t^2+m_b^2-2m_{W^+}^2) + (m_t^2-m_b^2)^2}, \tag{1.60}$$

where P_{H^+} and P_{W^+} are the center of mass momenta of the W^+ and H^+ particles in the rest frame of the top. The equation imply that the decay of top quark into charged Higgs is dominant in the region $\tan(\beta) \lesssim 1$ or in the region where $m_b^2\tan^2(\beta) \gtrsim m_t^2$.

The decay channel $t \to H^+b$ would enhance the decay process $t \to \tau^+\nu b$ since the H^+ couples preferentially to this heavy lepton as the condition $\tan(\beta) \lesssim 1$ is met ($BR \approx 90\%$ for $\tan(\beta) = 2$).

1.4 Open Questions

Despite the unquestionable success of the SM in predicting phenomena of nature, some open questions still remain. The effect of gravitational interactions is not included in the

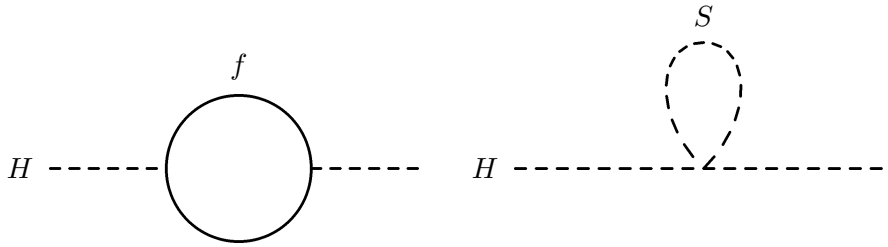

Figure 1.3: One-loop quantum correction to the Higgs mass due to a Dirac fermion f or a scalar S

model and it will eventually become important at energies of the order of the Plank scale $M_p = (8\pi G_{\text{Newton}})^{-1/2} = 2.4\times10^{18}$ GeV. The accessible energy range of the Tevatron, the last generation proton-antiproton collider, extends to about 200-300 GeV and experiments at the Large Hadron Collider will be sensitive to physics up to 10^3 GeV. The Plank scale still remains at energies 16 order of magnitude higher than the explored ones and new unknown physics could be present. The introduction of the Higgs field is needed to explain the Spontaneus Symmetry Breaking. However the presence of divergent corrections of the Higgs field potential due to the coupling with known or still unknown particles is quite troublesome.

Supersymmetric extensions of the SM provide an elegant explanation why the divergent terms should cancel out. A new symmetry is supposed to exist, which relates fermion and bosons belonging to the SM with respectivelly boson and fermion superpartners.

1.5 Introduction to Supersymmetry

The Higgs mass squared parameter μ^2, predicted in the SM may receive quantum corrections from the interaction with all the virtual particles that couple directly or indirectly with the Higgs field. Figure 1.3 represents two kind of processes, one with a Dirac fermion f with mass m_f, the other with a scalar boson S with mass m_S.

The first interaction would be given by a Lagrangian term $-\lambda_f H\bar{f}f$ generating a correction

$$\Delta\mu^2 = -\frac{|\,\lambda_f\,|^2}{8\pi^2}\Lambda_{UV}^2 + \mathcal{O}\left(\frac{1}{\Lambda_{UV}}\right), \tag{1.61}$$

where Λ_{UV} is an ultraviolet momentum cutoff used to regulate the loop integral. The cutoff value should be at least the energy scale at which new interactions start to alter the SM dynamics. If we suppose Λ_{UV} of the order of the Plank mass the correction is 30 order of magnitude higher than the Higgs mass itself. Each of the leptons and quarks of

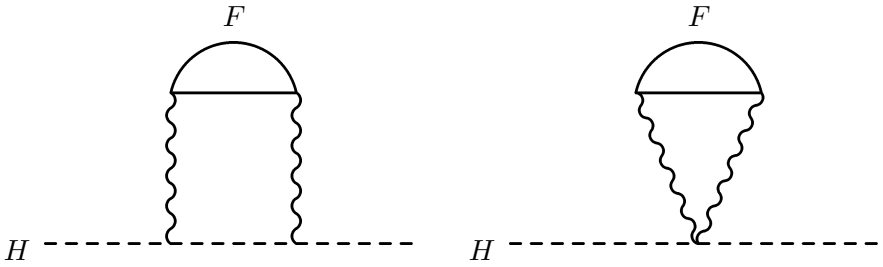

Figure 1.4: Two-loop quantum correction to the Higgs mass due to a fermion F that interacts indirectly to the SM Higgs boson through gauge interactions.

the Standard Model give its contribution and also possible unknown fermions.

The interaction with the scalar boson S would be represented by a Lagrangian term $-\Lambda_S \mid H \mid^2 \mid S \mid^2$ generating a correction to the Higgs mass

$$\Delta\mu^2 = -\frac{\mid \lambda_S \mid^2}{16\pi^2}\Lambda_{UV}^2 - 2m_S^2 ln(\Lambda_{UV}/m_S) + \mathcal{O}\left(\frac{1}{\Lambda_{UV}}\right). \tag{1.62}$$

We can see that all fermions or bosons would give diverging contribution to μ^2, and the same problem arises even considering particles that do not interact directly with the Higgs boson. They would generate corrections to the mass through diagrams in Figure 1.4, where we suppose the SM vector bosons to couple with the SM Higgs and with an exotic fermion field. Even this processes would give a correction $\Delta\mu^2 \propto \Lambda_{UV}^2$.

One may assume no other particle exists to couple to the Higgs field or there should be a cancellation of all the correction terms. The relative minus in the terms proportional to Λ_{UV} in 1.61 and 1.62 could allow a perfect cancellation of them if for each fermion two boson complex fields exist. This last assumption could be easily supported if we postulate a symmetry to exist between fermions and bosons. Even diagrams with higher number of loops can be canceled out. The symmetry relating fermion fields to boson fields is called supersymmetry. This symmetry is generated by the Supersymmetry spinor operator Q and its Hermitian conjugate $Q^\dagger$:

$$Q|boson\rangle = |fermion\rangle \tag{1.63}$$

1.5.1 Higgs Doublets

The single particle states of a supersymmetric theory fall into irreducible representations, called supermultiplets, where fermions and boson states are commonly known as superpartners of each other. The Higgs scalar boson of the SM should also reside in a supermultiplet, but it turns out that one chiral supermultiplet for the Higgs sector is not enough. If there

were only one Higgs supermultiplet, the electroweak gauge symmetry would suffer a gauge anomaly. The condition of cancellation includes $\mathrm{Tr}[T_3^2 Y] = \mathrm{Tr}[Y^3] = 0$, where T_3 is the third component of the weak isospin and Y the weak hypercharge. The trace runs over all the left-handed fermion degree of freedom in the theory and in the SM these conditions are satisfied by the known quark and lepton states. It is necessary to introduce another Higgs doublet, so that the Higgs supermultiplets have opposite hypercharges and the traces over the two fermion superpatners vanish by cancellation.

Supersymmetry requires that only the $Y = 1/2$ ($Y = -1/2$) Higgs chiral supermultiplets provides masses to the up-type (down-type) quarks. The MSSM therefore contains a Higgs sector as the 2HDM II already mentioned.

1.5.2 Top Decay in the MSSM Framework

The phenomenology of the decay $t \to H^+ b$ in the MSSM is substantially similar to the extension 2HDM II of the SM we presentented in Section 1.3. For a given mass of the charged Higgs the branching ratio $BR(t \to H^+ b)$ decreases moving to low value up to $\tan(\beta) \approx 7$ to increase again for large values of $\tan(\beta)$. In general the increase of the mass of th charged Higgs boson corresponds to a decrease in the amplitude of the decay channel.

The major difference of the MSSM from the 2HDM II is the dependency of the Yukawa coupling between the top and b quarks on the Higgs mass parameter. This parameter, μ, determine self-coupling of the Higgs supermultiplets in the superpotential of the MSSM. The masses of the Higgs bosons and their superpartners, the Higgsinos, is given by a term $\mu\epsilon^{\alpha\beta}(H_u)_\alpha(H_d)_\beta$. Large values of μ suppress the $BR(t \to H^+ b)$, while lower values enhance it.

At large values of $\tan(\beta)$ the decay channel $H^+ \to \bar{\tau}\nu$ dominates, regardless of the charged Higgs mass. As in the case of 2HDM II at $\tan(\beta) \gtrsim 1$ the decay channel in tau becomes dominant.

The branching ratios of top and charged Higgs are reported in Figure 1.5 as functions of the mass m_{H^+} and $\tan(\beta)$. The branching ratios are calculated using the program CPsuperH [12][13]. At values of $\tan(\beta) \approx 1$ and $\tan(\beta) \gtrsim 30$ the top decay channel into tau, b and neutrino is enhanced.

1.6 Concluding Remarks

In the Standard Model the top decay into semileptonic channel is expected to produce the same amount of electron, muon and taus. This property derives directly from the general rule of lepton universality in the electroweak interactions.

This chapter provided an outline of the SM, as well as two alternative extensions with multiple Higgs fields. As we have seen, the SM provides an excellent description of the experimental data and its prediction have been confirmed to very high precision levels.

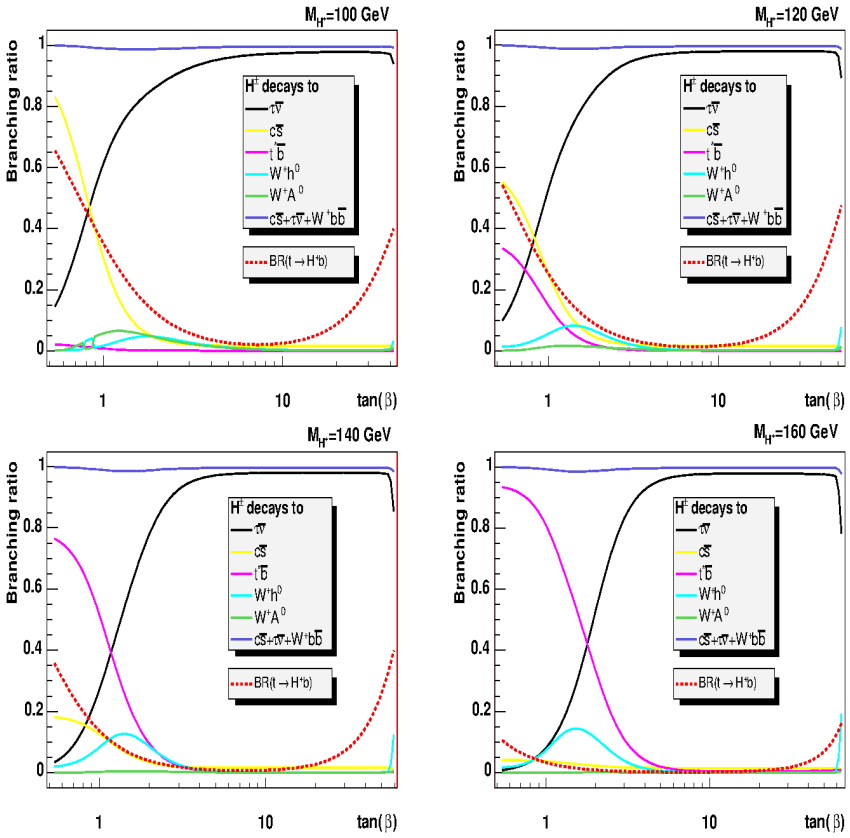

Figure 1.5: Top and charged Higgs branching ratios as functions of $\tan(\beta)$. The mass of the charged Higgs is set to 100 GeV/c^2, 120 GeV/c^2, 140 GeV/c^2, 160 GeV/c^2

Despite this fact, some of the assumptions of the SM are arbitrary and some elegant extensions can be introduced, which can become manifest at 100 GeV scale of energy. We refered in this text in particular to models, which include 2 Higgs doublet fields. These fields can strongly affect the properties of the third fermion generation. Therefore we underline that the fundamental goal of our study of the top decay is the exploration of alternative phenomenology of the Higgs sector.

Chapter 2

The Experimental Apparatus

2.1 Introduction

Although I joined the CDF experiment at end of 2008 and participate in the data taking from 2009 till the end of the Tevatron Run II in September 2011, the work reported here uses all the data that were collected since the beginning of Run II. It thus required a full knowledge of the evolution of the machine and CDF detector over the ten years duration of Run II.

It is essential to note here that indeed in this period both the machine and the CDF experiment went through important upgrades (after having undergone large upgrades for Run II) that had a significant impact on the analysis reported here. In particular it was decided by management to do the so called *electron cooling upgrade* of the Tevatron in 2005, that provided a drastic increase in luminosity and thus overall performances of the machine.

The CDF detector started Run II with all upgrades completed when the machine started to run in October 2001. This also included the so-called *beyond the baseline upgrades*. It did not stop CDF to pursue continuously small improvements in order to better cope with increase in luminosity and ageing effects. We will mention in this chapter some of these main aspects and impacts of this work.

2.2 The Accelerator Complex

The Tevatron Collider at the Fermi National Accelerator Laboratory was active until September 30^{th} 2011. Before the Large Hadron Collider (LHC) at CERN turned on in 2010, the Tevatron was the world's highest energy accelerator, colliding protons and anti-protons with a center of mass energy of $\sqrt{s} = 1.96$ TeV. While the

The Tevatron was the second proton-antiproton collider built after the Sp$\bar{\text{p}}$S collider at CERN, that ran from 1980 till 1991 with a center of mass energy of 547 and 630 GeV.

The first $p\bar{p}$ collisions at the Tevatron were induced in 1985 and CDF was the experiment running at that time. Since then several extensive upgrades to both the accelerators and experiments enabled operation above the initial design. Since the start of the Tevatron program in 1985 and up to the end of Run I (1992 to 1995), the accelerator ran at a center of mass energy of 1.8 TeV with a bunch crossing of 3.3 microseconds. Then a major upgrade took place between September 1997 and March 2001 for Run II.

The CDF experiment ran during the full collider operation, from October 1985 until September 2011, thus more than 25 years, and overcome successive major upgrades that maintained it at the forefront of the detector technology and physics achievements.

2.2.1 The Tevatron Collider

The Tevatron was the last stage of a complex system of accelerators (see Figure 2.1), used in successive steps to produce, store and accelerate protons and antiprotons. It was a circular synchrotron of 1 Km radius, employing 772 dipole, and 204 quadrupole superconducting magnets. Each of them was approximately 6 m long, 4 tons in mass, and was made of NbTi alloy filaments embedded in copper, kept at 4.3 K temperature by a large cryogenic system. The magnets produced a 4.2 T magnetic field necessary to keep the particles on their orbit, while they were accelerated by eight radio-frequency cavities (RF).

The Tevatron operated with 36 bunches of protons circulating clockwise, spaced by 396 ns, colliding with an antiproton beam with the same number of bunches and travelling in the opposite direction. There were two interaction points, located in two regions along the ring: B0, which was the site of the CDF experiment, and D0, where the D0 experiment was located.

The two most important collider parameters were: the center of mass energy, s, and the instantaneous luminosity, $\mathcal{L}$ which quantifies the number of $p\bar{p}$ interactions per unit of time and unit of surface. The rate of events was

$$rate[\text{events s}^{-1}] = \mathcal{L}[\text{cm}^{-2}\text{s}^{-1}] \times \sigma[\text{cm}^2] \tag{2.1}$$

Using the cross section from the previous equation 2.1, we can estimate the expected number of events n, given a specific process cross section σ and a total data taking time T,

$$n(T) = \int_0^T \mathcal{L}\sigma dt \tag{2.2}$$

Since the cross section is constant in time we can express the previous formula in the form $n(T) = \sigma \int \mathcal{L}dt$.

The main limit for the instantaneous luminosity of $p\bar{p}$ colliders was the availability of antiprotons that have to be produced, focused in a monochromatic beam and then transfered into the accelerator. Table 2.1 summarizes the relevant parameters of the Tevatron

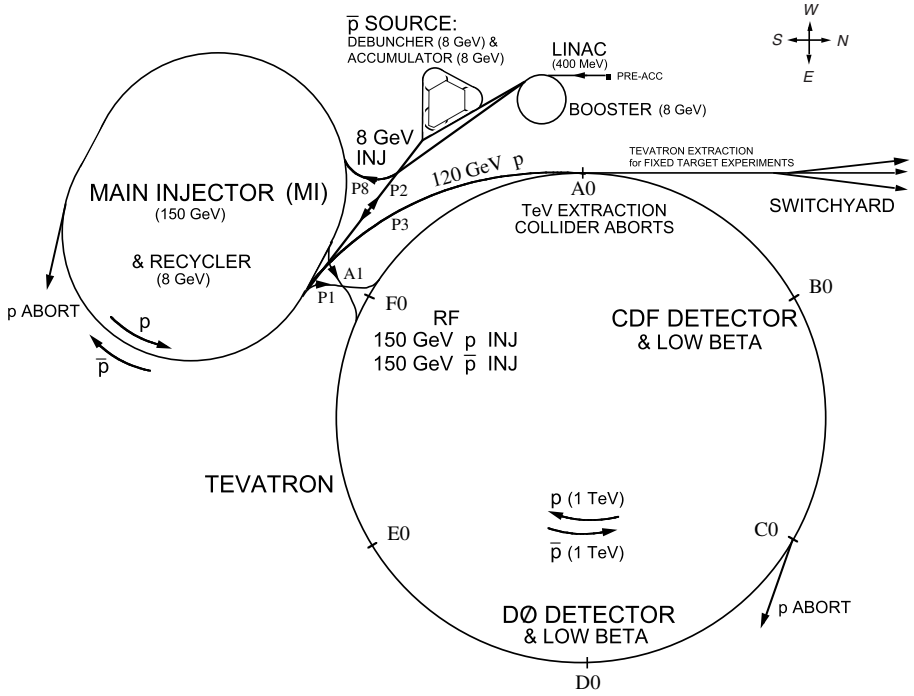

Figure 2.1: The accelerator system operating at FNAL.

collider during the Run II program.

The Tevatron typically achieved an initial instantaneous luminosity of 3.5×10^{32} cm^{-2}s^{-1} during the last two years, with a record of 4.31×10^{32} cm^{-2}s^{-1} on May the 3^{rd}, 2011. Figure 2.2 shows the peak luminosity for each store of colliding beams: the blue markers represent the initial instantaneous luminosity (the red points show the average of the instantaneous luminosity among 20 continuous stores). Figure 2.3 reports the weakly and the total integrated luminosity delivered by the Tevatron.

Figure 2.4 presents the luminosity delivered by the Tevatron and the luminosity recorded by the CDF experiment. The average data taking efficiency of the experiment was about 85%.

2.2.2 Proton Beam Production

The proton source was located in the 750 KV terminal of a Cockroft-Walton accelerator [14]. Protons originated from a hot hydrogen gas in the molecular state H_2, ionized by the passage through a magnetron. An electric field separated the ions and pushed the protons toward a negatively charged Cesium doped metal plate, where they captured two electrons. Incoming protons extracted the H^- from the surface of the metal plate and the electric field accelerated the H^- out of the Cockroft-Walton terminal.

Parameter Run II	
Circumference [Km]	6.28
Injection beam energy [TeV]	0.15
Maximum beam energy [TeV]	0.98
Number of bunches	36
Protons/bunch	$\sim 3 \times 10^{11}$
Antiprotons/bunch	$\sim \times 10^{11}$
Bunch length [cm]	$50(p)/45(\bar{p})$
Beam radius [μm]	$28(p)/16(\bar{p})$
Bunch spacing [ns]	396
Revolution frequency [kHz]	47.7

Table 2.1: Tevatron collider Run II configuration.

The H^- beam was then injected into the two-staged 150 m long linear accelerator, Linac (see Figure 2.1). In the first stage, a drift tube accelerator accelerated the H^- beam up to 116 MeV; it is then segmented into bunches, of about $5 \cdot 10^{12}$ protons, and with the help of radio frequency cavities their energy was increased to 400 MeV [15].

The H^- beam in then injected into the Booster [16], which was an alternating gradient synchrotron. It took the 400 MeV H^- ions and striped the electrons off via a carbon foil. The Booster then accelerated the protons to 8 GeV.

The bunches were injected in the Main Injector [17] and divided into 84 bunches which contained about 6×10^{10} protons.

2.2.3 The Main Injector

The Main Injector was a 3 km circular syncrotron, with 18 accelerating RF cavities and conventional magnets, which could accelerate particles to either 120 GeV or 150 GeV, depending on the operations mode of the machine.

Whereas the Main Injector's task was to produce the antiproton beam (*accumulation mode*), 8 GeV protons were extracted from the Booster to be accelerated up to 120 GeV. The beam was then sent to a rotating 7 cm thick Nickel target for antiproton production.

When the Main Injector was used to inject beams into the Tevatron (*collider mode*), bunches of protons (or aternatively antiprotons) were accelerated up to 150 GeV.

2.2.4 Antiproton Production

Antiprotons were produced in a rotating Nickel target as part of jets of hadrons from QCD mediated interactions. A spatially broad beam of particles was produced and then focused using a cylindrical Lithium Lens[1]. This beam, which had a bunch structure similar to the incident proton beam, was passed through a pulsed dipole magnet. The magnetic field

[1] Lithium was used to minimize beam loss from multiple-scattering.

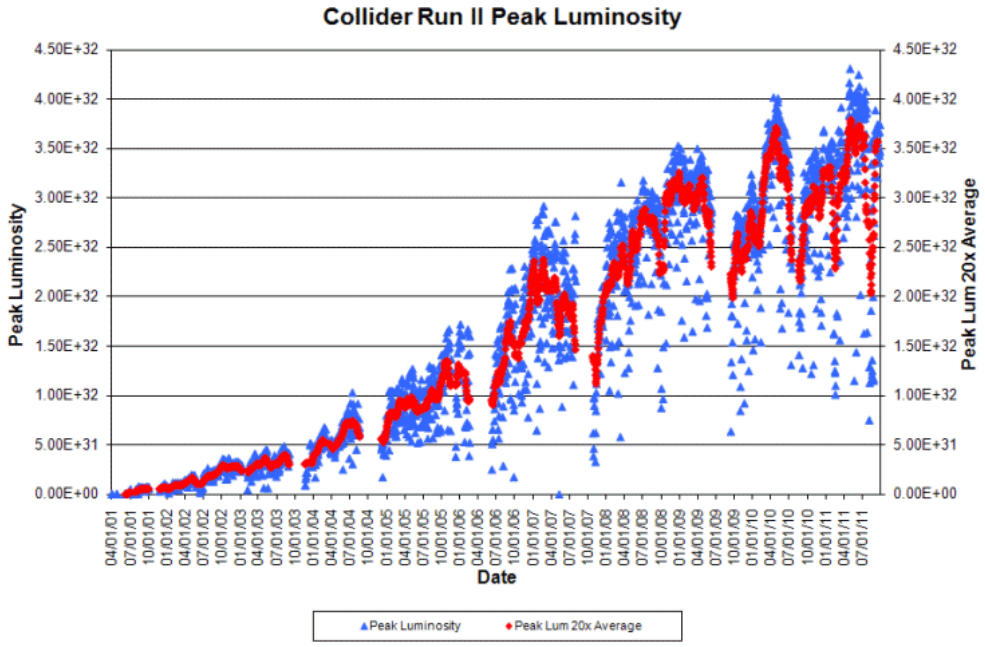

Figure 2.2: Peak luminosity of Tevatron collider during Run II. Blue markers show the luminosity at the beginning of each store, while red markers represent the peak average value among a set of 20 stores.

selected the negatively charged antiprotons with about 8 GeV of kinetic energy. About 20 antiprotons were produced for every 10^6 protons on target and then stored in the Debuncher [18], a triangular-shaped synchrotron with mean radius of 90 m. The beam was stochastically cooled [19][2] and then transferred to the Accumulator [18], another triangular-shaped synchrotron with a mean radius of 75 m.

The Accumulator was a storage ring for the antiprotons; they were stored at an energy of 8 GeV and cooled until needed. Since 2004, an additional Recycler Ring [21] was added in the same tunnel of the Main Injector and provided additional storage and cooling of the anti-protons. Later a relativistic electron cooling was implemented in the Recycler, further enhancing the Tevatron performance [20][3]. The antiprotons were then sent into the Main Injector, when needed and accelerated there to 150 GeV.

[2]Stochastic cooling is a technique used to reduce the beam emittance, without any accompanying beam-loss. When the particle deviates from its ideal orbit, an iterative feedback mechanism produces an electrical signal that brings it back.

[3]In the electron cooling process an electron beam propagates at the same average velocity of the particle beam and through Coulomb scattering the anti-protons loose energy until a thermal equilibrium is reached.

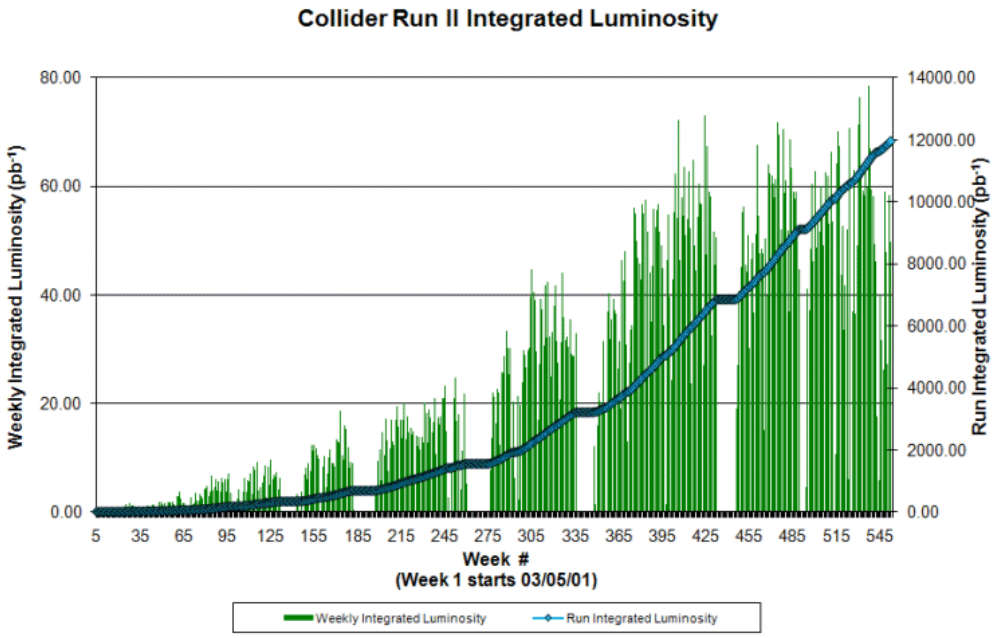

Figure 2.3: Weakly and total integrated luminosity of Tevatron collider during Run II.

2.2.5 Injection and Collision

The antiproton accumulation process usually took about 14 hours, then the accumulation was stopped and the accelerator was prepared for a new injection.

The first injection step was the extraction of a set of seven proton bunches from the Booster into the Main Injector, where they were accelerated up to 150 GeV. Within the Booster the protons were compacted into a single bunch of $\approx 300 \cdot 10^9$ particles. When the proton bunches were ready, they were moved into the Tevatron. This process was repeated until 36 proton bunches, separated by 396 ns, were loaded in the Tevatron central orbit. The proton injection preceded the anti-proton injection, because if proton bunch losses were large, the proton injection was aborted and restarted. At this stage the process could be quickly recovered, while a large antiproton lost needed a new accumulation.

Electrostatic separators were then activated to push the protons in a closed helicoidal orbit. This procedure prepares the Tevatron for the injection of antiprotons: the proton and the antiproton beams needed to be separated (by 5 mm in normal operation), to avoid beam interactions along the beam lines.

Antiproton bunches were extracted from the Recycler to the Main Injector after proton injection, accelerated to 150 GeV, then compacted into four bunches. Finally each bunch had $90 \cdot 10^9$ antiprotons. The four bunches, separated by 396 ns, were injected into the

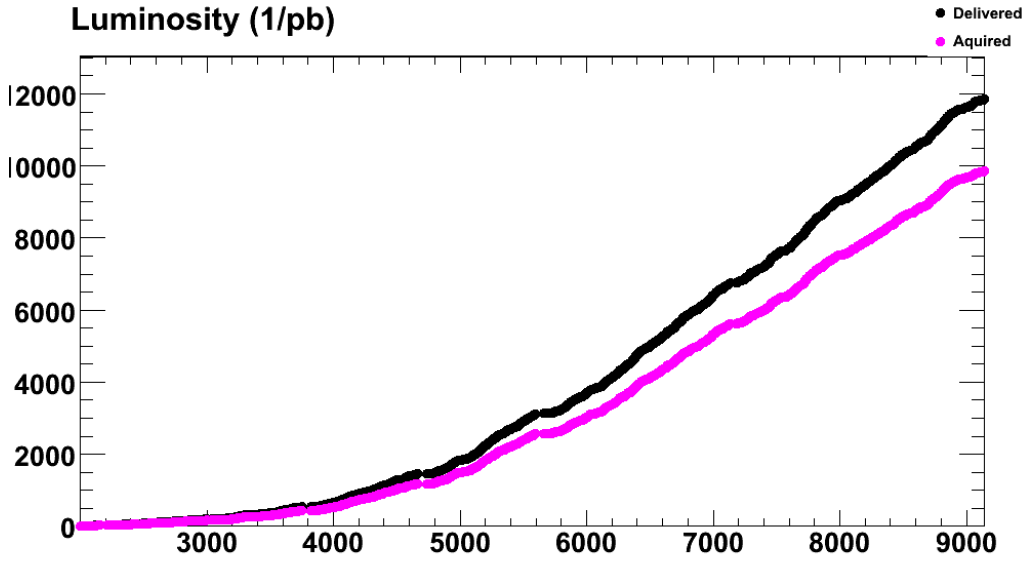

Figure 2.4: Total integrated luminosity delivered by Tevatron collider and acquired by CDF detector.

Tevatron, while protons were circulating in opposite direction. The antiproton injection was then repeated to have 36 bunches.

After the end of antiproton injection the "store" started, defined as the period of collisions for physics. The store duration varied from the beginning of Run II till the end (with an average of 14 hours). Performance was improved up to the end: a store could last one day and in addition the time between two stores decreased dramatically as well. The proton and antiproton bunches shared the same magnets and radio frequency acceleration system. After the injection the beams were accelerated up to 980 GeV in about one minute. The beams were brought into collision at the two instrumented interaction points: B0 and D0, where the CDF and D0 detectors were located.

Special high power quadrupole magnets ("low-β squeezers"), installed on the beam pipe at either side of the detectors, reduced the transverse spatial spread of the beams to maximize the collision rate in the interaction regions. The resulting transverse spatial distribution of the luminous region was approximately a two-dimensional Gaussian, with $\sigma_T \approx 30$ μm. The interaction regions had a roughly Gaussian distribution along the beam direction (z-axis), with r.m.s. width $\sigma_z \approx 28$ cm. The center of the luminous region was shifted toward the nominal interaction point by fine tuning of the squeezers. The 36 bunches of protons (antiprotons) were distributed in three equispaced "trains" of 12 bunches each. The inter-bunch spacing was 396 ns (21 buckets) within a train, while a 2.6 μs spacing was kept between trains.

Just after the final injection, a new antiproton accumulation cycle started. When the

antiproton stack was sufficiently large and the colliding beams were degraded, the store was dumped. The beam was extracted and sent to an absorption zone.

The improvements made to the accumulation of antiproton by the Recycler and electron cooling (see previous section) allowed the Tevatron Accelerator Divition to achieve higher luminosities, of the order of $10^{32}\text{cm}^{-2}\text{s}^{-1}$. Tuning of the beam optics allowed to reach gradually even higher luminosities. Since the beginning of 2008 the stores for physics data taking had typically initial peak luminosity greater than $2 \times 10^{32}\text{cm}^{-2}\text{s}^{-1}$ with an average of $3 \times 10^{32}\text{cm}^{-2}\text{s}^{-1}$.

The instantaneous luminosity of the beam during the store had an exponential profile due to the continuous degradation of the beam and beam particle losses. At the beginning of the store, with the $p\bar{p}$ cross section of 70 mb, the average number of primary interactions per bunch crossing was 12. So all the experimental apparatus was subject to big radiation fields due to multiple interactions. As will see the innermost tracking system, composed by Silicon microstrip suffered degradation due to radiation exposure. All the physics results took advantage of the ability to reconstruct efficiently the primary vertexes and limit the effects of this pile up. In this study we use methods to correct the jet energy for the effect of the multiple interactions, and include their effect in the estimate of systematic uncertainties and in the MC simulations.

2.3 The CDF Detector

The CDF experiment went through a drastic upgrade in order to fit with the new machine conditions as well as inheriting all the physics expertise gathered during the previous series of runs and especially Run I. Many components were replaced; this included completely new front-end electronics for all the components (to pass from 3 μs to 396 ns), a new overall tracking system (a new gaseous tracker able to work at this speed, COT; a high performing new Si tracking system with vertex and intermediate Si trackers), new end cap calorimetry, renewed muon system with extended coverage, new DAQ and triggering system with a L3 farm of PC, a new particle identification device (to distinguish between pion, kaon and proton) and a luminosity monitoring system.

The CDF II detector [22] was a large multipurpose solenoidal magnetic spectrometer, designed with an approximately cylindrically symmetric layout. Figure 2.5 shows the CDF II detector and the different subsystems in a solid cut away view, while Figure 2.6 shows the elevation view of one half of the detector.

The CDF II detector, consisted of several specialized subsystems arranged in concentric layers, each one meant to perform a specific task. Starting from the interaction point we encountered in sequence:

- a high precision tracking system: a silicon microstrips detector and an open-cell wire drift chamber, the Central Outer Tracker (COT);

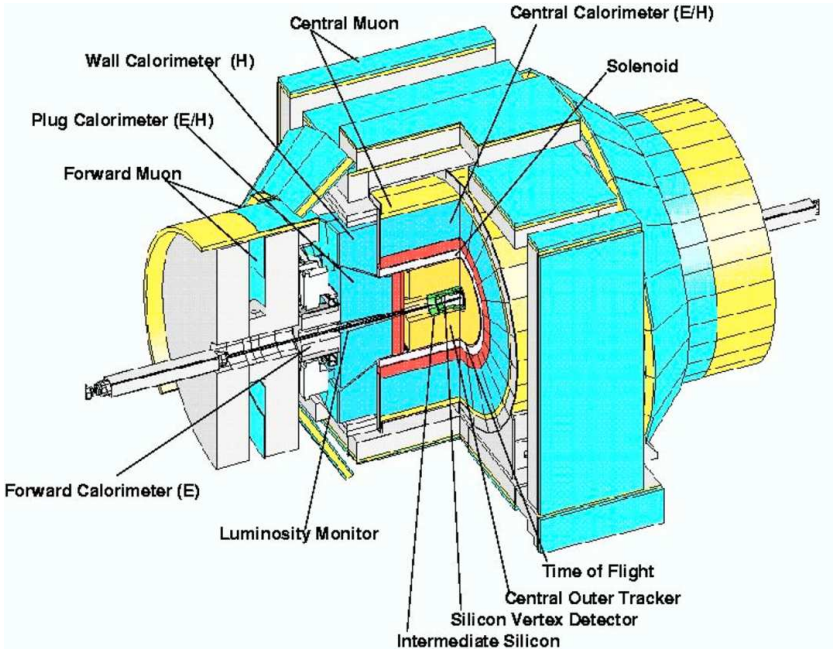

Figure 2.5: The CDFII detector with a quadrant cut to expose the different subdetectors.

- a solenoid magnet;
- a set of composite scintillation calorimeters with projective towers, designed to measure the energy of electron, photons in the innermost region and hadrons in the outer part;
- a set of drift chambers and scintillator counters, to detect muons;
- Cherenkov counters for measuring the instantaneous luminosity, are located in the forward region of the detector.

The measurement of top pair production into dileptons including tau leptons is a very challenging study as it requires excellent performances of all the detector components: calorimetry (electron identification, tau identification, jet reconstruction and measurement of the missing transverse energy), muon (muon identification), tracking system (track reconstruction for the 3 charged leptons, electron, muon and tau; b-tagging from the vertex detector). The use of these devices as well as associated trigger system is described in details in the Chapter 4, while in this Chapter we briefly describe each detector component emphasising its particular impact of one or several aspects of the event signatures tackled in this research.

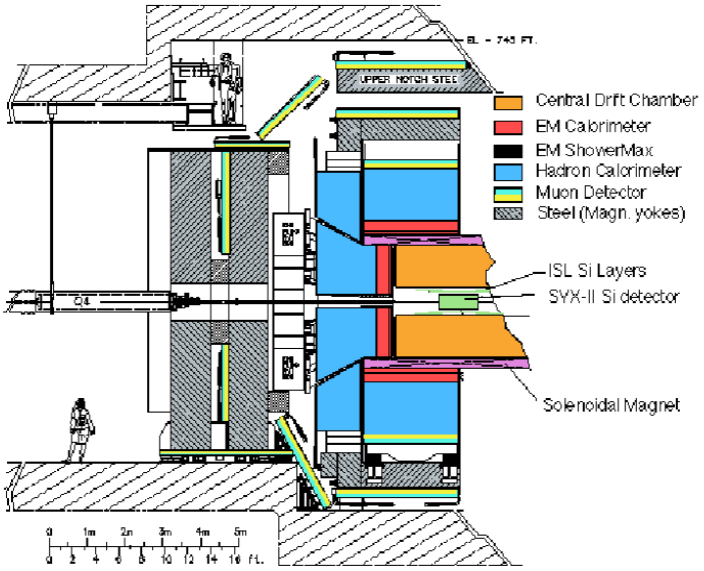

Figure 2.6: Elevation view of one half of the CDFII detector.

2.3.1 Coordinate System

CDF adopts a left handed cartesian coordinate system with origin at the nominal BØ interaction point, coincident with the center of the drift chamber (see Section 2.3.2). The positive z axis is defined by the direction of the proton beam (east). The $x-y$ plane is therefore perpendicular to the beam line, with the y-axis pointing upward and x axis in the horizontal plane, pointing radially outward with respect the center of the accelerator ring (Fig. 2.7).

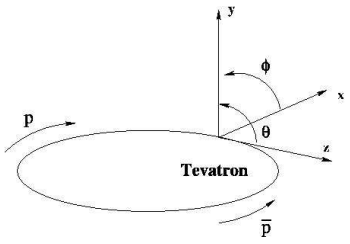

Figure 2.7: CDF coordinate system.

Since the colliding beams of the Tevatron are unpolarized, the resulting physical observations are invariant under rotations around the beam line axis. Also, the approximately cylindrically symmetry of the detector makes the cylindrical coordinate system (r, ϕ, z) particularly convenient to describe the detector geometry.

We define the azimuthal angle ϕ, and the polar angle θ via:

$$\tan(\phi) = \frac{y}{x}, \qquad \tan(\theta) = \frac{\sqrt{x^2 + y^2}}{z}. \tag{2.3}$$

In high energy collisions, where particles produced in the interaction are boosted along the beam line. It is useful to define a new variable, which is relativistically invariant and can be used in place of the polar angle θ: the *rapidity*, that is defined

$$Y = \frac{1}{2} \ln \frac{E + p_z}{E - p_z}, \tag{2.4}$$

where E is the energy and p_z is the z component of the momentum of the particle.

In the relativistic limit, or when the mass of the particle is ignored, rapidity becomes dependent only upon the production angle of the particle with respect to the beam axis. This approximation is called *pseudo-rapidity*, η, and is defined by

$$\eta = -\ln\left(\tan\frac{\theta}{2}\right). \tag{2.5}$$

It is particulary convinient to map the solid angles in the detector in terms of rapidity (or pseudo-rapidity) and azimuthal angle, because the density of particles in the final states of high energy collisions is approximatelly flat in the (Y, ϕ) space.

We define additional quantities, the *transverse momentum*, $p_T = p \cdot \sin\theta$, the *transverse energy* $E_T = E \cdot \sin\theta$ and the Lorentz-invariant angular distance $\Delta R = \sqrt{\eta^2 + \phi^2}$.

2.3.2 Tracking System

The tracking system was immersed in a 1.4 T solenoidal magnetic field for the measurement of charged particles momenta. We will describe this system, shown in Figure 2.8, starting from the device closest to the beam and moving outwards. The subdetectors were the Layer 00 (L00), the Silicon Vertex Detector (SVXII), the Intermediate Silicon Layers (ISL) and the Central Outer Tracker (COT).

The Silicon detector was meant for the precise measurement of the track displacement from the primary interaction point. This allowed the identification of particle like B hadrons, which decay close to the beam axis. This chapter contains a summary of the Silicon tracker geometry and the sensor properties, more details about the data acquisition system are postponed until Chapter 3.

The COT provided a very precise measurement of the track transverse momentum. The detector had axial and small angle sense wires which allowed to obtain a 3-dimentional reconstruction of the tracks.

Layer 00 (L00)

L00 [23], shown in Figure 2.9, was a single sided Silicon microstrip detector directly mounted on the beam pipe, with sensors mounted alternating at 1.35 cm and 1.62 cm of

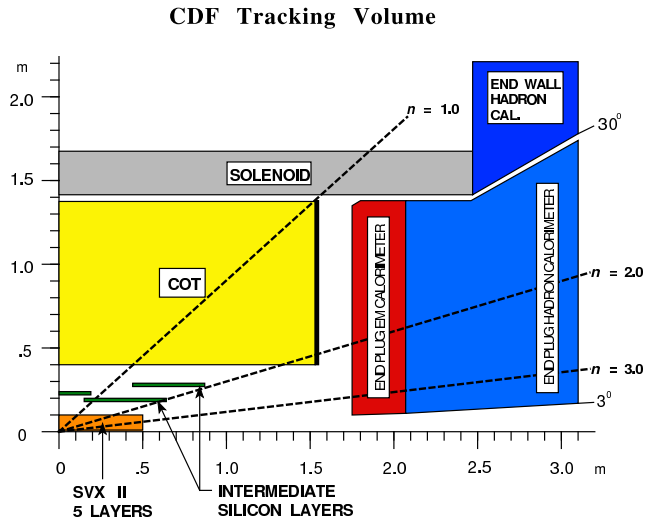

Figure 2.8: The CDFII tracker layout showing the different subdetector systems.

radius. The sensors closer to the beam pipe were the "narrow sensors", they were 8.4 mm wide, with 128 readout channels, while the "wide sensors" were connected to 256 readout channels and were 14.8 mm wide. The narrow sensors were produced by the Hamamatsu Photonics KK, while the narrow sensors were produced by the SGS-Thompson. The readout pitch of all the ladders was 50 μm and the total thickness of the sensors was 300 μm. The full subdetector was split in 2 subunits, "barrels", each 6 sensors long, for a total leght of 95 cm.

L00 provided a full coverage in ϕ and up to 4.0 in $|\eta|$. The strips were parallel to the beam axis, thus providing position measurement in the (r, ϕ) plane, with resolution up to 11 μm.

Silicon Vertex Detector (SVXII)

The SVXII [24], shown in Figure 2.10, was located outside of L00 and consisted of five layers of double sided Silicon miscrostrips detectors, extending from 2.45 cm to 10.6 cm of radius, full covering up to $|\eta| < 2.0$. The readout electronics were mounted directly to the surface of the silicon sensor at each end of the ladder. The system had a cylindrical geometry, coaxial with the beam and in the z coordinate was segmented into three 32 cm long "barrels". A SVX II barrel was segmented into 12 wedges, each covering approximately 30° in ϕ.

One side of the sansors had strips axially aligned to the beam, while on the other side had strips oriented at 1.2° in layer 2 and 4, and 90° in layers 0, 1 and 3. This alternation between small stereo angle and perpendicular microstrips was important to reject false hits in an experimental apparatus with multiple tracks traversing a sensor. The false

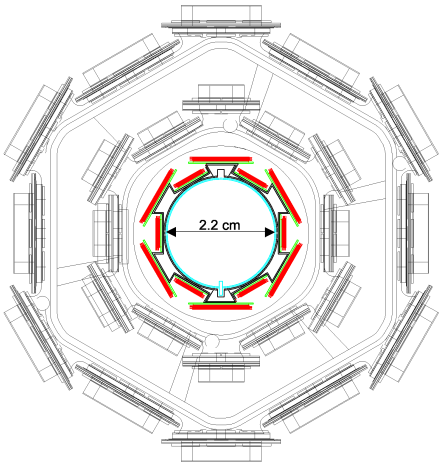

Figure 2.9: Representation of Layer 00 with the first two layers of SVXII.

hits in layers with different stereo angle were reconstructed displaced from the expected estrapolated position and the track reconstruction algorithm discarded them. The Silicon detector was able to provide precise reconstruction of r, ϕ and z coordinates, with a position resolution down to 9 μm.

The main features of the sensors are summarized in Table 2.2. The sensors located in layer 2 and 4 were manufactured by Micron Semiconductor, the remaining sensors by Hamamatsu Photonics KK.

Property	**Layer 0**	**Layer 1**	**Layer 2**	**Layer 3**	**Layer 4**
number of ϕ strips	256	286	640	768	896
number of z strips	256	576	640	512	896
stereo angle	90°	90°	+1.2°	90°	−1.2°
thickness	300 μm	300 μm	275 μm	300 μm	275 μm
ϕ strip pitch	60	62	60	60	65
z strip pitch	141	125	60	141	65
total width	17.1	25.9	40.3	47.9	60.2
total legth	74.3	74.3	74.3	74.3	74.3

Table 2.2: The geometry of the Silicon Vertex Detector sensors.

Intermediate Silicon Layer (ISL)

The ISL [25] was a Silicon tracker made of three layers, positioned outside the SVXII detector at different radii and covering specific regions in η. The subunits of ISL were the

"central", the "inner forward layer" and the "outer forward layer" As shown in Figure 2.10, the central layer ($|\eta| < 1.0$) was placed at $r = 22$ cm, and two pairs of forward layers ($1 < |\eta| < 2$) are located at 20 cm and 28 cm respectively.

All the silicon sensors of the ISL were identical and measure 58 mm in width and 74 mm in length (the maximum dimension for 2 sensors to be made from 6 inch Si wafers). Similarly to the sensors of layer 4 of the SVX II, the sensors were double-sided with axial and small angle strips (1.2°) on the two different sides. The axial strip pitch was 55 μm and the stereo strip pitch was 73 μm, but since the track occupancy was expected to be low, the readout pitch was doubled. The number of axial readout channels was 1024, while the number of stereo channels was 384.

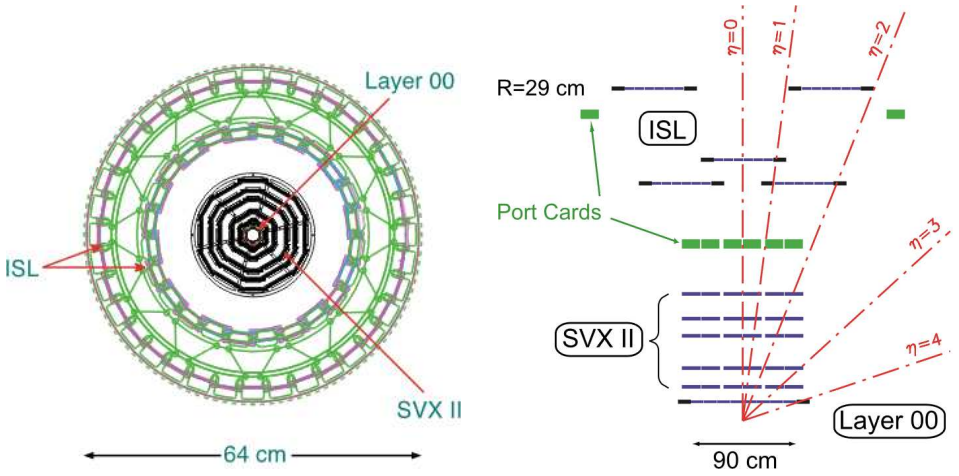

Figure 2.10: A radial view of the three Silicon subdetectors (left) and the coverage in the $r - z$ plane (right).

Central Outer Tracker (COT)

The COT drift chamber provided the tracking of charged particles in the pseudo-rapidity region $|\eta| < 1$, giving accurate information in the $r - \phi$ plane for the measurement of the transverse momentum. The COT contained 96 sense wire layers, which were radially grouped into eight *superlayers*. This can be seen from the end plate section shown in Figure 2.11.

The entire COT contained 30,240 sense wires spanning the entire length of the detector in z. Approximately half the wires ran along the z direction (*axial*). The other half were strung at a small angle (2°) with respect to the z direction (*stereo*). This allowed to perform track reconstruction in the $r - z$ plane. The active volume of the COT began at a radius of 43.4 cm from the beamline and extended out to a radius of 132.3 cm. The chamber was 310 cm long. Particles originating from the interaction point with $|\eta| < 1$ passed through all the 8 superlayers of the COT.

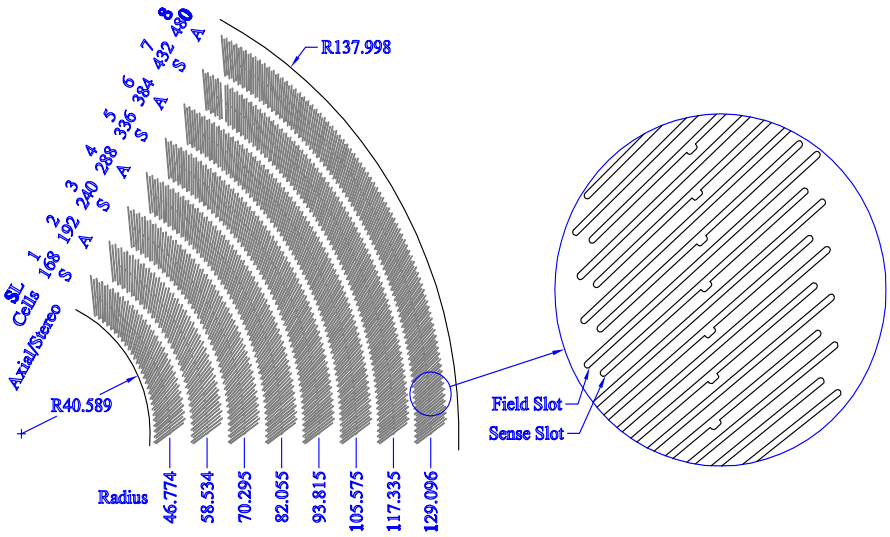

Figure 2.11: A 1/6 section of the COT end-plate (left).

The cell consisted of a wire plane containing sense and potential wires (for field shaping) and a field (or cathode) sheet on either side of the cell. Both the sense and potential wires were 40 μm diameter gold plated tungsten wires. The field sheet was 6.35 μm thick mylar with vapor-deposited gold on both sides. Each field sheet was shared with the neighbouring cell. The COT was filled with an Argon-Ethane gas mixture with Isopropyl alcohol added. The gas mixture was chosen to have a constant drift velocity across the cell width.

When a charged particle passed through the detector volume, the gas was ionized. Electrons drifted towards the nearest sense wire. The electric field in a cylindrical system grew exponentially with decreasing radius. As a consequence, an avalanche multiplication of charge happened inside the high electric field region, in the vicinity of the wire, due to *electron-atom* collisions. The avalanche discharge provided a gain of ~ 104. Due to the magnetic field, electrons drifted at a Lorentz angle of $\sim 35^\circ$ with respect to the radius. The cell was tilted by $\sim 35^\circ$ with respect to the radial direction to compensate for this effect.

The analysis we present in this thesis takes advantage of the fast timing (100 ns) and the transverse momentum resolution ($\sigma_{pT}/p_T^2 = 0.0017$ GeV/c^{-1}) of the COT detector. The fast collection of ionization charge allowed the use of the COT information for trigger decisions Level 1 (see Section 2.4), enhancing rejection of not interesting $p\bar{p}$ collision processes. This represented a key-factor for the success of our analysis since the trigger system was able to select efficiently events with low transverse momentum tracks and to limit the dead time of the overall acquisition system.

2.3.3 Calorimeter System

Outside the solenoid coil, sampling calorimeters, consisting of alternating layers of passive material and plastic scintillators, covered a region $|\eta| < 3.6$.

A detailed description of this system can be found in [22]. The CDF II calorimetry system was designed to measure energy and direction of neutral and charged particles leaving the tracking region. These calorimeters were organized in projective towers with a truncated pyramidal geometry, where the vertex point to the center of the detector and the base was a rectangular cell in the (η, ϕ) space. Each tower, finely segmented in solid angle around the collision point and coarsely segmented radially outward, was divided into two independent compartments: the inner one was devoted to the detection of the electromagnetic component of showers, the outer one measured the energy of hadrons.

The read-out system was composed of a set of wavelength shifting fibers and light guides, which collected the signal pulses generated in the scintillators and carryed them to a pair of photomultiplier tubes (PMT) for each tower. PMT's current amplitudes were converted into measurement of energy, which for a given tower consisted of the sum of the energy deposited in the electromagnetic and hadronic portions.

Particles hitting the calorimeter can be divided into two classes, according to their main interaction with the matter: electromagnetically interacting particles, such as *electrons* and *photons*, and hadronically interacting particles, such as *mesons* or *baryons*. To detect these two classes of particles, two different calorimetric parts were developed: an inner electromagnetic and an outer hadronic section.

The central sector of the calorimeter, covered the region $|\eta| < 1.1$ and was split in two halves at $\eta = 0$ and was divided into the Central Electromagnetic Calorimeter (CEM) and the Central Hadronic Calorimeter (CHA). A plug calorimeter was placed in the region $1.1 < \eta < 3.6$ and consisted of the Plug Electronic Calorimeter (PEM), and Plug Hadronic Calorimeter (PHA). A supplementary calorimeter, the Wall Hadronic Calorimeter (WHA), was located behind the CEM/CHA system and around the plugs, as shown in Figure 2.12, providing a coverage in the pseudorapidity region $0.9 < \eta < 1.3$.

The Central Calorimeter

The central calorimeters extended in the radial direction from 173 to 347 cm. Each of the three subsystems (CEM, CHA, WHA) was divided into four azimuthal arches (NE, NW, SE, SW) subtending 180° and organized in twelve 15° modules called wedges. The CEM consisted of alternating layers of lead and scintillator, while the CHA and WHA used iron layers as radiators.

A CEM wedge was made of 31 layers of 5 mm thick polystyrene scintillator, alternating with 3.2 mm thick lead sheets. The material thickness of the electromagnetic sector corresponded to 19 radiation lengths, X_0[4], with an energy resolution:

[4] The radiation length represented the mean distance, expressed in units of g/cm^2, over which a high

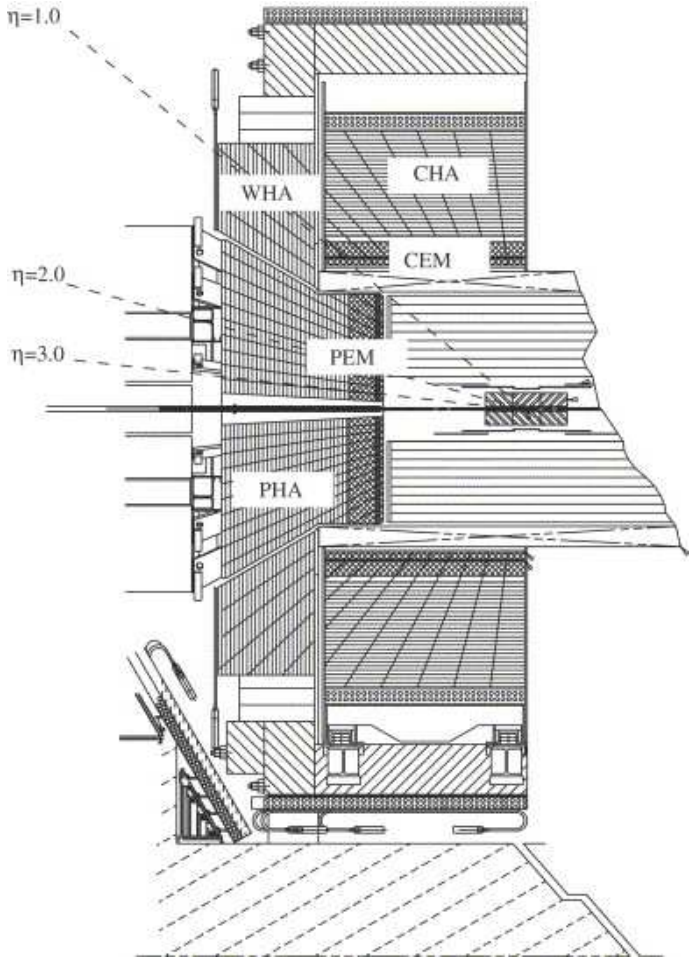

Figure 2.12: Elevation view of the CDF detector showing the components of the CDF calorimeter: CEM, CHA, WHA, PEM and PHA.

$$\frac{\sigma_E}{E} = \frac{13.5\%}{\sqrt{E_T[\text{GeV}]}} \oplus 2\%, \tag{2.6}$$

It was subdivided into 10 towers along pseudorapidity with a resulting segmentation of $0.11 \times 15^\circ$ in the (η, ϕ) space. Two towers (*chimneys*) in one wedge were missing to allow access to the solenoid, so the total number of instrumented towers was 478.

CHA and WHA detectors followed the same segmentation of CEM. CHA wedges were divided into 9 η towers matching in size and position the CEM towers. Each of them was made of 32 layers of 2.5 cm thick steel absorber and 1.0 cm thick scintillator. The WHA

energy electron loses all but 1/e of its energy by bremsstralung

consisted of 6 towers, 3 of them matching CHA; wedges were made of 15 layers of 5.1 cm thick steel absorbing material and 1.0 cm thick scintillator.

Both CHA and WHA had a total thickness corresponding to 4.5 interaction lengths λ_{int}[5], with an energy resolution that was respectively

$$\frac{\sigma_E}{E} = \frac{50\%}{\sqrt{E_T[\text{GeV}]}} \oplus 3\%, \tag{2.7}$$

and

$$\frac{\sigma_E}{E} = \frac{75\%}{\sqrt{E_T[\text{GeV}]}} \oplus 4\%. \tag{2.8}$$

A perspective view of a central electromagnetic calorimeter module (*wedge*) is shown in Figure 2.13, where both the arrangements in projected towers and the light gatering system are visible.

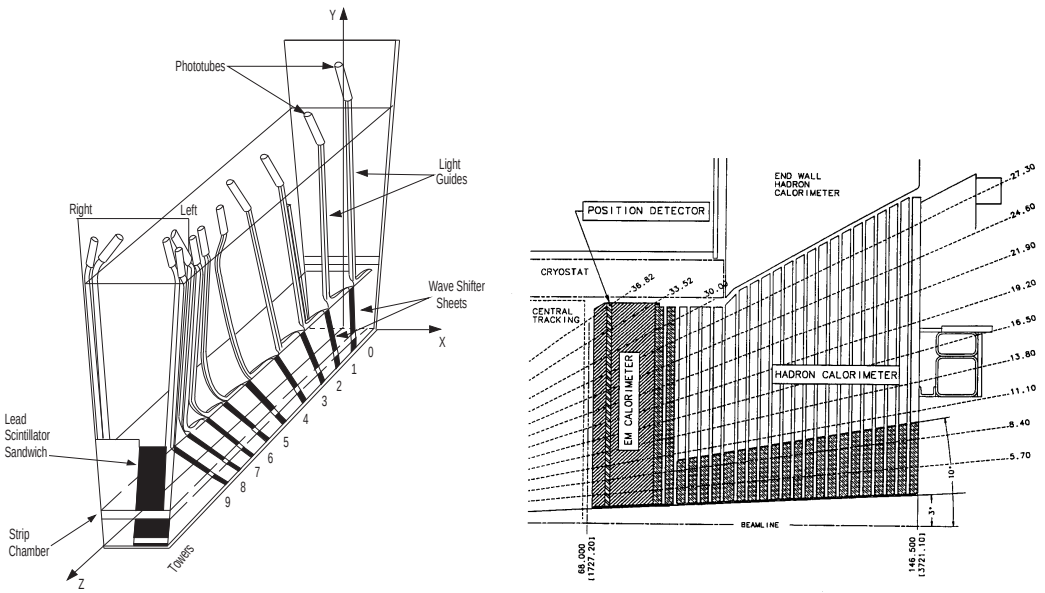

Figure 2.13: One azimuthal electromagnetic calorimeter wedge (left), and elevation view of one quarter of the plug calorimeter (left)

Two position detectors were embedded in the CEM in each wedge.

- The CEntral Strip multiwire proportional chamber (CES), was a two-dimensional strip-wire chamber embedded at the depth of maximum shower ($\sim$ 5.9 X_0). It

[5]The interaction length is defined as the average distance a paticle travels before interacting with a nucleus, expressed in units of g/cm^2. Here we refer to the interaction length of a charged pion.

measured the charge deposit of the electromagnetic showers, providing information on their pulse-height and position with a finer azimuthal segmentation than the calorimeter towers. This results was an increased purity of electromagnetic object reconstruction and the capability of discriminating a single photon shower from the one generated by a neutral pion. For the analysis described in this thesis, this feature allows the reconstruction of taus decaying into hadrons containing π^0 mesons.

We want to stress that we use the information of the CEM detector for the reconstruction and identification of electrons and π^0 from the hadronic decay of taus. We require the matching of the COT tracks with the CEM energy deposit to efficiently discard photon contamination.

- The Central Pre-Radiator (CPR), consisted of two wire camber modules placed immediately in front of the calorimeter. It acted as pre-shower detector by using the tracker and the solenoid coil material as radiators and was a very useful tool to reject pions from electrons and photons.

The Plug Calorimeter

The plug calorimeter was composed of two identical devices, installed on each sides of the detector, providing coverage in the forward regions ($1 < |\eta| < 3.6$). The Plug ElectroMagnetic calorimeter (PEM) was composed of 23 lead plates, 2.77 m in outer diameter, each 45 mm thick, built with a "doughnut" structure around a central hole, where the beam pipe was located. Scintillator tiles 4 mm thick were placed between these layers of absorbing material, organized in 24 15° wedges for $|\eta| > 2.1$ and 48 7.5° wedges for $|\eta| < 2.1$. Unlike the central calorimeter, the read-out system of each plug tower was made of a single PMT.

As in the central calorimeter, a preshower detector (Plug Pre-Radiator, PPR) consisting of a thicker (10 mm) scintillator, was installed in the first layer of the PEM, while a shower profile detector (the Plug showEr Maximum, PES) made of two tilted layers of scintillator strips, was located at a depth corresponding to 6 X_0. The total thickness of the material corresponded to 21 X_0, with an energy resolution of

$$\frac{\sigma_E}{E} = \frac{16\%}{\sqrt{E_T[\text{GeV}]}} \oplus 1\%, \tag{2.9}$$

The Plug HAdronic calorimeter (PHA) was divided into 12 wedges in ϕ, each subtending 30° and consisting of 23 layers of 5.08 cm thick iron absorbing material, alternated with 6 mm scintillator tiles. The total thickness corresponded to 7 λ_{int}, with an energy resolution given by

$$\frac{\sigma_E}{E} = \frac{74\%}{\sqrt{E_T[\text{GeV}]}} \oplus 4\%, \tag{2.10}$$

Calorimeter	CEM	CHA	WHA	PEM	PHA
η coverage	< 1.1	< 0.9	$0.9 < \|\eta\| < 1.3$	$1.3 < \|\eta\| < 3.6$	$1.3 < \|\eta\| < 3.6$
Absorber	Pb	Fe	Fe	Pb	Fe
Thickness	19 X_0,1 λ_{int}	4.5 λ_{int}	4.5 λ_{int}	21 X_0,1 λ_{int}	7 λ_{int}
Resolution (%)	$13.5\%/\sqrt{E_T} \oplus 2\%$	$50\%/\sqrt{E_T} \oplus 3\%$	$75\%/\sqrt{E_T} \oplus 4\%$	$16\%/\sqrt{E} \oplus 1\%$	$74\%/\sqrt{E} \oplus 4\%$

Table 2.3: Summary of the main characteristics of the CDF II calorimeter system.

2.3.4 Muon Detectors

Muons generated in the $p\bar{p}$ collisions at 1 GeV or above were minimum ionizing particles (MIP), which passed through the entire tracking system and calorimeter by depositing only a small fraction of their energy. Four independent devices, designed to detect such muons which escape from the inner volume of the detector, were placed radially outside the calorimeters [26].

The muon system was the outermost layer of the CDF II detector and consisted of drift cells and scintillation counters which were used to reconstruct segments of tracks, called *stubs*. Each chamber contained an array of drift tubes operating in proportional mode, with an Argon-Ethane gas mixture and a single sense wire each: the absolute time provided a measurement of the azimuthal coordinate, while the charge division at each end of a wire could be used to determine the z coordinate.

Stubs were matched with the COT information using dedicated algorithms in order to reconstruct the full trajectory of the muons. Some additional steel shielding layers, in between the chambers and the calorimeters, reduced the probability for other particles to escape the calorimetric system and mimic a muon signature.

The coverage in the $\eta - \varphi$ plane of the four muon subdetector systems is showed in Figure 2.14 and a description of the geometry is presented in the rest of this section.

CMU: The Central MUon (CMU) detector was located around the central hadronic calorimeter at a radius of 347 cm from the beamline with coverage $0.03 \lesssim |\eta| \lesssim 0.63$. It was segmented into 24 wedges of 15°. Only 12.6° in φ, with a gap of 2.4°, of each wedge was active, resulting in an overall azimuthal acceptance of 84%. Each wedge was further segmented into three 4.2° modules each containing four layers of four drift cells.

CMP: the Central Muon uPgrade (CMP) was the second set of muon drift chambers outside of CMU between an additional 60 cm thick steel absorbers. The material further reduced the probability of hadronic punch-through to the CMP. Muons needed a transverse momentum of about 2.2 GeV/c to reach the CMP. The CMP system was arranged in a box shape with similar acceptance as the CMU and conventionally served as a confirmation of CMU for higher momentum muons. The CMP and CMU had a large overlap in coverage and are often used together. Muon candidates which have both CMU and CMP stubs are the purest muons.

CMX: the Central Muon eXtension (CMX) consisted of drift tubes and scintillation counters (CSX) assembled in conically arranged sections. The CMX extended the pseudo-rapidity coverage to $0.6 \lesssim |\eta| \lesssim 1$. There were 8 layers of drift chambers in total with a small stereo angle between layers.

IMU: the Intermediate MUon system (IMU) extended the pseudo-rapidity coverage even further to $1.0 \lesssim |\eta| \lesssim 1.5$. The IMU was mounted on the old toroid magnets which provided shielding and consisted of the Barrel MUon chambers (BMU), Barrel Scintillation counters (BSU) and Toroid Scintillation counters (TSU).

Our analysis uses the central muon system to identify muons as part of the event signature and the full muon system to correct the missing transverse energy measurement from the calorimeters for muons. Another component of our event signature.

2.3.5 Luminosity Counters

The instantaneous luminosity of the Tevatron could be inferred from the average number $\bar{N}$ of inelastic interactions per bunch crossing, according to the formula

$$\bar{N} \times f_{b.c.} = \sigma_{p\bar{p}} \times \epsilon \times \mathcal{L}, \tag{2.11}$$

where $\sigma_{p\bar{p}} = 59.3 \pm 2.4$ mb was the total $p\bar{p}$ inelastic cross section resulting from the averaged CDF and E811 luminosity measurements at $\sqrt{s} = 1.8$ TeV, extrapolated to

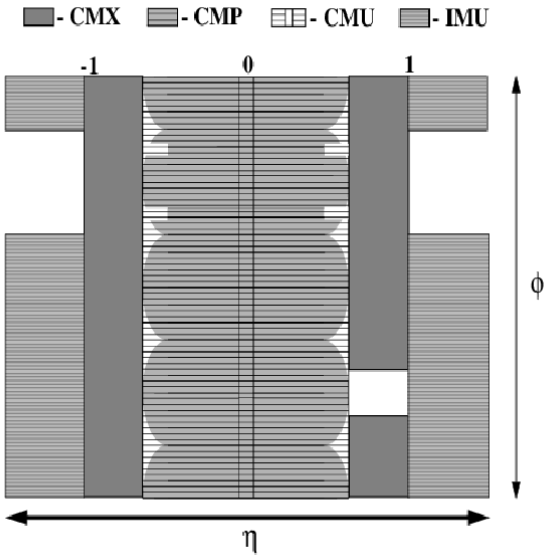

Figure 2.14: Muon detectors coverage in the $\eta - \phi$ plane.

$\sqrt{s} = 1.96$ TeV [27], $f_{b.c.}$ was the bunch crossing frequency known from the Tevatron RF and ϵ was the efficiency to detect inelastic interactions.

The average number of interaction per bunch crossing was measured with a couple of Cerenkov Luminosity Counters (CLC) [28], installed on both sides of the detector along the beam pipe, inside the end plug calorimeter. $\bar{N}$ was measured with an uncertainty of 4.4%, which combined with the 4% uncertainty on $\sigma_{p\bar{p}}$, leads to an instantaneous luminosity uncertainty of 5.9%.

The luminosity counters played an important role in all physics analyses and especially in the estimate of the cross sections (see Chapter 7 and 8)

2.4 Trigger System

At the instantaneous luminosity $\mathcal{L} \approx 4{\cdot}10^{32}$ cm^{-2}s^{-1}, and with an inelastic $p\bar{p}$ cross section of $\sigma_{p\bar{p}} \approx 60$ mb, approximately $2.5 \cdot 10^7$ inelastic collisions per second occur. Taking in consideration the volume of the information to be stored and the limits of the acquisition system, however, the maximum rate of acquired event ends up to be about 100 Hz.

Furthermore, because the average size of the information associated with each event is about 140 KB, even in the case of the detector capable of acquire and record all the events, a throughput and storage rate of 840 GB/s would be needed, beyond currert technology. For this reason a trigger system was implemented to acquire events interesting for data analysis.

The trigger system was segmented into three levels. A sketch of the logic chain is shown in Figure 2.15. Each level received the accepted event from the previous level, and verified if it passed selection requirements.

The CDF trigger system was organized with a progressively greater sophistication in event reconstruction and filtering. At each level, events were selectively accepted or discarded, with a reduction rate sufficient to allow data to be processed by the subsequent level with minimal dead time.

The pipelines at level 1 (L1) had a capacity of 14 events. It corresponded to an amount of time during which the L1 trigger had to decide to accept an event, otherwise the buffer content was overwritten: 396 ns x 14 = 5.5 μs. An event accepted by the L1 was then passed to the level 2 (L2) buffer, where the number of buffers in the pipeline was 4, giving 5.5 μs $\cdot$ 4 = 22 μs. If an event was accepted by the L1 and the L2 and the system did not have a free buffer for transfering the event, deadtime incurred.

L1 was based on hardware electronics, L2 consisted of a combination of custom hardware and commodity processors, while level 3 (L3) was implemented via software in a PC farm with over 500 CPU cores, organized in a modular and parallelized structure.

DAQ and trigger systems were the subject of a major upgrade for Run II that included novelties such as the level 1 COT and Silicon vertex level 2 trigger components.

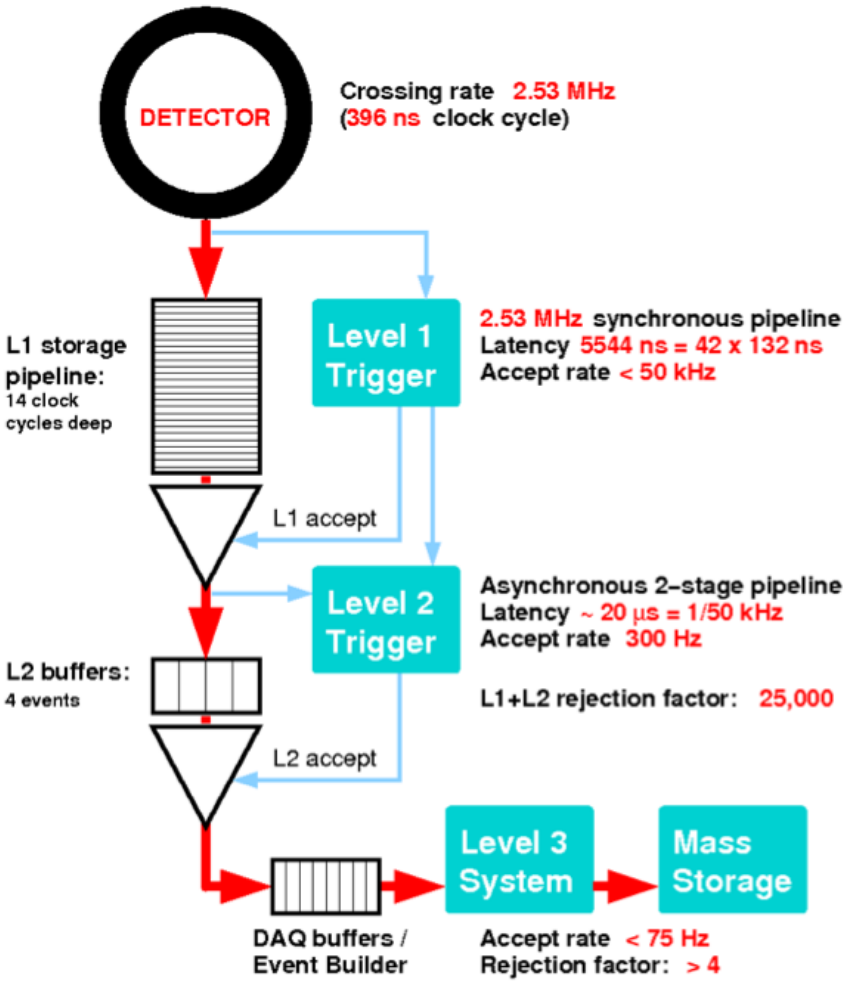

Figure 2.15: Diagram of the CDF trigger system data flow.

2.4.1 Level 1

The front-end electronics of each subdetector, packaged in Versa Module Eurocard (VME) modules, hosted in about 120 crates, was interfaced to a 42 cell deep pipeline, synchronized with the Tevatron clock cycle (132 ns)[6]. Since the interbunch time was three times larger, the pipeline collected data corresponding to a maximum of 14 bunch crossings; each event was kept up to 132 ns $\times 42 \approx 5.5\mu$s for the decision, before the buffer reused. The L1 maximum accept rate was about 30 kHz and was limited by the level 2 execution time.

[6]The CDF Run II detector trigger system was originally designed to operate with a Tevatron bunch spacing of 132 ns.

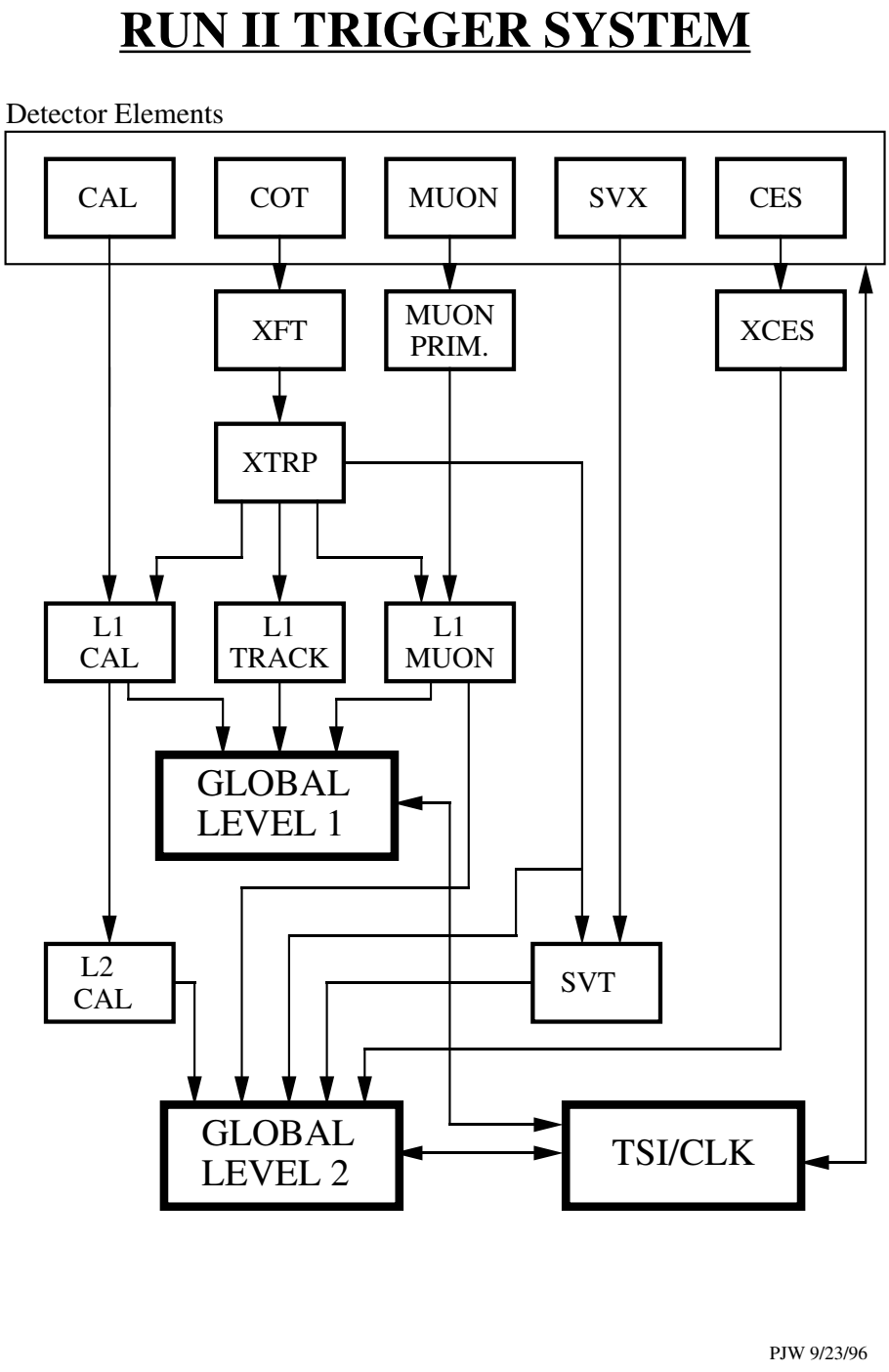

Figure 2.16: The trigger decision chain for the L1 and L2 systems at CDF II.

The L1 hardware system consisted of three parallel processing streams, which collected the basic raw information provided by three subdetectors (the calorimeters, the COT and the muon chambers) and built low resolution physics objects, called "primitives".

The information from the tracking system was merged with the information of the calorimeter and the muon chambers. The track trajectory was extrapolated to the calorimeters and to the muon detector. All information was fed to the global level 1 decision unit, where the L1 trigger decision was taken.

- The four axial superlayers of the COT were used by the eXtremely Fast Tracker (XFT) [29], a custom processor that identified two dimensional tracks in the (r, ϕ) plane. A pattern-matching algorithm searched for correspondences between the observed combination of hits in each superlayers and a set of predefined patterns, which represented a specific segment. If a coincidence between the segments crossing the four superlayers was found, the segments were linked to reconstruct a track. The algorithm returned the p_T and ϕ, by comparing each track to a set of about 2400 predetermined patterns, corresponding to tracks with $p_T > 1.5$ GeV/c originating from the beam line.

  An upgrade to the XFT system [30], which was necessary to keep trigger rates under control at high luminosity runs of the latest periods, allowed to reject axial tracks which were not confirmed by the outer three COT stereo segments (*SLAM* confirmation): fake tracks were thus reduced of about a factor of 7.

  The resulting track list was then sent to the eXTRaPolation module (XTRP), a digital system which extrapolated each of them to the central calorimeter wedges and to the muon chambers (CMU and CMX), thus allowing to create electron and muon objects primitives.

  Having the COT information at L1 was a unique and pioneering feature of CDF and it was a crucial feature for the selection of leptons and especially for the taus.

- Calorimetric primitives were built by merging towers in pairs along η, dividing the calorimeter into 24×24 trigger towers in the (η, ϕ) space, with a transverse energy for each tower which was measured with a granularity of 500 MeV.

  The information coming from each trigger tower was used to define two classes of primitives: global primitives were the sum of all transverse energy deposits above the threshold of 1 GeV in all trigger towers (ΣE_T) and the missing transverse energy $\not\!\!E_T$; object primitives were electrons, photons and jets, defined by evaluating the hadronic and electromagnetic transverse energy contributions of the trigger towers and by exploiting the information coming from the extrapolated XFT track (i.e. for the discrimination of electrons from photons).

- Muon primitives were generated by matching the information coming from the muon detectors (single or coincidence hits in the scintillators, pattern of hits in the wire chambers) with the XFT tracks.

2.4.2 Level 2

The trigger level 2 (L2) was an asynchronous system with a latency of 20 μs and a maximum accept rate of about 1 kHz. Events accepted by level 1 were transferred to a 4 cell buffer, which was integrated in the front-end electronics of each subdetector, and queued for the L2 decision. The buffering was organized as a two stage pipeline: in the first step signals from a particular section of the detector were analyzed; in the second stage the outcomes of step one were collected for the trigger decision. While data in the buffer were being processed, they could not be overwritten by a new event: if a L1 accept occurred when all four buffers were occupied, the system was subject to trigger dead time. Additional information coming from the shower maximum strips chambers in the central calorimeter and the axial hits in the SVX II was combined with L1 primitives, to produce L2 primitives.

- A raw energy clustering was performed by an iterative algorithm which merged the energy of adjacent towers which exceeded a predefined threshold, typically a few GeV. L2 clusters could be used to build objects to trigger on, by applying cuts on their total transverse energy, their position in the (ϕ, η) plane or their multiplicity. CDF upgraded the L2 calorimeter trigger [31]: the new system increased the energy resolution up to a granularity of 125 MeV, by exploiting the full 10 bit trigger tower information. It also implemented a new fixed cone clustering algorithm, which turned out to be less affected by fake cluster formation. A cluster was defined by adding the energy of all towers which lied within a radius $R = \Delta\eta^2 + \Delta\phi^2 = 0.7$ around a seed tower.

- The XCES boards processed the energy measurement registered by the shower maximum detectors, which provided a much better spacial resolution than the calorimeter towers. By combining CES clusters with L1 track information, electron and photon primitives were obtained, with a position accuracy of 2°.

- The Silicon Vertex Tracker (SVT) combined the precision information provided by the SVXII detector with the L1 XFT primitives, to form two-dimensional tracks with a reconstruction efficiency and a resolution close to the offline ones. In addition to the ϕ and p_T, also a measurement of the track impact parameter d_0 was performed.

  The SVT architecture was based on the pattern recognition technique: the algorithm received as input the axial COT tracks found by XFT and the digitized pulse-heights coming from the $r \times \phi$ sides of the SVXII layers. As a first step, the hit finder collected the Silicon hits and stores them in a buffer. Adjacent SVX detector channels were grouped into "superbins": candidate tracks, called "roads", were created by combining the XFT tracks with the superbins which contained hits from at least four different silicon layers. These roads were then compared to a set of pre-calculated combinations which were recorded in specially designed memories, called Associative Memories (AM): when a match was found, the hits belonging to that road were retrieved from the buffer and sent to the track fitter, where the track parameters were computed.

The impact parameter was measured by SVT with an r.m.s. width of $\sigma_{d_0} \approx 35\mu$m, thus allowing to efficiently trigger on displaced tracks with respect to the beam spot.

- L2 muon primitives were characterized by an improved ϕ matching up to 1.25°, between the XFT tracks and the hit segments in the muon chambers. With the upgraded XFT system [32], a 3D track reconstruction could now be performed, with a good resolution on $\cot\theta$ ($\sigma_{\cot\theta} = 0.12$) and z_0 ($\sigma_{z_0} = 11$ cm).

2.4.3 Level 3

When an event was accepted by level 2, all the raw detector output was sent via optical fibers to level 3, a Linux PC farm, for full reconstruction, performed by C++ based algorithms, similar to those used offline. These algorithms defined high level objects and benefit from the full detector information and an improved resolution, including 3D track reconstruction and a tighter matching between tracks, calorimeter clusters and muon stubs. The average processing time per event in L3 was of the order of a second and the accept rate is about 100 Hz.

2.4.4 Trigger Prescale

In high instantaneous luminosity conditions, the output rate of some triggers can easily exceed the maximum allowed, thus leading to unwanted dead time; this effect gained increasing relevance with the Tevatron performances improvements over the course of Run II.

A feature was implemented in the first two stages of the CDF trigger system to avoid such deadtime: a static prescale characterized by a fixed predefined prescale factor and a dynamic prescale, where the prescale factor was allowed to change during data taking, as function of instantaneous luminosity.

Some samples that we used in this analysis were collected with dynamically prescaled triggers. In the analysis we used data collected requiring CMX or CMUP muons or CEM electron (these triggers will be discussed in more detail in Section 4.2). The trigger for the CMX muon category was prescaled at high values of instantaneous luminosity (the specific settings changed over the course of Run II) and unprescaled at low instantaneous luminosities.

2.5 Concluding Remarks

The study we pursued uses all the major resources and components of the CDF experiment. The tracking is fundamental for both lepton reconstruction and the reconstruction of high p_T jets from B hadron decays, where the Silicon detector plays a key role. As will be explained later the analisys makes also extensive use of the central calorimeter.

Very important for the success of our study is the fast timing of the tracking system which allowed use of the track information in the level 1 decision. Fundamental is the association of the XFT+XTRP systems which connected tracking information to the calorimeter and muon chamber information [35]. This class of triggers allowed the selection of events containing the signature of tau leptons which is important for testing the prediction of the SM but also for searches of physics beyond the SM, particularly related to the Higgs sector [33].

This class of triggers allowed to set low p_T thresholds for leptons and track, extending the kinematic acceptance over regions not accessible to ordinary inclusive lepton triggers [34]. The requirement of the trigger algorithm will be presented in Section 4, together with the signature of the signal processes. More details of the specific requirements of the trigger algorithm are in Appendix A.

Chapter 3

Silicon Tracking System and its Perfomance

The search for the Higgs boson, measurement of top and bottom quark properties are top priorities in the CDF Run II physics program. All of these studies benefit from a high-resolution tracking detector and rely heavily on the efficient identification of displaced secondary vertices. Moreover, accumulation of data for these analyses increased by the capability to trigger on tracks not originating from the beam axis.

The CDF Silicon vertex (SVX) detector was designed to withstand 2–3 fb^{-1} of integrated luminosity, from the expected duration of the first phase of Run II (initially labelled as Run IIa). An upgrade of the detector was planned for the follow-on Run IIb, but canceled in 2003. Moroever, the duration of the Run II was extended to 2008 and beyond, due to the delay in the LHC start. The expected delivered integrated luminosity of Run II increased to $\sim 8-9$ fb^{-1}.

Later extensions brought the total integrated luminosity delivered by the Tevatron to over 12 fb^{-1} whereas the Silicon detector were supposed to sustain up to about half this luminosity. The cancelation of Run IIb led the CDF management to organize a strong operations task force around this device in particular in order to monitor the aging effects due to much larger radiation doses than anticipated. I became part of this team from 2009 until the end of the Tevatron Run II. This section reports on the main aspects and lessons learned from this work that was crucial in maintaining one of the center pieces of the CDF II experiment.

Several preventive measures were undertaken to keep the original detector operational and maintain its performance. The most important of these was the decrease of the operating temperature of the detector, which reduces the impact of chronic radiation exposure. Issues arising from radiation damage of the sensors, aging infrastructure and electronics were continuously addressed. We present in this chapter the study of the detector aging and the evolution of the performance.

In this channel we focus on the data acquisition system, operation and maintenance.

A description of the Silicon detector geometry is provided in Section 2.3.2.

3.1 Silicon Sensor Properties

Silicon sensors for particle tracking are commonly cristalline layers of Silicon. The opposite sides of the crystal is contaminated with dopants that create excess of donors (n-type Silicon) and acceptors (p-type Silicon). These impurities act in such a way that there is an eccess of free electrons in the n-type Silicon and holes in the p-type Silicon. The effect is that the Fermi level of the electrons in the n-type (p-type) Silicon is shifted towards the conduction (valence) band. The interface between the two types of Silicon is commonly called junction. The Fermi level has to be the same along the junction, so, some of the charge migrates from the p-type to the n-type Silicon generating a potential ("contact potential") across the junction. This potential forms a step in the valence and conduction band edges, labeled V_B and has by definition the same magnitude of the difference of the Fermi levels in the two types of Silicon. As a result a "depletion region" near the junction becomes depleted of both holes and electrons, forming an insulating region with almost no mobile charges; see Figure 3.1. There are, however, fixed, immobile charges due to dopant ions.

When raising of the potential of the p-type Silicon more electrons (holes) cumulate in the p-type (n-type) bulk, creating an higher electric field along the junction. In this condition the junction is said to be in a reverse bias regime due to the external potential V_R. The external potential induces an increase in the step in the band edges, which becomes $V_B + V_R$, and no direct current flows across the semiconductor, see Figure 3.1. When a reverse bias is applied the depletion region widens, and at some potential it can occur that there are no free electrons in the n-type bulk and no free holes in the p-type. In this condition, Silicon sensor is operating "fully depleted".

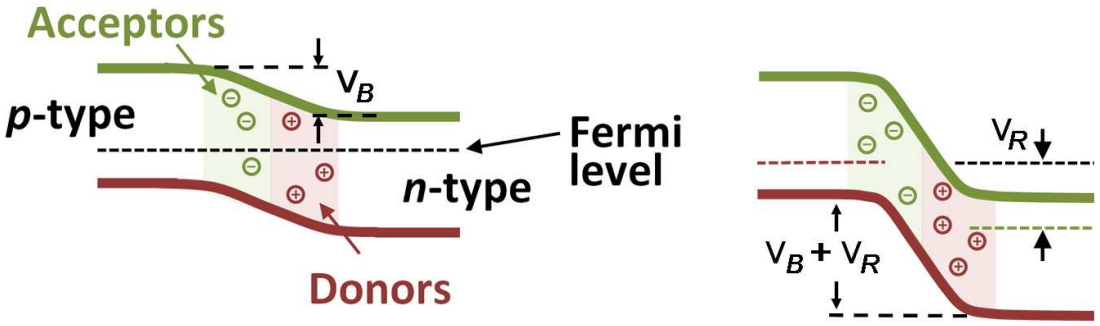

Figure 3.1: Junction betweem p-type and n-type Silicon with no external bias (left). The same junction with reverse bias, V_R (right).

The only charge in the depletion region is represented by immobile ionized donors and filled acceptors and this kind of charges do not contribute to conductivity. An ionizing

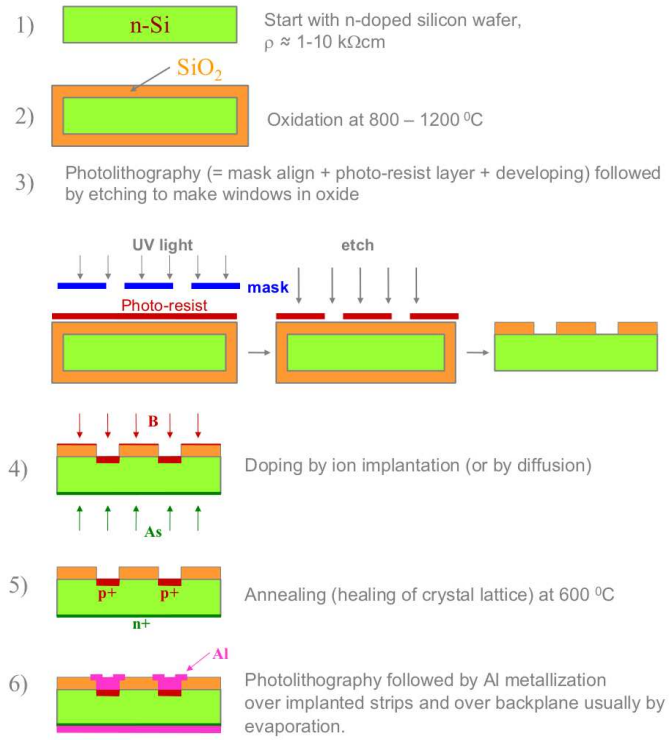

Figure 3.2: Steps in the fabrication of planar silicon diode detectors.

.

particle traversing the sensor creates electrons-holes pairs and the electric field in the depletion region pushes the free charge out of it. So in a reversed biased Silicon sensors we expect significant current flow at the passage of ionizing radiation.

The charge collected at the contacts is in first approximation proportional to the volume of the depleted region. So in most of the applications, when is necessary to maximize the charge collected, the Silicon sensors shall operate fully depleted.

The Silicon microstrip sensors used by the CDF experiment are produced through the steps summarized in Figure 3.1 (where the strips are only dug on one side). The aluminum contacts on the p^+-type Silicon measure the $r - \phi$ position of the particle, while the ones running on the ohmic contact (the n^--type Silicon) measure the $r - z$ position. The strip (readout) pitch in the CDF detector varies in a range from 25 μm (50 μm) to 73 μm (146 μm).

3.2 Silicon Signal Full Processing System

The data acquisition (DAQ) system of the Silicon tracking system read out the approximately 750,000 channels of the detector. The Silicon DAQ components operated in the context of the CDF trigger system, which selected a fraction of the events to be stored for analysis.

There were several major constraints on the design of the silicon detector data acquisition system. First, the front end (FE) readout chips had to comply with the digitization of information without interfering with the signal acquisition of the next beam crossings. Moreover the readout chips had to keep the information while the trigger system operated a L1 decision for a particular beam crossing and this delay could last up to 5.5 μs. The system was designed for a beam crossing rate of 132 ns, since this was expected to become the bunch crossing time in Run IIb. Instead there was no Run IIb and the Tevatron operated until the end with 396 ns bunch crossing time. For this reason the chips were designed with 42 cell analog pipelines.

The data of the $r-\phi$ strips of the SVX-II detector was readout every time the L1 trigger accepted the event; the charge in the strips was digitized and sent to the Silicon Vertex Trigger (SVT) [37]. The digitization and readout had to be very rapid – it started 6–7 μs after every level 1 accept (L1A).

A schematic of the Silicon detector DAQ system is shown in Figure 3.3. The main controller board for the data acquisition system was the Silicon Readout Controller (SRC). The SRC controlled the logic for the readout of the detector and provided the interface with the trigger system. The SRC received the clock signals from the CDF Master Clock and passed them on to the Fiber Interface Boards (FIB) along with a series of commands. For each SRC command a sequence was generated by the FIB module and sent out to two portcards attached to it. The portcards then decoded these commands and sent them to a number of *chip chains*. A chip chain was a daisy chain of SVX3D chips [36], containing a number of chips depending on the layer of the detector, between 2 and 16. The chip chains collected the charge from the Silicon sensors, digitized and processed the information with pedestal subtraction algorithms.

The SVX3D chip was an integrated circuit, with 128 parallel analog inputs and a 8 bit digital output bus. It was a mixed, analogue and digital, integrated circuit including 128 analog-to-digital converters and the digital processing for signal pedestal subtraction. It represented an innovative technology at the time it was designed, since the digitization was performed on the detector, and allowed to include the Silicon tracking information into the trigger. This was achieved with the use of associative memories able to process the Silicon detector information in realtime.

The chips were located in the volume of the Silicon detector and were subject to a extremely high radiation field. The fabrication technology was intended to be radiation hard. The chips were manifactured through the 0.8 μm bulk CMOS radiation hard Honeywell process.

The major cycles of operation for these parts were initialization, acquisition, digitization, and readout. During the initialization cycle a serial bit stream of digital data was fed into the chip to set various operational parameters of the devices like signal thresholds, pedestal subtraction settings and chip chain lenght. The initialization passed sequentially through the daisy chain of chips. The pipeline cell pointer was reset as part of the initialization sequence.

In the acquisition mode the integrator accepted the charge from the microstrips and in sequence transfered it to the pipeline cells at each clock cycle. The cells were in a circular buffer, and the information was overwritten, if no trigger signal was received before the cell is due to be used again. A signal from the trigger system caused the appropriate cell in the pipeline to be marked for readout and the chip logic skiped this cell until it was released for reuse.

The digitization cycle began with the receipt of the L1 accept signal, which caused the difference between the charge stored in the cell and the one in cell 47, to be presented to a 8-bit ADC. The SVX3D chip also had a unique feature of dynamic pedestal adjustment. The circuit used all channels to calculate in real time a common pedestal and then subtracted it from each channel during digitization.

In the readout cycle data were transmitted over an 8-bit bus, always accompanied with an Odd-Byte-Data-Valid (OBDV) signal on a separate line, which served as a timing reference and a data strobe.

The event information moved along the SVX3D chip chain bus to the portcard, where it was converted from an electrical to an optical signal using a 8 bit logic Digital Optical Interface Module (DOIM) transmitter. The DOIM light emission (one transmitter per sensor) was passed through optical fibers to a DOIM receiver, where it was converted back into an electrical signal and passed to a FIB module. The transmitters are an array of InGaAs/InP laser diodes matched with PIN-diodes of the same semiconductor. The FIB processed the data and combined the 5-byte wide data streams from multiple ladders into two 20-bit wide optical signals, and transmitted these signals to the VME Readout Buffer (VRB).

The VRB acted as a readout buffer for the incoming data. Each event in a VRB occupied one out of four buffers and awaited a L2 trigger decision. When accepted by the L2 trigger, the buffer was read out and the data was transmitted into the L3 trigger computer farm.

3.3 Effects of Radiation Exposure

The CDF Run II Silicon detector was located in a high radiation environment and was exposed to a radiation dose of 300 $\pm$ 60 kRad/fb^{-1} at a radius of 3 cm, with a 20% variation over the the z axis [38]. Assuming the increase of sensor bias current to be equal to the increase of leakage current it is possible to extract the relation between the distance

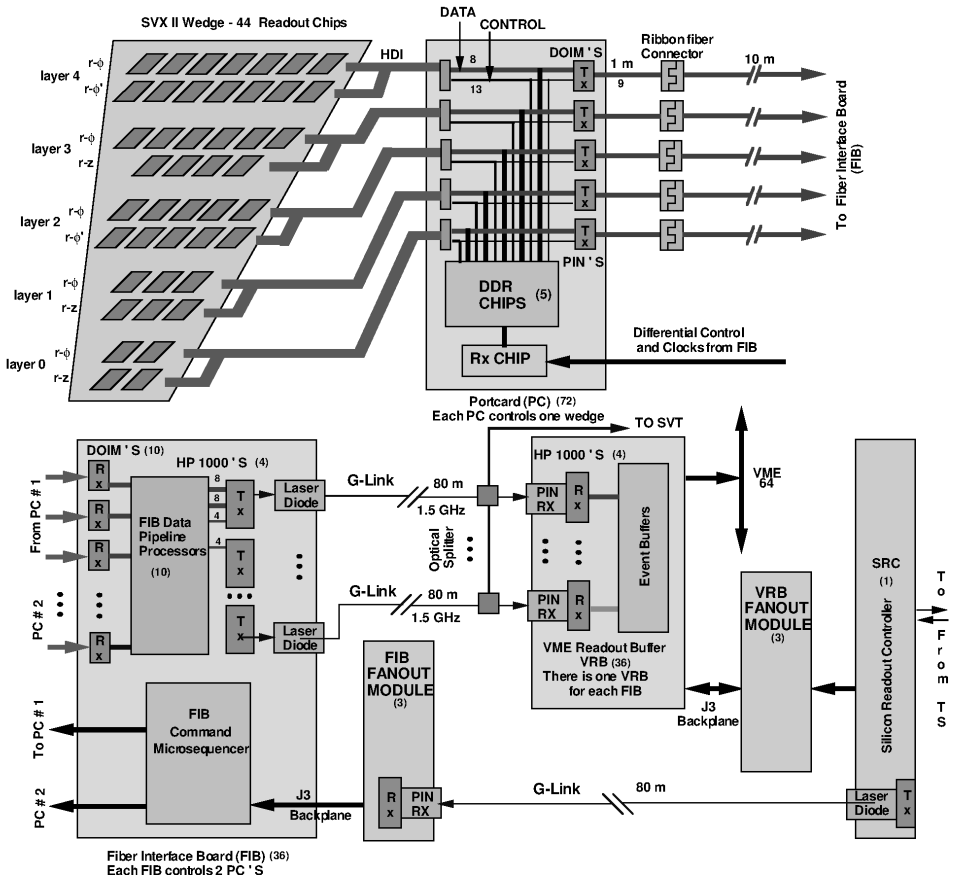

Figure 3.3: A schematic diagram of the silicon detector DAQ system.

of the sensor from the beam axis and the intensity of the radiation field [39]. With respect to the distance in radial direction the radiation field ϕ scales by the formula:

$$\phi \propto r^{\alpha}, \tag{3.1}$$

where $\alpha = 1.65$ with 30% systematic uncertainty due to the sensor temperature measurement. The flux to luminosity factor was measured using the increase in bias current of the sensors, resulting in 0.93 ± 0.26 (10^{13} MeV n equiv.)/cm^2/fb^{-1} for the innermost layer of SVX.

The main concern for the CDF detector operation was the displacement damage and defects in the lattice structure of the sensor, known as *crystal damage*, caused by non-ionizing energy loss. This generated an increase of shot noise, changes the effective doping concentration of the bulk and increased the charge carrier trapping. From the operational

point of view, these effects translated into performance degradation due to the increase of noise from the sensors and a decrease of charge collection efficiency. In addition, the modification of the effective doping caused the depletion voltage to steadily increase and this could eventually limit the lifetime of the sensors, since the bias current needed to be maintained below the sensor breakdown voltage or the high voltage specifications of the power supplies.

The lifetime of the overall detector was studied by monitoring the evolution of the full depletion voltage and also through the ratio of the average charge (from MIP tracks) over the noise of the sensor, which is called the signal-over-noise ratio (S/N).

3.3.1 Full Depletion Voltage Study

Maintaining full depletion voltage was fundamental in order to keep the noise of the sensor to a minimum level, while enhancing the collection efficiency of charge induced by ionization.

As radiation damage increases, the sensor begins a *type-inversion* effect[1], which appears as a change in the bulk the effective doping and mutates behavior of the n-type Silicon to p-type Silicon. This change occurs in a continuous way as the sensor is exposed to radiation and is visible by monitoring the depletion voltage, which decreases until the type inversion is complete. After that, the full depletion voltage increases linearly with the integrated dose of radiation [41].

The measurement of the full depletion voltage was performed several times for each sensor through the *signal-to-bias* scan technique. The signal-to-bias method consists of measuring the charge collected for particles as a function of the bias voltage. For a set of different bias voltages it is possible to measure the distribution of charge and through the interpolation with a Landau distribution. The charge is defined as the most probable value of the fitted curve. The charge collection as a function of bias voltage is well parametrized with a sigmoid function, and from the interpolation of the points it was possible to extract the depletion voltage. We defined the depletion voltage as the bias voltage which corresponds to a charge collection equal to 95% of the asymptotic value at the efficiency plateau, as shown in Figure 3.4.

The evolution of the depletion voltage with integrated luminosity facilitates quantitative studies on the aging of specific sensors. The measured values at different times are fitted with a three-degree polynomial to extract the inversion point and with a straight line to obtain the behaviour after inversion and obtain expectations for the future.

[1] This behaviour can be explained with nonlinearities in the electric field [40] in the Silicon sensors as a function of the depth. This consistent with a picture in which the electric field has two maxima at both n^+ and p^+ implants. This phenomenon is consequence of the charged carrier trapping in the crystal defects. Trapping of mobile carriers produces a net positive space charge density near the p^+ implant and a net negative space charge density near the n^+ implant. Positive space charge density corresponds to n-type doping and negative space charge to p-type doping, therefore they generate p-n junctions at both sides of the detector.

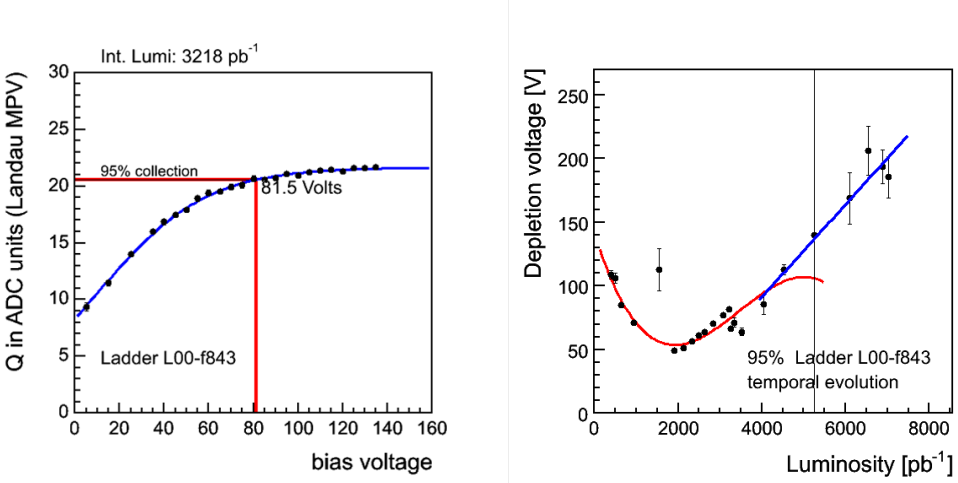

Figure 3.4: Evolution of the full depletion voltage of a sensor in CDF Layer-00 detector as a function of the integrated delivered luminosity.

Figure 3.5 shows the prediction based on the linear fits of the depletion voltage for sensors in L00, with the latest signal-versus-bias scan, corresponding to an integrated luminosity of 6.9 fb^{-1}. The predicted depletion voltages lie below the high voltage power supply limit of 500 V and the sensor breakdown region. Indeed the majority of the sensors worked properly until the end of Run II, i.e. a delivered luminosity of 12 fb^{-1}.

Figure 3.6 shows the predictions for sensors of SVX-L0. While the depletion voltages for all sensors will remain below the breakdown region through 10 fb^{-1} of delivered luminosity, many of them will likely not be able to be fully depleted for higher values of integrated luminosity.

If we consider outer layers of the Silicon detector the increase of the depletion voltage due to the radiation dose did not present an issue. If we take in account SVX-L1, the sensors belonging to it started to show a post-inversion behavior, but the linear extrapolation of the linear fit shows that all sensors were all fully depleted up to a delivered luminosity of $\sim$ 12 fb^{-1}.

3.3.2 Signal Over Noise Study

As mentioned above the monitoring of sensor aging does not provide direct information on how the aging impact the track reconstruction and thus the physics analysis. For evaluating this, the most common variable is the ratio of the most probable value of the charge collected in a particular sensor over the noise. This signal-to-noise (S/N) ratio is estimated using real data for the signal and pedestal-calibration data for the noise. Plots in Figure 3.7 and Figure 3.8 show the evolution of this variable for the sensors belonging to

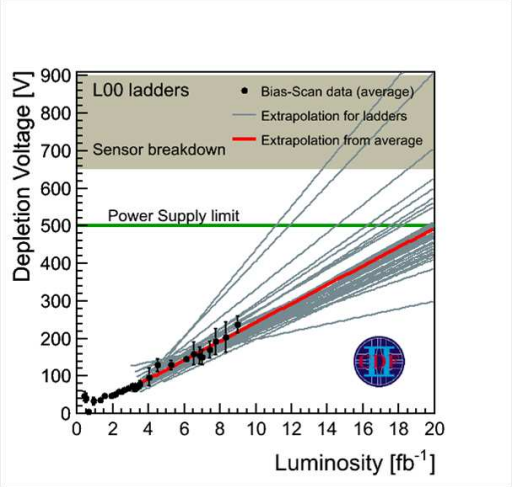

Figure 3.5: Summary of the extrapolation fits of L00 depletion voltage using data up to 6.9 fb^{-1}

the different layers of the SVX detector as fuction of the integrated delivered luminosity. The lines interpolating the points in Figure 3.7 show the expected values for S/N in the future. It has to be taken into account that the predicted values have to be considered valid in case of a fully depleted sensor, otherwise the signal value is expected to decrease faster and, in addition to this, the noise increases. The evolution of L00 is showing a knee that can be explained by a slight average underdepletion of the sensors.

The studies performed on the S/N evolution with time shows that the performance of the sensors of SVX-L0 degraded but most of the detector provided useful data for analyses through the end of the Run II. The innermost sensors, belonging to L00, demonstrated a decrease in S/N but the more recent flattening in the S/N evolution allowed CDF to collect data without any problem.

3.4 Detector Maintenence

Several operation procedures were undertaken in a way to minimize the effects of the radiation damage and aging of the Silicon detector. In this section a few of the routine operations are described, which represented the dominant maintenance efforts of the Silicon operation group during the last periods of data taking. They were part of my tasks in the CDF Silicon operation group.

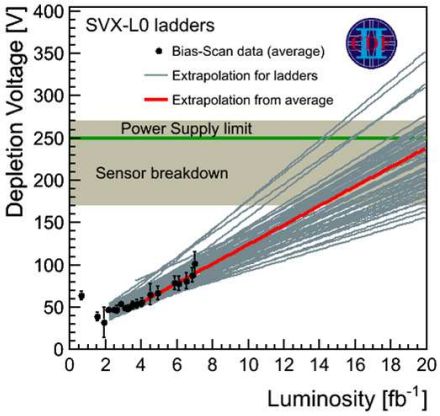

Figure 3.6: Summary of the extrapolation fits of SVX-L0 depletion voltage using data up to 6.9 fb^{-1}

3.4.1 Maintenance of the Power Supplies

The FE electronics and the bias voltage of the sensors were provided through custom power supplies (PS) manufactured by CAEN. The PS were connected with two separate channels to the analog and to the digital components of the SVX3D chips and provided also the sensor bias voltage. Two other lines provided power to the portcards: a 5 V line allowed the data processing of the portcards, while a 2 V line was used to control the light emission of the DOIM trasmitters [42]. The nominal potential for the optical transmitters is equal to the difference of the 5 V and 2 V line, and the lowest potential line can be adjusted to modify the intensity of the light emission.

The stability of the output lines of the PS is fundamental to the proper operation of the FE electronics. The aging of PS components and in particular of the condensators was affecting the voltage of the output lines for the analog, digital component of the SVX3D chips and the portcards. A drift from the nominal voltage of the low voltage lines of the portcards could affect the digital transmission of data. Some of the digital bits could remain in a frozen logical state and cause the partial or total loss of a Silicon sensor information.

The PS crate controller (CEAN SY527) could be used to diagnose the paramenters of the PS modules. The PS were replaced usually before malfunctioning. On average, they needed repair after about 3 years of operation.

3.4.2 Maintenance of Optical Trasmission

The optical fiber trasmission between the portcards and the FIB's was continuously affected by aging effects due to the radioactive environment. The trasmitters on the portcard were

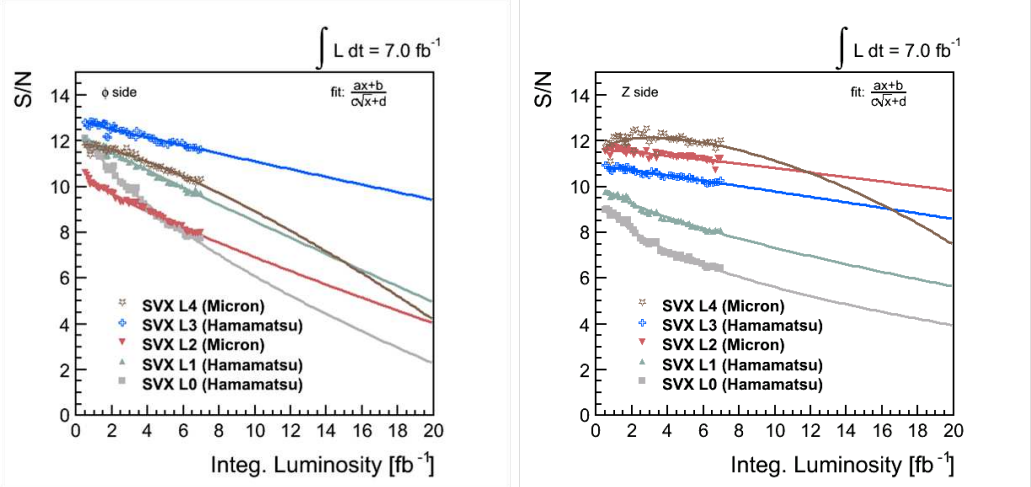

Figure 3.7: Evolution of the S/N of all the layers of the SVX detector of CDF as a function of integrated luminosity.

directly immersed in the radiaction induced by the $p\bar{p}$ collisions and the receivers were also affected by the radiation induced by the beam in the CDF collision hall.

Problems of the digital transmission showed up as stuck bits and could be easily diagnosed observing the distribution of the charge induced by particle ionization. In addition the position of track passage is also affected by these errors and cause the tracks to not be reconstructed. In more serious cases the bit error affects the transmission of the chip identification number and a complete loss of the sensor information could happen.

The radiation exposure caused a the reduction of the light intensity emitted by the transmitters. In most of the cases the proper light level could be restored with a tune of the 2 V line of the portcard. The measurement of the light intensity, required to diagnose the problem and changing the PS settings could only be done from within the CDF collision hall. A decrease of the output intensity is observed to be linear with the absorbed dose and the slope has been measured: $\sim$ 10% every 200 kRad [43] (corresponding to about 4 fb^{-1} of integrated delivered luminosity).

In some cases the radiation could reduce the sensitivity of the DOIM light receivers. In these cases we substituted the problematic receiver mounted on the FIB. Also this repair required access to the collision hall.

3.4.3 Sensor Bias

In the last periods of data taking the inner layers of the Silicon detector experienced a bulk type inversion (see Section 3.3), namely the layer 00, SVX layer 0 and layer 1. To maintain the sensors fully depleted the bias voltage was periodically increased on the base

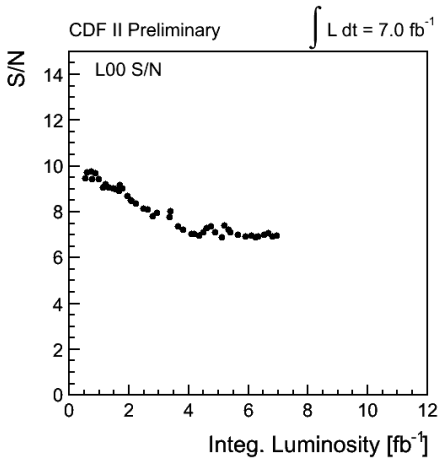

Figure 3.8: Evolution of the S/N of the sensors in L00 as function of integrated luminosity.

of the integrated luminosity and the average linear extrapolation of the depletion voltage fit (see for example Figure 3.6). This procedure was made remotely from the CDF control room and allowed to maintain a value of the S/N compatible with a good rejection of the background.

3.5 Efficiency Study

The efficiency for a particular sensor is defined as the ratio between the number of tracks crossing the sensor with an associated hit and the total number of tracks crossing the sensor. The efficiency for an entire layer of the detector is defined as the average of the efficiency over all of its sensors.

Note that these efficiencies are a quantitative estimate of the performace of the sensors, but do not represent the real efficiency of reconstructing a track. The tracking efficiency is dependent on the algorithm settings in the fit of the hits (for example the minimum number of Silicon hits required and the cut in the χ^2 of the fit). However the variation in the real efficiencies is reflected in the overall efficiency of the system.

Figure 3.9 shows the efficiency for L00 and each layer of SVX-II during the first nine years of running. The outer three SVX-II layers show a very slow decrease in efficiency and present no concern until the end of Run II. The efficiency of SVX-II L0 has decreased $\sim 20\%$. This is linked to the decrease in signal-to-noise ratio (see Figure 3.7 and 3.8).

The Layer 00 shows a dip in efficiency between 4 and 6.5 fb^{-1}. This is not due to aging but known operational problems: a cooling incident in 2007 and inaccurately performed calibrations for this layer.

3.6 Conclusions

The CDF Run II Silicon Detector was exposed to large radiation dose since 2001, much beyond what was originally anticipated. For this reason, the radiation damage was continuously monitored in order to keep the detector working as well as possible. The detector provided good performance even if the inner layers progressed through doping inversion. Most of the sensors in L00 and SVX-L0 operated with high efficiency up to the end of Run II (12 fb^{-1} delivered luminosity).

Most of the aging studies have been obtained irradiating sensors with acute dose of radiation for short periods of time. The monitoring studies performed by the CDF experiment provide important information on the long term behaviour of the Silicon sensors and the effectiveness of constant maintainance. The experiments at LHC, have made extensive use of Silicon technology for particle tracking. The high radiation field of the pp collisions at LHC will affect the inner layers of the trackers. The sensors will likely experince type inversion and it will eventually degrade the operative capability of the detector. The aging of the CDF Silicon tracker represents in this sense an important test for Silicon technology applications at hadron colliders.

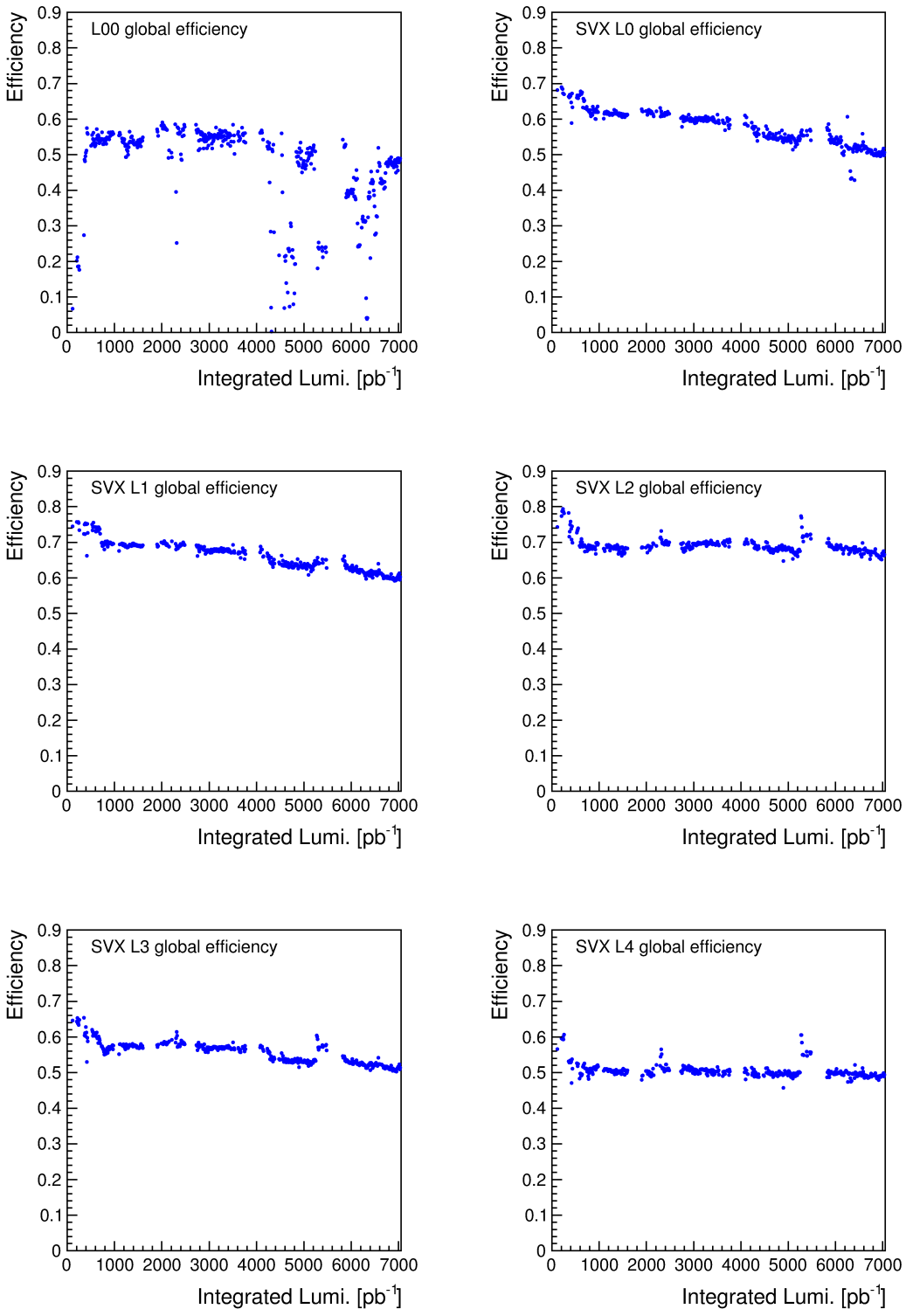

Figure 3.9: Efficiencies for L00 and each layer of SVX-II from February 2002 to May 2009.

Chapter 4

Data Samples and Particle Identification

In this chapter we present the kinematic of the process we study, together with the data sample selection and the basic particle identification techniques of CDF. The data samples for our signal selection was collected with triggers that require two objects:

- one track with $p_T > 8$ GeV/c linked to a cluster in the electromagnetic calorimeter or to a hit in the muon detectors;
- a second track with $p_T > 5$ GeV/c pointing to a narrow energy deposition in the calorimeter.

The low momentum requirement of the trigger gives us a good efficiency of top pair events decaying in two tau leptons (ditau top decay), with one decaying into hadrons and the other decaying into an electron or muon. The signature of this process is similar to the decay of top pairs where one of the W bosons decays into a tau and the other W decays directly into an electron or muon (lepton plus tau). We will show later in this thesis (see Chapter 6) our technique to discriminate these two processes.

4.1 Event Signature

The signature of the processes we want to select contain one electron or one muon, one jet of hadrons from a tau decay and two jets of hadrons from the b quark decay.

The event should contain at least three jets of hadrons. One of the jets should have features like invariant mass, track multiplicity and isolation compatible with a tau decay. The other two jets should have tracks displaced from the primary interaction point, compatible with the tracks originating from the decay of B hadron.

The neutrinos represent an invisible part of the decay products and their number is three in case the electron or muon comes directly from the W boson decay or five in case

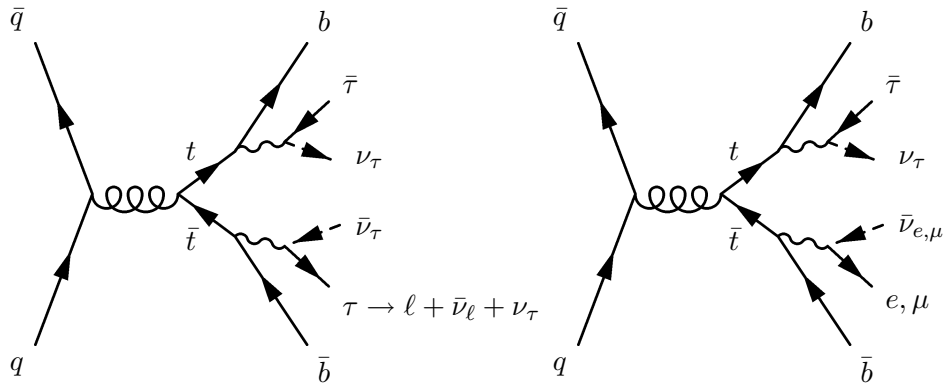

Figure 4.1: On the left a top pair decay into a "ditau" channel where ℓ stands for e or μ. On the right a top decay into "tau plus lepton" channel.

the electron or muon originates from a tau decay. Figure 4.1 shows the two decay modes we select. The neutrinos appear as an imbalance in the energy deposited in the calorimeter.

4.2 Signal Data Sample

This analysis uses the full CDF II data corresponding to a total integrated luminosity of about $\mathcal{L} = 10$ fb^{-1}. Depending on the lepton type in addition to the hadronic tau, three classes of trigger paths[1] are used in our analysis. All these triggers are generally denoted as *lepton plus isolated track* and are summarizes in Table 4.1.

Trigger Families	**Trigger Paths**
"Electron plus isolated track"	TAU_ELECTRON8_TRACK5_ISO
"CMUP muon plus isolated track"	TAU_CMUP8_TRACK5_ISO
"CMX muon plus isolated track"	TAU_CMX8_TRACK5_ISO
	TAU_CMX8_TRACK5_ISO_LUMI_200
	TAU_CMX8_TRACK5_ISO_LUMI_250
	TAU_CMX8_TRACK5_ISO_DPS

Table 4.1: "Lepton plus isolated track" trigger paths used in this analysis.

The four trigger paths belonging to the class "CMX muon plus isolated track" where never active at the same time during data taking. Three triggers of this class were luminosity enabled or dynamically prescaled to maintain a more constant trigger accept rate and a low data acquisition system dead time.

[1] The chain of trigger selection at Level 1, Level 2 and Level 3 are called here trigger path.

- TAU_CMX8_TRACK5_ISO_LUMI_200: trigger is enable at instantaneous luminosity below 2.0×10^{32} cm^{-2}s^{-1}.
- TAU_CMX8_TRACK5_ISO_LUMI_250: trigger is enable at instantaneous luminosity below 2.5×10^{32} cm^{-2}s^{-1}.
- TAU_CMX8_TRACK5_ISO_DPS: trigger is subject to a dynamic prescale (DPS) that is applied at trigger level 2.

Details of the requirements of each trigger path at each trigger level are provided in Appendix A.

We required the data for our analysis to had been taken while the CDF detector subsystem were in a good operational condition. We required a good calorimetry and good Silicon tracker operational condition as baseline for the signal selection. This baseline condition is imposed to the sample of events with CEM electron. In case the events have been selected by the muon based triggers, CMUP (both CMU and CMP) and CMX detectors are required also to be operative. We want to stress that the trigger paths in Table 4.1 are active only when the COT tracking is properly functioning.

After the selection on the good detector operation the total integrated luminosity reduces from about 10 fb^{-1} to 9.3 fb^{-1} for the sample "Electron plus isolated track", 8.7 fb^{-1} for the sample "CMUP muon plus isolated track" and 8.2 fb^{-1} for the sample "CMX muon plus isolated track". The difference in the luminosity between the CMUP and CMX trigger is caused by the trigger prescale applied to the CMX path.

4.3 Trigger Efficiency

Analysis objects (electrons, muons and hadronic taus in our case) are generally defined at offline reconstruction and identified with tighter requirements than those applied at trigger level. In any case, the trigger selection effects the sample population because of lower resolution of the measurements, inefficiencies and coverage of the system.

The efficiency of the trigger needs to be correctly estimated and is used to evaluate the expected number of events, i.e. when we compute the number of events from Monte Carlo (MC) simulation that pass the signal selection.

The trigger paths require a lepton and an isolated track. At L2 duplicate leptons are removed with the request of two distinct tracks and moreover in the trigger path "Electron plus isolated track" the electron seed tower should not be contained in the tau tower cluster. This feature allows the treatment of the overall trigger efficiency as the product of the selection efficiencies of these two objects separatly. Changes in the trigger selection and in the detector performances at different luminosity have been taken into account.

It has been demonstrated that the lepton part of the "lepton plus isolated track" trigger efficiency is at the plateau when electrons have $E_T > 10$ GeV and muons have $p_T >$

10 GeV/c [44][45][47]. Another class of trigger, the "high-p_T" (Appendix A) selects events with the signature of an electron or a muon with respectivelly $E_T > 18$ GeV or $p_T > 18$ GeV/c. Despite the difference in the energy of the trigger requirements, it has been demonstrated that the efficiency at the plateu of the "lepton plus isolated track" triggers is consistent with the one measured for the "high-p_T" triggers [46, 47][2]. So for the overall data taking we consider the trigger efficiency of the electron and muon legs of the "high-p_T" sample that have been provided by the CDF collaboration.

For the tau leg (the trigger object called "isolated track") we perform an independent study of the trigger efficiency that is reported in the Section 4.7.

4.4 Electron Identification

Central electrons, are characterized by a very narrow energy deposition in the central electromagnetic calorimeter, i.e. in only one or two calorimeter towers. The "cluster" of calorimeter towers has to match a track that originates fron the primary interaction point.

Electron candidates are selected through a set of quality and fiducial requirements which are summarized in Table 4.2 and described below. The selection variables are taken from the standard CDF electron selection, the values of the thresholds are equal to the ones used in previous CDF analysis (for example the search for neutral MSSM Higgs bosons [48]).

- E_T: the transverse component of the electron energy, defined as $E_T = E \times \sin\theta$ where θ is the polar angle calculated with respect to the interaction vertex; E is the energy deposited in the electromagnetic calorimeter cluster.

- E_{HAD}/E_{EM}: the ratio of the energy deposited by the electron in the hadronic to the electromagnetic compartments of the calorimeter. A real electron deposits most of its energy in the EM calorimeters: by requiring E_{HAD}/E_{EM} to be smaller than a selected value, it is possible to distinguish electrons from hadronic particles, which release a large fraction of their energy in the HAD calorimeters.

- *Conversion*: the cut intends to remove electrons generated from photon conversion in the material of the tracker. The electron does not pass the selection if another track is reconstructed with opposite charge, $\Delta\cot\theta = 0.02$ and $\mathrm{D}_{xy} = 0.1$, where D_{xy} is the distance between the two tracks at the closest approach. The electron is recovered if a third track is found with equal charge (a *trident*). In this last case the two additional tracks are interpreted as conversion of a radiated photon.

- E/P: the ratio of the energy of the EM cluster associated to the electron and the momentum of the track measured in the COT. For high energies, real electrons

[2] At trigger level the inefficiency of the lepton selection is dominated by the effect of XFT track reconstruction. XFT reconstruction is at the plateau at ∼4 GeV/c

can be considered as massless and their energy should equal the magnitude of the momentum, thus E/P is expected to be ~ 1.

- L_{shr}: a variable which describes the shape of the lateral shower profile of the electron calorimeter cluster.

- E_{rel}^{iso}: the relative calorimeter isolation, defined as the fraction of the transverse energy contained in a cone $\Delta R < 0.4$ (after subtracting the energy of the electron itself) and the transverse energy associated to the electron candidate.

$$E_{rel}^{iso} = \frac{E_T^{\Delta R=0.4} - E_T}{E_T} \tag{4.1}$$

- E_T^{iso}: the absolute calorimeter isolation, defined as the transverse energy contained in a cone $\Delta R < 0.4$

$$E_{rel}^{iso} = E_T^{\Delta R=0.4} - E_T \tag{4.2}$$

- p_T: the transverse component of the momentum of the track associated to the electron object. The variable is obtained through the track curvature in the magnetic field of the spectrometer.

- z_0: the z coordinate of the track at the beam line.

- $|\Delta Z_{CES}|$: the distance in the (r, z) plane between the coordinates of the track, extrapolated to the plane of the CES detector, and the position of the nearest CES cluster.

- $Q \times \Delta x_{CES}$: the distance in the (r, ϕ) plane between the coordinates of the extrapolated track and the CES cluster, multiplied by the charge of the track. It takes into account asymmetries in the shapes of the calorimeter clusters, originated from electrons subject to bremsstrahlung.

- $CES\chi^2_{strip}$: a χ^2 comparison of the CES shower profile in the (r, z) plane to the expected one as measured in the electron test-beam.

- $N_{COT}(axSL)$: number of axial COT superlayers belonging to the electron track that had 5 or more hits.

- $N_{COT}(stSL)$: number of stereo COT superlayers belonging to the electron track that had 5 or more hits.

We validated our electron identification reproducing the CDF standard procedure to measure the efficiency of electron identification. We compared the efficiency measurement of each requirement with the relative result of the CDF Collaboration.

Variable	Requirement
Region	CEM
Fiducial	SMX Fiducial
E_T	≥ 10 GeV
Track p_T	≥ 8 GeV/c
Track z_0	≤ 60 cm
COT AxSL	≥ 3
COT StSL	≥ 2
Conversion	veto
E_{HAD}/E_{EM}	$\leq (0.055 + 0.00045 \times E)$
Isolation	≤ 0.1
$Lshr$	≤ 0.2
E/P	≤ 4.0 or $p_T \geq 50$ GeV/c
CES ΔZ	≤ 3.0 cm
CES $q\Delta X$	$-3.0 \leq q\Delta X \leq 1.5$ cm
CES Strip χ^2	≤ 10.0

Table 4.2: Standard CDF requirements for electron identification selection.

4.5 Muon Identification

At the GeV energy scale, muons are Minimum Ionizing Particles (MIP): they thus traverse the entire detector with very little energy depositions in the tracking systems and in the calorimeters. Muon candidates are selected by matching COT tracks to segments left in the outer drift chambers.

Two different categories are used in the analysis: central muons reconstructed in the CMU+CMP and in the CMX detectors. All the identification variables, except those already described for the electron case, are described below. The quality cuts applied to muon candidates are described below and summarized in Table 4.3 and 4.4. All the variables used in the identification are taken from the standard CDF muon selection, the values of the thresholds are equal to the ones used in previous CDF analysis ([48]).

- p_T: the transverse component on the muon momentum corrected for non-uniformity of the magnetic field.
- z_0: the position on the z coordinate of the track origin.
- d_0^{corr}: the impact parameter corrected for the measured position of the beam at the corresponding run. Different cuts are applied if the track reconstructed has Silicon hits or if it does not.

Variable	Requirement
p_T	$>$ 10 GeV
$\|z_0\|$	$>$ 60 cm
$\|d_0^{corr}\|$	$<$ 0.2 cm
E_{rel}^{iso}	$<$ 0.1 (if $p_T \geq 20.$)
E_T^{iso}	$<$ 2.0 GeV (if $p_T \leq 20.$)
COT AxSL	≥ 3
COT StSL	≥ 2
ρ_{COT}	$>$ 140 cm

Table 4.3: Standard CDF requirements for muon identification selection.

- E_{rel}^{iso}: similarly to the electron identification, the calorimetric isolation is defined as

$$E_{rel}^{iso} = \frac{E_T^{\Delta R=0.4}}{p_T}. \tag{4.3}$$

- E_T^{iso}: similarly to the electron identification, the calorimetric isolation is defined as

$$E_T^{iso} = E_T^{\Delta R=0.4} - E_T \tag{4.4}$$

- ρ_{COT}: the radius at which the track appears to leave the end plates of the COT. Our requirement ensures that the reconstructed muon traverse the full COT radial width.
- E_{EM}: energy deposited in the central electromagnetic calorimeter.
- E_{HAD}: energy deposited in the central hadronic calorimeter.
- Δx_{CMU}: distance along the x coordinate of the CMU detector, between the extrapolated track and the stub in the muon chamber.
- Δx_{CMP}: distance along the x coordinate of the CMP detector, between the extrapolated track and the stub in the muon chamber.
- Δx_{CMX}: distance along the x coordinate of the CMX detector, between the extrapolated track and the stub in the muon chamber.
- χ^2: the χ^2 of the matching of the track extrapolation to the muon detector and the position of the track in the chamber.

We validated our muon identification, as in the case of the electron, reproducing the procedure to measure the efficiency of standard CDF muon identification. We compared the efficiency of our measurements with the results of the CDF Collaboration.

Variable	Requirement, $p_T > 20$ GeV	Requirement, $p_T < 20$ GeV
E_{EM}	$< 2 + max(0,\ 0.0115 * (p - 100))$ GeV	2 GeV
E_{HAD}	$6 + max(0,\ 0.028 * (p - 100))$ GeV	$3.5 + (p_T/8.0)$ GeV
$\lvert\Delta_{CMU}\rvert$ (CMUP muon)	< 3 cm	< 3 cm or $\chi^2_{CMU} < 9.0$
$\lvert\Delta_{CMP}\rvert$ (CMUP muon)	< 7 cm	< 7 cm or $\chi^2_{CMP} < 9.0$
$\lvert\Delta_{CMX}\rvert$ (CMX muon)	< 6 cm	< 6 cm or $\chi^2_{CMX} < 9.0$

Table 4.4: Requirements for muon identification selection.

Variable	Requirement, $p_T > 20$ GeV	Requirement, $p_T < 20$ GeV
E_{EM}	$< 2 + max(0,\ 0.0115 * (p - 100))$ GeV	< 2 GeV
E_{HAD}	$< 6 + max(0,\ 0.028 * (p - 100))$ GeV	$< 3.5 + (p_T/8.0)$ GeV
$\sum p_T^{iso}$	< 4 GeV	< 4 GeV
E_{rel}^{iso}	< 0.2	–
E_T^{iso}	–	< 4.0 GeV

Table 4.5: Requirements for minimum ionizing particle selection.

4.5.1 Minimum Ionizing Objects

For background veto purposes (see section 6.2.1) we defined the selection for minimum ionizing particles. This class of particles can be muons which do not pass the standard identification of CMUP or CMX muons. The selection of this category of objects has been defined in our analysis and is not a standard CDF identification.

We required a small deposition of energy in the crossed calorimeter tower as in the identification of muons, but relaxed requirements on the isolation. The isolation requirement is used to keep the contribution of muon from heavy flavor decays low).

Our requirements are summarized in Table 4.5.

4.6 Tau Reconstruction and Identification

The fraction of taus decaying into hadrons corresponds to about 65% and the remaining fraction accounts for the decay into electrons or muons. We cannot identify tau decays into electrons and muons, since they appear as isolated leptons, but we can rather use the missing transverse energy, $\not\!\!E_T$ (see Section 4.9) and kinematics of the event to select them because of the presence of ν_τ and $\bar{\nu}_{e,\mu}$.

The mass of the tau lepton is much smaller than the transverse energy in the laboratory reference frame. This feature lets the jet of hadrons from tau decays to appear as a narrow

energy deposit in the calorimeter. We show in this section how this property is exploited for identifying taus, but first we think it is important to spend few lines to summarize the offline procedure to reconstruct taus.

4.6.1 Tau Reconstruction

The offline reconstruction starts with the tagging of "seed" calorimeter towers with transverse energy $E_T^{seedtwr} > 6$ GeV. Shoulder towers with energy $E_T^{shtwr} > 1$ GeV are added to form a calorimeter cluster. The request of a narrow cluster is translated into a cut in the number of tower contributing to the cluster, $N^{twr} \leq 6$.

The search of a "seed" track follows the cluster selection. This track has to match the position of the seed tower and has $p_T^{seedtrk} > 4.5$ GeV. If several tracks are found, the one with highest energy is selected as the seed track. The direction of the seed track is then used as reference direction for selecting the offline tau decay products.

A cone that contains the tracks of tau decay products is defined with a variable amplitude $\theta_{sig} = min(0.17, 5.0/E^{cluster}[\text{GeV}])$ rad [3] (shrinking cone). An isolation annulus, 30 degrees wide, surrounding the signal cone, collects tracks whose features are used for discriminating taus from jets generated by pure QCD interaction. Tracks associated to the tau jet and the isolation tracks have to match the vertex Z coordinate of the seed track with a separation $\Delta Z = 5$ cm.

The neutral pions are selected exploiting the information from the central calorimeter and the CES detector. CES clusters of 5 wires/strips, not associated to charged tracks determines the z and ϕ of the neutral pion, the energy is measured through the CEM associated towers. The reconstructed neutral pions in the event could be added to the tau decay products or be used for veto purposes depending on the relative angle with the tau seed track. The shrinking cone[4] and the isolation annulus, are used for delimiting the particle category.

The tracks and neutral pions in the signal cone are then used to compute the four-momentum of the hadron tau decay. This is called the visible momentum.

4.6.2 Tau Identification

We have based our tau identification requirement on the method used by previous CDF searches [48]. Our tau identification differs for the requirement on tau cluster transverse energy, $E_T^{cluster}$. For 1 and 3 prong taus it should be higher than 10 and 15 GeV respectively. This change is implemented to reduce the amount of events with fake taus. Moreover a cut is added to remove the contamination from misidentified muons, $E/P > 0.4$, where E represents the cluster energy and P the sum of signal track transverse momenta. We

[3] To prevent the signal cone to become too small to be sensitive to track resolution a lower limit is set to 0.05 rad

[4] The lower limit on the amplitude for the neutral pions is set in this case to 0.10 rad

had to modify the requirement on the tau seed track transverse momentum when selecting events with tau plus muon. We raised the requirement, $p_T > 8$ GeV. This choice is made to be consistent with the trigger requirement of the "lepton plus track" sample used for estimating the background from fakes (Section 5.4).

To have a good momentum reconstruction we require that the intersection of the seed track with the CES detector does not coincide with the calorimeter cracks, $9.0 <\mid Z_{CES} \mid < 230.0$ cm.

The mass of tau lepton is $M_\tau = 1.777$ GeV, and having a neutrino in the hadronic final state, the mass of the decay products is lower than this value. The visible momentum is then used to calculate the mass of the tau jet, M^{vis}, that is constrained to be lower than 1.8 GeV.

We know from previous studies that the hadronic part of the tau calorimeter cluster has the energy underestimated by 10% in the MC samples [49]. We rescaled it in the MC to account for this effect.

A variable, ξ', is defined to suppress electrons or muons releasing a large fraction of electromagnetic energy in the calorimeter. The variable is related to the ratio between hadronic energy and the sum of track transverse momentum, defined by ξ

$$\xi = \frac{E_{had}}{\Sigma \mid \vec{p}_i \mid} = \frac{E_{tot}}{\Sigma \mid \vec{p} \mid} \left(1 - \frac{E_{EM}}{E_{tot}}\right), \tag{4.5}$$

where E_{tot}, E_{EM} and E_{had} are respectively the total, hadronic and electromagnetic calorimeter energy, and $\vec{p}_i$ are the momenta of the tracks belonging to the reconstructed tau. The variable ξ' represent a modification of ξ. It is intended for a better rejection of the background with a negligible loss of tau identification efficiency. It is given by:

$$\xi' = \frac{E_{tot}}{\Sigma \mid \vec{p}_i \mid} \left(0.95 - \frac{E_{EM}}{E_{tot}}\right); \tag{4.6}$$

Figure 4.2 shows the rejection of electrons, muons and the selection of tau decay products.

The requirements for selecting tau candidates are summarized in Table 4.6.

4.7 Trigger Efficiency for Isolated Tracks

The efficiency is computed as ratio between the number of events that should have been selected and the actual number selected.

The first step in the computation of the trigger efficiency is the definition of an offline object that in our case are the jets of hadrons passing the tau identification requirements. This kind of objects, the *triggerable objects*, have to belong to a sample that has no trigger bias. When this condition is met, the events represent the starting pool of the study and their number is the denominator of the efficiency measurement.

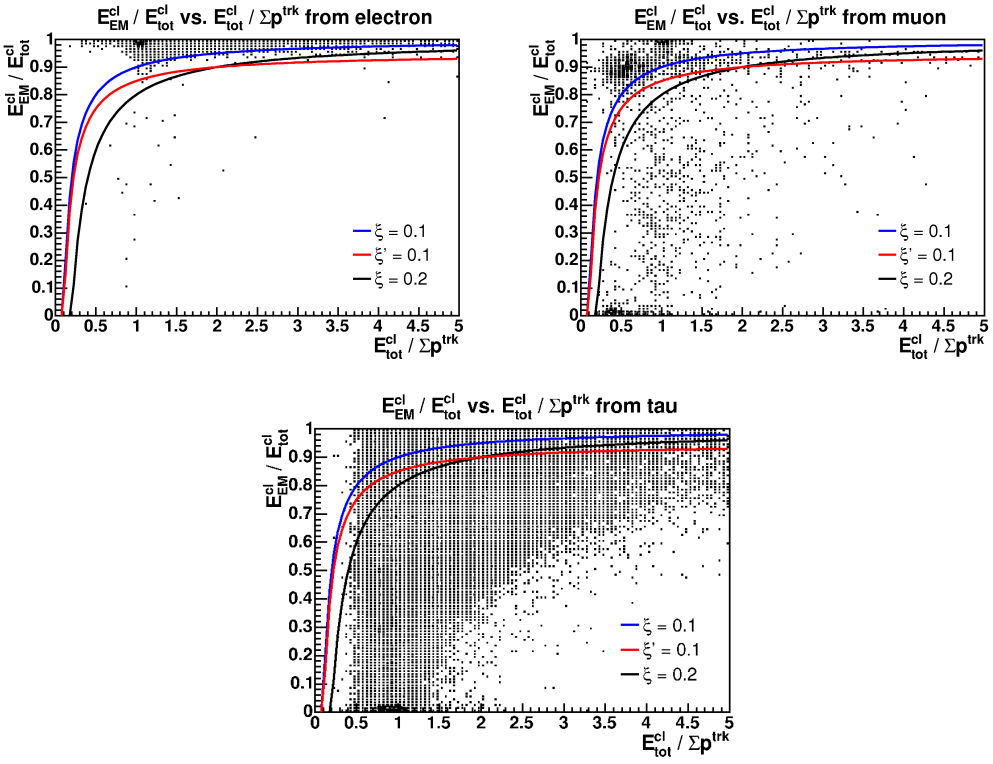

Figure 4.2: The plots above show the rejection of ξ and ξ' cuts on electrons (left) and on muons (right). On the bottom the effect of the same cuts on the tau sample. The scatter plots are obtained from a simulation with Pythia [50] MC and Tauola [51] library for tau lepton decay.

Variable	Requirement
$E_T^{SeedTwr}$	$\geq$ 6.0 GeV
$p_T^{SeedTrk}$	$\geq$ 6.0 geV or $\geq$ 8.0 GeV when selecting muon candidates
$E_T^{Cluster}$	$\geq$ 10.0 GeV for 1 prong taus or $\geq$ 15.0 GeV for 3 prong taus
p_T^{Vis}	$\geq$ 15.0 GeV/c for 1 prong taus or $\geq$ 20.0 GeV/c for 3 prong taus
$\mid Z_{CES} \mid$	$9 \leq \mid Z_{CES} \mid \leq 230$ cm
Σp_T^{iso}	$\leq$ 2.0 GeV
$\Sigma E_T^{\pi^0 iso}$	$\leq$ 1.0 GeV
p_T^{iso}	$\leq$ 1.5 GeV
COT Ax. Seg.	≥ 3
COT St. Seg.	≥ 2
E_T^{shtwr}	$\geq$ 1.0 GeV
N^{twr}	≤ 6
θ_{sig}	$min(0.17, \frac{5.0}{E^{Cluster}[GeV]})$rad
ξ'	≤ 0.1
E_{tot}/p	≥ 0.4
M^{vis}	$\leq$ 1.8 GeV
$N^{\pi^0 iso}$	≤ 0
N^{trk}	$= 1, 3$
Charge	± 1
$d_0^{seedtrk}$	0.2 cm

Table 4.6: Tau identification requirements.

For every event recorded CDF keeps track of all the triggers that "fired". If the events containing the triggerable object has been selected, it is counted in the numerator.

It is possible to see in Appendix A that the "isolated track" requirement in our data sample have minor differences between the trigger paths with an electron or a muon. The trigger TAU_ELECTRON8_TRACK5_ISO requires at trigger level 2 a cluster to be matched with a 5 GeV XFT track.

As natural consequence we studied separately the trigger efficiency of the tau "leg" in the sample with an electron object (TAU_ELECTRON8_TRACK5_ISO) and in the sample with a muon object, restricting it to the trigger path TAU_CMUP8_TRACK5_ISO.

4.7.1 Samples

We used two classes of samples to estimate the efficiency of the tau "leg" in the "lepton plus isolated track" trigger family:

- "calibration sample" which contains events with electrons or muons of 8 GeV (trasverse energy or momentum):
  1. MUON_CMUP8_DPS,
  2. ELECTRON_CENTRAL_8_L2_DPS.
- "high-p_T sample" which contains events with electrons or muon of 18 GeV:
  1. MUON_CMUP18,
  2. ELECTRON_CENTRAL_18.

In the name of the trigger paths the "DPS" stands for the dynamic prescale which is applied at trigger level 2. The samples were triggered with trigger requirements on the electron and the muon objects similar to the ones in the "lepton plus isolated track" sample. The differences of the calibration sample are summarized below.

- L1: same requirements.
- L2: the electron object has the same requirements; the muon object is not required to have the *SLAM confirmation* we briefly described in Section 2.4.1 (the recent XFT update was introduced in "lepton plus isolated track trigger".
- L3: the electron object has $E_{HAD}/E_{EM} < 0.055$ instead of $0.055 + 0.00045 \times E$; the muon object uses different matching with the detector chamber.

The high-p_T sample has been collected with the same quality requirements on the track of the lepton, but with different requirement on the transverse momentum (or energy of the cluster for the electron). Some differences appear in the muon selection in the matching of the track with the chambers and these features have been taken into account in the evaluation of the systematics of the efficiency measurement.

4.7.2 Selection and Result

We need to have a collection of events from the high-p_T and calibration sample which contains a lepton with equal or tighter requirements than the ones in the "lepton plus isolated track" sample. In this way we intend to obtain an uniform selection of the lepton leg which cancels out the effects of the lepton leg trigger selection.

We required the events in the calibration sample to have a muon with the identification requirements listed respectively in Table 4.3 and 4.4. No attempt is made to reproduce the SLAM requirement on the muon track, we are going to show the effect. For what concerns the electron we required it to pass all the selection listed in Table 4.2, but instead $E_{HAD}/E_{EM} < 0.055$.

The events belonging to the high-p_T sample are only required to pass our identification requirements with a modification on the transverse momentum. Electrons need to have $E_T > 20$ GeV and $p_T > 10$ GeV/c, muons $p_T > 20$ GeV/c

The *triggerable object* in this measurement is the tau candidate identified through the requirements in Table 4.6. To increase the purity of real taus we asked the electric charge of the tau and of the other lepton to be opposite. The number of these events gives us the denominator of the efficiency measurement.

The events are then required to pass the "lepton plus isolated track" trigger selection;

- TAU_ELECTRON8_TRACK5_ISO for events with electrons;
- TAU_CMUP8_TRACK5_ISO for events with muons.

We want to remark that the path names indicate with "ISO" the isolation requirement of the 5 GeV track. The trigger efficiency measured in the electron samples are summarized in Figure 4.3 and 4.4 respectively for the calibration electron sample and the high-p_T electron sample.

It is possible to notice that the calibration electron sample has high statistical uncertainties. The ELECTRON_CENTRAL_8_L2_DPS trigger is unfortunatelly signficantly prescaled (on average it is prescaled by a factor of $\sim$5.)

We can notice in Figure 4.4 a decrease of the trigger efficiency for one and three prong taus using the high-p_T sample (the same drop is also present in the measurement using the calibration electron sample). The drop is understood and is the effect of a wrong parameter setting in the L2 trigger: a rejection of duplicates was intended to discard taus if their seed towers were identical to the electron ones, or formulating it in a mathematical form

$$\eta_\tau^{seedtower} = \eta_e^{tower} \quad and \quad \phi_\tau^{seedtower} = \phi_e^{tower} \tag{4.7}$$

Instead, in data taking periods from 15 to 30, the *"and"* condition was mistakenly replaced with an *"or"*, decreasing the overall acceptance of the trigger.

The trigger efficiency measured in the CMUP muon samples are summarized in Figure 4.5 and 4.6 respectively for the calibration muon sample and the high-p_T muon sample.

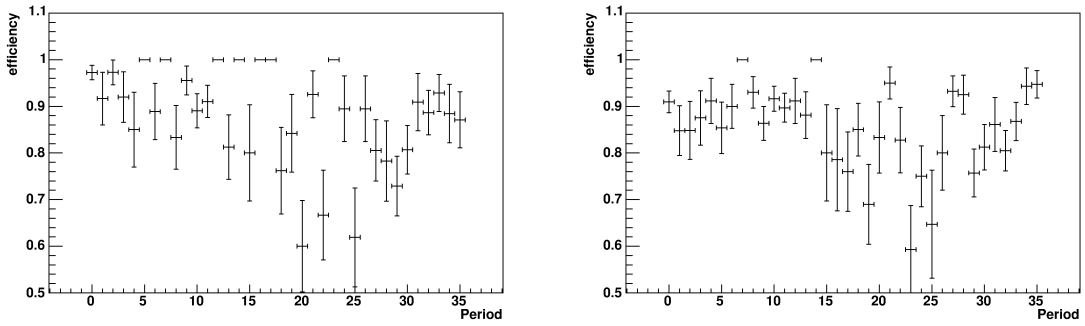

Figure 4.3: Trigger efficiency of one prong taus (left) and three prong taus (right), measured with the calibration electron sample, as a function of the run periods from very beginning of Run II untill the end.

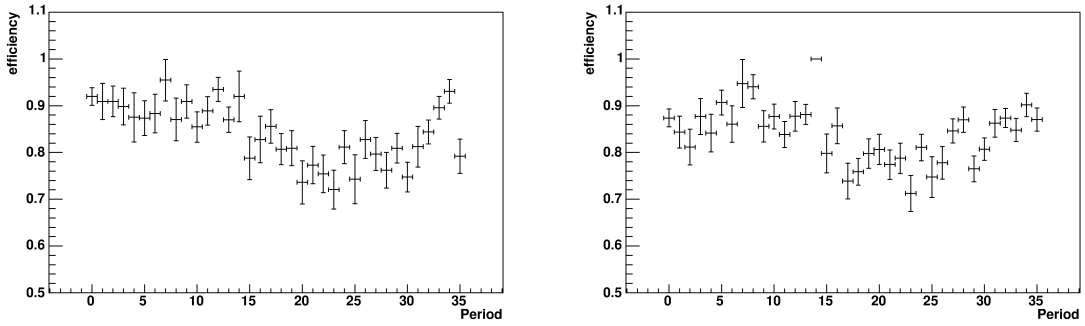

Figure 4.4: Trigger efficiency of one prong taus (left) and three prong taus (right), measured with the high-p_T electron sample, as a function of the run periods from very beginning of Run II untill the end.

The trigger efficiency of the tau leg in the CMUP muon sample shows signs of a small decrease after data taking period 10. This effect is more visible for one prong taus and can be linked to the new XFT requirements that were implemented starting from period 11. It corresponds indeed to the upgrade of the XFT to include both axial and stereo COT superlayers and thus pass from 2D to 3D tracking in the trigger.

We grouped the measurements of the trigger efficiency in data taking periods that have similar trigger requirements and are thus expected to have same efficiency. Table 4.7, 4.8 and 4.9 summarize the trigger measurement for 1 and 3 prong tau candidates using the calibration electron, the high-p_T electron and the average of the two samples. Table 4.10, 4.11 and 4.12 report the results using CMUP samples, respectively the calibration muon, the high-p_T muon and the average of the two samples. We want also to underline that

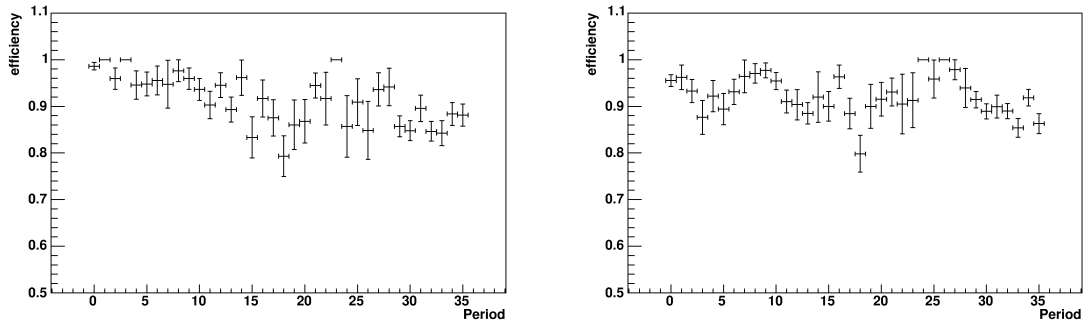

Figure 4.5: Trigger efficiency of one prong taus (left) and three prong taus (right), measured with the calibration CMUP muon sample, as a function of the run periods from very beginning of Run II untill the end.

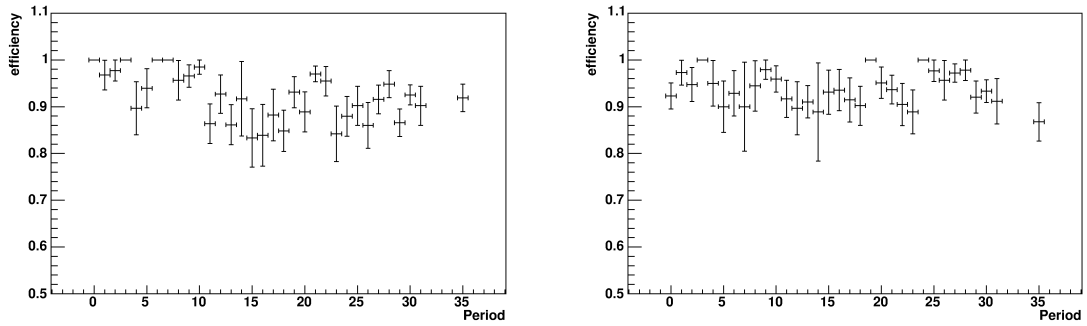

Figure 4.6: Trigger efficiency of one prong taus (left) and three prong taus (right), measured with the high-p_T CMUP muon sample, as a function of the run periods from very beginning of Run II untill the end.

the group of data periods we define correspond to periods with increase in luminosity and with performances that are rather equivalent over each lapse of time.

The results of the measurement of the trigger efficiency obtained with the calibration and the high-P_T sample are mostly in agreement within the statistical uncertainty. The difference are considered as systematic uncertainty of the average value.

We choose to estimate 3% systematic uncertainty for the measured trigger efficiency. This uncertainty, considered in all data taking periods, covers properly the discrepancies between the results obtained with different samples.

Track Multiplicity	Periods 0-14	Periods 15-30	Periods 31-35
1 tracks	0.944 ± 0.010	0.819 ± 0.019	0.901 ± 0.023
3 tracks	0.898 ± 0.011	0.856 ± 0.014	0.900 ± 0.018

Table 4.7: Trigger efficiency of the tau leg measured with the calibration electron sample.

Track Multiplicity	Periods 0-14	Periods 15-30	Periods 31-35
1 tracks	0.901 ± 0.009	0.790 ± 0.009	0.864 ± 0.013
3 tracks	0.876 ± 0.008	0.801 ± 0.008	0.867 ± 0.011

Table 4.8: Trigger efficiency of the tau leg, measured with the high-p_T electron sample.

4.8 b-Quark Induced Jet

Top quarks are expected to always decay into W and b quarks in the SM framework. All quarks in nature are observed bound in composite states like mesons or baryons as consequece of the non-Abelian gauge group of the strong interaction. Particles containing the b quark are unstable and decay after travelling a lenght of ~ 4 mm. The mass of the B hadrons is small compared to the momentum, so the products of its decay are emitted as jets. In about 30% of the cases such jets contain a lepton (semileptonic decays) but in the rest of the cases contain exclusively hadrons.

Several hadron jet reconstruction algorithms have been developed at CDF. Some algorithms make use of tracking information in searching for charged particle jets or in measuring their transverse momenta. The jet algorithm used in this analysis, called JETCLU[55], relies only on the information of the calorimeters. JETCLU proceeds through the following steps.

- Search for towers with $E_T > 1$ GeV, calculated using the vector from the primary vertex with highest $\sum p_T$, to the geometrical center of the tower.
- The towers above 1 GeV are marked as precluster seeds and ordered with increased E_T.
- From the highest E_T seed 7×7 tower squares are constructed, defining a precluster. Seeds cannot belong to more than one precluster. The centroid of the precluster is calculated as the E_T weighted center of the seeds.
- A $\Delta R = 0.4$ cone[5] is drawn around the centroid and all towers with $E_T > 0.1$ GeV in the cone are summed. The centroid is then recalculated.
- The step above is iterated until the algorithm riches a stable point.

[5]In our analysis we use such jet cone definition that is considered more reliable. Algorithms with $\Delta R = 0.7, 1.0$ exist as well.

Track Multiplicity	Periods 0-14	Periods 15-30	Periods 31-35
1 tracks	0.919 ± 0.007	0.796 ± 0.008	0.873 ± 0.011
3 tracks	0.884 ± 0.006	0.813 ± 0.007	0.877 ± 0.009

Table 4.9: Average of the trigger efficiency of the tau leg, measured with the high-p_T and calibration electron samples.

Track Multiplicity	Periods 0-10	Periods 11-35
1 tracks	0.973 ± 0.006	0.888 ± 0.006
3 tracks	0.952 ± 0.006	0.907 ± 0.005

Table 4.10: Trigger efficiency of the tau leg measured with the calibration CMUP muon sample.

- The procedure can lead to jets including the same amount of energy. In this case, if the 75% of the transverse energy of one jet candidate is included in another, the two are merged, otherwise the tower energy is assigned to the closer jet candidate.

We now describe the CDF correction of the hadronic energy scale of the jets and the technique to tag secondary vertices.

4.8.1 Jet Selection

Since the jet is only required to have a cluster in the calorimeter, a sample of jets contains not only jet of hadrons, but also electrons, taus, photons. We do not consider jets if an identified lepton is close to it ($\Delta R > 0.4$).

In our analysis we apply the following selection on the jets:

- $\eta \leq 2.0$
- $E_T > 20$ GeV for the leading jet, 15 GeV for the subleading ones.
- $E_{EM}/E < 0.9$

where E_{EM}/E represents the electromagnetic fraction of the jet cluster energy and E_T the jet corrected transverse energy. The correction is described in the section below.

4.8.2 Jet Energy Scale Correction

The energy assigned to the jets, obtained with the calorimeter information, can be affected by inaccuracy of the detector and misreconstruction on the clustering algorithm. The "raw energy" of a jet, as measured after the JETCLU algorithm (see above, Section 4.8), has to be multiplied by a CDF standardized set of corrections [52].

These corrections are organized in levels in order to correct separatly for each mismodeling cause. In our analysis we use the first 5 levels.

Track Multiplicity	Periods 0-10	Periods 11-35
1 tracks	0.972 ± 0.010	0.929 ± 0.006
3 tracks	0.955 ± 0.010	0.943 ± 0.007

Table 4.11: Trigger efficiency of the tau leg, measured with the high-p_T CMUP muon sample.

Track Multiplicity	Periods 0-10	Periods 11-35
1 tracks	0.972 ± 0.005	0.907 ± 0.004
3 tracks	0.953 ± 0.005	0.919 ± 0.004

Table 4.12: Average of the trigger efficiency of the tau leg, measured with the high-p_T and calibration CMUP muon samples.

L0, Online/Offline calibration. Electromagnetic compartments of the calorimeter are calibrated by imposing that the reconstructed mass of the Z boson in the $Z \to e^+e^-$ decay mode is consistent with the mass measured at LEP.

The calorimeter stability is monitored online by means of various calibration methods: laser systems, radioactive CO^{60} sources, gain variations are tracked via J/ψ muons and mininum bias trigger rates. WHA scale and tower gain variations are studied with source calibrations.

L1, η Dependent Correction. L1 correction accounts for the nonuniformities of the CDF calorimeter along pseudorapidity. A lower response derives from the poorly instrumented regions, for example, close to "cracks" like at $\eta \approx 0$ or $\eta \approx 1.1$. In other words, at the border of the calorimeter sections there could be some unwanted energy loss in passive material.

The correction in obtained using the "dijet balancing method", under the assumption that the transverse energy of two jets in exclusive of two jet events should be equal. This property is used to scale jets outside the $0.2 < |\eta| < 0.6$ region to jets inside the region. This is done because CEM and CHA are the best understood calorimeters in CDF and the selected region is far away from the cracks.

L2, L3. They do not exist anymore! L2 was used in Run I to remove any time dependence of the calorimeter PMT's, L3 was used in a brief period during Run II to account for differences between MC and data observed in photon+jets events. These differences have been cured.

L4, Multiple Interaction. Multiple $p\bar{p}$ collision can take place during the same bunch crossing and their energy can enter in the jet clusters, increasing the energy of the measured jet. This correction substracts the average contribution. It is derived from minimum bias data. The contribution is parameterized as a function of the number of vertices in the event.

L5, Absolute Correction. The procedure is based on MC simulations. Its accuracy depends on the calorimeter response to a single particle (*calorimeter simulation*) and to the multiplicity and p_T spectrum of the particles therefore produced (*fragmentation simulation*). It transforms the measured jet energy into the energy corresponding to the underlying particle jet.

4.8.3 Secondary Vertex Tag

This technique takes advantage of the long lifetime of a b flavoured hadron to identify jets originating from a bottom quark through the presence of a decay vertex displaced from the primary interaction vertex. It operates on a per jet basis, where tracks within the jet cone are considered for each jet in the event. A displaced vertex requires at least two tracks, which passed track quality cuts and are selected using the significance S_{d0} of their impact parameter with respect to the primary vertex.

The algorithm uses a two step approach to find secondary vertices. In the first pass, using tracks with $p_T > 0.5$ GeV/c and $|S_{d0}| > 2.5$, it attempts to reconstruct a secondary vertex which includes at least three tracks (at least one of the tracks must have $p_T >$ 1 GeV/c). If the first pass is unsuccessful, it performs a second pass which makes tighter track requirements ($p_T > 1$ GeV/c and $|S_{d0}| > 3$) and attempts to reconstruct a two-tracks vertex (one track must have $p_T > 1.5$ GeV/c) [53].

Once a secondary vertex is found in a jet, the two dimensional decay length of the secondary vertex L_{xy} is calculated as distance from the primary vertex in the transverse plane (see Figure 4.7). Secondary vertices corresponding to the decay of b and c flavoured hadrons are expected to have large L_{xy} while the secondary vertices from random mismeasured tracks are expected to be less displaced from the primary vertex. The tagged jet is then defined as a jet containing a secondary vertex with significance of the two dimensional decay length $|S_{Lxy}| = |L_{xy}/\sigma_{Lxy}| > 3$.

To measure the efficiency for tagging heavy flavor hadrons, a sample of low p_T muon data is used which is enriched in semileptonic decays of bottom and charm hadrons. This method is described in detail in [54]. Figure 4.8 shows the dependency of these efficiencies on jet E_T and jet pseudorapidity η.

There is a possibility that b-tagged jets do not result from the fragmentation of a heavy quark. We call such jets mistags. They are caused mostly by a random overlap of tracks which are displaced from the primary vertex due to tracking mismeasurements, or they comes from K_S and Λ meson decays and nuclear interactions with the detector material (the beam-pipe or the inner silicon layers). Figure 4.9 shows the mistag rates obtained from data for the tight and loose version of the SecVtx tagger.

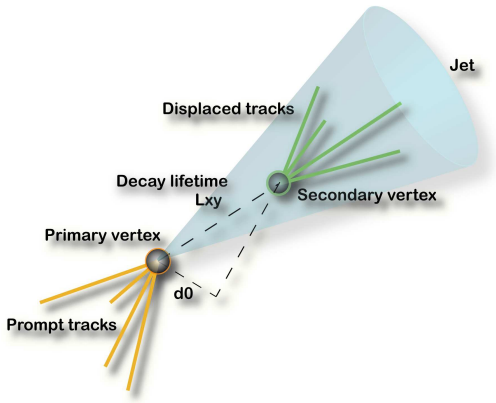

Figure 4.7: Sketch of the b quark decay, showing the decay length of the secondary vertex L_{xy}

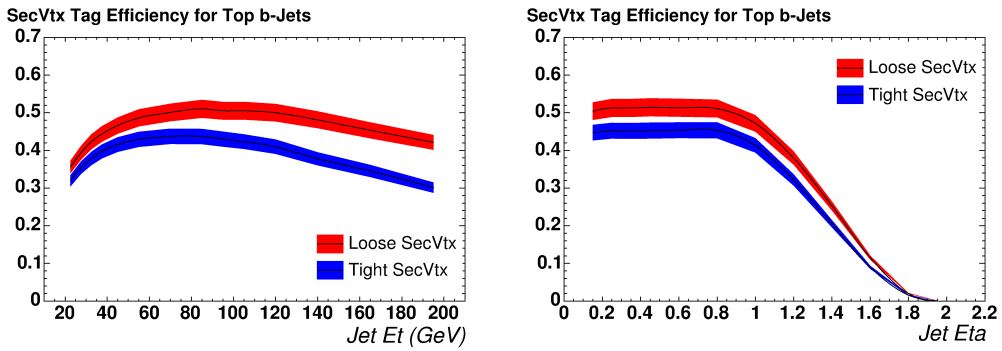

Figure 4.8: The b quark tagging efficiency using tight or loose SecVtx tagger, on the right the dependency on E_T of the jet, on the left the dependency in η.

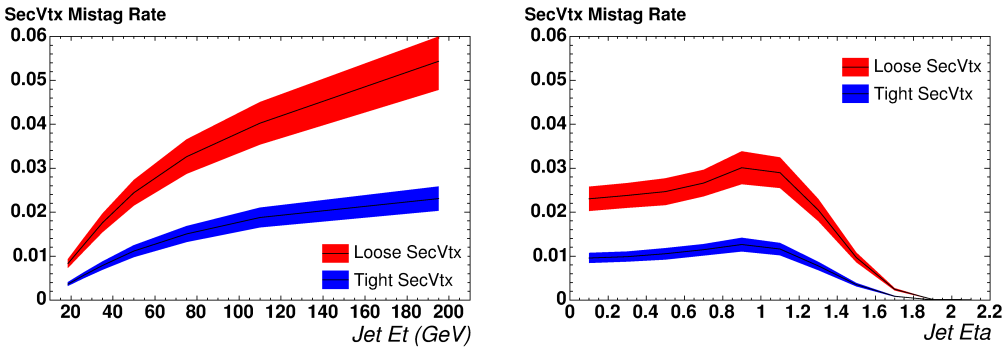

Figure 4.9: The mistag rates obtained from data for tight or loose SecVtx tagger, on the right the dependency on E_T of the jet, on the left the dependency in η.

4.9 Missing Transverse Energy

Every calorimeter tower is in a certain direction from the center of the detector and the energy deposition in the tower lets us reconstruct an energy vector. Taking the vectorial sum of all these vectors and taking the projection in the transverse plane we obtain a fundamental quantity for the study of the kinematic of the events. The $\not\!\!E_T$ is defined as the modulus of this vectorial sum and the direction is taken opposite to it.

The $\not\!\!E_T$ in the event, apart from instrumental mismeasurement, indicates the presence of particles that do not interact with the material of the calorimeter. We know that muons deposit small fraction of their energy since they normally traverse the detector at minimum ionizing regime, but neutrinos do not interact in the detector.

In our study we need to measure the transverse component of all the neutrino momenta. We obtain this information taking the $\not\!\!E_T$ as estimate, but we first apply correction to it.

- We correct the $\not\!\!E_T$ taking into account the jet energy correction: we subtract separately in the x and y coordinate the projection of the jet corrections.
- In events with muons we subtract the x and y components of the track transverse momentum of identified muons and minimum ionizing particles.
- A further correction is applied considering the primary vertex position instead of center of the detector for its calculation.

4.10 Concluding Remarks

We have described in this chapter all the objects we use in our analysis. It is possible to notice how demanding is the signature of the process, since it requires the identification

of all the charged leptons and b jets tagging. In Chapter 6 we are going to show the implementation of the selection and the techniques for the background suppresion.

Our analysis greatly exploits all the main features and assets of the CDF detector to measure the $t\bar{t}$ production cross section in this complicated and rare decay mode. We want to remark that the quality tracking system of CDF is fundamental in the achievement of this work and particularly important is the trigger system which allows the tracking to be included in the level 1 and the level 2 selection. This feature allows the perfect acceptance for this tau-based search and at the same time an acceptable trigger rate.

Chapter 5

Signal and Background Events

We discussed in Section 4.1 the signature of the processes we want to select and in the rest of the chapter the identification of the particles and missing transverse energy (an estimate of the neutrino momenta) belonging to the signature. We describe in this chapter the sample of simulated events modeling the signal events and, before proceeding to the details of the event selection, we want to present the processes that can simulate the signature of the signal. These processes constitute the background to our signal.

The background can be classified in two types:

- the background that comes from events with the same particles in the final state as the signal, i.e. *physical background* or *irreducible background*;
- the background introduced by events with different particles in the final state, but where one of the particle is misidentified in such a way that the final signature becomes indistinguishable from signal events, i.e. *background with fakes*, or misidentified particles.

We estimate the physics background of our selection using simulated data samples. We rely on the simulation to describe the overall selection acceptance but we apply scale factors to account for small mismodeling.

For what concerns the background with fakes of the tau candidate we have two major sources: events where QCD induced jets are misidentified as tau decay products and a smaller group of events where an electron or a muon is misidentified as a tau.

We implemented a technique to evaluate the background with QCD hadron jets faking taus which is based on the calculation of the probability of jets to pass the tau identification cuts, generally named "tau fake rate". We want to underline that this method is completely data driven.

The component to the background caused by electrons or muons misidentified as taus is evaluated through simulated data.

5.1 Monte Carlo Simulation

The Monte Carlo (MC) simulation method is one of the most common tool in high energy physics to estimate the amount of events expected to pass a certain selection.

The simulated events used in our study are in most cases generated with PYTHIA [50] or ALPGEN [56]. For systematic uncertainty studies (see Chapter 7) we also used HERWIG [57] generated events. PYTHIA, ALPGEN and HERWIG generators use matrix elements for tree level parton scattering processes and in our simulated samples the parton distribution function is the CTEQ5L [58].

PYTHIA is a general purpose event generator, containing models for several physics aspects. It is based on the Lund model [59] for parton showering, contains also routines for hadronisation, and considers also initial and final state radiation, multiple parton interactions, beam remnants and parton photon production.

The ALPGEN generator calculates the matrix element for a fixed number of partons in the final state. In comparison with PYTHIA it allows a better simulation of events with high jet multiplicities. ALPGEN describes final states with multiple partons at first order in perturbation theory and does the exact evaluation of the relevant Feynman diagrams in QCD and electro-weak interactions. The evaluation of the matrix elements gives a more exact description for processes with high jet multiplicities with large transverse momenta than the parton shower based approach where the additional jets are generated during the shower evolution. ALPGEN does not include any form of hadronization of the partons. Thus the fragmentation and hadronization is handled (inside CDF) in a separate step with routines from PYTHIA.

The HERWIG Monte Carlo program, as PYTHIA, is a general purpose particle physics event generator, which includes numerous routines for describing hadron-hadron collision events. It differs from PYTHIA in several aspects of the computation algorithm, but strictly for what concern our signal events the main difference is in the different parton showering model. For this reason we compare HERWIG with PYTHIA Monte Carlo to estimate the dependece on the jet simulation.

It is important to note that tau leptons are considered as stable particles by the generator. Their decay is handled by a simulation package called Tauola [51], which takes into account the polarization and first order QED corrections in the leptonic decays.

The standard CDF II simulation is based on the GEANT 3 [60] package. GEANT is currently the most common software package for the simulation of the passage of particles through matter since it collects the most complete description of particle interaction with matter. Such interactions are for instance ionization, bremsstrahlung, nuclear interactions and multiple scattering of charged particles. The GEANT software takes as input the information such as the coordinates and the four-momenta of the particles with lifetime long enough to be detected by the detectors.

A detailed description of the detector geometry and the composition of the CDF subdetectors is included in GEANT. It allows to correctly account for the material budget

of the tracking system and, more in general, the energy loss in passive elements of the detector supports. A sensitive aspect of the tracking simulation is the description of the Silicon detectors since it represents on average about 15% of the radiation lenght. Its geometry (see Section 2.3.2) has been reconstructed [61] as well as the width of the different elements. Most of the components of the Silicon detectors are considered such as the sensors, the readout electronics and the fragments of cooling lines and cables close to the portcards. However part of the plastic pipes of the cooling lines are not considered as well as the contribution (less relevant) of the detector supports made of beryllium and carbon fibers. The difference between selection in the data and in the simulation events are fully included in the scale factors used to reweight the identification efficiency of the particles in the signal signature.

The output of the detector simulation is stored in files with the same format as real data and thus can be studied with the same analysis code.

5.1.1 Expected Number of Events

The expected number of events we estimate through Monte Carlo simulation is derived by the formula:

$$N^i = \sigma^i \times A^i \times \epsilon_{trg} \times \epsilon_{ID} \times \epsilon_{vtx} \times \int \mathcal{L} dt \tag{5.1}$$

where the index i refers to the type of process we include in the physics background estimate and the other quantities are

- the cross section, σ, of the processes obtained from theoretical prediction or fit from experimental measurement;
- the acceptance, A, which accounts for both the detector geometry and the kinematic requirements of the selection;
- the efficiency of the online trigger selection, ϵ_{trg};
- the efficiency of the offline particle identification, ϵ_{ID}, which is the product of the identification efficiencies of the leptons in the event.
- the efficiency of the vertex requirement, ϵ_{vtx}, i.e. requiring its position to be in the center of the detector $|Z_0^{vtx}| < 60$ cm;
- the integrated luminosity of the analyzed data sample, $\int \mathcal{L} dt$, with the appropriate data taking good run list.

We obtain the term $A^i \times \epsilon_{trg} \times \epsilon_{ID} \times \epsilon_{vtx}$ from the Monte Carlo simulation. We validated the identification of the electron and muon lepton comparing the efficiency of our selection requirements separately with the standard procedures of the CDF collaboration [62, 63].

5.2 Simulated Data for Signal Events

To guide our selection of $t\bar{t}$ events with single or both top quarks decaying into tau, ν_τ and b, we prepared an artificial sample of $t\bar{t}$ events. Events are generated in the SM picture using Monte Carlo technique with the PYTHIA event generator. To increase the efficiency of the generation we configured PYTHIA to decay each top quark semileptonically, i.e. only into electron, muon or tau, plus neutrino and b with 1/3 branching ratio each. Events were then passed through the CDF detector simulation based on GEANT. The result, 4,928,270 $t\bar{t}$ events correspond to an integrated luminosity of 6260 fb$^-$1 in LO in the Standard Model. The events have dileptons at the generator level, 279,703 events have both leptons within CDF detector acceptance and transverse momentum above our identification requirement (30,066 ditau events with an electron or a muon plus a tau decay in hadrons, 249,637 events with an electron or muon from a W decay plus a tau induced jet). In this pool of events the events that have both leptons reconstructed as either electron, muon or tau object by the CDF software are 205,592 (21,890 ditau events, 183,702 lepton plus tau events).

5.3 Physics Background

The requirement of an isolated electron or muon plus a tau decaying into hadrons allows the following physics background to be selected:

- Drell-Yan production with Z/γ^* decay into two taus, with cross section $\sigma_{Z/\gamma} = 355$ pb^{-1}, $M_{Z/\gamma} \geq 20$ GeV;
- WW boson production with both bosons decay in leptons, with cross section $\sigma_{WW} = 11.3$ pb^{-1};
- Diboson production such as WZ and ZZ with the Z (or W) boson decay into tau, with cross sections of $\sigma_{WZ} = 3.2$ pb^{-1} and $\sigma_{ZZ} = 3.6$ pb^{-1} respectively.

The requirement of two additional jets suppresses the first two sources listed above, but the production cross sections are such that the major background derives from the Drell-Yan processes.

The Drell-Yan process represents the main irreducible background and we choose to model it using the ALPGEN generator. This choice is driven by the need to have a good understanding of the jet multiplicity. Each ALPGEN sample is generated with a certain parton multiplicity that is how many partons have E_T above 15 GeV. Since this requirement is different from the offline jet energy requirements, parton showering and a imperfect measurement of the jet energy may cause events to migrate between different jet multiplicities. The sum of all the simulated samples guarantee a good modelling of the processes. The LO cross section of each sample has been reweighted by a scaling factor to NLO cross section [64] *k-factor*, $k = 1.40$ ($\pm$15% in the two jet multiplicity bin).

Process	Inst. Lum.	Gen.	N. Events	σ_{prod}
$Z/\gamma^* \to \tau\tau$ + 0p $M_Z = [20, 75]$ GeV	Low Lum.	Alpgen	1'236'000	224 pb^{-1}
$Z/\gamma^* \to \tau\tau$ + 1p $M_Z = [20, 75]$ GeV	Low Lum.	Alpgen	1'159'000	12 pb^{-1}
$Z/\gamma^* \to \tau\tau$ + ($\geq$ 2p) $M_Z = [20, 75]$ GeV	Low Lum.	Alpgen	2'270'000	2.5 pb^{-1}
$Z/\gamma^* \to \tau\tau$ + 0p $M_Z = [75, 105]$ GeV	Low Lum.	Alpgen	5'860'000	221 pb^{-1}
$Z/\gamma^* \to \tau\tau$ + 1p $M_Z = [75, 105]$ GeV	Low Lum.	Alpgen	5'723'000	30 pb^{-1}
$Z/\gamma^* \to \tau\tau$ + ($\geq$ 2p) $M_Z = [75, 105]$ GeV	Low Lum.	Alpgen	2'263'000	5.8 pb^{-1}
$Z/\gamma^* \to \tau\tau$ + 0p $M_Z = [20, 75]$ GeV	High Lum.	Alpgen	400'000	224 pb^{-1}
$Z/\gamma^* \to \tau\tau$ + 1p $M_Z = [20, 75]$ GeV	High Lum.	Alpgen	400'000	12 pb^{-1}
$Z/\gamma^* \to \tau\tau$ + ($\geq$ 2p) $M_Z = [20, 75]$ GeV	High Lum.	Alpgen	800'000	2.5 pb^{-1}
$Z/\gamma^* \to \tau\tau$ + 0p $M_Z = [75, 105]$ GeV	High Lum.	Alpgen	2'401'000	221 pb^{-1}
$Z/\gamma^* \to \tau\tau$ + 1p $M_Z = [75, 105]$ GeV	High Lum.	Alpgen	2'401'000	30 pb^{-1}
$Z/\gamma^* \to \tau\tau$ + ($\geq$ 2p) $M_Z = [75, 105]$ GeV	High Lum.	Alpgen	953'000	5.8 pb^{-1}
WW	Low Lum.	PYTHIA	1'095'000	11.3 pb^{-1}
WZ	Low Lum.	PYTHIA	1'083'000	3.2 pb^{-1}
ZZ	Low Lum.	PYTHIA	1'090'000	3.6 pb^{-1}
WW	High Lum.	PYTHIA	1'100'000	11.3 pb^{-1}
WZ	High Lum.	PYTHIA	1'102'000	3.2 pb^{-1}
ZZ	High Lum.	PYTHIA	1'102'000	3.6 pb^{-1}

Table 5.1: Monte Carlo samples used in this analysis.

The diboson production, WW, WZ and ZZ, have been modeled using the PYTHIA generator which provides inclusive productions.

We want to underline that we excluded double counting of the background with misidentified particles in the Monte Carlo samples. All the leptons should originate from a Z, W boson (*mother* particle) and the electron or muon could originate also from a tau lepton.

The samples that have been used are listed in Table 5.1. We used low instantaneous luminosity samples to account for the periods from 0 to 17, the high instantaneous luminosity ones for periods from 18 to 38.

5.4 Background of Jets Misidentified as Taus

We compute the background with fake leptons via the probability of QCD jets to be misidentified as tau candidates. Jets of hadrons are generally produced through the emission of gluons or quarks in QCD processes or the production of quarks in Electro-Weak interactions.

The method accounts both for events which contain real electron or muon, and events where those leptons come from hadron misidentification. The physics processes that can

contribute to the background with fakes are:

- the QCD mediated production of quark pairs, which provides mainly events with double fake leptons;
- the production of W with associated jets and top pair production in the single lepton decay channel, which contribute to the class of events with one real electron or muon plus a fake tau.

Our method intends to obtain an estimate of this source of background with small statistic and systematic uncertainty. The statistic is enriched by selecting hadron jets, which represent the potential misidentified taus, with loose requirements. This choice will give a big pool of fakable tau object with a small probability to be misidentified as taus. The systematic uncertainty has been reduced with an improved method for estimating the fake rate (see Section 5.4.4).

5.4.1 Hadron Jet Misidentification

The hadron jets originating from the light quark and gluon production of QCD processes are characterized by higher track multiplicity and a wider angular distribution of tracks than the tau induced jets. Despite this, some of them can be generated with features that lead them to be misidentified as a tau decaying into hadrons. The measurement of the probability of a jet to pass the tau selection provides a measurement of one of the major background for our event selection.

The probability for a jet to pass the tau selection is generally called tau fake rate. We measured the tau fake rate starting from samples of loosely selected jets, that we call "fakable tau object" and that we define in the next section.

5.4.2 Definition of Fakable Tau Object

A fakable tau object is a jet that passes a loose preselection for taus. The jet has to be reconstructed as a tau (see section 4.6.1) and has to pass the cuts listed in Table 5.2. The main difference with the tau selection given in Table 4.6 are isolation requirements used in the tau identification and the limit on the invariant mass of the system obtained through the visible momentum. The requirements on isolation and invariant mass are fundamental to reject contamination of QCD induced jets.

The Z^{CES} cut represents the z coordinate position of the track extrapolated into the CES detector: the cuts on ξ' and E/P intends to remove electron or muon contamination as explained in Section 4.6.2.

Variable	Tau ID
$p_T^{SeedTrk}$	$\geq$ 6.0 geV or $\geq$ 8.0 GeV when selecting muon candidates
$E_T^{Cluster}$	$\geq$ 10.0 GeV for 1 prong taus or $\geq$ 15.0 GeV for 3 prong ones
$\mid Z^{CES} \mid$	$9 \leq \mid Z^{CES} \mid \leq 230$ cm
E_T^{ShTwr}	$\geq$ 1.0 GeV
N^{Twr}	≤ 6
ξ'	≤ 0.1
E/P	≥ 0.4

Table 5.2: Fakable tau object selection.

5.4.3 Samples and Trigger Bias Removal

The tau fake rate has been computed using different jet data samples. They are collected with triggers that require the event to have at least a calorimeter cluster with energy above a certain threshold. They are commonly identified by the value of the threshold: "Tower 5" requires one calorimeter tower with an transverse energy deposition of 5 GeV, "Jet 20", "Jet 50", "Jet 70" and "Jet 100" require a calorimeter cluster with transverse energy with 20, 50, 70 and 100 GeV respectively. All data samples, apart from the Jet 100, have been collected with prescaled triggers, and the ones with lower energy threshold have higher prescale values. For our study we uses all the samples to have the highest number of jets at all energies.

For simplicity we have not considered in our study all data taken during CDF Run II. The samples are chosen to get the proper distribution of the Tevatron instantaneous luminosity. The samples belong to 4 sets of data taking periods, restricted to periods from 1 to 4, 9 and 10, from 11 to 13, and from 18 to 28 (see Appendix A). The last periods, from 29 to 38, are characterized by the small differences in the Tevatron instantaneous luminosity, we did not use the data from the jet samples during those periods. As will be later explained we use the result obtained for periods 18 to 28 to the last periods of data taking.

Our trigger bias removal is intended to remove the bias induced from the trigger selection of jets. The bias removal is applied separately at each trigger level 1, 2 and 3. We first require objects to pass the jet trigger requirements (for example, a calorimetric tower 5 and a level 2 cluster with 40 GeV for the JET_50 trigger) then we disregard the events which contain only one objects passing the requirements.

We used the information that is stored in the bank of the calorimeter towers of the trigger level 1, the cluster information of level 2 and the jet collection belonging to level 3. The main part of the events is selected by trigger paths JET_CAL_SINGLETOWER_5, JET_20, JET_50, JET_70, JET_100, which belong respectively to data samples Tower 5, Jet 20, Jet 50, Jet 70 and Jet 100 (more details on the trigger selection are in Ap-

Triggers	Level 1	Level 2	Level 3
JET_CAL_SINGLETOWER_5	$E_T^{tower} > 5$ GeV	-	-
JET_20	$E_T^{tower} > 5$ GeV	$E_T^{cluster} > 15$ GeV†	$E_T^{jet0.7} > 20$ GeV
JET_50	$E_T^{tower} > 5$ GeV	$E_T^{cluster} > 40$ GeV	$E_T^{jet0.7} > 50$ GeV
JET_70	$E_T^{tower} > 10$ GeV	$E_T^{cluster} > 60$ GeV	$E_T^{jet0.7} > 70$ GeV
JET_100	$E_T^{tower} > 10$ GeV	$E_T^{cluster} > 90$ GeV	$E_T^{jet0.7} > 100$ GeV

Table 5.3: Transverse energy required for the triggers at the 3 levels. †The transverse energy requirement changed indicativelly after period 13 to $E_T^{cluster} > 20$ GeV

pendix A). The jet data samples may contain, however, a small fraction of events selected by triggers without level 2 requirements but with higher prescale factor (for example JET_20_NO_L2). We considered all trigger paths in the jet data samples and we applied the criteria of trigger bias removal to all the events. The E_T requirements of the trigger paths are summarized in Table 5.3; where we indicate with $E_T^{jet0.7}$ the transverse energy of the jets of trigger level 3 obtained with JETCLU algorithm set with cone $\Delta R < 0.7$ (see Section 4.8); $E_T^{cluster}$ the transverse energy of the calorimeter tower clusters reconstructed at trigger level 2; E_T^{tower} the transverse energy of the calorimeter towers at trigger level 1.

5.4.4 Measurement of Tau Fake Rate

The pool of jets used for the fake rate measurement should not include real taus decaying in hadrons. This event selection has to veto the physics events that produce tau leptons and represent background for QCD jet production. The dominant processes are the production of W boson decaying into $\tau + \nu$ and the production of Z/γ^* decaying into two taus. The production of heavy flavor quarks may also generate tau leptons in the final state, but these taus in most of the cases are not isolated. A smaller contribution could be due to the production of top quark pair decaying in leptonic or dileptonic modes with a hadronic tau in the final state. Some Electroweak mediated processes could generate also two vector bosons decaying in leptonic modes; these processes have, however, a very small cross section.

Missing transverse energy originates from the neutrinos in the processes described before, and in particular from the process that involves a W boson. Taking this into account we require the missing transverse energy to be small compared to the sum of the energy deposited in the calorimeter. We imposed $\not\!\!E_T < 20 + \sqrt{\Sigma E_T}$ GeV where ΣE_T is the scalar sum of the calorimeter transverse energy. The $\not\!\!E_T$ and ΣE_T have been corrected through the latest version of jet energy correction (up to the last data period). All jets with cone $\Delta R = 0.4$, with raw $E_T > 10$ GeV and in the pseudorapidity region $\mid \eta \mid < 2.4$ have been corrected up to level 5 (see Section 4.8.2). Z decays into two taus can also generate a lepton through a tau decay in leptons. For this reason we do not take into account events that

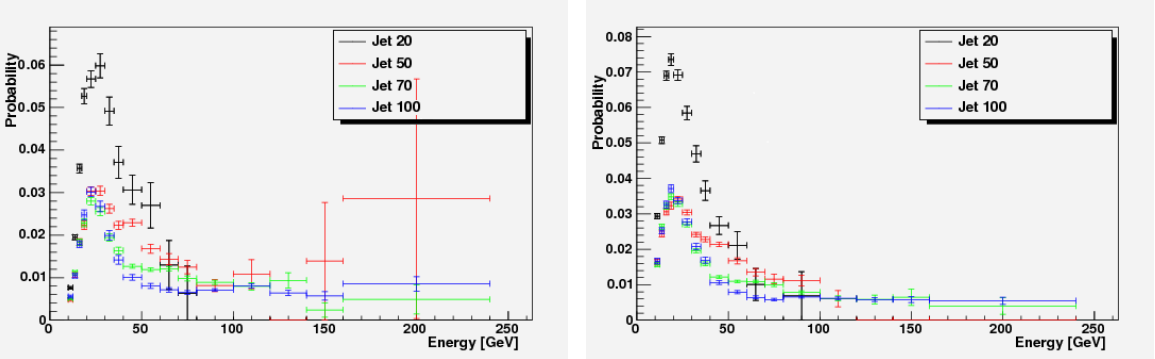

Figure 5.1: The τ fake rate for periods from 18 to 28. On the left, the result for 1 prong taus, and on the right, 3 prong taus.

contain objects identified as electrons with $E_T > 10$ GeV in the central electromagnetic calorimeter or as tight muons with $E_T > 10$ GeV and a corresponding CMUP or CMX stub (identification requirements as described in Chapter 4).

Previous measurements of the fake rate were commonly done excluding the leading jet, because it was generally considered biased by the trigger selection. The fake rate was evaluated only with the remaining jets passing the fakable object selection. As discussed in CDF note [65], these measurements of the fake rate showed a strong dependency on the jet sample. Since there was no a priori criteria to prefer the result from a sample rather than another one, the fake rate was obtained taking the average of all the measurements and assigning as systematic uncertainty the difference with the highest and lowest result.

We repeated this method and computed the fake rate removing the leading jet if it was the only one to pass the trigger requirement. We parametrized the probability of a fakable tau object to pass the tau identification as function of the transverse energy of the tau calorimeter cluster and the track multiplicity (1 or 3 prongs). The result of this computation is shown in Figure 5.1 where the fakable objects have passed the requirements in Table 5.2 except that we required a lower transverse energy and momentum for three prong taus: $E_T^{Cluster} \geq 10.0$ GeV, and in the identification: $p_T^{Vis} \geq 15.0$ GeV.

The discrepancy among the different results is evident in Figure 5.1 and for every choice of the nominal value of the fake rate, the estimated systematic uncertainty is $\sim 25\%$. We observed that the fake rate so obtained tends to underestimate the probability of jets to fake taus.

As underlined [65], the sample dependence is small considering separately the first (leading) and the second (subleading) highest transverse energy jets in the computation of the fake rate. In our study we have evaluated the fake rate with this methodology.

The leading jets have on average higher fake rate than the subleading ones. It may be pointed out that this property is linked to the fraction of gluon induced jets in the

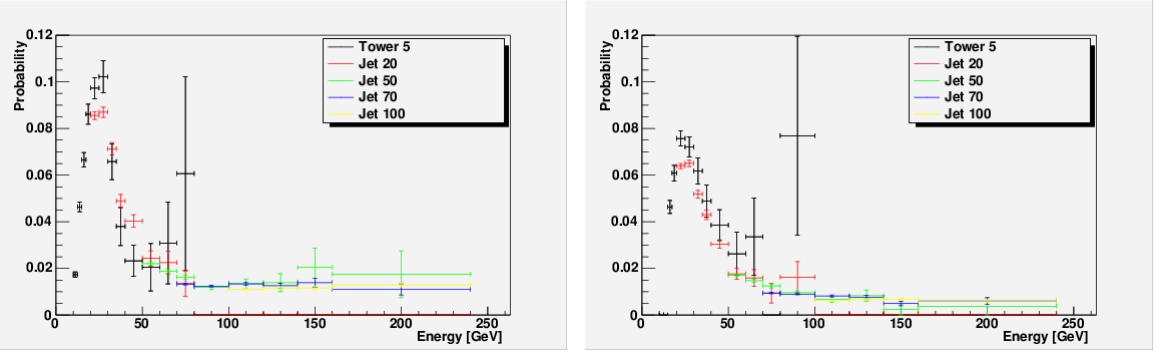

Figure 5.2: The τ fake rate for periods from 18 to 28 for the leading jet case. On the left, the result for 1 prong taus, and on the right, 3 prong taus.

two categories of jets. The gluon jets have a wider distribution of energy and they have a smaller probability to pass the isolation requirements of the tau candidate identification. Leading jets have a smaller probability to be gluon jets than the subleading ones. For this reason the results for leading and subleading jets may be used as high and low systematic bounds of the tau fake rate measurement.

Previous studies observed a dependecy of the fake rate on the E_T and $|\eta|$ of the cluster and on the track multiplicity of the hadron jet. To maintain a low systematic uncertainty on the estimate of this background we parametrized the probability of a fakable tau object to pass the tau identification as function of the three parameters just named.

Once the events that do not satisfy the trigger bias removal (5.4.3) are removed we calculate the fake rate for fakable tau objects separately when they are matched with the leading and subleading jets. The jets considered for the measurement of the fake rate are selected requiring them to have cluster pseudorapidity $\mid \eta \mid < 1.2$, since the tau candidates cam have a cluster only in the central calorimeter. So we want to stress here that the leading jet used in the fake rate measurement is the leading in the detector central region and not necessarily the leading one in the event.

The results corresponding to data sets of periods from 18 to 28 are shown in Figure 5.2, for the leading, and in Figure 5.3, for the subleading jets. The results, parametrized as function of cluster E_T, is obtained with fakable tau objects having the seed track with transverse momentum $p_T > 6$ GeV/c. It can be noticed that the results obtained with different jet samples are generally in agreement within the statistical uncertainty, and (as commented above) that the subleading jet, passing the fakable tau object selection, has generally smaller probability than the leading one.

The fake rate for the leading and the subleading jets is obtained separately collecting the values from each jet sample in specific jet energy ranges. We choose the ranges of transverse energy such that they are over the trigger threshold of the sample and below the trigger threshold of the next jet sample. In this way we use at a certain transverse

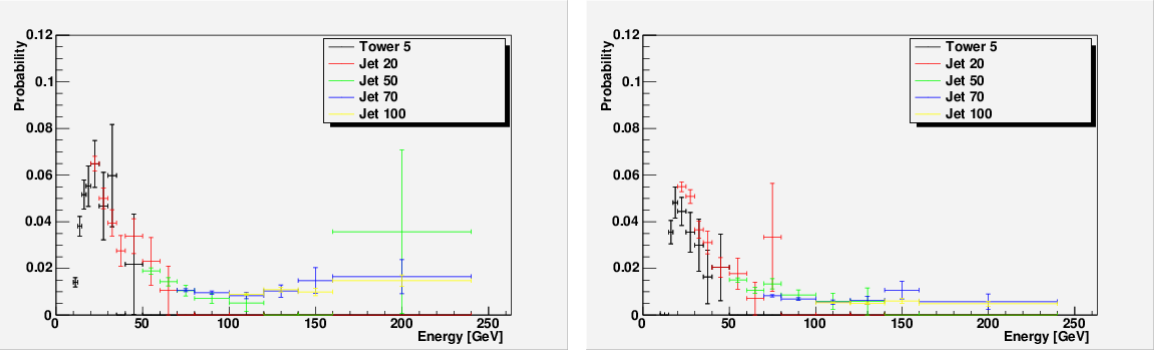

Figure 5.3: The τ fake rate for periods from 18 to 28 for the subleading jet case. On the left, the result for 1 prong taus, and on the right, 3 prong taus.

energy the fake rate from the sample which has the smaller statistical uncertainty. We then stitched the results together. The ranges considered are:

- from 10 GeV (or 15 GeV for 3 prong fakable objects) to 20 GeV use Tower 5 sample;
- from 20 GeV to 50 GeV use Jet 20 sample;
- from 50 GeV to 70 GeV use Jet 50 sample;
- from 70 GeV to 100 GeV use Jet 70 sample;
- from 100 GeV to 240 GeV use Jet 100 sample.

Jets with $Et > 240$ GeV were not considered because their contribution was negiglible. Figure 5.4 shows the fake rate for 1 prong tau fakable objects in case they match the leading jet or the subleading jet (seed track $p_T > 6$ GeV/c). Figure 5.5 shows the same, for 3 prong fakable objects.

The fake rate we will use in our analysis is the average between the results obtained with the leading jet and the subleading one. The mean value is computed using the method of minimum χ^2 and the standard deviation is obtained accordingly. To account for the systematic disagreament between the leading and subleading jets, a systematic uncertainty is assigned taking the difference between the average and the leading or subleading jet values.

The mean values shown in Figures 5.4 and 5.5 with its systematic band is shown in Figure 5.6. The systematic error is shown in light blue, when the leading jets selected as fakable objects have a higher probability to pass the tau identification than the subleading jets. When the opposite happens the systematic error is showed in red.

The estimate of events with fakes for the electron and muon is obtained using different samples. As better explained in Section 5.4.5, we modify the transverse momentum

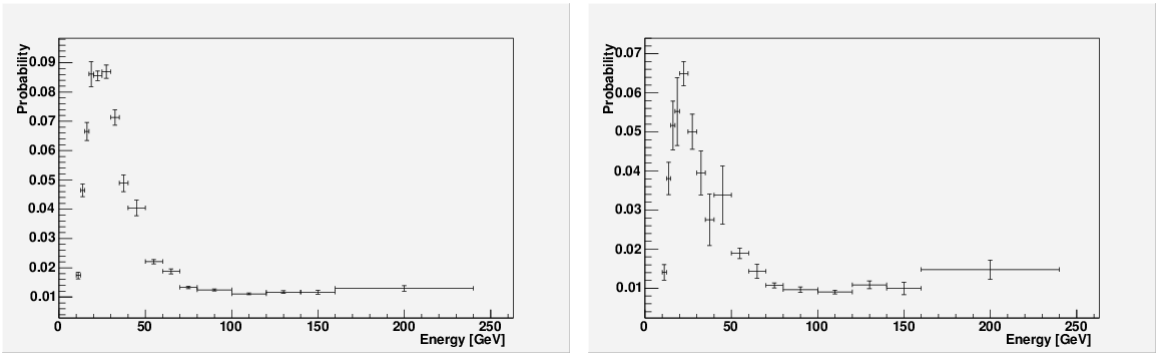

Figure 5.4: The τ fake rate for periods from 18 to 28. On the left, the result for 1 prong fakable tau objects when it is a central leading jet, and on the right the subleading one.

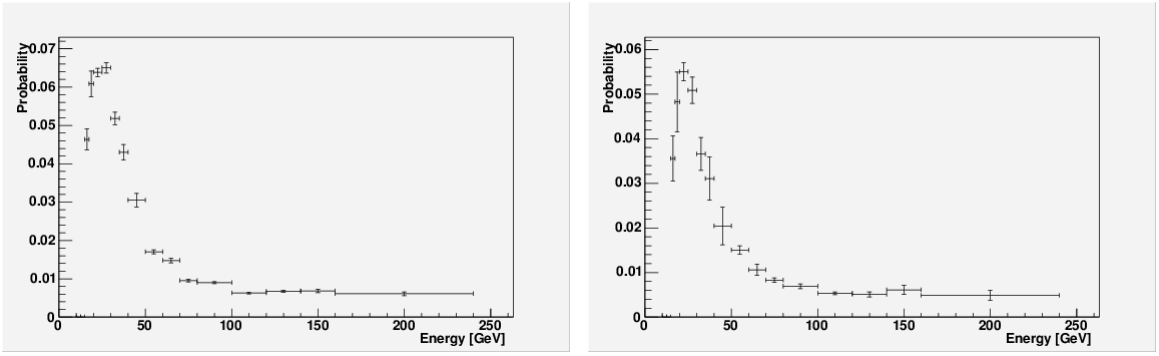

Figure 5.5: The τ fake rate for periods from 18 to 28. On the left, the result for 3 prong fakable tau objects when it is a central leading jet, and on the right the subleading one.

requirement of the tau seed track to be consistent with the trigger requirement of the sample with CMX muons. At the same time we need to modify in the way the requirement of the fakable tau object. Employing the same procedures as before, but setting $Pt^{SeedTrk} > 8$ GeV we obtain the fake rates shown in Figure 5.7.

In Figure 5.8 we show the ratio between the measurements of tau fake rate measured on sample on the Jet 20 sample from periods 18 to 28, using the two different seed track requirements for fakable tau object. It shows the ratio of the fake rate with seed track $Pt^{SeedTrk} > 6$ GeV over the fake rate with $Pt^{SeedTrk} > 8$ GeV. It is possible to notice that there is a difference of 3% between the two results.

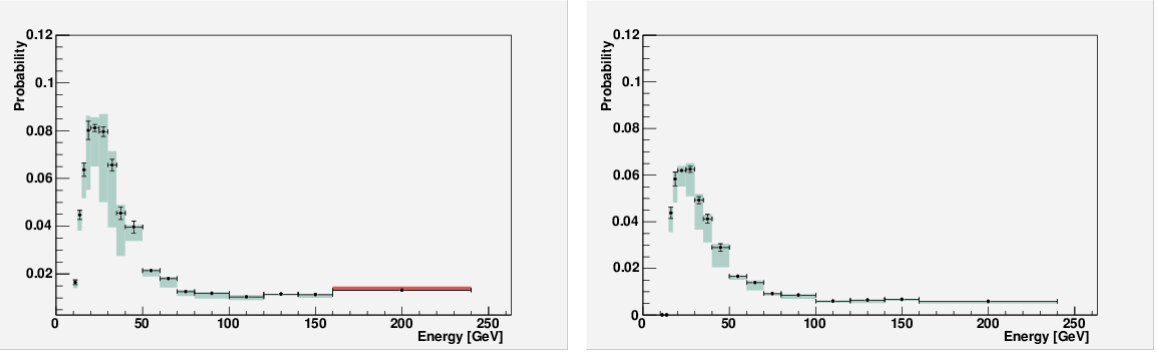

Figure 5.6: The mean value for periods from 18 to 28. On the left, the result for 1 prong taus, and on the right, 3 prong taus, where the mean value is computed from the leading and subleading samples.

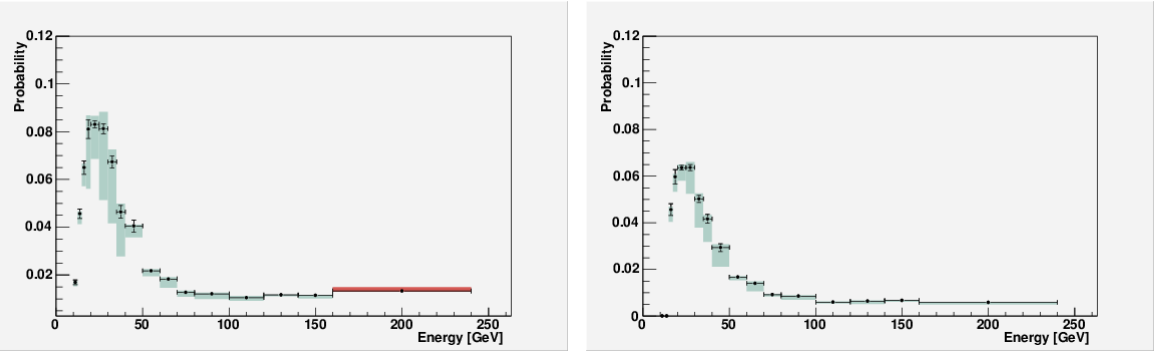

Figure 5.7: The mean value for periods from 18 to 28 requiring $Pt^{SeedTrk} > 8$ GeV. On the left, the result for 1 prong taus, and on the right, 3 prong taus, where the mean value is computed from the leading and subleading samples.

Dependency of the Tau Fake Rate on Data Taking Period Range

The measurement of the tau fake rate using the sample from data period 18 to 28 was repeated with earlier data taking periods. Figures 5.9, 5.10, 5.11 show the fake rate of periods from 1 to 4, 9 and 10, 11 to 13 respectively.

We compared the tau fake rates in different data periods calculating the ratio of the measurements corresponding to the same jet sample. We calculated the ratio as function of the same transverse energy bins. Figures 5.12, 5.13, 5.14, 5.15 and 5.16 are showing the ratio between data period range 1 to 4 with range 18 to 28, respectively for jet samples Tower 5, Jet 20, Jet 50, Jet 70 and Jet 100. Figures 5.17, 5.18, 5.19, 5.20 and 5.21 show the results using the same procedure on data period range 11 to 13 with range 18 to 28.

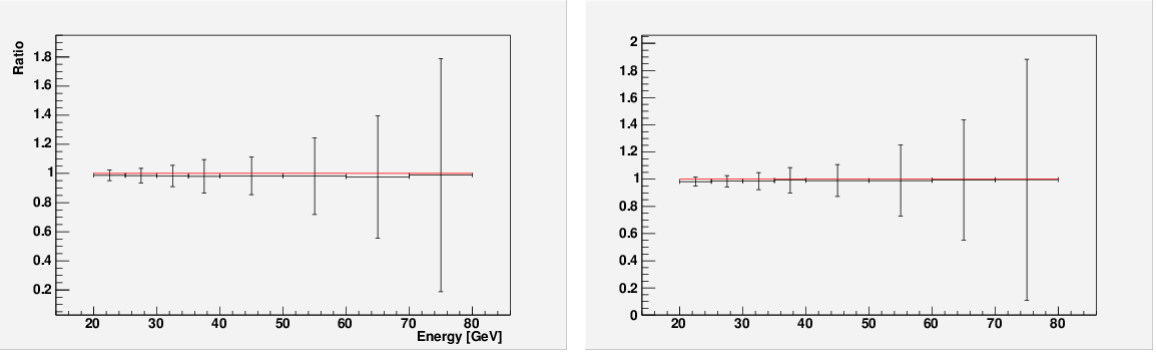

Figure 5.8: The ratio of the fake rate computed requiring $Pt^{SeedTrk} > 6$ GeV over the fake rate with $Pt^{SeedTrk} > 8$ GeV for periods from 18 to 28. On the left, the result for 1 prong taus, and on the right, 3 prong taus, where the mean value is computed from the leading and subleading samples.

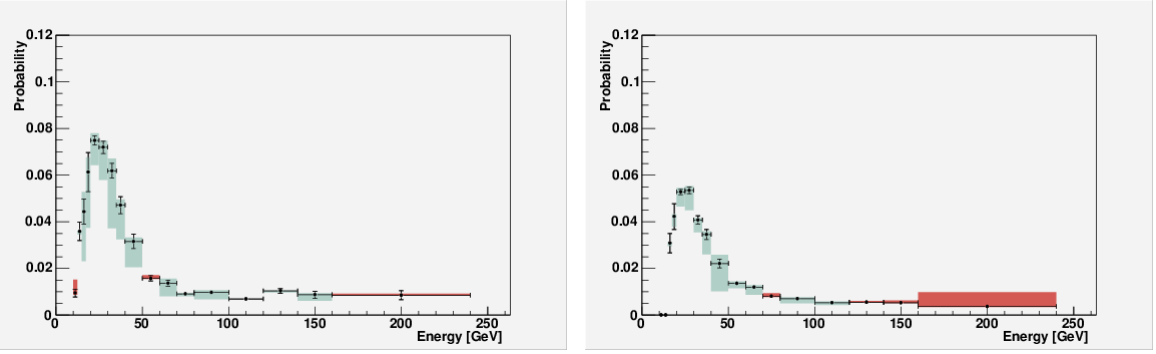

Figure 5.9: The mean value for periods from 1 to 4. On the left, the result for 1 prong taus, and on the right, 3 prong taus, where the mean value is computed from the leading and subleading samples.

The ratio between the different data periods is often not compatible with unity. It can be noticed that the fake rate from periods 18 to 28 is in general higher than the other ones. Qualitatively the fake rate calculated in periods from 18 to 28 is more similar to the one in periods from 11 to 13 than the one in periods from 1 to 4. We can deduce from this that instantaneous luminosity can affect the measurement of the tau fake rate.

In Figures 5.22, 5.23, 5.24 we show the comparison between the results obtained in periods from 1 to 4 and periods from 11 to 13, restricted just to jet samples Tower 5, Jet 20 and Jet 50. It is possible to notice that most of the points are compatible with unity within their statistical uncertainty.

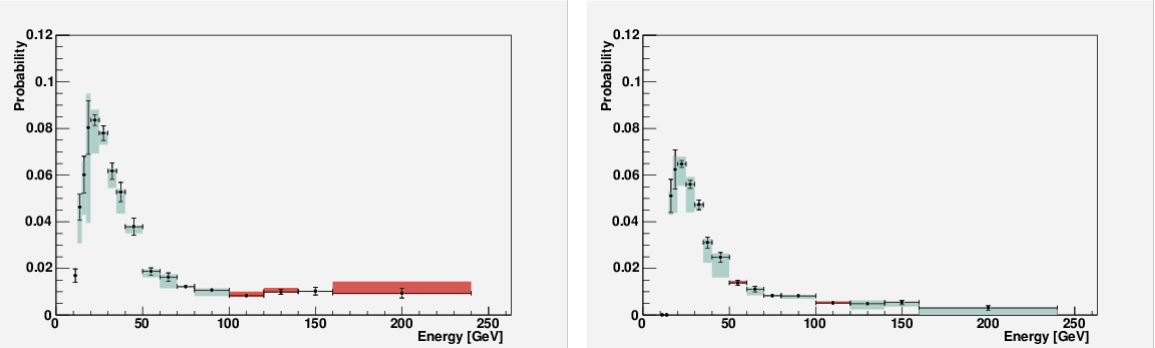

Figure 5.10: The mean value for periods 9 and 10. On the left, the result for 1 prong taus, and on the right, 3 prong taus, where the mean value is computed from the leading and subleading samples.

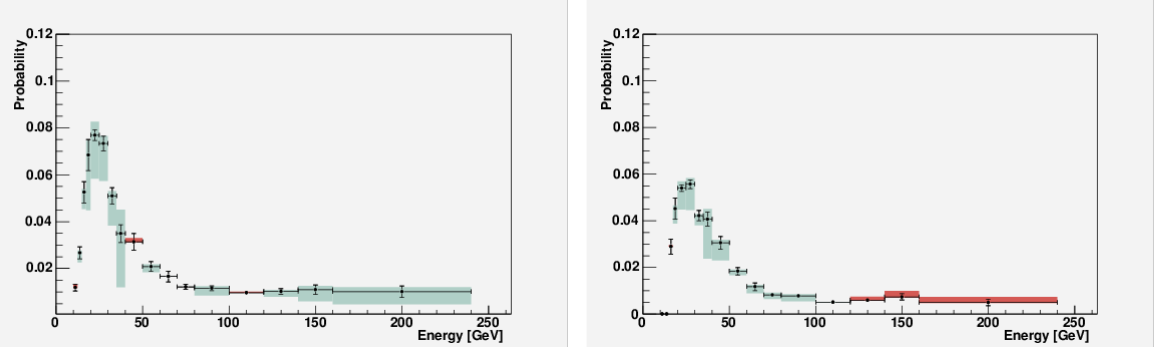

Figure 5.11: The mean value for periods from 11 to 13. On the left, the result for 1 prong taus, and on the right, 3 prong taus, where the mean value is computed from the leading and subleading samples.

5.4.5 Data Sample for Background with Fakes

We measure the background due to jets misidentified as tau through the calibration lepton samples, "Calibration Electron", "Calibration Muon", and the sample "Lepton plus Track". We report in Appendix A a description of trigger paths associated to these samples. The "Calibration Electron" sample is used to compute the background with tau fakes when one electron candidate is present; the "Calibration Muon" and the "Lepton plus Track" samples when one CMUP or one CMX muon candidate is present. The triggers used are dynamically prescaled, so we reweight the integrated luminosities of these paths to the ones belonging to the "Lepton plus Isolated Track", used for signal extraction.

We use for the evaluation of fakes the tau fake rates shown in the previous sections. We will collect events with one electron or one muon candidate paired with at least a fakable

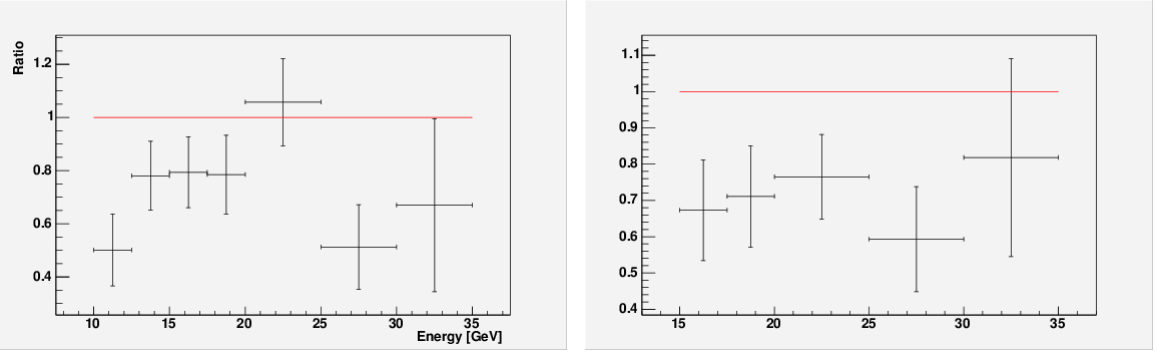

Figure 5.12: The ratio between the mean value computed with Tower 5 samples in periods from 1 to 4 and 18 to 28. On the left, the result for 1 prong taus, and on the right, 3 prong taus, where the mean value is computed from the leading and subleading samples.

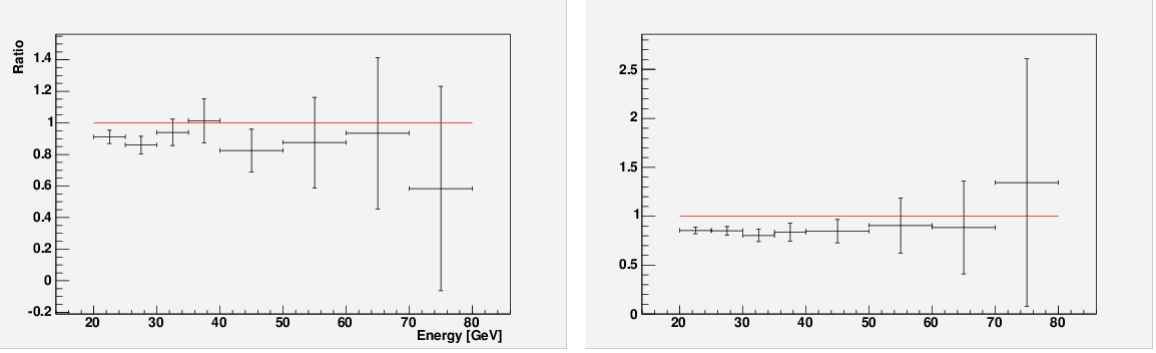

Figure 5.13: The ratio between the mean value computed with Jet 20 samples in periods from 1 to 4 and 18 to 28. On the left, the result for 1 prong taus, and on the right, 3 prong taus, where the mean value is computed from the leading and subleading samples.

tau object. The fakable tau object in the muon samples is required to have $p_T^{seedtrk} \geq 8$ GeV both for CMUP and CMX categories consistent with the trigger requirement of the "Lepton plus Track" trigger. Every fakable tau object is then considered as a possible selected event weighted by the probability of the fakable object to be misidentified.

The tau fake rate has been computed with different data samples and some deviations are observed between different periods of data taking. For this reason we consider the tau fake rate dependent on the data taking period range. The average of the fake rate computed in periods 1 to 4, 9 and 10, 11 to 13 is used for events belonging to data periods from 1 to 13 (calibration triggers were not included in data period 0), the fake rate computed in periods 18 to 28 is used for events belonging to data periods from 18 to 35 (we reweight for the integrated luminosity of the analysis sample up to data period 38).

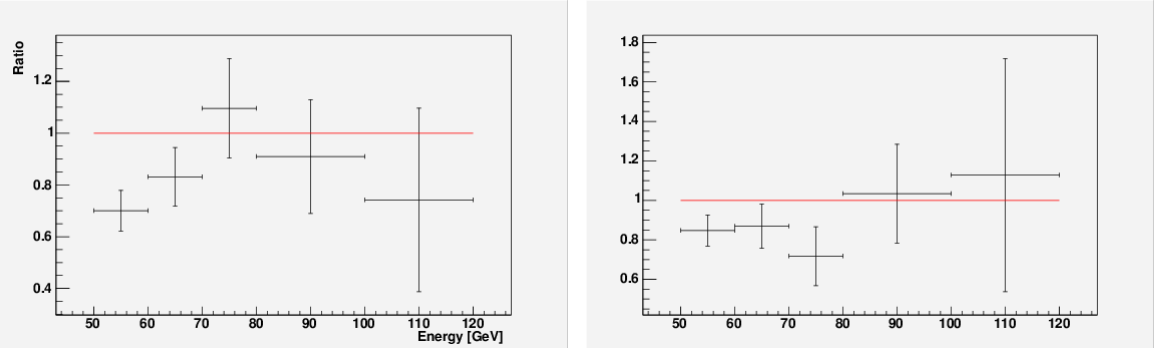

Figure 5.14: The ratio between mean value computed with Jet 50 samples in periods from 1 to 4 and 18 to 28. On the left, the result for 1 prong taus, and on the right, 3 prong taus, where the mean value is computed from the leading and subleading samples.

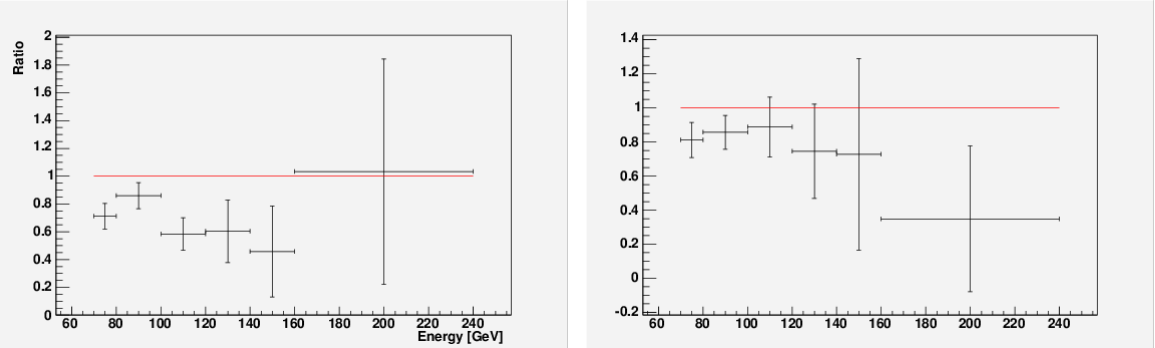

Figure 5.15: The ratio between the mean value computed with Jet 70 samples in periods from 1 to 4 and 18 to 28. On the left, the result for 1 prong taus, and on the right, 3 prong taus, where the mean value is computed from the leading and subleading samples.

We parametrize the fake rate as function of the coordinate $|\eta|$ and of the jet cluster E_T. The validation plots of the fake rate method will be shown in Appendix B.

5.5 Concluding Remarks of the Tau Fake Rate

We have estimated the tau fake rate induced by misidentified QCD jet events, which represent the dominant background to our analysis. We implement in our top analysis the results we obtained. We first select data events with a single identified lepton and at least a fakable tau jet, and second, we count each fakable tau as an event weighted by the fake rate corresponding to it.

The dependence on the run period range is one of the important point for this analysis

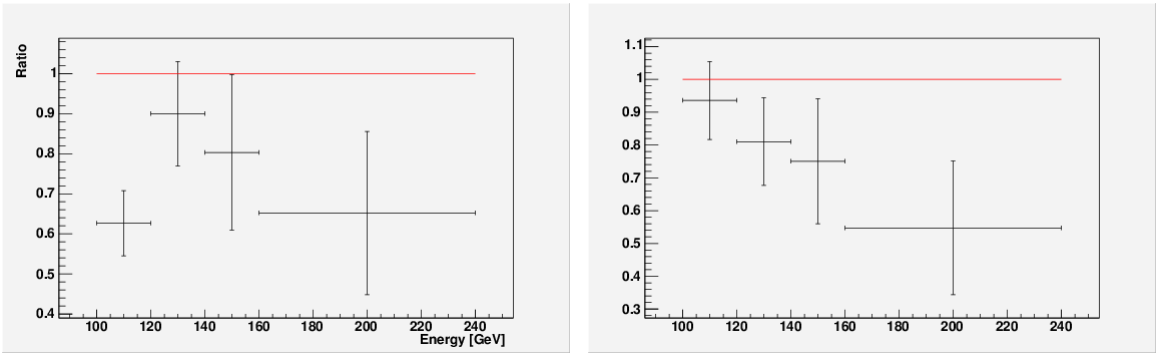

Figure 5.16: The ratio between the mean value computed with Jet 100 samples in periods from 1 to 4 and 18 to 28. On the left, the result for 1 prong taus, and on the right, 3 prong taus, where the mean value is computed from the leading and subleading samples.

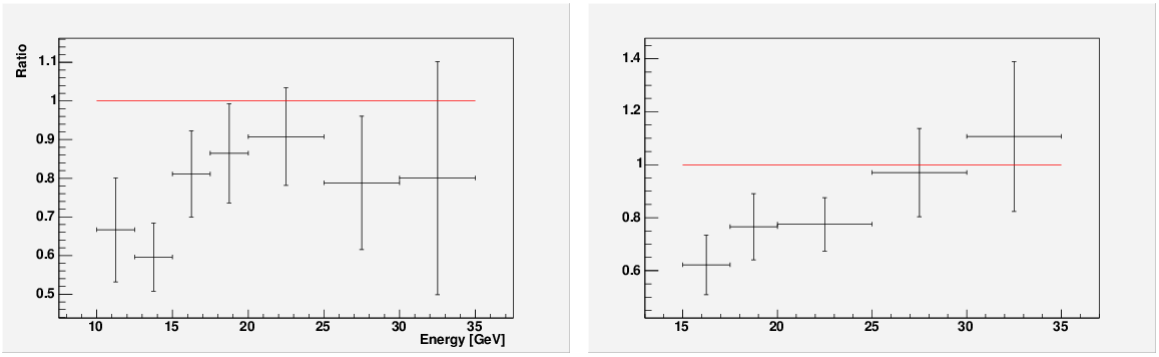

Figure 5.17: The ratio between the mean value computed with Tower 5 samples in periods from 11 to 13 and 18 to 28. On the left, the result for 1 prong taus, and on the right, 3 prong taus, where the mean value is computed from the leading and subleading samples.

that covers all the Run II recorded data. We analyzed it and we decided to average the results that are similar and correspond to similar Tevatron instantaneous luminosity regimes.

The effect of using the fake rate of the leading or the subleading jet has been studied as well. We observed, as expected, that the leading jet has higher probability to be misidentified as tau. We show in Appendix B that the fake rate of the leading and of the subleading jets represent correctly the upper and lower limits of the tau fake rate in two different control regions: a sample enriched by QCD events and W plus jets events.

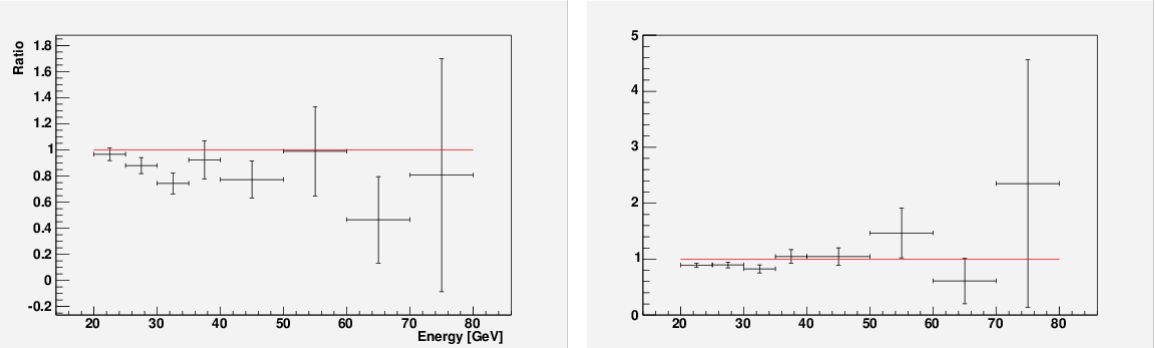

Figure 5.18: The ratio between the mean value computed with Jet 20 samples in periods from 11 to 13 and 18 to 28. On the left, the result for 1 prong taus, and on the right, 3 prong taus, where the mean value is computed from the leading and subleading samples.

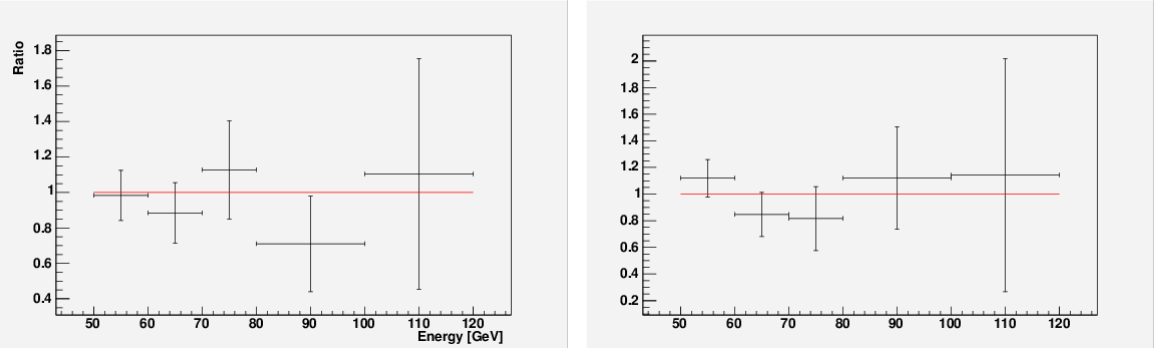

Figure 5.19: The ratio between the mean value computed with Jet 50 samples in periods from 11 to 13 and 18 to 28. On the left, the result for 1 prong taus, and on the right, 3 prong taus, where the mean value is computed from the leading and subleading samples.

5.6 Electron or Muon Misidentified as Tau

The production of a Z boson, with decay $Z \rightarrow ee/\mu\mu$, represents a possible source of background. This happens when one of the leptons passes the tau identification requirements. We estimate the expected numbers of background events from this source through ALPGEN generated samples listed in Table 5.4.

As in the case of $Z \rightarrow \tau\tau$ (see section 5.3), the LO cross section of each sample has been reweighted by a scaling factor to NLO cross section [64] *k-factor*, $k = 1.40$ ($\pm 15\%$ in the two jet multiplicity bin).

Process	**Inst. Lum.**	**Gen.**	**N. Events**	σ_{prod}
$Z/\gamma^* \to \mu\mu$ + 0p $M_Z = [75, 105]$ GeV	Low Lum.	Alpgen	2'659'000	221 pb^{-1}
$Z/\gamma^* \to \mu\mu$ + 1p $M_Z = [75, 105]$ GeV	Low Lum.	Alpgen	2'652"000	30 pb^{-1}
$Z/\gamma^* \to \mu\mu$ + 2p $M_Z = [75, 105]$ GeV	Low Lum.	Alpgen	4'660'000	4.8 pb^{-1}
$Z/\gamma^* \to \mu\mu$ + 3p $M_Z = [75, 105]$ GeV	Low Lum.	Alpgen	536'000	0.77 pb^{-1}
$Z/\gamma^* \to \mu\mu$ + ($\geq$ 4p) $M_Z = [75, 105]$ GeV	Low Lum.	Alpgen	530'000	0.14 pb^{-1}
$Z/\gamma^* \to ee$ + 0p $M_Z = [75, 105]$ GeV	Low Lum.	Alpgen	2'639'000	221 pb^{-1}
$Z/\gamma^* \to ee$ + 1p $M_Z = [75, 105]$ GeV	Low Lum.	Alpgen	2'625'000	30 pb^{-1}
$Z/\gamma^* \to ee$ + 2p $M_Z = [75, 105]$ GeV	Low Lum.	Alpgen	536'000	4.8 pb^{-1}
$Z/\gamma^* \to ee$ + 3p $M_Z = [75, 105]$ GeV	Low Lum.	Alpgen	524'000	0.77 pb^{-1}
$Z/\gamma^* \to ee$ + ($\geq$ 4p) $M_Z = [75, 105]$ GeV	Low Lum.	Alpgen	525'000	0.14 pb^{-1}
$Z/\gamma^* \to \mu\mu$ + 0p $M_Z = [75, 105]$ GeV	High Lum.	Alpgen	1'020'000	221 pb^{-1}
$Z/\gamma^* \to \mu\mu$ + 1p $M_Z = [75, 105]$ GeV	High Lum.	Alpgen	1'021'000	30 pb^{-1}
$Z/\gamma^* \to \mu\mu$ + 2p $M_Z = [75, 105]$ GeV	High Lum.	Alpgen	1'793'000	4.8 pb^{-1}
$Z/\gamma^* \to \mu\mu$ + 3p $M_Z = [75, 105]$ GeV	Low Lum.	Alpgen	192'000	0.77 pb^{-1}
$Z/\gamma^* \to \mu\mu$ + ($\geq$ 4p) $M_Z = [75, 105]$ GeV	Low Lum.	Alpgen	192'000	0.14 pb^{-1}
$Z/\gamma^* \to ee$ + 0p $M_Z = [75, 105]$ GeV	High Lum.	Alpgen	1'024'000	221 pb^{-1}
$Z/\gamma^* \to ee$ + 1p $M_Z = [75, 105]$ GeV	High Lum.	Alpgen	1'024'000	30 pb^{-1}
$Z/\gamma^* \to ee$ + 2p $M_Z = [75, 105]$ GeV	High Lum.	Alpgen	1'793'000	4.8 pb^{-1}
$Z/\gamma^* \to ee$ + 3p $M_Z = [75, 105]$ GeV	Low Lum.	Alpgen	192'000	0.77 pb^{-1}
$Z/\gamma^* \to ee$ + ($\geq$ 4p) $M_Z = [75, 105]$ GeV	Low Lum.	Alpgen	192'000	0.14 pb^{-1}

Table 5.4: Monte Carlo samples used in this analysis.

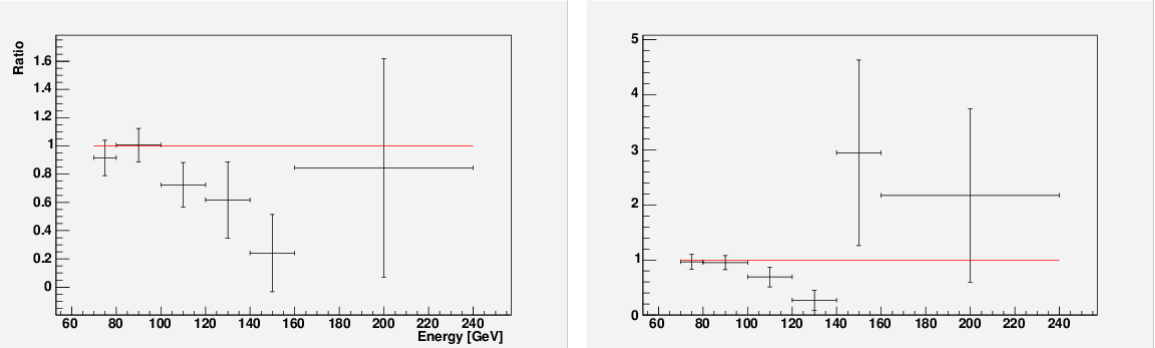

Figure 5.20: The ratio between the mean value computed with Jet 70 samples in periods from 11 to 13 and 18 to 28. On the left, the result for 1 prong taus, and on the right, 3 prong taus, where the mean value is computed from the leading and subleading samples.

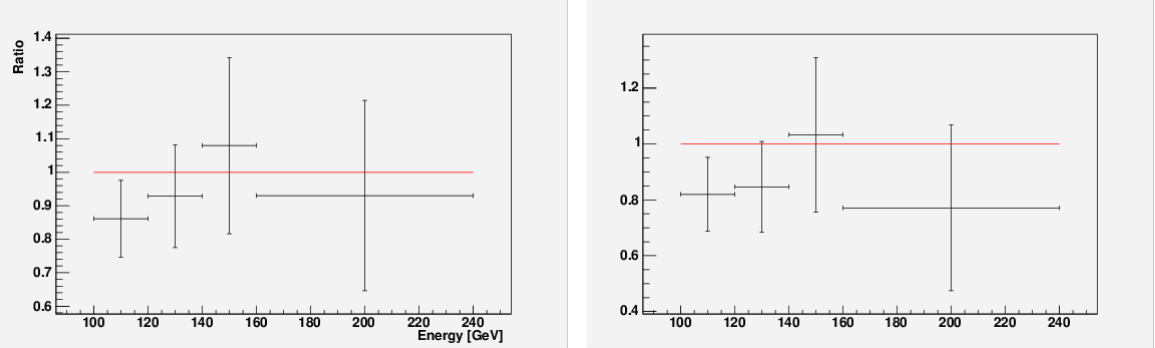

Figure 5.21: The ratio between the mean value computed with Jet 100 samples in periods from 11 to 13 and 18 to 28. On the left, the result for 1 prong taus, and on the right, 3 prong taus, where the mean value is computed from the leading and subleading samples.

5.7 Concluding Remarks

In this chapter we have presented the MC method, which is used to obtain the samples of simulated events we use to evaluate the efficiency of the signal selection and of the irreducible background selection. We presented the processes that are the major sources of irreducible background for our analysis and the methods we use to estimate their contribution.

We spent a large effort to evaluate the background of events with jet misidentified as tau candidates. We implemented a data based estimate of the events with fakes to obtain a small systematic unncertainty. Indeed the evaluation of events with tau fakes obtained through MC simulation has large systematic uncertainties due to the uncertainty in the

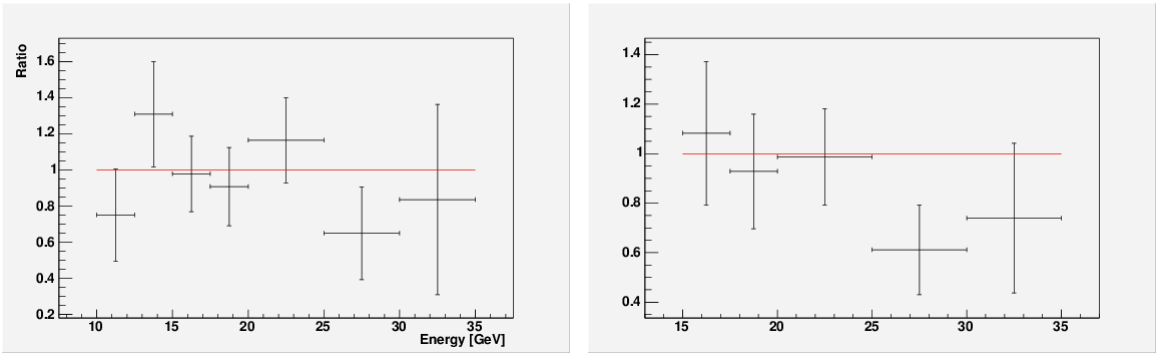

Figure 5.22: The ratio between the mean value computed with Tower 5 samples in periods from 1 to 4 and from 11 to 13. On the left, the result for 1 prong taus, and on the right, 3 prong taus, where the mean value is computed from the leading and subleading samples.

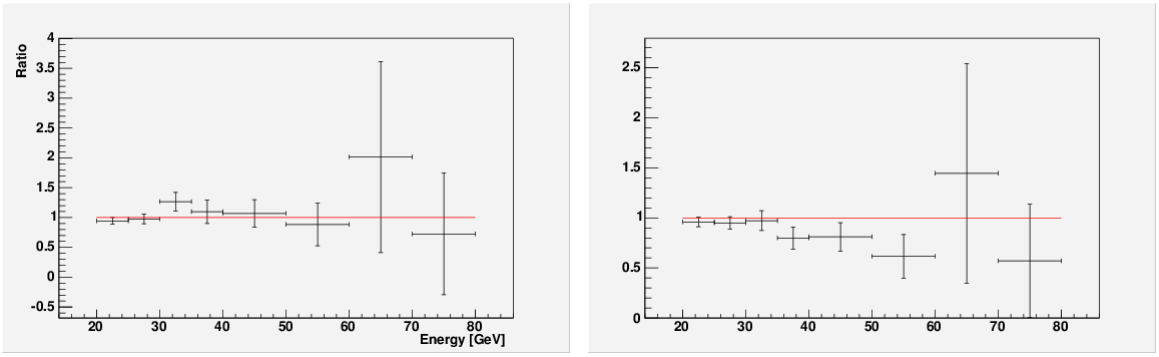

Figure 5.23: The ratio between the mean value computed with Jet 20 samples in periods from 1 to 4 and from 11 to 13. On the left, the result for 1 prong taus, and on the right, 3 prong taus, where the mean value is computed from the leading and subleading samples.

parton showering model. Through the use of a loose fakable tau object selection we also obtain the evaluation of expected background events with a small statistic uncertainty.

The systematic uncertainty connected to the evaluation of each background source is evaluated and presented in Chapter 7.

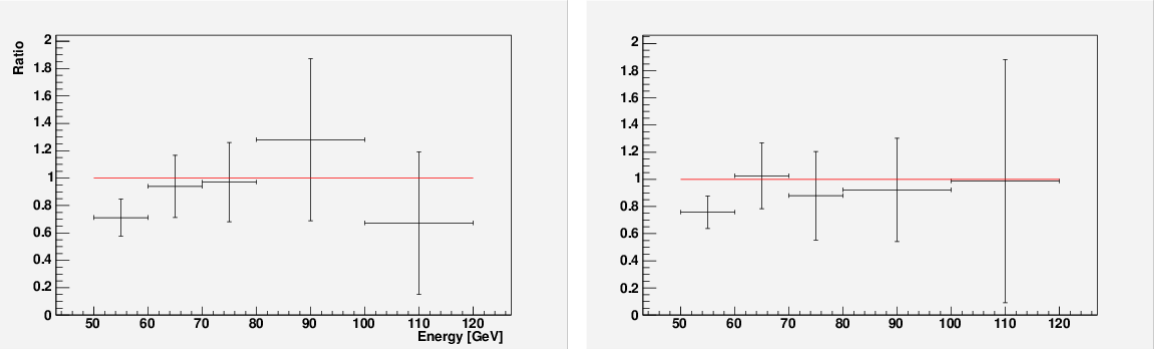

Figure 5.24: The ratio between the mean value computed with Jet 50 samples in periods from 1 to 4 and from 11 to 13. On the left, the result for 1 prong taus, and on the right, 3 prong taus, where the mean value is computed from the leading and subleading samples.

Chapter 6

Event Selection

6.1 Initial Selection

The CDF trigger wrote all tau plus electron or muon events into the "E stream"[1]. After reconstruction events in the stream were split into data samples, in our case the lepton plus isolated track, "etlp0d" through "etlp0p". The last two characters in the data sample identifier denote the reconstruction pass used. Small improvements were made to the reconstruction as instantaneous luminosity increased to keep the tracking efficiency high. The data samples used are the latest reconstruction passes of CDF. The data samples were then converted into N-tuple format and our analysis starts here.

In a first selection we select events with an electron, a tau and a good event vertex. The vertex should be reconstructed with at least 2 COT tracks[2] that are with ± 3 cm at the beam axis. Similarly for the muon case. This selection results in 184,475 electron and 177,770 muon events of the 835,333,474 events in the lepton plus track data sample. The selections are stored on a scientific workstation to allow fast additional selections.

We apply the same preliminary selection to the $t\bar{t}$ Monte Carlo sample to obtain a smaller sample for our studies. We obtain 4,840 events from top pair decay in the ditau channel with one electron in the final state and 5,027 events of ditau with one muon; 45,999 events from top pair decay in the electron plus tau channel and 44,397 in the muon plus tau channel.

6.2 Kinematic Selection

The first set of requirements of our selection are:

[1] The E stream contains all triggers of data samples used mainly for searches, such as the search of the Higgs bosons in ditau and $b\bar{b}$ final states, or supersymmetric phenomena in multi-lepton event analysis.

[2] The minimum quality requirement for COT tracks correspond to at least 5 hits on the axial wires and 2 on the small angle stereo wires.

- exactly 1 tau candidate;
- exactly 1 electron or 1 muon candidate;
- opposite electric charge between the tau and the other lepton;
- 2 or more jets;
- missing transverse energy $\not\!\!E_T \geq 10$ GeV.

The objects above are selected with the identification criteria described in Chapter 4. To remove background from Drell-Yan processes we apply a veto that is described in the next section.

6.2.1 Z/γ^* Veto

Drell-Yan processes with electron or muon pairs can contribute to our selection if one of the leptons is misidentified as a tau candidate. Another smaller contribution is expected from events where one of the leptons escapes detection and a hadronic jet is misidentified as tau candidate.

We use a cluster based rejection method for the electron misidentified as tau and a track based method to reduce muons in the tau sample. The background from hadron jet misidentification is included in the fake rate and a sample with an inclusive selection of electrons.

$Z/\gamma^* \to e\bar{e}$ Veto

Electrons appear in the detector as a narrow cluster in the electromagnetic calorimeter. They can be easily misidentified as 1 prong tau if no $\xi' \geq 0.1$ requirement is made (see Section 4.6.2). After the cut a contamination from misidentified electrons still remains.

We consider all jets with high electromagnetic energy fraction, $E_{HAD}/E_{EM} \geq 0.9$, in pseudorapidity region $|\eta| < 2$ as potential non identified electrons. Figure 6.1 represents the invariant mass spectrum of electron and electromagnetic jet pairs. The figure has been obtained using data taken in periods from 18 to 28 (3 fb^{-1}) requiring exclusively one tau and one electron without electric charge requirement. The Z resonance peak is evident and a continuum up to low invariant mass (≈ 10 GeV). The Drell-Yan processes with low invariant mass (≈ 5 GeV) are instead removed by the requirement of $\Delta R > 0.4$ between the electron and jet direction.

Some of the events in the continuum in Figure 6.1 may have genuine taus, so we remove only those events where the invariant mass is $86 \leq M_{inv} \leq 96$ GeV.

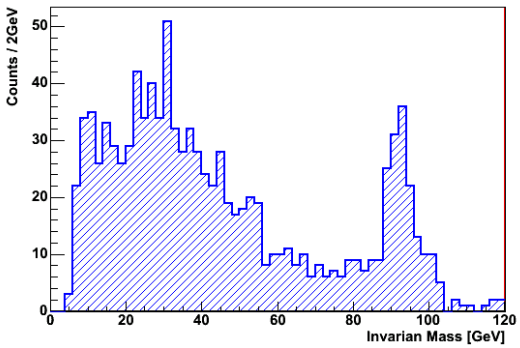

Figure 6.1: Invariant mass of the electron candidate and calorimeter clusters with electromagnetic fraction of 90%.

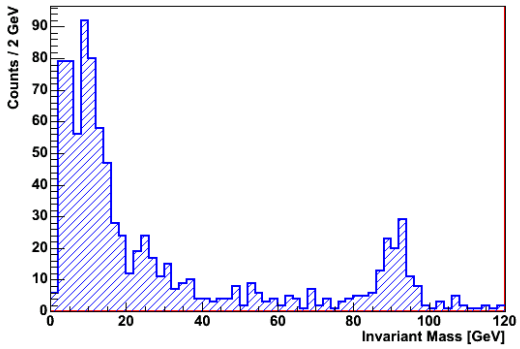

Figure 6.2: Invariant mass of the muon candidate and the tagged MIP.

$Z/\gamma^* \to \mu\bar{\mu}$ Veto

Muons originating from the $p\bar{p}$ collisions can traverse the CDF detector without leaving a stub in one of the muon chambers. This is due to both the gaps between muon detectors and the finite efficiency. For this reason muons can appear as isolated tracks traversing a calorimeter tower with small energy deposition.

We consider each MIP (defined in Section 4.5.1) as potential non-identified muon. We show in Figure 6.2 the invariant mass distribution of the system composed by the muon candidate and the MIP. The figure has been obtained using data taken in periods from 18 to 35 (5.5 fb^{-1}) requiring exclusively one tau and one muon without electric charge requirement on the two leptons. In the mass spectrum it is possible to identify the Z boson resonance and two other resonances at $\sim$ 10 GeV and $\sim$ 3 GeV corresponding respectively to the production of the Y and J/ψ.

We expect the MIP definition to select few tau decays in hadrons and the spectrum in Figure 6.2 shows a smaller continuum compared to the electron case in Figure 6.1. For this reason we applied a wider veto rejecting events with muon plus MIP invariant mass $76 \leq M_{inv} \leq 106$ GeV and $M_{inv} \leq 15$ GeV.

6.2.2 H_T Requirement

We then select events using a variable defined as scalar sum of the E_T of the objects in the event:

$$H_T = \not{E}_T + E_T^{tau} + \sum_i E_T^{jet_i}, \tag{6.1}$$

where E_T^{tau} is the cluster E_T of the tau decay products, $E_T^{jet_i}$ is the E_T of jet i passing the jet requirements. We do not include in H_T the E_T of the electron or p_T of the muon since this would favour single tau over ditau $t\bar{t}$ events. We require $H_T \geq 150$ GeV in the case of 1 prong taus and $H_T \geq 155$ GeV in the case of the 3 prong taus.

6.3 Result

We apply the selection reported in Section 6.2, 6.2.1 and 6.2.2 on all the MC samples summarized in Table 5.4, Table 5.1 and described in Section 5.2. We evaluate the expected number of events through the Formula 5.1.

We evaluate the background with fakes requiring at least a fakable tau object in the event. Each fakable tau object is then treated as a possible tau candidate and each event identified with a fakable object is required to pass the same cuts as for the signal selection. The events passing the selection are weighted by the probability of the jet to be misidentified as a tau.

After applying the selection we obtain the result summarized in Table 6.1. Figures 6.3, 6.4, 6.5 and 6.6 show the basic characteristic kinematic distributions of the samples. The figures correspond to the selection on the electron plus isolated track sample, CMUP and CMX muon plus isolated track samples and the sum over all the samples respectively.

The comparison of observed data events and the expected ones is already in agreement within the statistical uncertainty.

6.4 B-tag Requirement

The selected events still contain a severe contamination of events with fake taus and the irreducible background due to Drell-Yan processes in two taus. To remove the contamina-

Process	Muon Sample	Electron Sample	Total
Fakes	35.6 ± 1.5	63.9 ± 3.7	99.6 ± 4.0
$Z/\gamma^* \to \tau\tau$	43.3 ± 1.1	50.6 ± 1.2	94.0 ± 1.6
$Z/\gamma^* \to \ell\ell$	3.5 ± 0.3	3.5 ± 0.2	7.0 ± 0.4
Diboson	1.8 ± 0.2	2.4 ± 0.2	4.2 ± 0.3
$t\bar{t} \to \tau\ell + X$	23.7 ± 0.1	30.7 ± 0.1	54.5 ± 0.2
$t\bar{t} \to \tau\tau + X$	2.5 ± 0.0	3.2 ± 0.0	5.7 ± 0.1
Total Expected	110 ± 1.9	154 ± 3.9	265 ± 4.3
Observed	115	175	290

Table 6.1: Expected events and data events passing the kinematic selection.

tion we require at least one secondary vertex tag from the tight SECVTX algorithm (see Section 4.8.3).

The jets having a SECVTX tag could contain a contamination of light flavoured jets erroneously tagged as b induced jets, commonly called "mistags". In the computation of the expectations we use data, only to account for events with jets misidentified as taus, and MC simulated samples for other processes. The correct number of tags and mistags jets is naturaly obtained from the data samples, however for what concern the MC simulated samples we do not rely on the SECVTX selection of light flavoured jets. For this reason we implement a more sofisticated method.

We select jets in simulated events, which are matched in $\Delta R < 0.4$ with b flavoured hadrons. This class of jets is used to compute the number of genuine SECVTX tags. If the events have at least one genuine tag, it passes the selection. The jets not matched are considered as possible SECVTX mistags. The CDF Collaboration provides the probabily of jets to be mistagged, parametrized by a set of variables like the η of the jets and the number of multiple vertices in the event [53]. Eventually the events with light flavoured jets are weighted by the sum of all the mistag probabilities.

After applying this further requirement we obtain the result summarized in Table 6.2. Figure 6.7 shows the basic charactristic kinematic distributions of the events from all lepton categories.

We can notice in Figure 6.7 that most of the irreducible background is rejected, still a small fraction of Drell-Yan processes in tau is remaining. After the requirement of a tight SECVTX tag still we observe a non negligible expectation from events with fake taus. This stimulated us to investigate further the source of this background.

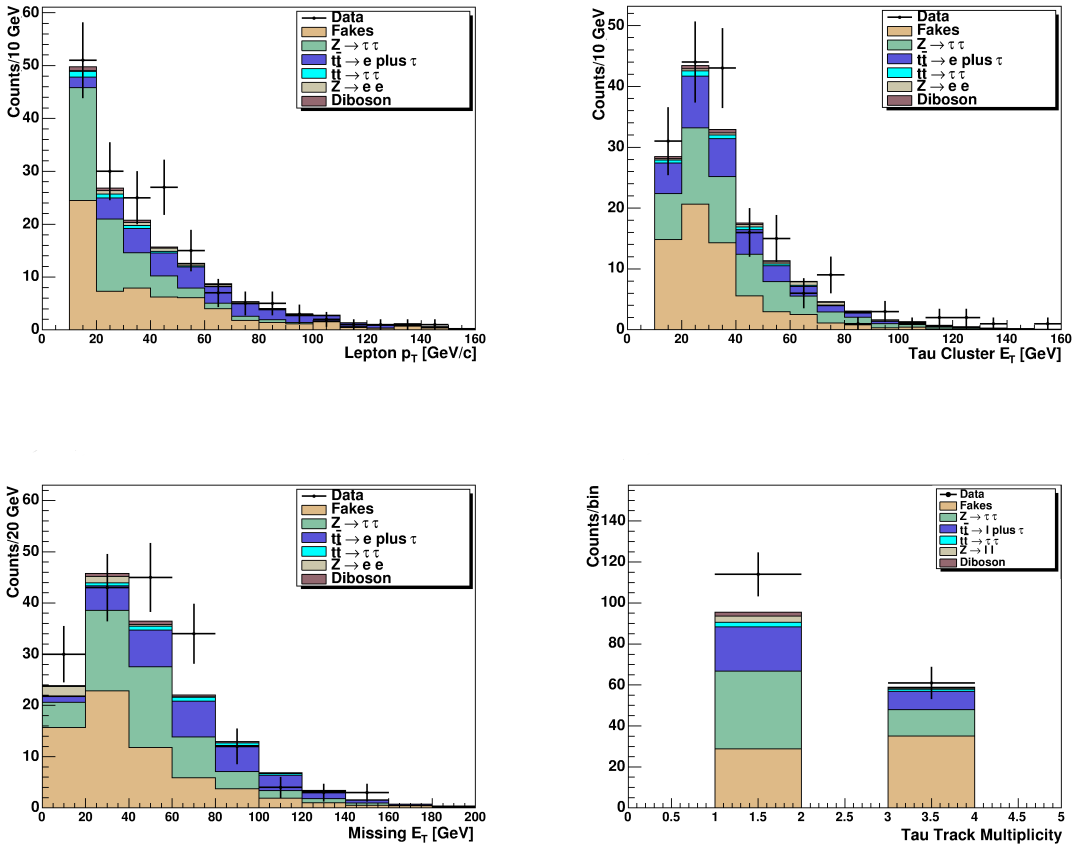

Figure 6.3: Distribution of CEM electrons E_T (top left), of tau cluster E_T (top right), $\not\!\!E_T$ (bottom left), and track multiplicity of tau induced jet (bottom right).

6.5 Study of the Background with Fake Taus

Before looking at the event kinematic to search for variables that allow us to distinguish signal and background we need to understand the origin of events with misidentified taus a bit more. Events with misidentified taus show high p_T electron or muon, missing transverse energy and a b induced jet (or an object being misidentified as such). Ignoring double misidentifications for a moment, the presence of a high p_T lepton and missing E_T suggest events to contain a W boson (or Z boson with one lepton not reconstructed). Moreover the transverse mass of the system composed by the lepton and the $\not\!\!E_T$, in Figure 6.8, shows a significant peak at the expected transverse mass of the W boson.

Three background sources come to mind: $t\bar{t}$ with only one top decaying into electron or

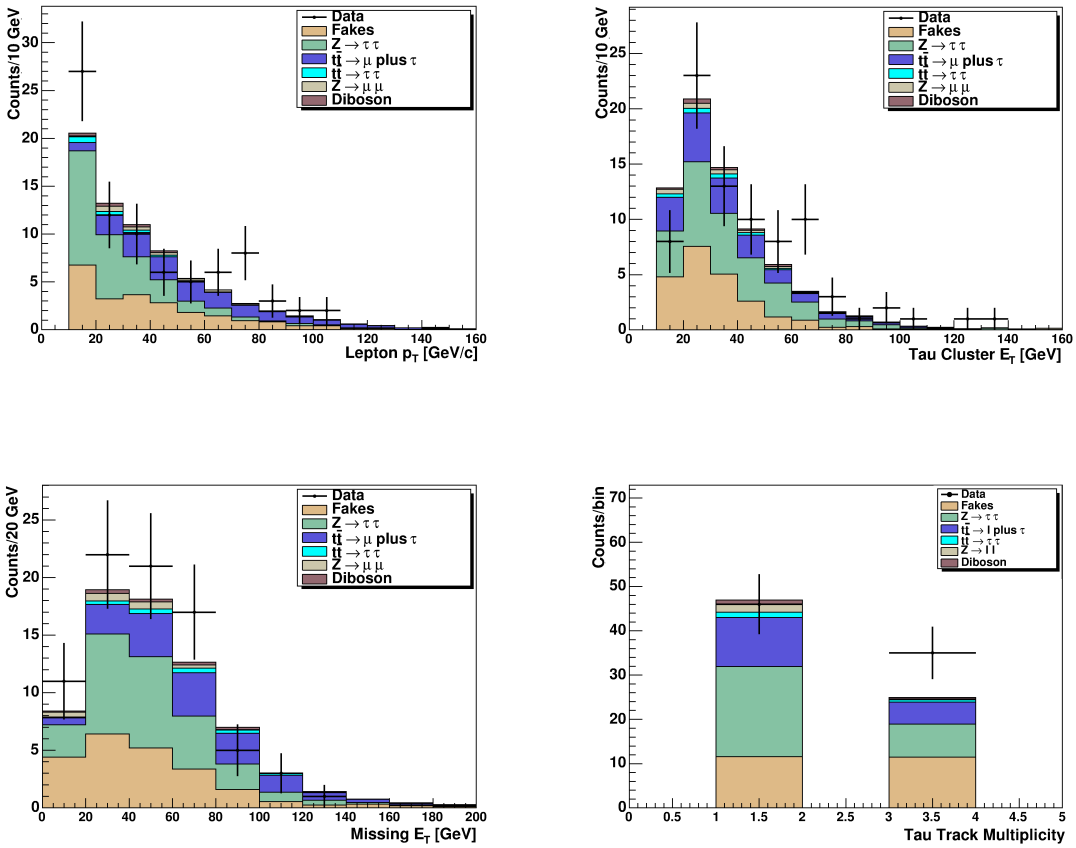

Figure 6.4: Distribution of CMUP muon p_T (top left), of tau cluster E_T (top right), $\not\!\!E_T$ (bottom left), and track multiplicity of tau induced jet (bottom right).

muon, single top production with decay into electron or muon and W plus $b\bar{b}$ production. In all cases we have one (or more) b induced jet. Single top has a small cross section and one b-jet compared to the two b-jets of $t\bar{t}$ and $W + b\bar{b}$, i.e. its contribution to the misidentified tau background should be smaller. Looking at double misidentification, a mistagged b-jet is more likely than a misidentified electron or muon. This points us again to W bosons but without b induced jet. The b induced jet mistag rate being significantly smaller than the b tagging efficiency suggests this background to not be larger than the W plus genuine b-jet contribution in the misidentified tau background.

To study in more detail the dominant contributions in the misidentified tau background we use a $t\bar{t}$ and $W + b\bar{b}$ Monte Carlo sample, reported in Table 6.3.

We restrict our study to events with one electron candidate and for each hadronic jet in

Process	**Muon Sample**	**Electron Sample**	**Total**
Fakes	5.47 ± 0.59	10.78 ± 1.63	16.25 ± 1.74
$Z/\gamma^* \to \tau\tau$	1.70 ± 0.09	2.17 ± 0.10	3.87 ± 0.14
$Z/\gamma^* \to \ell\ell$	0.15 ± 0.03	0.12 ± 0.01	0.26 ± 0.03
Diboson	0.11 ± 0.02	0.13 ± 0.03	0.24 ± 0.03
$t\bar{t} \to \tau\ell + X$	13.50 ± 0.10	17.46 ± 0.11	30.96 ± 0.15
$t\bar{t} \to \tau\tau + X$	1.44 ± 0.03	1.83 ± 0.04	3.27 ± 0.05
Total Expected	22.4 ± 0.6	32.5 ± 1.6	54.9 ± 1.7
Observed	18	40	58

Table 6.2: Expected events and data events passing the kinematic selection and the requirement of one tight SECVTX tag.

Process	**Inst. Lum.**	**Gen.**	**Size**	σ_{prod}
$W(\to \ell\nu_\ell) + b\bar{b} + 0p$	Low Lum.	Alpgen	1'541'000	4.1 pb
$W(\to \ell\nu_\ell) + b\bar{b} + 1p$	Low Lum.	Alpgen	1'546'000	1.2 pb
$W(\to \ell\nu_\ell) + b\bar{b} + (\geq 2p)$	Low Lum.	Alpgen	1'498'000	0.4 pb
$t\bar{t}$	All Lum.	Pythia	6'719'000	7.5 pb

Table 6.3: Monte Carlo samples used in this analysis.

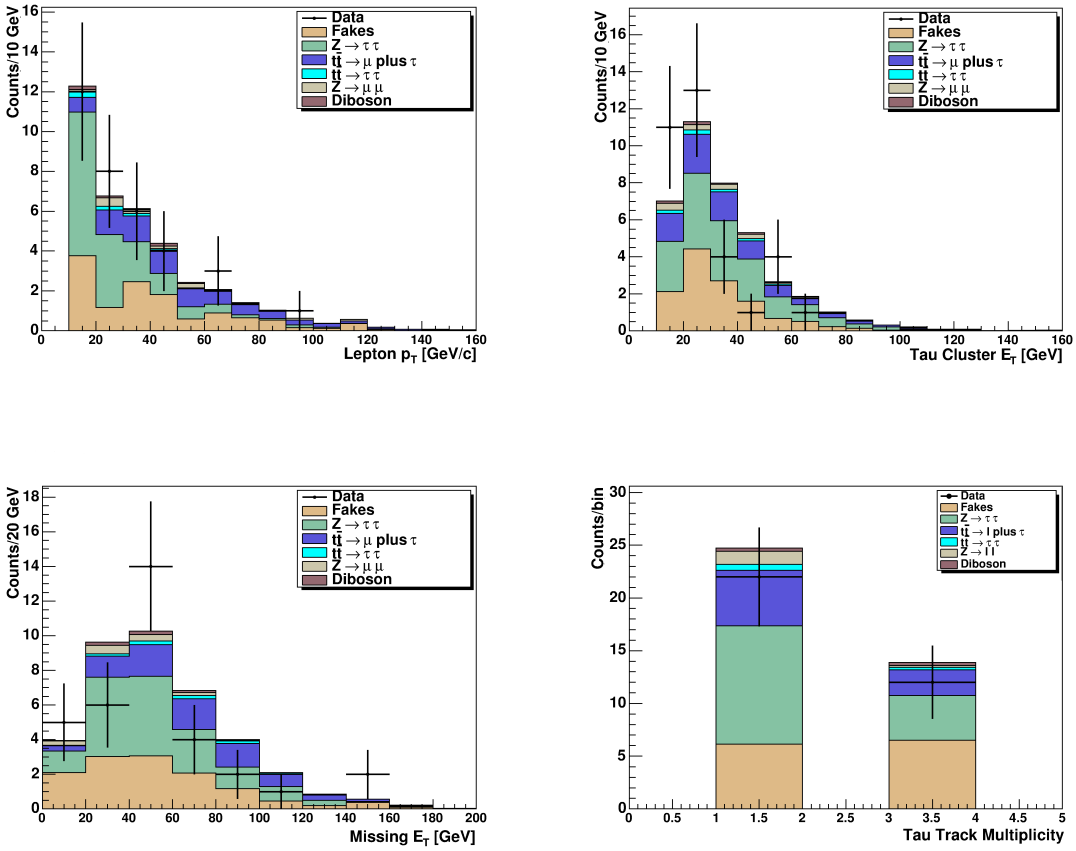

Figure 6.5: Distribution of CMX muon p_T (top left), of tau cluster E_T (top right), / E_T (bottom left), and track multiplicity of tau induced jet (bottom right).

the event, we look up the probability as calculated in Section 5.4.4 for it to be misidentified as hadronic tau. We treat the jet passing the fakable tau selection as tau candidate, weight the event by the probability and pass it through the selection and analysis program. In the case of $t\bar{t}$ an event has four chances passing selection and analysis: the two b-jets from the top decay and the two jets from the hadronic W decay could each be misidentified as tau. For the $W + b\bar{b}$ each of the two b-jets and any additional parton, from higher order production, could be misidentified as tau.

Table 6.4 shows the result. Before applying any b-tag we expect about 63.9 events with misidentified taus. Our study shows about 15.5 events to be due to single lepton $t\bar{t}$ and about 1.1 events to be due to $W + b\bar{b}$, i.e. only about a quarter of events is accounted for considering those two sources. After the one tight b-tag about 15.2 events are expected

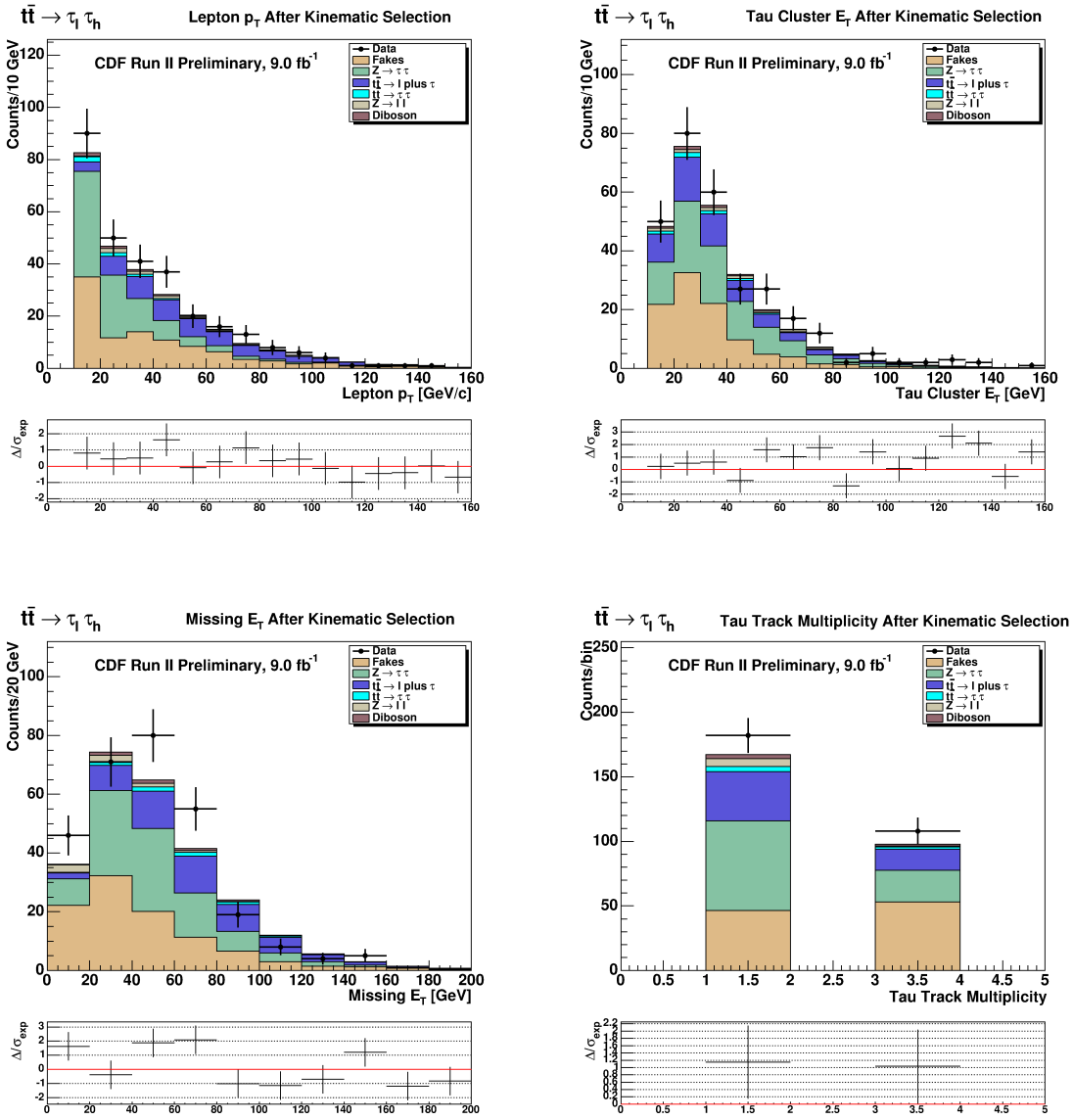

Figure 6.6: Distribution of electron E_T and muon p_T (top left), of tau cluster E_T (top right), $\not\!\!E_T$ (bottom left), and track multiplicity of tau induced jet (bottom right).

from misidentified taus. The two sources now account for over half of the events: about 8.83 events are expected from single lepton $t\bar{t}$ and about 0.42 events from $W + b\bar{b}$.

The study shows that the single largest contribution in the misidentified tau background comes from $t\bar{t}$ producton with one W decaying into electron or muon and the other

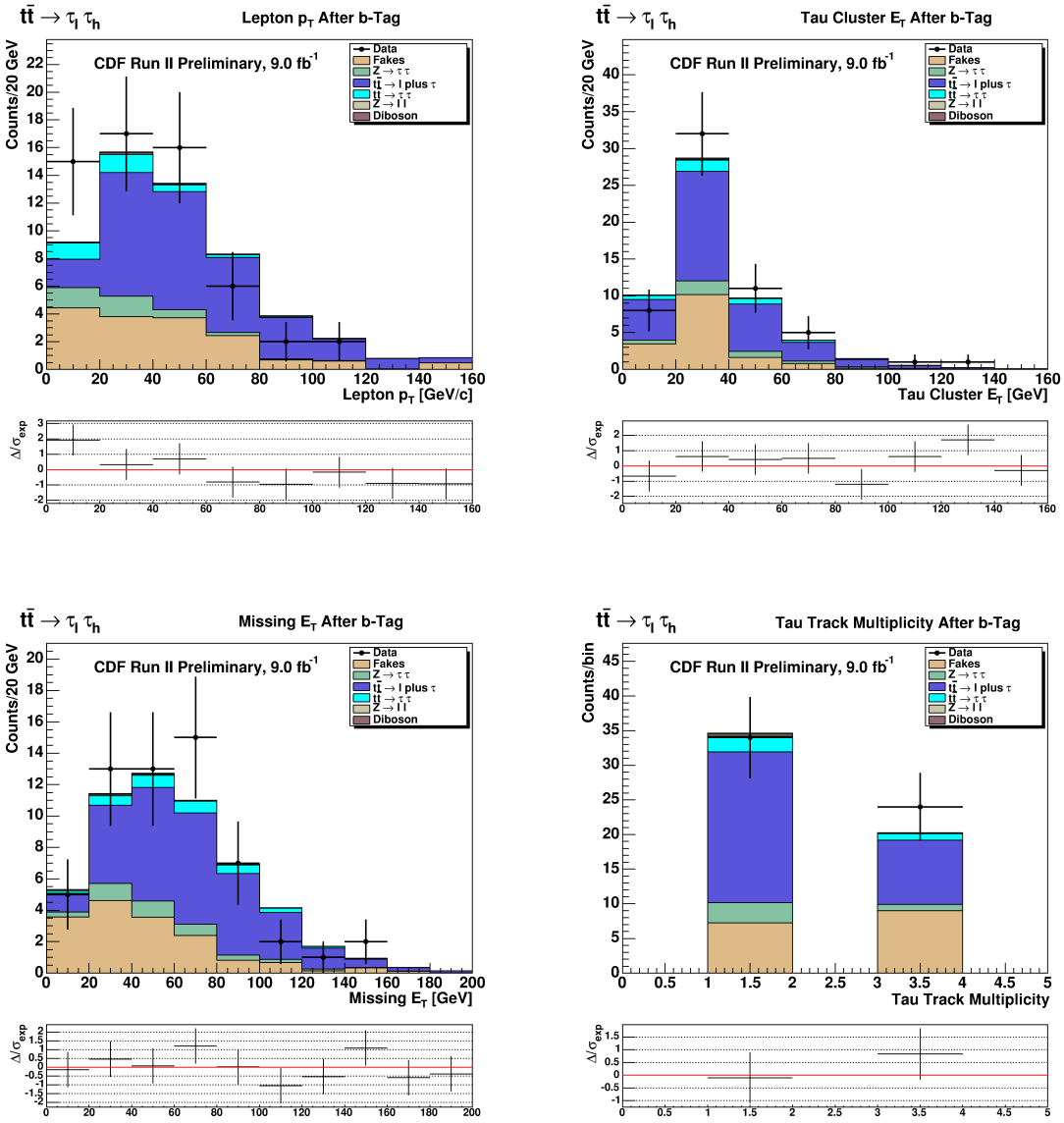

Figure 6.7: Distribution of electron E_T or muon p_T (top left), of tau cluster E_T (top right), $\not\!\!E_T$ (bottom left), and track multiplicity of tau induced jet (bottom right).

hadronically. While this is $t\bar{t}$ production, it is never-the-less background for our dilepton $t\bar{t}$ with tau analysis.

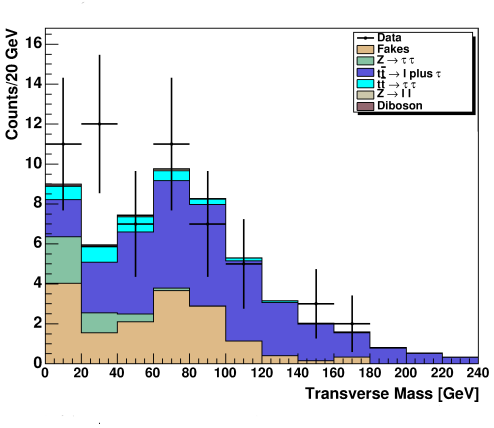

Figure 6.8: The transverse mass of the system composed by the electron or muon plus the $\not\!\!E_T$ of the event.

Samples	Pre SECVTX tag	1 loose SECVTX
$W(\rightarrow \ell\nu_\ell) + b\bar{b} + n \cdot p)$	1.11	0.42
$t\bar{t}$	15.5	8.83
Observed	63.9	15.2

Table 6.4: Monte Carlo samples used in this analysis.

6.6 Concluding Remarks

We note that the 58 events selected by our kinematic event selection and one tight b tag so far are dominated, about 34.8 events, by $t\bar{t}$ production with one top decaying into electron or muon and the other into tau. The second largest contribution is coming from misidentified taus, about 20.4 events. Drell-Yan production of tau pairs and $t\bar{t}$ with one electron or muon and one top into tau decay, about 4.1 and 3.6 events, are the next largest contributions. All other processes contribute less than an event.

In this chapter we have presented the kinematic selection of the events and the first comparison between the expected and observed events. The SECVTX b tag proved to be very useful to discriminate the background processes and we can reach a 60% purity of top pair production in the dilepton decay channel with a tau

We believe that a more sophisticated analysis can yield even better signal over square root of background. Before we can engage in such an analysis, we need to understand the precision of our signal and background prediction and evaluate the associated systematic uncertainties.

Chapter 7

Systematic Uncertainty

To interprete the result of our event selection we need to understand the sources that may have impacted it or may be inaccurately simulated in our Monte Carlo events. The systematic uncertainties we discuss in this chapter fall into three classes: uncertainties on the data measurement, uncertainties that affect the Monte Carlo simulations and uncertainties on theoretical calculations we use. The first and last of those classes impact mainly the total number of events (and cross section measurements) while uncertainties in the second class can also impact the shape of distributions we cut on or use to interpret the data.

7.1 Luminosity Measurement

The CDF experiment measures the luminosity with the Cherenkov Luminosity Counters, CLC. The acceptance of the counters and the inelastic $p\bar{p}$ cross section are the dominant uncertainties in the luminosity measurement. Our analysis uses both integrated luminosity (to convert observed events to a cross section measurement) and instantaneous luminosity (to estimate multiple interactions per beam-beam crossing). The total uncertainty on the luminosity measurements is 6%.

7.2 Uncertainty of Monte Carlo Samples

The event generators used to prepare the various samples that we use in this analysis approximate the physics processes to the best of our current understanding. The Monte Carlo techniques allow us to unfold the complex process of a proton-antiproton collision into more managable sub-processes of parton dynamics, hard scattering, particle decay, fragmentation and hadronization. However, our understanding of even all those subprocesses is incomplete or based on models, i.e. yields only a certain level of precision.

The detector simulation is based on a very detailed but never-the-less simplified model of the physical detector. The response of detector components is simulated based on test

beam measurements and models. Remaining differences that were found analysing mainly J/ψ, Z and jet data have been corrected. However, aging effects of the detector, pile up and exact material maps (including all the cabling) will leave small differences between simulation and physical detector.

7.2.1 Choice of Generator

This section describes the uncertainty of the theoretical and phenomenological models used to generate the particle interaction and the final state particles. For what concern the events of $t\bar{t}$ the crucial elements of the MC generation are:

- the *matrix element* of the parton interaction;
- the *parton distribution function* (PDF), the distribution of the momenta fraction of the initial state partons;
- the *color reconnection*, that represent the strong interaction among initial and final partons;
- the *initial* or *final state radiation* of gluons, radiated from the initial of final state partons respectively;
- the *parton showering* generated with phenomenological models to describe non perturbative QCD.

This analysis uses a PYTHIA MC sample which describes the interaction with a leading order matrix element and uses the parton showering to simulate higher order interaction. We studied the dependency on the showering model without evaluating the effect of the matrix element which is expected to not be significant. Therefore the major sources of possible systematic mismeasurement are the parton showering, color reconnection, parton distribution functions (PDFs), initial and final state radiation (ISR and FSR).

For the study of this systematics we used the samples that are listed in Table 7.1. The "standard" PYTHIA sample and the ones with more or less ISR/FSR are obtained with "Tune A" [66]. This tuning was implemented to describe the underlying events in the jet data from CDF Run I. The PYTHIA samples "Apro" and "ACRpro" are obtained with Tune A, including a tuning framework known as the "Professor" [67] to reproduce LEP, JADE and the Tevatron Run II data. Apro and ACRpro respectively exclude and include color reconnection description.

We present in the next section the variation of the selection efficiency due to the uncertainty on the different elements of the MC generator.

Tuning	Gen.	N. Events
Apro	PYTHIA	6'707'000
ACRpro	PYTHIA	6'715'000
more ISR/FSR	PYTHIA	2'798'000
less ISR/FSR	PYTHIA	2'801'000
standard	HERWIG	5'595'000
standard	PYTHIA	6'719'000

Table 7.1: $t\bar{t}$ Monte Carlo samples used signal selection systematics.

Parton Showering

The parton showering is modeled differently in the MC simulation. The differencies are evaluated simply by replacing the standard $t\bar{t}$ PYTHIA MC sample with another popular generator, HERWIG. For this study we use a PYTHIA sample different from the one used of our signal selection. Repeating the selection to obtain the selection efficiencies:

- $(2.24 \pm 0.05)\%$, electron sample with PYTHIA ($(1.94 \pm 0.05)\%$, muon sample);
- $(2.15 \pm 0.05)\%$, electron sample with HERWIG ($(1.80 \pm 0.05)\%$, muon sample);

We consider the efficiencies obtained not compatible with the statistic uncertainty. With a conservative assuption, we quote as systematic uncertainty propagated from the parton showering equal to 4% of the overall selection efficiency.

Color Reconnection

We measured the color reconnection systematic uncertainty replacing the standard $t\bar{t}$ PYTHIA MC samples with top mass 172.5 GeV and with two tuning: Apro and ACRpro. We compute again the efficiency measurement, but as these samples use different tune parameters than the standard PYTHIA 172.5 GeV $t\bar{t}$ MC, we do not compare the measured cross section to the nominal value. The measured efficiencies are:

- $(2.18 \pm 0.05)\%$, electron sample with tune Apro ($(1.91 \pm 0.05)\%$, muon sample);
- $(2.08 \pm 0.05)\%$, electron sample with tune ACRpro ($(1.79 \pm 0.05)\%$, muon sample);

We consider the efficiencies obtained are compatible in the statistic uncertainty. In this case we use the statistic uncertainty as estimate of the systematic uncertainty.

Initial and Final State Radiation

Gluons radiated from the incoming or outgoing partons of the interaction can generate extra jets in the event and modify the result of the selection. Indeed these jets can reduce the isolation of the leptons or modify the kinematic of the final state partons.

We use two $t\bar{t}$ PYTHIA MC samples with top mass 172.5 GeV. These samples have more ISR and FSR, and less ISR and FSR, since this processes are fully correlated in the QCD model. Repeating the selection on these samples the efficiency obtained is:

- $(2.02 \pm 0.06)\%$, electron sample, with more I/FSR ($(1.60 \pm 0.06)\%$, muon sample);
- $(1.93 \pm 0.06)\%$, electron sample, with less I/FSR ($(1.84 \pm 0.06)\%$, muon sample);

The measured efficiency is lower than the one obtained with the nominal PYTHIA sample and the tune of the MC simulation differs only by the emission of initial and final state radiation. For this reason we quote as systematic uncertainty the difference between the average efficiency of the PYTHIA sample on the different lepton categories and the average of the shifted samples. We symmetrize the result and we quote 8% systematic uncertainty on the nominal efficiency.

Our selected sample of data events is expected to contain ~ 10 events over a total of 58 events from top pair decays into electron or muon plus jets (as pointed out in Section 6.5). This class of events has a signature containing an additional jet. The E_T distribution of the third highest transverse energy jet is a possible discriminant and we can obtain a useful variable for the background discrimination. Figure 7.1 represent the transverse energy of the first most energetic, the second and the third jets from electron plus hadronic tau simulated events with more and less ISR and FSR. The first and the second jet are less energetic in the sample with increased ISR and FSR: as expected the final state partons radiate more gluons and loose part of their momentum. There are few third jets more in the sample with increased ISR and FSR and thus they will appear more similar to top pair events in electron or muon plus jet decay mode.

Particle Distribution Function

We determine the systematic uncertainty due to the uncertainty in the PDFs by using different sets: CTEQ5L considered as our standard, MRST72, MRST75, CTEQ6L, CTEQ6L1 and CTEQ6M. In the CTEQ6M we vary the 20 eigenvectors of the model by $\pm 1\sigma$, obtaining 40 different weights.

This systematic uncertainty is evaluated using only the MC sample used for the signal selection. The reweighting method is obtained extrancting the value of the momentum fraction of the initial state partons and getting the probability of finding those partons in such state. Then every event with its associated weight is used to compute the selection efficiency. Figure 7.2 represents the results of this study.

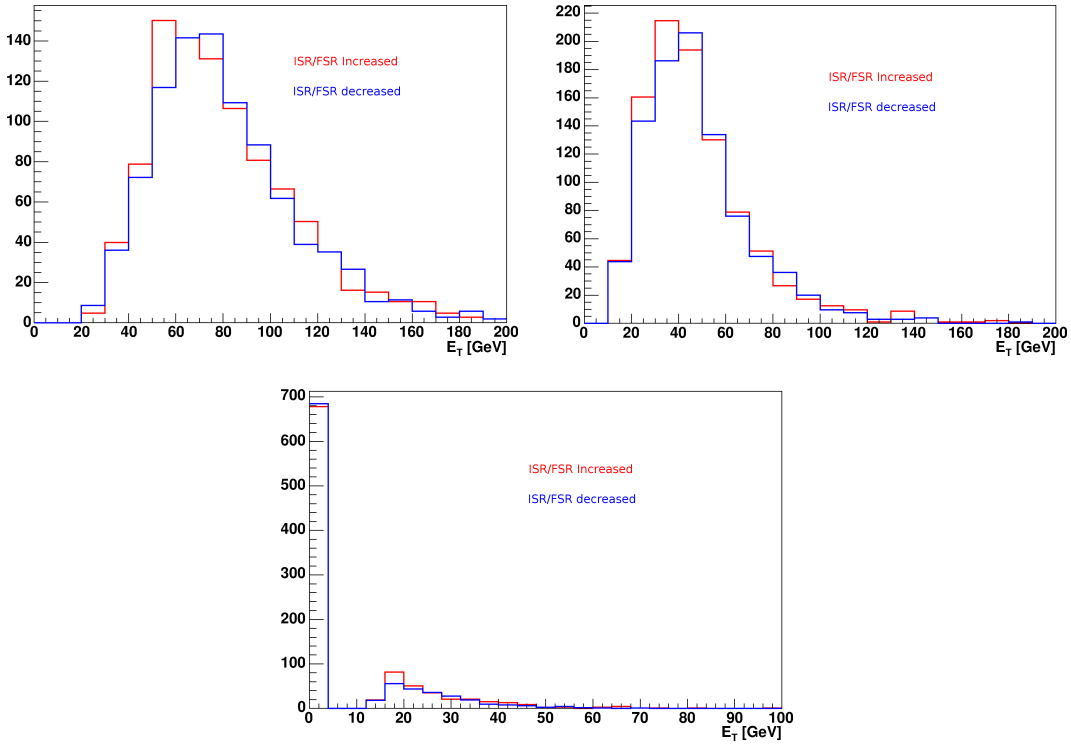

Figure 7.1: The transverse energy of the first most energetic jets (top left), the second jets (top right) and the third jets (bottom), from electron plus hadronic tau simulated events with more and less ISR and FSR.

We add in quadrature the difference between CTEQ6M 20 eigenvector result compared to the nominal value from the CTEQ6M. The sum of the different fluctuations is 0.21% for the ditau and 0.24% for the electron plus tau channel. The results obtained from the other PDFs are contained in a 0.5% difference from the nominal result.

7.2.2 Jet Energy Scale

We apply a set of jet energy corrections (JEC) to jets in data and in MC as described in Section 4.8.2. The different levels of corrections have been measured with uncertainties which propagate to the measurement of the selection efficiency. The different corrections are related to uncorrelated effects and therefore could be treated as uncorrelated. We can calculate the jet systematic uncertainty in two different ways: calculating the effect of individual jet uncertainties on the observables and later adding them in quadrature or adding all jet uncertainties in quadrature and calculate the effect of this shift. In our analysis we followed the second procedure.

The jets in the simulated events have actually different origins. The Drell-Yan events

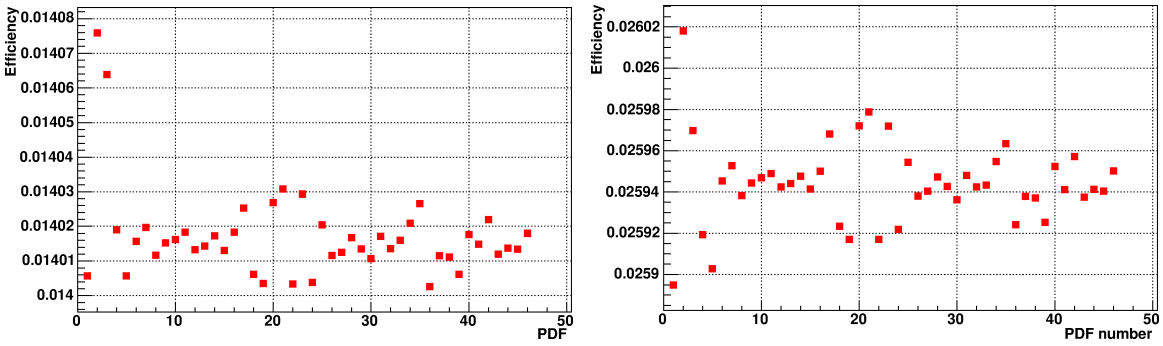

Figure 7.2: In both figures the values on the x axis refer to the PDFs used: CTEQ5L, MRST72, MRST75, CTEQ6L, CTEQ6L1, CTEQ6M plus 40 corresponding to the 20 eigenvectors fluctuated $\pm 1\sigma$. On the right the selection efficiency for the ditau channel (with one electron in the final state), on the left the result for the electron plus tau channel.

Process	**JEC Up** 1σ	**Nominal**	**JEC Down** 1σ
$Z/\gamma^* \to \tau\tau$	3.98 ± 0.14	3.87 ± 0.14	3.68 ± 0.14
$Z/\gamma^* \to \ell\ell$	0.27 ± 0.03	0.26 ± 0.03	0.25 ± 0.03
Diboson	0.25 ± 0.04	0.24 ± 0.03	0.24 ± 0.04
$t\bar{t} \to \tau\ell + X$	31.18 ± 0.15	30.96 ± 0.15	30.57 ± 0.15
$t\bar{t} \to \tau\tau + X$	3.30 ± 0.05	3.27 ± 0.05	3.22 ± 0.05

Table 7.2: Expected events passing the signal selection with the nominal jet energy correction and with $\pm 1\sigma$ shifted corrections.

contain jets generated by initial state radiation or underlying events. Differetly, diboson processes and top pair events contain jets for the event signature itself, and therefore the average transverse energy of the jets is higher. The overall uncertainty of the jet energy corrections slightly increases with the energy of the jets, from 2.0% and 2.5% in the energy range from 10 GeV to 200 GeV [52]. We do not expect significant variation of the selection efficiency at the $\pm 1\sigma$ variation of the JEC.

We require a minimum E_T in the jet selection, moreover the energy on the jets affect also the kinematic of the event, so we expect differences in the acceptance of the MC modeled processes representing the signal and the background. The systematic uncertainty is estimated by applying $\pm 1\sigma$ shifts to the energy scale. The results on the total expected events from MC is shown in Table 7.2, where we sum the result from the electron and muon samples.

We observe small fluctuations in the expected number of events, which, for the MC

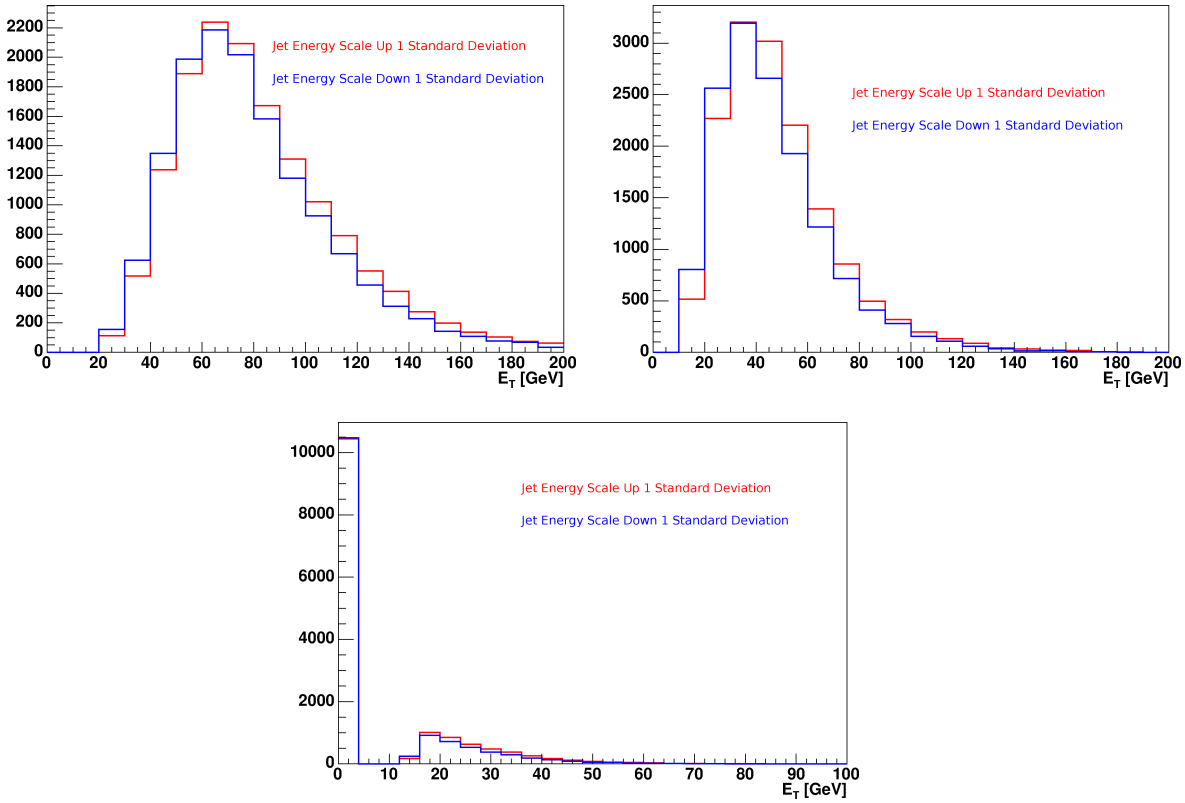

Figure 7.3: The transverse energy of the first most energetic jets (top left), the second jets (top right) and the third jets (bottom), from electron plus hadronic tau simulated events, with energy correction shifted $\pm 1\sigma$.

modeled backgrounds, are statistically compatible with the nominal result. We quote as systematic uncertainty the statistic uncertainty: 8% for $Z/\gamma^* \to \tau\tau$, 11% for $Z/\gamma^* \to \ell\ell$ and 15% for diboson prosesses. For what concerns the signal expectation, we quote a 2% and 3% uncertainty in the lepton plus tau and ditau processes respectively.

Figure 7.3 represents the transverse energy spectrum of the first, the second and the third most energetic jets, with energy correction shifted $\pm 1\sigma$. We observe in the histograms related to the third jet E_T few entries more when the energy correction is shifted up but no significant variation in the distributions.

The transverse energy of the third most energetic jet could represent, as discussed in the ISR and FSR related section, a potential background discriminant. As shown in Figure 7.3 the shift of the JEC modify slightly the result of a possible selection based on the third jet energy spectrum, since a higher jet energy correction increases the number of jets passing the minimal requirements. In general we expect a higher JEC to increase the selection efficiency and to increase the number of events with three jets but the rejection

based on the third jet energy spectrum will reject part of those events. A lower JEC would cause opposite effects, so the use of the third jet E_T spectrum would partially compensate the variation of the overall selection efficiency due to the shift of the JEC.

7.2.3 Secondary Vertex Tag

We explained in Section 6.3 the procedure to select events with the tight SECVTX tagging. The simulated event with genuine SECVTX tag should be reweighted by a scale factor equal to 96.0%, with a systematic uncertainty of 5%. The light flavor jets in the simulated events that could be mistagged by SECVTX are weighted by the mistag probability and in this case the systematic uncertainty is about 20%.

The total uncertainty is given by the sum over all the events of the systematic uncertainty of the tag and the mistag. The two uncertainties are considered related.

7.2.4 Pile Up

The number of primary vertices caused by beam interaction is proportional to the Tevatron instantaneous luminosity. The presence of multiple interactions generate a higher number of tracks and a higher activity in the calorimeter, which generally cause a degradation in the isolation requirements for leptons. The increase of instantaneous luminosity results in an overall decrease of the selection efficiency.

The evaluation of the uncertainty of the selection efficiency was done reweighting the MC events on the base of the primary vertex multiplicity. We generated the templates of vertex multiplicity in the signal $t\bar{t}$ MC and in the data. We considered two instantaneous luminosity regimes as lower and upper limits, one for data taken in periods from 0 to 17 and one in period from 18 to 28 respectively. For this purpose we used data events from the electron plus isolated track sample loosely selected requiring one tau and one electron.

The templates obtained from data are shown in Figure 7.4, together with a comparison between the low luminosity and MC template.

We run the selection using the low and high luminosity template and the template that represents the total data sample average (the nominal value). The numbers of MC events passing the selection are showed in Table 7.3.

We consider symmetric errors and we take conservative bounds of the propagation of the pile up systematic. We obtain $\pm 2.5\%$ uncertainty for the lepton plus tau channel and $\pm 3\%$ for the ditau channel.

7.2.5 Tau Related Systematics

The systematics we consider related with the tau lepton selection are of three type. The first is relative to the fake rate measurement and propagates into the expected number of events with fakes. The second is related to the uncertainty on the scale factors to be

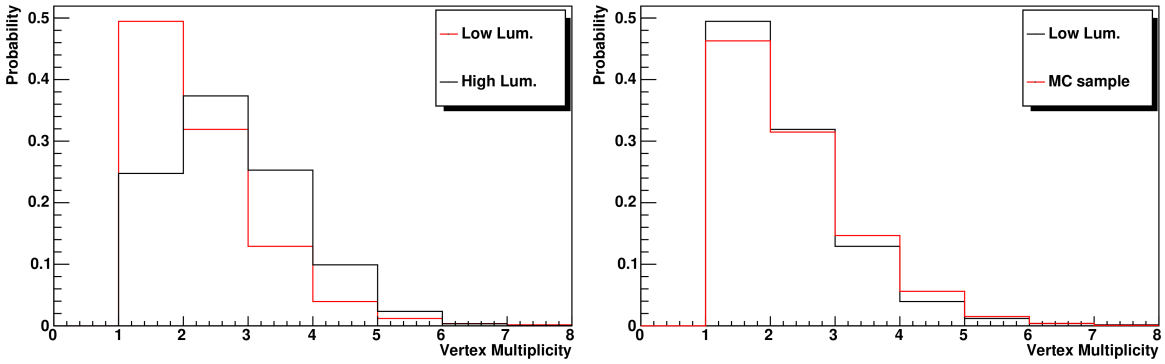

Figure 7.4: Vertex multiplicity distribution for data taken in periods from 0 to 17, and periods 18 to 28 (left); vertex multiplicity in MC and data periods from 0 to 17 (right).

Process	**High Lum.**	**Nominal**	**Low Lum.**
$t\bar{t} \to \tau e + X$	15323 (-0.4%)	15380	15495 (+0.7 %)
$t\bar{t} \to \tau\tau_e + X$	1557 (-1.1%)	1574	1607 (+2.1%)
$t\bar{t} \to \tau\mu + X$	13359 (-2.0%)	13631	13939 (+2.3%)
$t\bar{t} \to \tau\tau_\mu + X$	1389 (-2.2%)	1420	1456 (+2.5%)

Table 7.3: Simulated events passing selection with low, nominal and high vertex multiplicity templates .

multiplied to the estimate from MC. The last systematic uncertainty is the uncertainty in the energy scale of the tau cluster of the hadronic calorimeter towers.

We show in Appendix B how the tau fake rate with its systematic uncertainty well describes the sample in two control regions, one QCD dominated and one W plus jet dominated. The systematic uncertainty of the fake rate propagates in the evaluated number of events with fakes passing the selection:

- $10.8 \pm 1.6^{+0.8}_{-2.3}$, for the electron sample;
- $5.5 \pm 0.6^{+0.3}_{-1.0}$, for the muon sample.

Another source of systematic is described in Section B.1. It is due to the measurement of the acceptance correction for the trigger selection for the "calibration electron" sample. The trigger requires the electron trigger primitive to have $E_{HAD}/E_{EM} \leq 0.055$, which is tighter than the identification requirement $E_{HAD}/E_{EM} \leq (0.055 + 0.00045 \times E)$. We estimate the correction factor, equal to 1.04, to be affected by a $\sim 2\%$ uncertainty.

Process	**Hadr. Scale** +5%	**Nominal**	**Hadr. Scale** −5%
$Z/\gamma^* \to \tau\tau$	3.89 ± 0.14	3.87 ± 0.14	3.84 ± 0.14
$Z/\gamma^* \to \ell\ell$	0.27 ± 0.03	0.26 ± 0.03	0.26 ± 0.03
Diboson	0.24 ± 0.04	0.24 ± 0.04	0.24 ± 0.04
$t\bar{t} \to \tau\ell + X$	31.04 ± 0.15	30.96 ± 0.15	30.88 ± 0.15
$t\bar{t} \to \tau\tau + X$	3.28 ± 0.05	3.27 ± 0.05	3.26 ± 0.05

Table 7.4: Expected events passing the signal selection with the nominal tau hadronic energy scale (+10%) and with ±5%.

The scale factors we apply on the MC selection is obtained from previous studies [47] since our tau identification requirements differ only for the tau seed track p_T (8 GeV/c for taus selected in the muon plus isolated track samples) and the cluster E_T. No scaling is applied for the requirement of the seed track since the effect is negligible.

For what concern the tau cluster E_T we rescaled the fraction of the energy collected by the hadronic calorimeter by ±5%. We obtained in this way the evaluation of the effects of the systematic uncertainty of the tau hadronic scale, which are summarized in Table 7.4.

The results with the shifted tau transverse energies are compatible with the ones with the nominal value. We use the statistical uncertainty as estimate of the effect on this systematic uncertainty.

7.3 Cross Section

A source of systematic uncertainty is the uncertainty of the cross section assigned to each physics process estimated with MC samples. The MCFM program [68] has been used to compute a NLO calculation for the diboson processes (WW, WZ and ZZ) [69]. It has an uncertainty of 6%. The experimental uncertainty of Drell-Yan events is obtained from a recent CDF result [64]. We assign an uncertainty of 15% to this class of processes deriving from the LO and NLO comparison in the two jet bin multiplicity.

7.4 Summary of Systematics

Table 7.5 summarizes the uncertainty in the selection efficiency due to the propagation of the systematic uncertainties. We will describe in the next chapter the multivariate technique to reject the background with fakes and the evaluation of the effects of the systematic uncertainties after this additional step.

Process	$Z/\gamma^* \to \tau\tau$	$Z/\gamma^* \to \ell\ell$	**Diboson**	$t\bar{t} \to \tau\ell + X$	$t\bar{t} \to \tau\tau + X$	**Fakes**
Trigger	±3%	±3%	±3%	±3%	±3%	±3%
Cross Section	±15%	±15%	±6%	–	–	–
PDF	–	–	–	±0.5%	±0.5%	–
Showering	–	–	–	±4%	±4%	–
Color Recon.	–	–	–	±3%	±3%	–
ISR/FSR	–	–	–	±8%	±8%	–
Pile Up	–	–	–	±2.5%	±3%	–
JEC	±8%	±11%	±15%	±2%	±3%	–
τ E_T scale	±4%	±11%	±15%	±0.5%	±1.5%	–
τ ID scale	±3%	–	±3%	±3%	±3%	–
SECVTX Tag	±5%	±5%	±5%	±5%	±5%	–
SECVTX Mistag	±20%	±20%	±20%	–	–	–
Fake Rate	–	–	–	–	–	$^{+7\%}_{-20\%}$

Table 7.5: The summary table of the systematic uncertainties.

Chapter 8

Results

Knowing the limits of our Monte Carlo simulations, tau misidentification and data, we can resume our selection of top pair production in the dilepton channel with a tau and rejection of background. For this we will employ a log-likelihood method to discriminate our signal from the largest remaining background in the selection, misidentified taus. The result will be used to derive a $t\bar{t}$ cross section times branching ratio measurement. To obtain from this measurement a top into tau, neutrino and b-quark branching ratio we assume the top into electron or muon, neutrino and b branching ratio to be equal to the branching ratio of W into electron or muon plus neutrino and use for the $t\bar{t}$ production cross section the CDF measurement based on electron and muon events.

Our data sample contains two $t\bar{t}$ contributions: where one top decayed into electron or muon and the other into tau (lepton plus tau) and where both top quarks decayed into taus. If we are able to separate the two channels we can measure the top into tau, neutrino and b-quark branching ratio more directly (or more precise the difference between $BR(t \to e/\mu\nu b)$ and $BR(t \to \tau\nu b) \cdot BR(\tau \to e/\mu\nu\nu)$ without depending on the $t\bar{t}$ production cross section. We will construct a second log-likelihood function to separate lepton plus tau and di-tau channels.

New physics, like the presence of a charged Higgs boson, can enhance the branching ratio of top into tau. We use our branching ratio measurement to place limits on a charged Higgs contribution in top decays.

8.1 Likelihood Discriminant

We now know the uncertainties of the kinematic and b-tagging selection described in Chapter 6 and can proceed to a more detailed study of the sample. Table 8.1 summarized the number of expected events of our selection.

To separate $t\bar{t}$ production in the dilepton decay channel with tau from the main background of misidentified taus, we look for variables that distinguish the two sources. The

Process	Muon Sample	Electron Sample	Total
Fakes	$5.47 \pm 0.59^{+0.34}_{-0.98}$	$10.78 \pm 1.63^{+0.83}_{-2.29}$	$16.25 \pm 1.74^{+1.17}_{-3.27}$
$Z/\gamma^* \to \tau\tau$	$1.70 \pm 0.09 \pm 0.37$	$2.17 \pm 0.10 \pm 0.47$	$3.87 \pm 0.14 \pm 0.85$
$Z/\gamma^* \to \ell\ell$	$0.15 \pm 0.03 \pm 0.04$	$0.12 \pm 0.01 \pm 0.03$	$0.26 \pm 0.03 \pm 0.07$
Diboson	$0.11 \pm 0.02 \pm 0.03$	$0.13 \pm 0.03 \pm 0.03$	$0.24 \pm 0.03 \pm 0.06$
$t\bar{t} \to \tau\ell + X$	$13.5 \pm 0.96 \pm 1.62$	$17.4 \pm 0.11 \pm 2.10$	$30.96 \pm 0.15 \pm 3.73$
$t\bar{t} \to \tau\tau + X$	$1.44 \pm 0.03 \pm 0.18$	$1.83 \pm 0.04 \pm 0.23$	$3.27 \pm 0.05 \pm 0.41$
Total Expected	$22.4 \pm 0.6^{+1.7}_{-2.5}$	$32.5 \pm 1.6^{+2.3}_{-3.8}$	$54.9 \pm 1.7^{+3.9}_{-6.3}$
Observed	18	40	58

Table 8.1: Expected events and data events passing the kinematic selection and the requirement of one tight SECVTX tag.

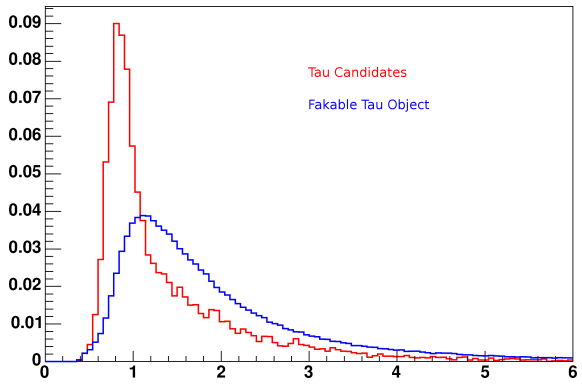

Figure 8.1: Ratio between cluster energy and the modulus of sum of the track momenta of taus and fakable tau objects. The distributions are obtained with simulated top pair events in the dilepton decay mode with electron and hadronic tau, and electron plus jet events.

two tau identification variables most sensitive to misidentified taus are the $E^{Cluster}/p$ and tau isolation, Σp_T^{iso}.

We expect the jets from W decay into quarks to have a different fraction of neutral hadrons compared to the jet induced by tau decay. For this reason the ratio between the energy in the calorimeter and the sum of the track momenta is expected to be different. In Figure 8.1 we present the ratio of the calorimeter cluster energy and the modulus of the sum of the track momenta of taus and fakable tau objects. The distributions are obtained with simulated top pair events in the dilepton decay mode with electron and hadronic tau, and electron plus jets events. The distribution of this variable looks promising for separating signal from background events.

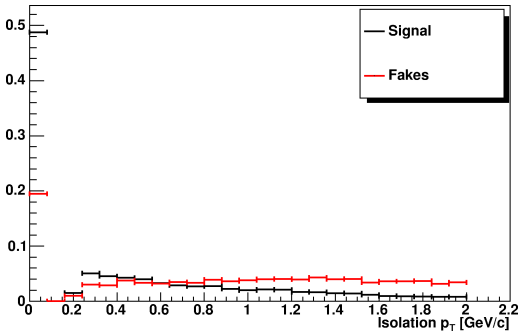

Figure 8.2: The transverse momentum of the tracks in the tau isolation cone; tau candidate distribution from simulated events, fakable tau distribution from data events.

We expect the track based tau isolation of misidentified taus to be distributed differently than for genuine taus. Although the identification requirements impose the QCD jets to have invariant mass and track multiplicity similar to real taus, they are produced along with soft emission of hadrons from radiated gluons. This soft radiation enters usually in the isolation annulus of the reconstructed tau.

We now look at the kinematic of those single lepton $t\bar{t}$ events and identify variables to distinguish them from our signal events. Figure 8.3 shows sketches of a top quark decay into electron plus tau, di-tau and in single electron mode. In the top pair decay in single lepton mode there is an additional jet from the W boson decay into quarks and moreover the dilepton decay processes involving tau induced jets have 2 or 4 more neutrinos. For these reasons we expect

- the missing transverse energy,
- the transverse mass of the electron plus $\not\!\!E_T$ system, $M_T(e, \not\!\!E_T)$ and
- the transverse energy of the third highest E_T jet,

to be the most significat variables to discriminate the signal $t\bar{t}$ process from the lepton plus jet decay modes.

Figure 8.4 shows the distribution of the missing transverse energy and the transverse mass of the electron plus $\not\!\!E_T$ for signal and background $t\bar{t}$ events. Figure 8.5 shows the third jet E_T distributions. The distributions are obtained with the two samples of top pair simulated events: the $t\bar{t}$ sample in Section 5.2 for the signal events and the sample of $t\bar{t}$ events in Table 6.3 filtered to have single electron plus jets. We requires the event to pass the selection as stated in Section 6.2 including the request of one SECVTX tight tag. The distributions in Figure 8.4 and 8.5 are normalized to unit area.

We have now E_{tot}/p, Figure 8.1, and tau isolation defined Σp_T^{iso}, Figure 8.2, along with the kinematic variable above listed to be the useful discriminating variables for our

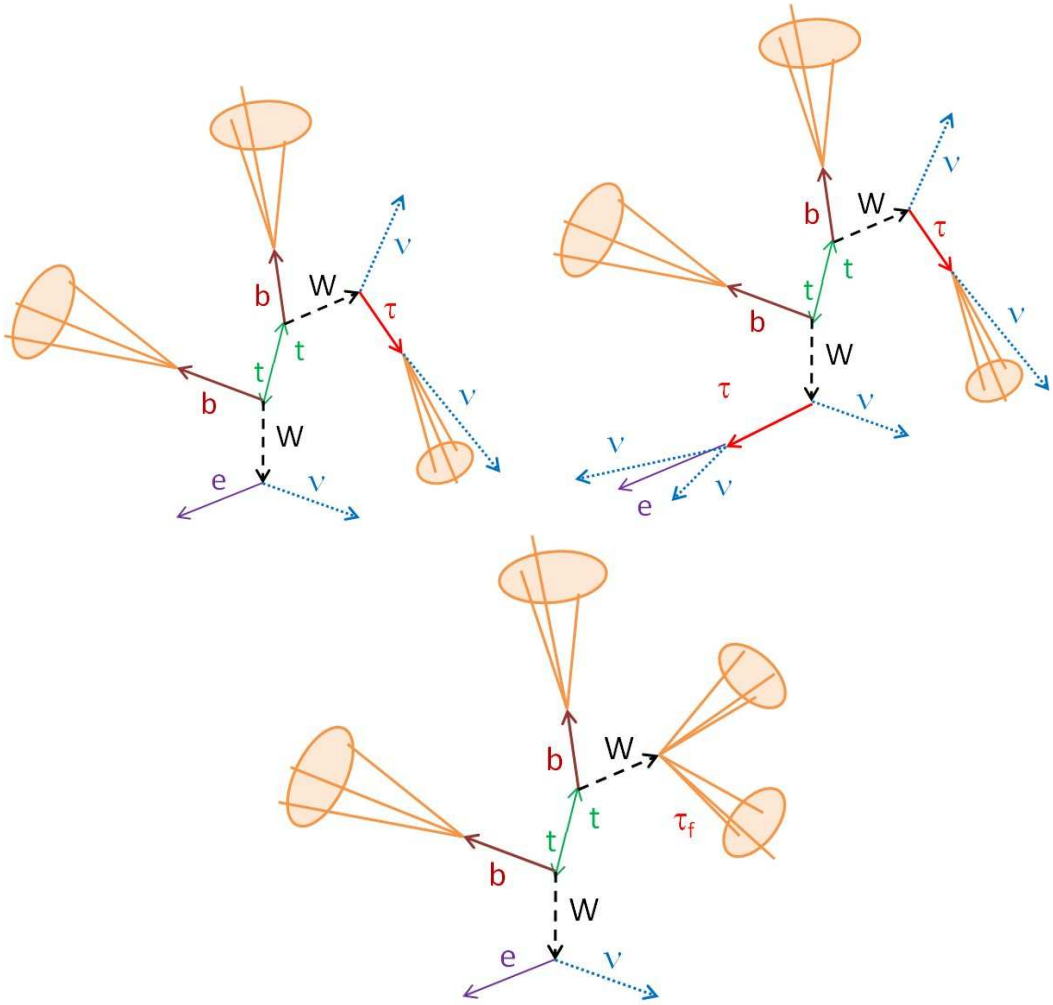

Figure 8.3: Sketches of top pair decay in electron plus tau mode (left) di-tau mode (right) and in single electron mode (below).

background rejection.

At this stage of the analysis the use of sequential one dimensional cuts can not provide an efficient signal selection: we have already exploided the most significant properties of the top pair decay kinematic to define the cuts for the background rejection. At the same time a selection based on the definition of multidimentional areas requires large samples of event, to well define the efficiency of the signal extraction and rejection of the background.

We decided to exploit all the information available in a multivariate technique instead of a cut based selection. A typical class of techniques is represented by the so called *Artificial Neural Networks* (ANN) consisting of an interconnected group of nodes, or *neurons*,

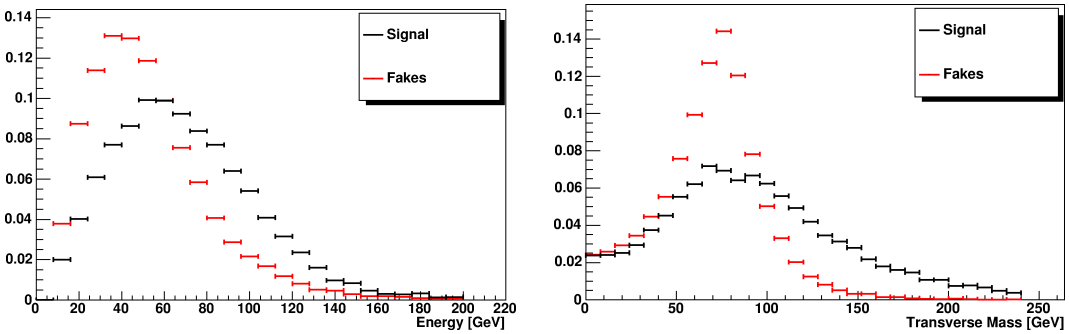

Figure 8.4: The module of the missing transverse energy (right); the transverse mass of the electron plus $\not\!\!E_T$ system (left).

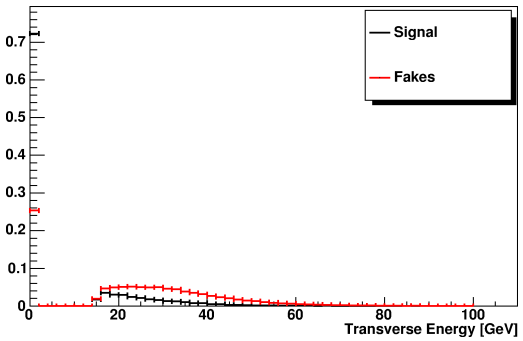

Figure 8.5: The transverse energy of the third highest E_T jet.

which compute the outputs from the input variables and trasfer the output through some nonlinear activation functions. The ANN is powerful technique, which is able to exploit the correlations among variables to increase the separation between signal and background events. The disadvantage of the ANN's is the need to be trained with large signal and background samples. The tool itself represents a "black box" not well described with analytic relations, the stability of the selection result has to be carefully checked. The trained ANN are a has to be tested with independent samples to ensure that the selection efficiency is consistent among the same type of samples, i.e. to exclude an "overtraining" of the tool. For this reasons we decided to not use such a tool.

We implemented in our analysis a Likelihood based selection. This method represents an alternative powerful method for discriminating signal events. It combines in a single distribution the information provided by different characteristic variables. The method we implemented does not make use of the correlation between the input variables, but uses their *probability distribution functions* (*pdf*) obtained with the projections of the event variables on the axis of the single observables. The method we implement is known as *log-*

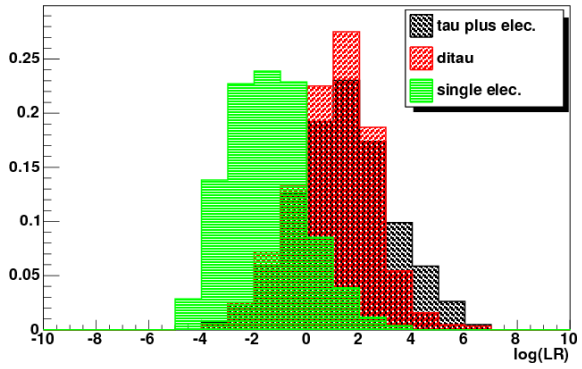

Figure 8.6: Distributions of the variable $\ln(LR)$ for events from top pair decay into electron plus hadronic tau, di-tau with one electron from tau decay and single electron mode.

likelihood ratio (LLR) discriminant: the tool is easily obtained combining one-dimensional distribution templates of background and signal events.

In a multidimensional space, events are represented by vectors $\vec{x} = (x_1, ..., x_n)$, where the coordinates are the observed variables characterizing it. Supposing two hypothesys, H_0 or H_1, related to the signal and background processes, the events $\vec{x}$ are distributed with *pdf*'s $p_0^i(x^i)$ and $p_1^i(x^i)$, where $i = 1, ..., n$. We define LLR in the following way:

$$\ln(LR) = \ln\left(\frac{P_0(\vec{x})}{P_1(\vec{x})}\right), \tag{8.1}$$

where the $P_0(\vec{x})$ and $P_1(\vec{x})$ are defined

$$P_0(\vec{x}) = \prod_{i=1,...,n} p_0(x^i), P_1(\vec{x}) = \prod_{i=1,...,n} p_1(x^i), \tag{8.2}$$

The *pdf*'s we used are the binned distributions in Figure 8.4: the third jet E_T, in Figure 8.5 and the tau identification variables in Figure 8.2 and Figure 8.1. We obtain those *pdf*'s requiring the event to pass the selection reported in Section 6.2 including the request of one SECVTX tight tag. Each hadron jet in the single electron decay channel is required to pass the fakable tau object selection. All the distributions used are normalized.

We use the LLR ($\ln(LR)$) as a discriminating variable, and we expect the signal events to cumulate in the positive region and background event in the negative region.

Figure 8.6 shows the distribution of the variable $\ln(LR)$ for the background events of top pair in single electron mode and top pair in dileptonic decay modes with an electron and a tau jet.

We can derive from the distribution in Figure 8.6 that the requirement $\ln(LR) \geq 0$ removes $\sim$ 86% of the background, while having $\sim$ 79% efficiency in selecting the top decay mode in electron plus tau and $\sim$ 77% efficiency in the di-tau channel with electron.

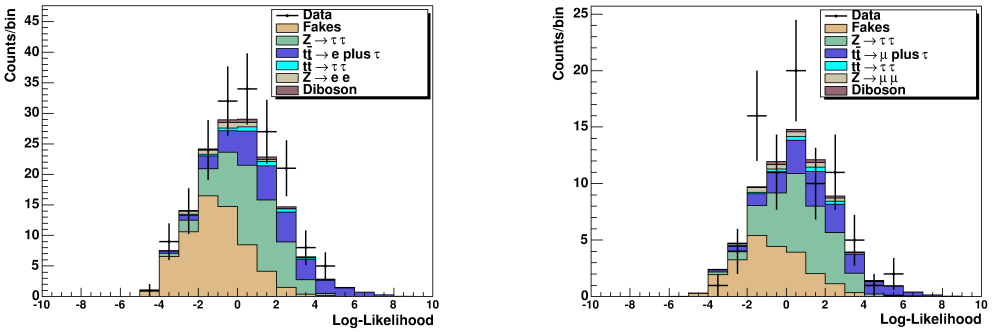

Figure 8.7: Validation plots of $\ln(LR)$ distribution using samples with electron (right) and with CMUP muon. Selection without SECVTX tag requirement.

We applied $\ln(LR) \geq 0$ both for the sample with electrons and the sample with muons.

We show in Figure 8.7 the comparison between the distribution of $\ln(LR)$ in data and expectated events. We show separately electron and CMUP muon samples, with the selection requirements reported in Section 6.2 before the SECVTX tag.

We show in Figure 8.8 the comparison between data and expectation for the full data sample, before and after the SECVTX tag. The modelling of the data events looks in excellent agreement with in the statistical uncertainty.

The results obtained with the likelihood selection is summarized in Figure 8.9. It is possible to notice a significant reduction of the background with fake taus.

8.2 Systematic Uncertainties

We analyzed the propagation of the systematic uncertainties on the expected number of events after the LLR discrimination. We applied the same methods we already described in the Chapter 7 and Table 8.2 summarizes the uncertainty in the selection efficiency for each systematic uncertainty. We did not find relevant differences from the results shown in Table 7.5.

The expected events from background and signal processes are summarized in Table 8.3, where we report the propagation of systematic uncertainties. After the requirement $\ln(LR) > 0$ described in the previous section, a significant reduction can be noticed in the number of background events with fake taus.

We just described the selection we implemented and the evaluation of the errors due to systematic uncertainties. We continue now to describe, the next steps of our analysis: the measurement of the top pair cross section and branching ratio of top decaying into tau, neutrino and b quark.

Process	$Z/\gamma^* \to \tau\tau$	$Z/\gamma^* \to \ell\ell$	**Diboson**	$t\bar{t} \to \tau\ell + X$	$t\bar{t} \to \tau\tau + X$	**fakes**
Trigger	±3%	±3%	±3%	±3%	±3%	±3%
Cross Section	±15%	±15%	±6%	–	–	–
PDF	–	–	–	±0.5%	±0.5%	–
Showering	–	–	–	±3%	±3%	–
Color Recon.	–	–	–	±4%	±4%	–
ISR/FSR	–	–	–	±9%	±9%	–
Pile Up	–	–	–	±2.5%	±3%	–
JEC	±9%	±20%	±20%	±2%	±3%	–
τ E_T scale	±4%	±20%	±20%	±0.5%	±1.5%	–
τ ID scale	±3%	–	±3%	±3%	±3%	–
SECVTX Tag	±5%	±5%	±5%	±5%	±5%	–
SECVTX Mistag	±20%	±20%	±20%	–	–	–
Fake Rate	–	–	–	–	–	$^{+7\%}_{-20\%}$

Table 8.2: The summary table of the systematic uncertainties.

Process	**Muon Sample**	**Electron Sample**	**Total**
Fakes	$1.80 \pm 0.31^{+0.13}_{-0.31}$	$2.20 \pm 0.64^{+0.18}_{-0.48}$	$4.01 \pm 0.71^{+0.31}_{-0.80}$
$Z/\gamma^* \to \tau\tau$	$1.12 \pm 0.07 \pm 0.25$	$1.41 \pm 0.08 \pm 0.29$	$2.53 \pm 0.11 \pm 0.53$
$Z/\gamma^* \to \ell\ell$	$0.10 \pm 0.03 \pm 0.03$	$0.03 \pm 0.01 \pm 0.01$	$0.13 \pm 0.03 \pm 0.04$
Diboson	$0.09 \pm 0.02 \pm 0.03$	$0.09 \pm 0.02 \pm 0.03$	$0.17 \pm 0.03 \pm 0.05$
$t\bar{t} \to \tau\ell + X$	$10.56 \pm 0.08 \pm 1.34$	$13.73 \pm 0.10 \pm 1.75$	$24.29 \pm 0.13 \pm 3.09$
$t\bar{t} \to \tau\tau + X$	$1.07 \pm 0.03 \pm 0.14$	$1.37 \pm 0.03 \pm 0.18$	$2.44 \pm 0.04 \pm 0.32$
Total Expected	$14.7 \pm 0.3^{+1.6}_{-1.7}$	$18.8 \pm 0.6^{+2.1}_{-2.1}$	$33.6 \pm 0.7^{+3.7}_{-3.8}$
Observed	12	24	36

Table 8.3: Expected events and data events passing the kinematic selection plus the requirements of one tight SECVTX tag and $\ln(LR) > 0$.

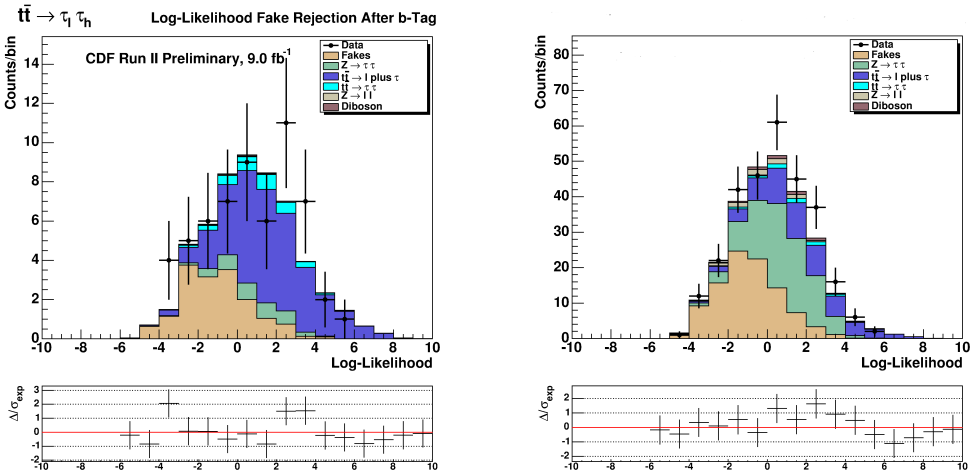

Figure 8.8: Validation plots of $\ln(LR)$ distribution using electron and muon samples. On the right there is no requirement of a SECVTX tag, on the left one tight SECVTX tag is required.

8.3 Cross Section Measurement

After the log likelihood cut of Section 8.1 we are left with 36 events, of which 6.4 are expected to be from background processes. This selection allows us to calculate our first restult, the $t\bar{t}$ cross section measurement.

$$\sigma_{t\bar{t}} = \frac{N_{sel} - \sum N^i_{bg}}{\sum_{CMX,\ CMUP,\ CEM}[(BR_{\ell\tau}\epsilon_{\ell\tau} + BR_{\tau\tau}\epsilon_{\tau\tau}) \int \mathcal{L}dt]} \tag{8.3}$$

where N_{sel} is the number of selected signal events of the lepton plus tau and di-tau channel; N_{bg} is the number of expected background events; the sum extends over the lepton categories used in our analysis, namely the electron reconstructed with CEM detector and muon with CMUP and CMX muon chambers; $BR_{\ell\tau}$ represents the combinatory product of top quark decay branching ratio into electron or muon, $BR(t \to \ell\nu b)$, and top decay into hadronically decaying tau $BR(t \to \tau\nu b) \cdot BR(\tau \to \text{jet } \nu)$:

$$BR_{\ell\tau} = 2 \cdot BR(t \to \ell\nu b) \cdot BR(t \to \tau\nu b) \cdot BR(\tau \to \text{jet } \nu); \tag{8.4}$$

$BR_{\tau\tau}$ is the branching ratio of top pair decay into leptonically decaying tau plus hadronically decaying tau:

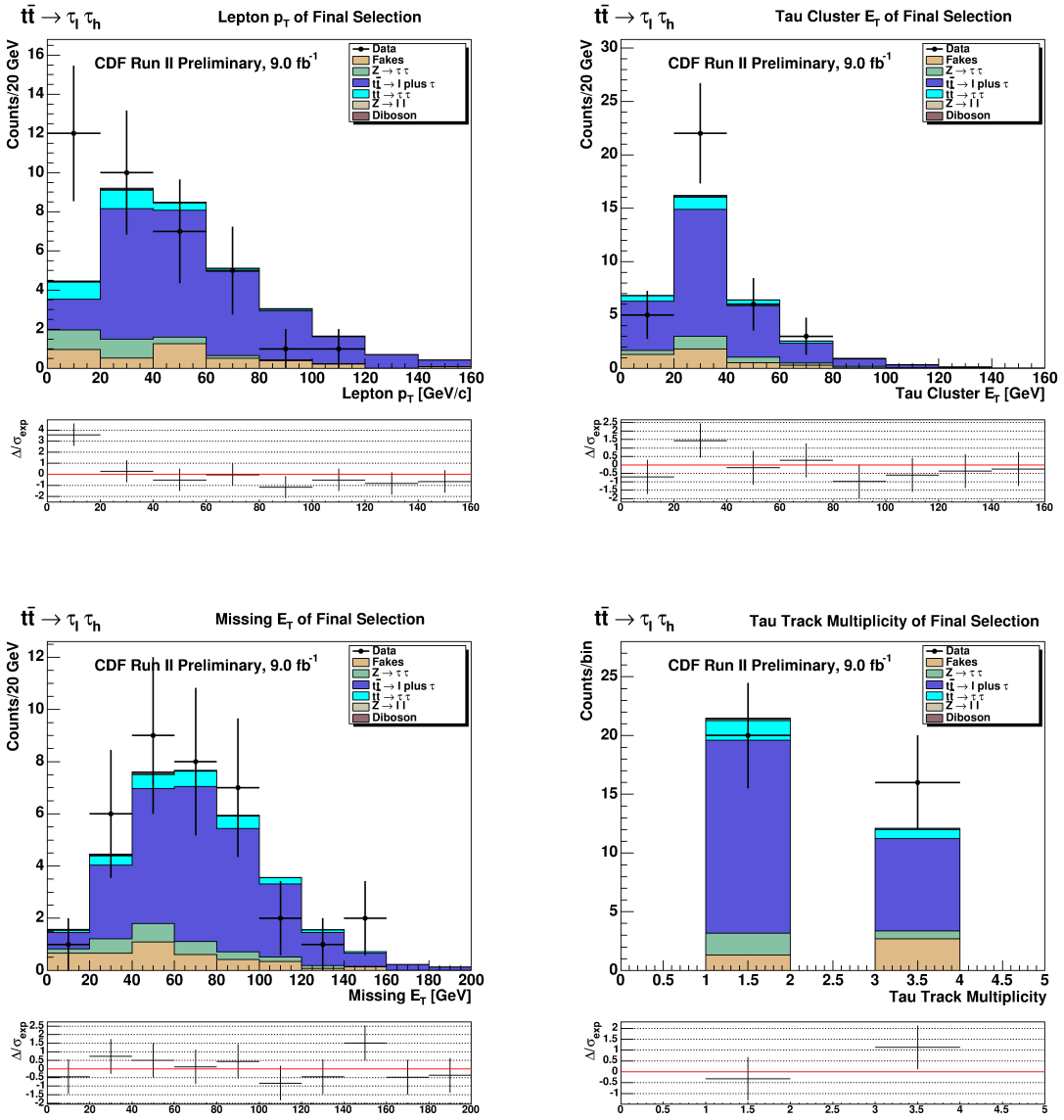

Figure 8.9: Distribution of electron E_T or muon p_T (top left), of tau cluster E_T (top right), $\not\!\!E_T$ (bottom left), and track multiplicity of tau induced jet (top right). Results obtained with kinematic selection, one b-jet tagging and LLR discriminant.

$$BR_{\tau\tau} = 2 \cdot BR(t \to \tau\nu b)^2 \cdot BR(\tau \to \ell\nu\nu) \cdot BR(\tau \to \text{jet } \nu); \tag{8.5}$$

	Di-Tau (electron)	**Electron + Tau**
ϵ_e	0.384 ± 0.003	0.460 ± 0.002
ϵ_τ	0.251 ± 0.003	0.250 ± 0.001
ϵ_{sel}	0.249 ± 0.008	0.272 ± 0.004

Table 8.4: The efficiency to reconstruct and identify electrons, ϵ_e, the efficiency to reconstruct and identify a hadronic tau decay, ϵ_τ, and the efficiency of the signal selection. Results obtained after the requirement at the MC generator level of leptons in the region of $|\eta| < 1.2$ with $p_T > 8$ GeV.

	Di-Tau (muon)	**Muon + Tau**
ϵ_μ^{CMUP}	0.222 ± 0.002	0.252 ± 0.002
ϵ_μ^{CMX}	0.113 ± 0.002	0.131 ± 0.001
ϵ_τ	0.237 ± 0.002	0.242 ± 0.001
ϵ_{sel}	0.253 ± 0.008	0.277 ± 0.005

Table 8.5: The efficiency to reconstruct and identify CMUP and CMX muons, ϵ_μ^{CMUP} and ϵ_μ^{CMX} respectively, the efficiency to reconstruct and identify a hadronic tau decay, ϵ_τ, and the efficiency of the signal selection. Results obtained after the requirement at the MC generator level of leptons in the region of $|\eta| < 1.2$ with $p_T > 8$ GeV.

$\epsilon_{\ell\tau}$ and $\epsilon_{\tau\tau}$ are the overall selection efficiencies for the di-tau and lepton plus tau channel, which can be expressed:

$$\epsilon_{\ell\tau} = A_{\ell\tau} \cdot \epsilon_\ell \cdot \epsilon_\tau \cdot \epsilon_{sel} \cdot \epsilon_{trig}, \quad (8.6)$$

$$\epsilon_{\tau\tau} = A'_{\ell\tau} \cdot \epsilon_\ell \cdot \epsilon_\tau \cdot \epsilon_{sel} \cdot \epsilon_{trig}; \quad (8.7)$$

In the previous equations, $A_{\ell\tau}$ and $A'_{\ell\tau}$ are the product of geometrical and kinematical acceptance of the top pair simulated events in lepton plus tau and di-tau decay modes respectivelly. At the event generator level we consider central leptons, with $|\eta| < 1.2$ and $p_T > 8$ GeV, $A_{e\tau} = 0.518 \pm 0.002$ and $A_{\mu\tau} = 0.520 \pm 0.002$, $A'_{e\tau} = 0.369 \pm 0.002$ and $A'_{\mu\tau} = 0.378 \pm 0.002$.

In Equation 8.7 the factor ϵ_ℓ is the efficiency to reconstruct and identify a lepton of type ℓ and ϵ_τ the efficiency to reconstruct and identify a hadronic tau decay; ϵ_{sel} is the efficiency of the kinematic selection, b-tagging and log-likelihood ratio selection. After requiring at the MC generator level the leptons to be in the region of $|\eta| < 1.2$ and $p_T > 8$ GeV the efficiencies of our signal selection are collected in Table 8.4 and Table 8.5.

The overall trigger efficiency ϵ_{trig} is 78% for the CMX sample, 79% for the CMUP sample and 79% for the CEM sample.

To derive a $t\bar{t}$ cross section measurement from this we assume a 100% branching ratio of top into W and b and use the measured tau into electron or muon and hadrons branching ratios from the PDG [7]. We propagate the systematic uncertainties that are summarized in Table 8.2 individually, correlated among channels within each source of uncertainty and uncorrelated among different uncertainties. We include also the statistic uncertainty from the selection of the Monte Carlo events. We obtain a measurement of $t\bar{t}$ cross section:

$$\sigma_{t\bar{t}} = 8.2 \pm 1.7(stat.)^{+1.2}_{-1.1}(syst.) \pm 0.5(lum.) \text{ pb}. \tag{8.8}$$

The result is dominated by the statistical uncertainty of the 36 events that pass our selection. The largest source of systematic uncertainty is the tuning of initial and final state radiation, followed by the uncertainty in the b-tagging efficiency.

Our measurement of the $t\bar{t}$ cross section assuming Standard Model top decay is in good agreement with the combination of all electron and muon channels from CDF, $\sigma_{t\bar{t}} = 7.5 \pm 0.5$ pb [70], and from the most recent measurement in the dilepton channels at DØ, $\sigma_{t\bar{t}} = 7.6 \pm 0.8$ pb [71].

The $t\bar{t}$ cross section times branching ratios is given by

$$\sigma_{t\bar{t}} \times (BR_{\ell\tau} + BR_{\tau\tau}) = 0.145 \pm 0.030(stat)^{+0.022}_{+0.019}(syst.) \pm 0.008 \text{ pb}, \tag{8.9}$$

8.4 From Cross Section to Branching Ratio of $t \to \tau\nu b$

In this section we compute the branching ratio of the process $t \to \tau\nu b$. The measurement is obtained considering as signal sample the top pair events with electron or muon plus tau in the final state. The procedure of evaluation is similar to the one given in the previous section. We start from Equation 5.1 expressed in the form

$$N_{\ell\tau} = \sigma_{t\bar{t}} \sum_{CMX,\ CMUP,\ CEM} BR_{\ell\tau}\epsilon_{\ell\tau} \int \mathcal{L}dt, \tag{8.10}$$

where $N_{\ell\tau}$ is the number of selected signal events of the lepton plus tau channel, $BR_{\ell\tau}$ is the branching ratio of top decay in lepton plus tau mode, $\epsilon_{\ell\tau}$ is the overall efficiency of the signal selection, $\int \mathcal{L}dt$ is the integrated luminosity and $\sigma_{t\bar{t}} = 7.5 \pm 0.5$ pb is the average top pair cross section measured by CDF.

The number of lepton plus tau events is

$$N_\ell = N_{sel} - \sum N^i_{bg} \tag{8.11}$$

where N_{sel} is the number of data events passing the selection and N^i_{bg} differently from the previous section contains also the contribution of top pair decay into the di-tau channel.

We assume $BR_{\ell\tau} = 2BR(t \to \ell\nu b)BR(t \to \tau\nu b)$, where $BR(t \to \ell\nu b) \approx BR(W \to \ell\nu)$. In our equation we substitute $BR(W \to \ell\nu)$ with the average decay branching ratio of the W into muon neutrino and into electron neutrino, $10.8 \pm 0.10\%$. We assume the top decay branching ratio into electron or muon plus neutrino and b to be equal to the branching ratio $BR(W \to e/\mu\nu)$. $BR(t \to \tau\nu b)$ represents the branching ratio to be evaluated. Using Equation 8.10 and 8.11 we obtain

$$BR(t \to \tau\nu b) = \frac{1}{2BR(W \to \ell\nu)} \frac{N_{sel} - \sum_i N_{bg}^i}{\sigma_{t\bar{t}} \sum_{CMX,\ CMUP,\ CEM} \epsilon_{\ell\tau} \int \mathcal{L}dt}. \tag{8.12}$$

The overall selection efficiencies on the simulated events are

- $\epsilon_{e\tau}^{CEM} = 1.28\%$,
- $\epsilon_{\mu\tau}^{CMUP} = 0.69\%$,
- $\epsilon_{\mu\tau}^{CMX} = 0.36\%$.

Each of the efficiencies account for the geometrical acceptance of the detector, the identification efficiencies of the leptons and their scale factors, the kinematic selection, the secondary vertex reconstruction and the trigger efficiency.

Substituting the efficiency values in Equation 8.12 we obtain

$$BR(t \to \tau\nu b) = (12.0 \pm 2.7_{stat})\% \tag{8.13}$$

We varied the number of expected events and the selection efficiency of the lepton plus tau to acount for the systematic uncertainties as done in the previous section. We considered also the uncertainty of the measured top pair production cross section. This is obtained from the CDF combination of the studies in lepton plus jet, dilepton and all hadronic modes. These channels correspond to $\sim 80\%$ of the top decay width and in particular, the lepton plus jet channel (electron or muon), corresponding to $\sim 30\%$, has kinematic constraints that allow a good rejection of the background. For these reasons we use the most recent CDF combination, 7.5 ± 0.5 [70], which is more precise than the result we obtained. We calculated the propagation of the systematics into the $BR(t \to \tau\nu b)$ and computed the quadratic sum of the fluctuations. The result is

$$BR(t \to \tau\nu b) = 0.120 \pm 0.027(stat.)^{+0.022}_{-0.019}(syst.) \pm 0.007(lum.), \tag{8.14}$$

in good agreement with the SM prediction on the top decay process $t \to Wb$ and the branching ratio values of W boson leptonic decay fitted by the Particle Data Group [7]:

- $BR(W \to \ell\nu) = (10.80 \pm 0.09)$ % (average over e, μ, τ decay modes),
- $BR(W \to \tau\nu) = (11.25 \pm 0.20)$ %.

Our measurement of the branching ratio $BR(t \to \tau\nu b)$ indicates that we may limit the branching ratio $BR(t \to H^{\pm}b)$, since in the MSSM picture the $H^{\pm} \to \tau\nu$ is the dominant decay channel for $\tan(\beta) > 1$ and $M_{H^{\pm}} < M_t$.

8.5 Di-Tau Component Discriminant

The aim of our analisys is to perform a measurement of the branching ratio of top quark decay in tau in case the involved process is the top pair decay mode with two taus. For this measurement we need to discriminate the signature of the lepton plus tau decay from the di-tau processes.

We implemented a second log-likelihood ratio (we report as LLR') discriminant method to separate the two processes.

Sketches of the top pair dileptonic decay modes which have a final state involving an electron and a tau induced jet are reported in Figure 8.3. The small phase space available to the tau decay products causes them to be alligned in most of the cases to the original tau direction.

We espect top pair decay into di-tau to differ from the electron (or muon) plus tau channel for the energy spectrum of the charged lepton and the fraction of $\not\!\!E_T$ along the direction of the charged lepton. To build the LLR' discriminant we looked for variables which maximize the separation between the processes. We found:

- the transverse mass of the electron (or muon) plus $\not\!\!E_T$;
- the azimuthal angle between electron and $\not\!\!E_T$.
- the electron (or muon) transverse energy (momentum);

The templates used are obtained with sample of events from MC simulation (the simulated event sample described in Section 5.2). We require the kinematic selection described in Section 6.2, tight SECVTX tag and $\ln(LR') > 0$. We present in Figure 8.10 and 8.11 the templates.

We show in Figure 8.12 the distribution of $\ln(LR')$ for simulated events from electron plus tau and di-tau decay channel.

We represent in Figure 8.13 the distribution of $\ln(LR')$ for data events compared to the SM expectations. For the camparison we used the full data sample and the electron and muon categories. The statistic of the sample is low and we cannot select easily the di-tau component with a cut based selection. We then use the distributions of expected and data events in the log-likelihood ratio to estract the branching ratio of top in tau, neutrino and b quark. The next section will describe the result obtained with a likelihood fit.

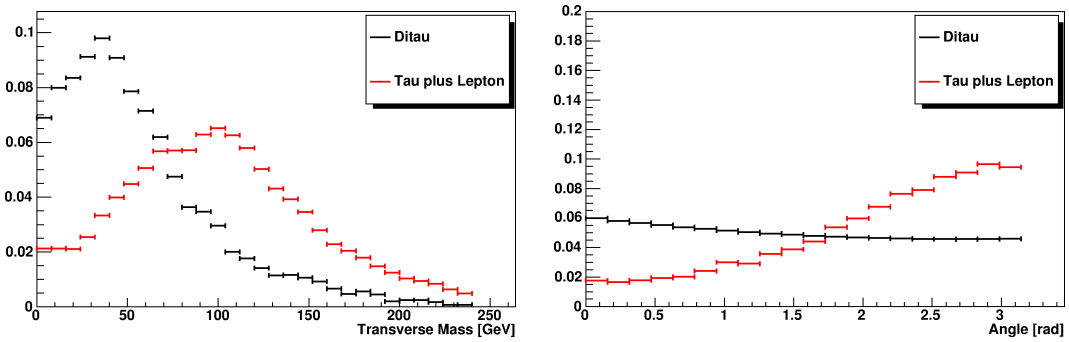

Figure 8.10: Templates of the transverse mass of the electron plus $\not\!\!E_T$(left), templates of the azimuthal angle between electron and $\not\!\!E_T$(right).

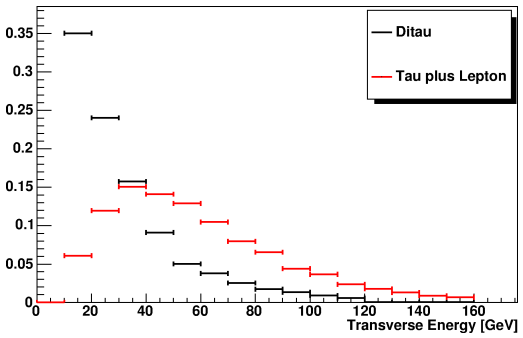

Figure 8.11: Distribution of electron transverse energy.

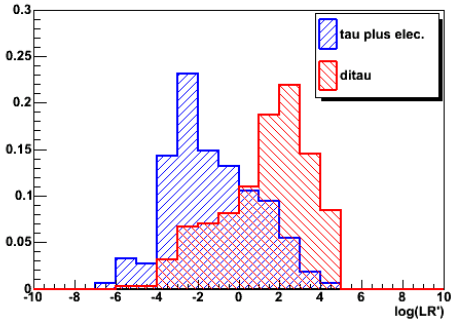

Figure 8.12: The distribution of the variable $\ln(LR')$ for simulated events from electron plus tau and di-tau decay channel with one tau decay in electron.

8.5.1 Branching Ratio Measurement

We use the MClimit package [85] to fit the event expectation to the data event distibution and estract the branching ratio $BR(t \to \tau\nu b)$. The branching ratio is an unconstrained

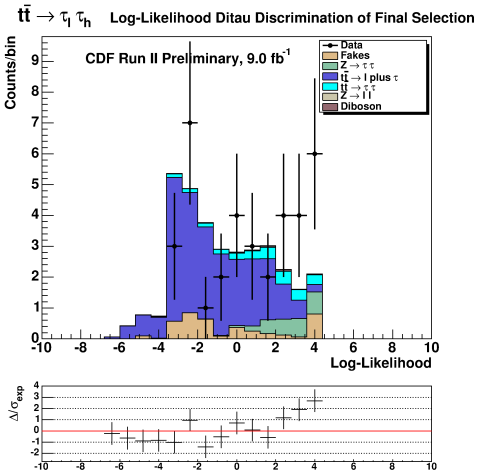

Figure 8.13: Comparison of data and expectation distribution of $\ln(LR')$ using electron and muon samples.

parameter of the fit. The top pair contribution in the lepton plus tau and the di-tau decay channels are set respectivelly to be linearly and quadratically dependent on the parameter $BR(t \to \tau\nu b)$. The systematic uncertainties of the counting experiment are used as nuissance parameters of the fit. The top pair cross section measurement from the CDF combination is used to constrain the top pair contribution. Its uncertainty is used as rate systematic for the fit.

The result of the fit is:

$$BR(t \to \tau\nu b) = 0.098 \pm 0.022(stat.) \pm 0.014(syst.) \tag{8.15}$$

From the fit it is possible to obtain also the upper limit of the branching ratio of top into tau. This limit is fundamental to constrain the decay of top pair into charged Higgs in the hypothesys that the mass of the charged Higgs is lower than the top quark mass.

For this measurement we repeated the fit of the expected distributions to data rescaling the MC expectations of signal top events on the base of the branching ratio. The lepton plus tau channel and the di-tau channel scale linearly and quadratically respectivelly with the $BR(t \to \tau\nu b)$. We obtain

$$BR(t \to \tau\nu b) < 0.159 \text{ at } 95\% \text{ C.L.} \tag{8.16}$$

To set a limit for charged Higgs production in top quark decays, we need to consider the contribution in the $t \to \tau\nu b$ through the SM predicted decay process $t \to Wb$ with $W \to \tau\nu$. We also assume that the kinematic of the processes which involve the charged

Higgs does not modify the acceptance of the selection measured with the simulated events in the SM hypothesis. We assume

$$BR(t \to W^+b) + BR(t \to H^+b) = 1, \tag{8.17}$$

$$BR(H^\pm \to \tau\nu) = 1. \tag{8.18}$$

The latest condition corresponds to the condition of a "tau-philic charged Higgs boson", which is valid in the case of $\tan(\beta) > 1$ (see Section 1.3). Starting from the equation

$$BR(t \to \bar{\tau}\nu b) = BR(t \to W^+b) \cdot BR(W^+ \to \bar{\tau}\nu) + BR(t \to H^+b) \cdot BR(H^+ \to \bar{\tau}\nu), \tag{8.19}$$

we obtain the branching ratio of top decay into charged Higgs boson and b quark espressed as:

$$BR(t \to H^+b) = \frac{BR(t \to \bar{\tau}\nu b) - BR(W^+ \to \bar{\tau}\nu)}{1 - BR(W^+ \to \bar{\tau}\nu)}. \tag{8.20}$$

We use our measurement of $BR(t \to \tau\nu b)$ and the $BR(t \to Wb)$ obtained by the Particle Data Group (0.1080 ± 0.0009 [7]) and propagate the uncertainty of these two branching ratios in the final measurement of the $BR(t \to H^+b)$. We consider the uncertainties on $BR(t \to \tau\nu b)$ and $BR(t \to Wb)$ to be uncorrelated and thus sum them in quadrature. The 95% confidence level upper limit is

$$BR(t \to H^+b) < 0.057 \text{ at } 95\% \text{ C.L.} \tag{8.21}$$

8.6 The Top in Tau Signature as Window to the Higgs Sector

The study reported in this thesis is motivated by a twofold purpose. In first place a measurement of a poorly known top decay channel into tau. The study of this decay channel has been so far limited by small branching ratios and by the high background of jets misidentified as taus. In second place the search for phenomena beyond the Standard Model in the study of the third generation of fermions (both top quark and tau lepton). Indeed we have already underlined the importance of the measurement of the branching ratio $BR(t \to \tau\nu b)$ as a test for the Higgs sector.

We want to mention that the top dileptonic decay with a hadronic tau has a signature similar to the neutral Higgs decay into two taus, in particular when the Higgs production mechanism happens through the so called vector boson fusion [7]. In this channel we expect the signature of the two leptons coupled with two jets in the forward region of the detector.

The CMS and the ATLAS collaborations recently annouced the discovery of a resonance at $\approx 125-126$ GeV due to the decay of a neutral boson particle [72][73]. Both collaborations

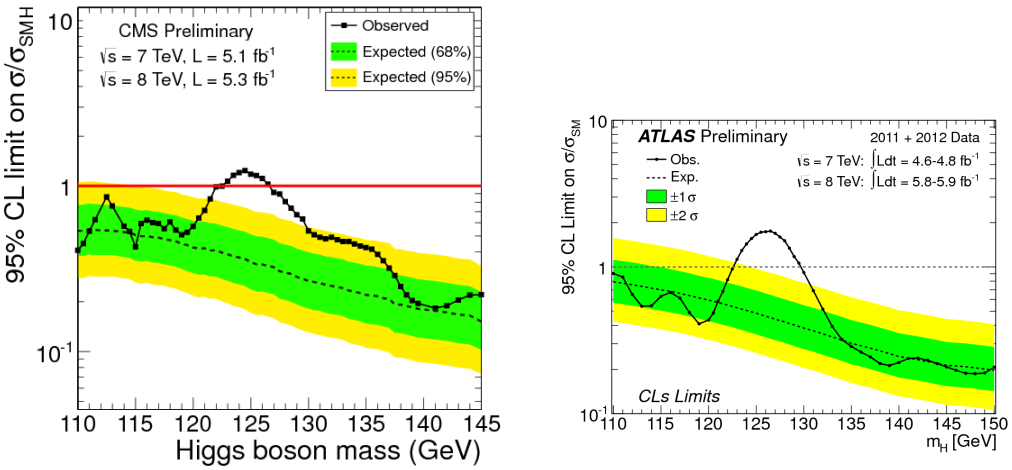

Figure 8.14: Observed and expected 95% CL upper limits on the ratio to the SM cross section, as functions of the neutral Higgs boson mass for CMS (left) and ATLAS (right).

measure a cross section statisticly compatible with the production of the SM Higgs boson. These results have been obtained combining the searches with the proton-proton collisions at $sqrts = 7$ TeV and 8 TeV, in the 2011 and 2012 data taking respectivelly. The evidence is clear in the final states with two photons and the final states with two lepton pairs, which allow the best invariant mass reconstruction (CMS combines also channels with $b\bar{b}$, $\tau\bar{\tau}$, WW and ZZ with jets in the final state). The ratios of the 95% CL expected and observed limits of ATLAS and CMS experiments to the SM cross section are shown in Figure 8.14.

The CDF and DØ collaborations recently conbined their results in the search of the Standard Model Higgs [74]. With the Higgs boson mass $m_H = 120$ GeV the two experiments obatain a p-value for background fluctuation corresponding to a local significance of 3.0 standard deviations. The ratios of the 95% CL expected and observed limits to the SM cross section are shown in Figure 8.15.

The branching ratio of the Standard Model Higgs boson decay into taus is expected to be relatively high, of the order of 7%, and the measurement of decay branching ratio of the channel together with other channels will be fundamental to discriminate between SM and supersymmetric theories.

We provide in this study of the measurement of $BR(t \to \tau\nu b)$ which is obtained with the assumption $BR(t \to (e/\mu)\nu b) \approx BR(W \to (e/\mu)\nu)$. If a charged Higgs boson is produced the process would compete with the decay into W. Since the charged Higgs would decay predominantly into a tau lepton, the decay $t \to H^{\pm}b$ would reduce the top decay into the electron or the muon channels. In this case the measurement of the branching ratio in lepton plus tau decay channel would soften the effects of a violation of lepton universality.

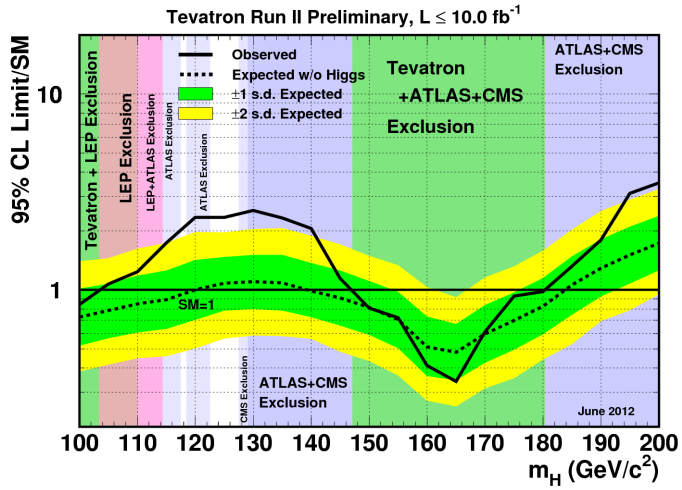

Figure 8.15: Observed and expected 95% CL upper limits on the ratio to the SM cross section, as functions of the neutral Higgs boson mass for the combined CDF and D0 analyses. The LHC and the LEP exclusion region are also reported.

The measurement of the di-tau channel allows to remove the dependency on the top pair cross section and the ratio of the number of lepton plus tau events and di-tau events is a direct test of lepton universality. The measurement of the di-tau channel is an important refinement of our analysis and we achieve this goal with the use of statistical treatment of the distribution in $\ln(LR')$.

The presence of a charged Higgs in the decay of top pair enhances the di-tau signature so the discrimination of this decay mode would allow to limit the parameter space of supersymmetric models. Using a likelihood (MCLimit [82]) we perform the search of charged Higgs boson.

Previously the CDF Collaboration presented a search for a charged Higgs bosons in the decay of top pairs with a tau jet in the final state. The result was obtained with a sample of Run II data corresponding to 193 pb^{-1} and limited the accessible space of variables in the context of the MSSM [83]. The result of the exclusion is shown in Figure 8.16 in the space of variables $M_H^{\pm}$ and $\tan(\beta)$), using dilepton, lepton plus jets and lepton plus tau signatures. The same figure reports the limits in terms of the variables $M_H^{\pm}$ and $BR(t \to H^{\pm}b)$ assuming $BR(H^{\pm} \to \tau\nu) = 1$ (valid for $\tan(\beta) > 1$ and Higgs mass $M_H^{\pm} < M_t$).

A limit on $BR(t \to H^{\pm}b)$ was also obtained by the DØ Collaboration. It improved the CDF limits using Run II data corresponding to 1 fb^{-1} [84]. The most stringent limit was obtained with a global fit that uses the correlation among the different final states of the top quark decay. It uses the measurements of top pair production cross section in the

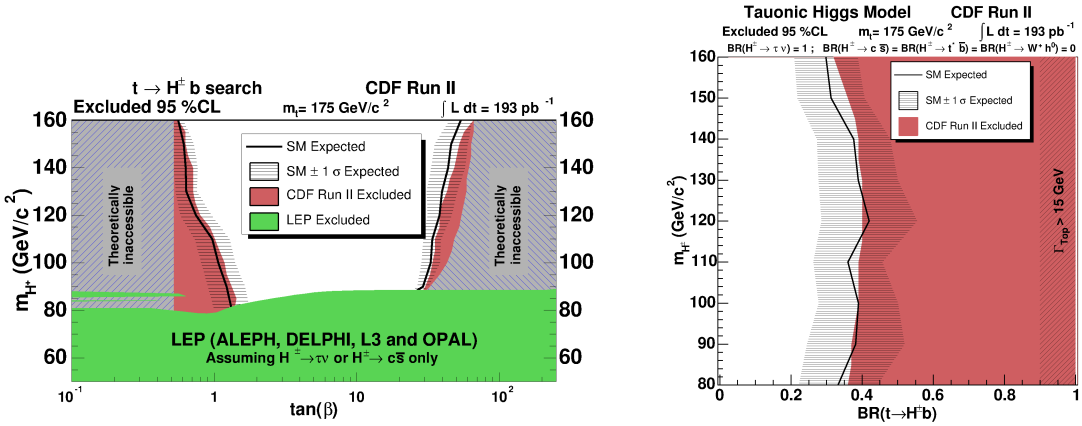

Figure 8.16: Exclusion limits expected from SM and the observed limits from CDF and LEP (left). The SM and CDF Run II excluded region in the plane $(M_H^{\pm}, BR(t \to H^{\pm}b))$ assuming $BR(H^{\pm} \to \tau\nu) = 1$ (right)

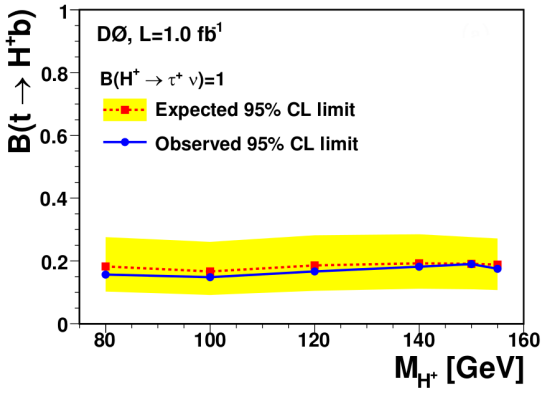

Figure 8.17: The upper limit on $BR(t \to H^{\pm}b)$ for the tauonic model $(BR(H^{\pm} \to \tau\nu) = 1)$.

final states lepton plus jets, dilepton and lepton plus tau [78][86]. Figure 8.17 shows the expected upper limits with error bands of ± 1 standard deviation and the observed upper limits for the tauonic model $(BR(H^{\pm} \to \tau\nu) = 1)$.

Experiments at LHC presented recently results in the search of the charged Higgs boson in the decay $H^{\pm} \to \tau\nu$ in $t\bar{t}$ events. They could not observe phenomena beyond the SM and limited drastically the parameter space of the MSSM theory.

ATLAS Collaboration with 4.6 fb^{-1} of pp collision data selected events of the lepton plus tau channel and the tau plus jets decay channel, where the tau decays into hadrons [87]. This search reduced the previous Tevatron upper limit on the $BR(t \to H^{\pm}b)$ by an order

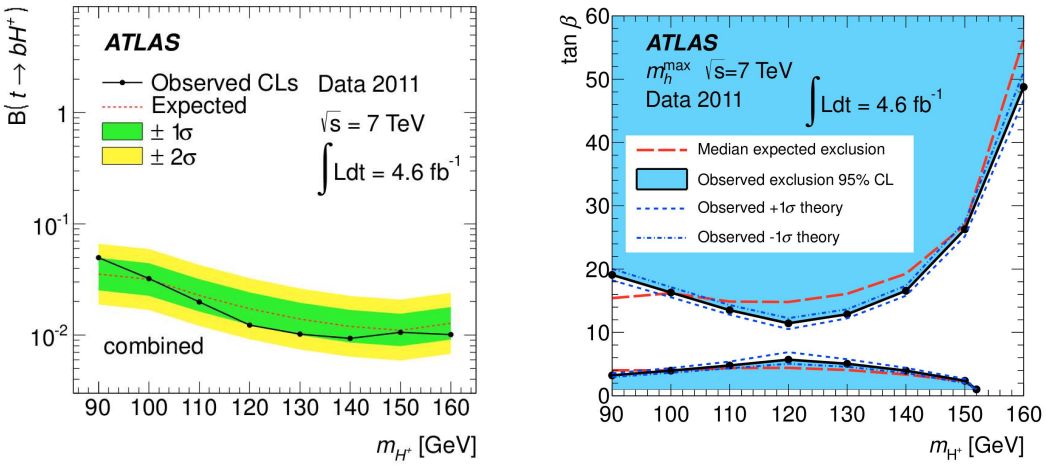

Figure 8.18: Expected and observed 95% CL exclusion limits on $BR(t \to H^{\pm}b)$ from top quark decay as function of the mass $M_H^{\pm}$, assuming $BR(H^{\pm} \to \tau\nu) = 1$ (left). Exclusion limits in the plane $(M_H^{\pm}, BR(t \to H^{\pm}b))$, in the context of the MSSM scenario.

of magnitude: it is placed between 5% and 1% for charged Higgs boson masses from 90 to 160 GeV. Figure 8.18 shows the expected and observed exclusion limits from the combination of the three channels.

The CMS Collaboration showed preliminary results at the Moriond 2012 Conference on the charged Higgs search [88] using 2 fb^{-1} of data collected in pp collisions at $\sqrt{s} = 7$ TeV. Three top pair decay final states are used: the all hadronic channel with a hadronically decaying tau in association with jets, the dilepton channel with a hadronically decaying tau and the dilepton channel with electron and muon (both from tau decay in lepton). The result of the combination of these studies, assuming $BR(H^{\pm} \to \tau\nu) = 1$, allowed to set an upper limits on the $BR(t \to H^{+} + b)$ ranging from 2% to 3% as function of the boson mass. Figure 8.19 shows the upper limit obtained from this analysis.

8.7 Results from Other Experiments

Previous measurement accomplished by the CDF and DØ collaboration used a partial amount of data of the Tevatron Run II program. Our analysis is performed with the full CDF data sample and thus strongly reduces the uncertainty of the previous cross section measurements in the final states with one lepton and a hadronic tau. We provide also an decisive improvement in the estimate of the $t \to \tau\nu b$ decay branching ratio measured with the CDF experiment.

The previous CDF result, obtained with the same channels, was accomplished with 350 pb^{-1}. It provided an hint of the top pair decay into lepton plus tau with a *p-value*

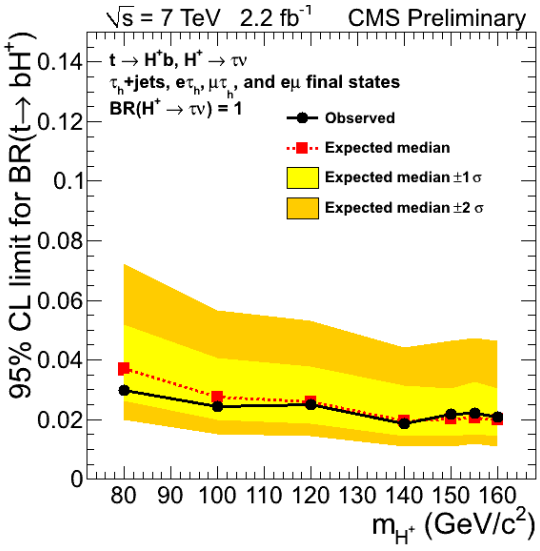

Figure 8.19: The upper limit on $BR(t \to H^{\pm}b)$ assuming $BR(H^{\pm} \to \tau\nu) = 1$ as a function of $M_H^{\pm}$ obtained from the combination.

of 15% [75]. More recently the DØ collaboration measured the top pair production cross section in the lepton plus tau mode with 1 fb^{-1} of integrated luminosity. The result was $7.8^{+2.9}_{-2.5}$ pb [76].

The CDF and DØ collaborations provided also the top pair cross section using events in the tau plus jets channel [77] [78]. The results of both collaborations are in agreement with the SM predictions and with the result we report, within the uncertainties. Table 8.6 summarizes the top pair production cross section measured by the CDF and DØ collaborations in channels with taus. With our measurement we complete the set of top pair cross section measurements achieved at the Tevatron.

Experiment	Channel	Luminosity	Result
DØ	$\tau\ell$ [76]	2.1 fb^{-1}	$7.3^{+1.8}_{-1.7}$ pb
	$\tau+$ jets [78]	1 fb^{-1}	$6.9^{+1.5}_{-1.4}$ pb
CDF	$\tau\ell$ [75]	350 pb^{-1}	15% p-value
	$\tau+$ jets [77]	2.2 fb^{-1}	$8.8^{+4.0}_{-4.0}$ pb
	$\tau\ell + \tau\tau_\ell$	**9.0 fb^{-1}**	$8.2^{+2.3}_{-2.0}$ **pb**

Table 8.6: Summary of the top pair production cross section measurements at the Tevatron with a tau lepton in the final state.

The results achieved by the DØ collaboration, listed in Table 8.6, are obtained with an neural network for the identification of tau leptons and rejection of jet background. This neural network is not aimed at the rejection of electrons and muons. The signal samples include also top pair decay channels with electrons and muons passing the tau identification.

The ATLAS and CMS experiments at the Large Hadron Collider have recently obtained new measurements of the top pair production cross section. This cross section, with pp collisions at $\sqrt{s} = 7$ TeV, is expected to be more than 20 times higher than the one obtained by the $p\bar{p}$ collisions at the Tevatron. Indeed the SM prediction in the NNLO calculation is $\sigma_{t\bar{t}} = 163^{+7}_{-5}(\text{scale}) \pm 9(\text{PDF})$ pb[81].

The CMS Collaboration has recently published a study on top pair decay in dilepton final states with an electron or muon plus a tau lepton [79]. The data samples used correspond to 2 fb^{-1} for the electron channel and 2.2 fb^{-1} for the muon channel. The top pair production cross section at $\sqrt{s} = 7$ TeV is $\sigma_{t\bar{t}} = 143 \pm 14_{stat} \pm 22_{sys} \pm 3_{lum}$ pb in agreement with the theoretical prediction.

The ATLAS Collaboration also measured the top pair production cross section in the final state with a hadronically decaying tau plus jets [80]. The measured cross section is $\sigma_{t\bar{t}} = 200 \pm 19_{stat} \pm 43_{sys}$ pb also in agreement with the SM theoretical prediction.

The measurement of the top pair production cross section we performed in this thesis is in agreement with the theoretical predictions and with the CDF measurements done in the lepton plus jets, dilepton and all hadronic modes. Figure 8.20 and Figure 8.21 summarize the top pair production cross section measured by the CDF and DØ collaborations respectively.

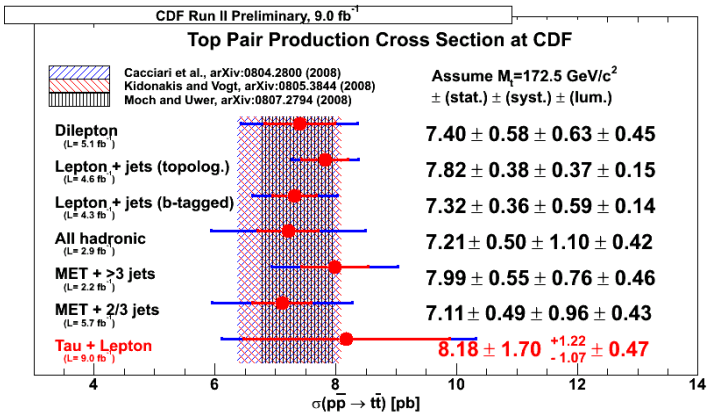

Figure 8.20: The most recent measurements of CDF collaboration of top pair production cross section, assuming top mass $M_T = 172.5$ GeV/c^2. The measurement on the bottom is obtained by our study.

The measurement of the branching ratio of top decay into tau neutrino and b quark is

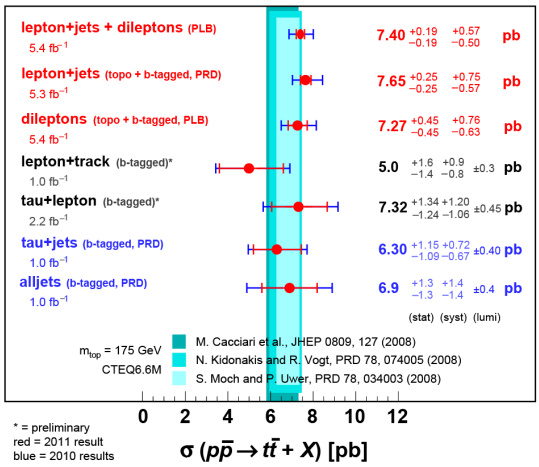

Figure 8.21: The most recent measurements of DØ, assuming $M_T = 175$ GeV/c^2.

not explicitly provided by LHC experiments, despite high precision of their measurements of the top production cross section in tau plus jets and tau plus lepton channels.

The previous measurement obtained by the DØ collaboration [78] in the tau plus jet channel is

$$BR_{\tau_h \text{ jets}} = 0.074^{+0.029}_{-0.027}, \tag{8.22}$$

where $BR_{\tau_h \text{ jets}}$ is the overall branching ratio of the decay channel with one hadronic tau plus jets. In the SM picture, with $BR(\tau \to \text{jet}) = 64.8$ and $BR(W \to \text{jets}) = 67.6\%$ this measurement leads to

$$BR(t \to \tau\nu b) = 0.084^{+0.033}_{-0.031}, \tag{8.23}$$

We measured the branching ratio $BR(t \to \tau\nu b)$ with signal events from the top pair decay in lepton plus tau channel.

$$BR(t \to \tau\nu b) = 0.120 \pm 0.027(stat.)^{+0.022}_{-0.019}(syst.) \pm 0.007(lum.), \tag{8.24}$$

Previous top pair studies were not able to estimate the number of events from the top dileptonic decay channel with two taus since it was limited by extremely low statistic. The branching ratio of the di-tau decay channel, accounting also for the tau decay modes, is about $\sim 1/5$ of the lepton plus tau channel. Moreover the E_T spectrum of the lepton from tau decay is almost halved by the requirement $E_T > 10$ GeV.

We expect 2.44 signal di-tau events to pass the selection of this analysis and we use the log-likelihood discriminant to separate the lepton plus tau and di-tau decay modes. The limited number of expected events does not allow to obtain an evaluation of the top pair

production cross section in the di-tau decay mode. However we use the distribution of the log-likelihood variable to extract a measurement of the branching ratio $BR(t \to \tau\nu b)$. In this case the measurement is independent from the assumption on the top decay branching ratio into electron or muon plus neutrino and b quark. The fit to data on the log-likelihood gives

$$BR(t \to \tau\nu b) = 0.098 \pm 0.022(stat.) \pm 0.014(syst.) \tag{8.25}$$

From the fit to data it is also possible to obtain a limit of the branching ratio measurement and give an upper limit on it at 95% confidence level:

$$BR(t \to \tau\nu b) < 0.159 \text{ at } 95\% \text{ C.L.} \tag{8.26}$$

This last result is used to set a limit on the branching ratio of top decay into charged Higgs in the tauonic hypothesis. In the assumption that the kinematic of the top decay with charged Higgs has the same probability to pass our selection of the SM decay process, we obtain

$$BR(t \to H^+ b) < 5.7\% \text{ at } 95\% \text{ C.L.} \tag{8.27}$$

This represents the most stringent constraint on the charged Higgs production in top decay obtained with Tevatron $p\bar{p}$ collision data.

Appendix A

Trigger Requirements

We describe in this appendix the trigger paths used to select signal events of top pair collected in the datasample "lepton plus isolated track".

Two more samples have been used for measuring the trigger efficiency in the selection of the "isolated track" object: the high-p_T lepton samples and the calibration lepton samples. The calibration lepton sample and the "CMX plus track" belonging to the SUSY dilepton sample have been used also to compute the background with misidentified tau lepton.

The measurement of the jet probability to be misidentified as tau candidates has been accomplished using the hadron jet samples. We describe here the trigger paths used for these measurements.

A.1 Data Taking Periods

The datasets which have been analyzed in this measurement, covers the run range from 141544 (from the good run list) to 312510, corresponding to the full CDF Run II data taking. In Table A.1 we report for each run period the specific run range and the approximated luminosity.

A.2 Lepton Plus Track Triggers

Several paths are included in this trigger category, according to the lepton type and detector involved: CEM electron, CMU+CMP and CMX muon. In each path an isolated track is paired with the lepton.

The trigger paths were modified to comply with the trigger specification, reducing the trigger acquisition rate and compensating the increase of Tevatron instantaneous luminosity over the time. Some changes had a small impact on the trigger behaviour. The improvement adopted to XFT and L2 cluster took place in the years 2006 and 2007 and presented the more relevant effects both on the lepton and the isolated track. Another

important change involved the L3 track isolation, which was modified after run 209770.

Table A.2 summarize the triggers of the class lepton plus track.

A.2.1 TAU_ELECTRON8_TRACK5_ISO

This trigger requires an electron with $E_T \geq 8$ GeV, defined by a XFT track matched to a central calorimeter cluster, and an additional isolated track with $p_T \geq 5$ GeV/c. The isolation requirements for the track is summarized in Table A.3, where ΔZ^{iso} is the maximum difference between the intersection of the seed track and the track in the isolation annulus on the beam axis.

Table A.4 summarizes the trigger selection corresponding to tag 12.

The main modification done to the trigger are the following.

- Tag 4: a second L2 XFT track in required.
- Tag 8: the second L2 XFT track has to match a calometer cluster with $E_T \geq 4$ GeV and $N_{twr} \leq 5$; new L3 isolation for is implemented.
- Tag 10: the L1 XFT track should pass 4 Super Layers.
- Tag 12: upgrade in L2 clustering algorithm for electron and isolated track. The isolated track should match a cluster with $N_{twr} \leq 5$.

A.2.2 TAU_CMUP8_TRACK5_ISO

The trigger is collects events characterized by central muons identified by a XFT track with $p_T \geq 8$ GeV/c matched stubs in both the CMU and CMP chambers. The trigger muon should be paired with a track with $p_T \geq 5$ GeV/c, satisfying the isolation requirements just before described.

The detailed list of trigger selections applied at each level is reported in Table A.5 for tag 11, which corresponds to the last version used in the analysis.

The most relevant modifications occurred from the first to the last version of this trigger are the following.

- Tag 7: a L2 XFT track is require with $p_T \geq 8.34$ GeV/c matched the muon chambers.
- Tag 8: a second L2 XFT track with $p_T \geq 5.19$ GeV/c is required.
- Tag 9: the new L3 track isolation definition is implemented.
- Tag 10: stereo confirmation[1] is required for muon and isolated track.

[1] Section 2.4.1 describes the L1 upgrade and the SLAM stereo confirmation

A.2.3 TAU_CMX8_TRACK5_ISO (and Later Paths)

These triggers collect muons which have a reconstructed XFT track with $p_T \geq 8$ GeV/c, matched to stubs in the CMX Arches, CMX Miniskirt or Keystone detectors. Similarly to other lepton plus track triggers, an additional isolated track with $p_T \geq 5$ GeV is required.

The detailed list of trigger selections applied at each level is reported in Table A.5 where we describe the last version, which is dinamically prescaled.

The major changes of the trigger paths that we consider were implemented to the TAU_CMX8_TRACK5_ISO, before the luminosity enabled or prescaled trigger were introduced. The changes are described below.

- Tag 7: the requirement of two L2 XFT tracks added, the first one ($p_0T \geq 8.34$ GeV/c) matched to a CMX stub.
- Tag 8: new L3 track isolation.

The latest triggers had modification on the luminosity activation or to the prescale value but did not have relevant changes.

A.3 Jet Triggers

As explained in section 5.4 we used the jet sample to measure the probability of an hadronic jet to be misidentified as a tau candidate. We imployed five classes of jet triggers, here ordered by increasing transverse energy requirement, Tower 5, Jet 20, Jet 50, Jet 70 and Jet 100. The previous triggers respectively require a calorimetric tower of 5 GeV, or a cluster of 20, 50, 70 and 100 GeV.

All the jet triggers have a fixed prescale value that has been modified during CDF Run II to maintain the trigger acquisition rate at a reasonable level despite the increase of Tevatron instantaneous luminosity. They were subject to the upgrade of the L2 clustering algorithm, but no other particular changes were implemented in these triggers.

Tower 5 triggers, JET_ST5, require a L1 calorimeter tower with a deposition of $E_T >$ 5 GeV. No L2 or L3 requirements. The trigger is highly prescaled: factor 50′000 in the last version (tag 6).

The requirements of the JET_20 trigger are reported in Table A.7. Before the upgrade of the L2 clustering algorithm, the L2 cluster was required to have a transverse energy deposit of 15 GeV.

The requirements of the JET_50 trigger are summarized in Table A.8.

The requirements of the JET_70 trigger are summarized in Table A.9.

The requirements of the JET_100 trigger are summarized in Table A.10. Some versions had at L1 the requirement of a single tower in the calorimeter with $E_T \geq 10$ GeV.

A.4 High p_T Lepton Triggers

A.4.1 ELECTRON_CENTRAL_18

This trigger requires one electron candidate with a XFT track of 9 GeV of transverse momentum matched to a $E_T \geq 18$ GeV central calorimeter cluster. The electron have also to satisfy some quality requirements as L_{shr}, $|\Delta Z_{CES}|$ and E_{HAD}/E_{EM} to reduce the overwhelming QCD induced background.

The complete list of selections at each level is reported in Table A.11

This trigger path was modified few times and the most important changes are the following.

- Tag 6: the minimum number of COT layers of the XFT track was reduced from 4 to 3.
- Tag 8: L_{shr} and $|\Delta Z_{CES}|$ requirement were added.
- Tag 9: the minimum number of COT layers of the XFT track was increased at L1 and L2 from 3 to 4.
- Tag 13: the new clustering algorithm was implemented after the L2 calorimeter upgrade

A.4.2 MUON_CMUP18

This trigger selects high-p_T muon candidates with a reconstructed XFT track with $p_T \geq$ 18 GeV/c. The track have to match stubs both in the CMU and in the CMP chambers. The requirements are shown in Table A.12 for the last version. The main change occurred to this trigger path is between tag 7 and 8 and is related to the XFT upgrades.

- Tag 3: requirement of a XFT track at L2 with $p_T \geq 8.34$ GeV/c.
- Tag 7: the L2 track has to match the CMU and CMP stubs.
- Tag 8: the p_T requirement was incrased to 14.77 GeV at L2, coupled with a stereo confirmation request.

A.5 Calibration Lepton and Lepton Plus Track Triggers

The calibration lepton samples contain three classes of trigger paths depending on the categories of leptons: CEM electron, CMUP and CMX muon. The electron is required to have cluster $E_T/geq8$ GeV, the muon a track $p_T/geq8$ GeV/c. To reduce the trigger acquisition rate the CMX muon path is heavily prescaled (on average ≥ 100).

In substitution of the CMX trigger path (MUON_CMX8) we used in our analysis the trigger path MUON_CMX8_&_TRACK8_DPS, and the previous version MUON_CMX8_&_TRACK8. This last triggers are generaly called "CMX muon plus track" and require a CMX muon with track $p_T \geq 8$ GeV/c plus a generic track with $p_T \geq 8$ GeV/c.

A.5.1 ELECTRON_CENTRAL_8_L2_DPS

This trigger requires one electron candidate with a XFT track of 8 GeV of transverse momentum matched to a $E_T \geq 8$ GeV central calorimeter cluster. The electron have also to satisfy some quality requirements as L_{shr}, $|\Delta Z_{CES}|$ and a tight E_{HAD}/E_{EM} to reduce the QCD induced background.

The complete list of selections for the last version of this trigger is reported in Table A.13.

At the beginning of data taking period 0 this trigger was not dinamicaly prescaled. Before that change major changes were implemented, but they interest a small fraction of the data acquired. This trigger path was then modified few times in the prescale factor and the L2 clustering algorithm (tag 8).

A.5.2 MUON_CMUP8_DPS

The trigger is collects events characterized by central muons identified by a XFT track with $p_T \geq 8$ GeV/c matched stubs in both the CMU and CMP chambers. The trigger is dinamicaly prescaled.

The detailed list of trigger selections applied at each level is reported in Table A.14 for tag 11, which corresponds to the last version used in the analysis.

Previous versions of this trigger existed without prescale: MUON_CMUP8, tags 1 to 9. At tag 8 the trigger included the requirements of 4 COT Super Layers in the XFT track at L2.

During data taking period 3 the trigger was modified to be dinamicaly prescaled. Then few modification of the scale factors were implemented, but no relevant selection changes were needed.

A.6 Lepton Plus Track Triggers

The trigger is collects events characterized by central muons identified by a XFT track with $p_T \geq 8$ GeV/c and matched with a stubs in the CMX chambers. A second track with $p_T \geq 8$ GeV/c is also required. The last version trigger is dinamicaly prescaled.

The detailed list of trigger selections applied at each level is reported in Table A.15 for tag 11, which corresponds to the last version used in the analysis.

Period	Run Range	Lum. [pb^{-1}]	Total Lum. [pb^{-1}]	Dates
0	138425-186598	520	520	04 Feb 02 - 22 Aug 04
1	190697-195408	130	650	07 Dec 04 - 18 Mar 05
2	195409-198379	130	780	19 Mar 05 - 20 May 05
3	198380-201349	100	880	21 May 05 - 19 Jul 05
4	201350-203799	100	980	20 Jul 05 - 04 Sep 05
5	203819-206989	150	1130	05 Sep 05 - 09 Nov 05
6	206990-210011	120	1250	10 Nov 05 - 14 Jan 06
7	210012-212133	50	1300	14 Jan 06 - 22 Feb 06
8	217990-222426	210	1510	09 Jun 06 - 01 Sep 06
9	222529-228596	200	1710	01 Sep 06 - 22 Nov 06
10	228664-233111	290	2000	24 Nov 06 - 30 Jan 07
11	233133-237795	260	2260	30 Jan 07 - 31 Mar 07
12	237845-241664	180	2440	01 Apr 07 - 13 May 07
13	241665-246231	320	2760	13 May 07 - 04 Aug 07
14	252836-254686	60	2820	28 Oct 07 - 03 Dec 07
15	254800-256824	180	3000	05 Dec 07 - 27 Jan 08
16	256840-258787	140	3140	27 Jan 08 - 27 Feb 08
17	258880-261005	190	3330	28 Feb 08 - 16 Apr 08
18	261119-264071	410	3740	18 Apr 08 - 01 Jul 08
19	264101-266513	290	4030	01 Jul 08 - 24 Aug 08
20	266528-267718	260	4290	24 Aug 08 - 04 Oct 08
21	268155-271047	520	4810	12 Oct 08 - 01 Jan 09
22	271072-272214	290	5100	02 Jan 09 - 10 Feb 09
23	272470-274055	230	5330	15 Feb 09 - 21 Mar 09
24	274123-275848	280	5610	22 Mar 09 - 04 May 09
25	275873-277511	240	5840	05 May 09 - 13 Jun 09
26	282976-284843	190	6030	15 Sep 09 - 25 Oct 09
27	284858-287261	400	6430	25 Nov 09 - 06 Jan 10
28	287294-289197	330	6760	06 Jan 10 - 25 Feb 10
29	289273-291025	360	7120	25 Feb 10 - 12 Apr 10
30	291294-293800	460	7580	13 Apr 10 - 19 Jun 10
31	293826-294777	170	7750	20 Jun 10 - 17 Jul 10
32	296645-299367	430	8180	21 Aug 10 - 01 Nov 10
33	299377-301303	380	8560	01 Nov 10 - 24 Dec 10
34	301952-303854	360	8920	06 Jan 11 - 06 Mar 11
35	304266-306762	360	9280	12 Mar 11 - 13 May 11
36	306791-308554	400	9680	13 May 11 - 04 Jul 11
37	308570-310441	170	9850	05 Jun 11 - 16 Aug 11
38	310472-312510	250	10000	16 Aug 11 - 30 Sep 11

Table A.1: Data acquired by the CDF detector in the run periods considered.

Trigger Families	Trigger Paths	Tags
"Electron plus isolated track"	TAU_ELECTRON8_TRACK5_ISO	1 - 12
"CMUP muon plus isolated track"	TAU_CMUP8_TRACK5_ISO	1 - 11
"CMX muon plus isolated track"	TAU_CMX8_TRACK5_ISO	1 - 8
	TAU_CMX8_TRACK5_ISO_LUMI_200	1
	TAU_CMX8_TRACK5_ISO_LUMI_250	1
	TAU_CMX8_TRACK5_ISO_DPS	1 - 4

Table A.2: "Lepton plus isolated track" trigger paths used in this analysis.

Variable	Requirement (run $\leq$ 209770)	Requirement (run $>$ 209770)
annulus	$0.175 \leq \Delta R \leq 0.524$	$10^\circ \leq \Delta\theta \leq 30^\circ$
p_T^{iso}	$\leq$ 1.5 GeV/c	$\leq$ 1.5 GeV/c
ΔZ^{iso}	15 cm	5 cm

Table A.3: L3 trigger selection for the isolated track.

Trigger Level	Path	Object	Requirement
1	L1_CEM8_PT8	CAL cluster	$E_T \geq 8$ GeV
			$E_{HAD}/E_{EM} \leq 0.125$
		XFT track	COT layers ≥ 4
			$p_T \geq 8.34$ GeV/c
2	L2_TAU4_PT5_CEM8_PT8_CES3	CES cluster	$E_T \geq 3$ GeV
		CAL cluster 1	$\|\eta\| \leq 1.1$
			$E_T \geq 8$ GeV
			$E_{HAD}/E_{EM} \leq 0.125$
		XFT track 1	$p_T \geq 8.34$ GeV/c
		CAL cluster 2	$\|E_T\| \leq 5$
			$E_T \geq 4$ GeV
		XFT track 2	$p_T \geq 5.19$ GeV/c
			$\Delta\phi^{SL6}_{trk1/trk2} \geq 10°$
3	L3_CEM8_TRACK5_ISO	electron	central
			$\chi^2_{strip} \leq 20$
			$L_{shr} \leq 0.4$
			$\|\Delta Z_{CES}\| \leq 8$ cm
			$E_T \geq 8$ GeV
			$p_T \geq 8$ GeV/c
		track	$\|\eta\| \leq 1.5$
			$p_T \geq 5$ GeV/c
			isolation (Table A.3)
			$\Delta R_{e-track} \geq 0.175$
			$\|\Delta Z_{e-track}\| \leq 15$ cm

Table A.4: Trigger requirements for the TAU_ELECTRON8_TRACK5_ISO path, tag 12.

Trigger Level	Path	Object	Requirement
1	L1_CMUP6_PT4	CMU stub	$p_T \geq 6$ GeV/c
			CMP hit
		XFT	$p_T \geq 4.09$ GeV/c
2	L2_CMUP6_PT8_TRK5_3D	muon	CMUP
		XFT track 1	$p_T \geq 8.34$ GeV/c
			stereo confirmed
		XFT track 2	$p_T \geq 5.19$ GeV/c
			stereo confirmed
3	L3_CMUP8_TRACK5_ISO	muon	CMUP
			$p_T \geq 8$ GeV/c
			$\Delta x_{CMP} \leq 20$ cm
			$\Delta x_{CMU} \leq 15$ cm
		track	$\|\eta\| \leq 1.5$
			$p_T \geq 5$ GeV/c
			isolation (Table A.3)
			$\Delta R_{e-track} \geq 0.175$
			$\|\Delta Z_{e-track}\| \leq 15$ cm

Table A.5: Trigger requirements for the TAU_CMUP8_TRACK5_ISO path, tag 11.

Trigger Level	Path	Object	Requirement
1	L1_CMX6_PT4	CMX stub	$p_T \geq 6$ GeV/c
			CSX hit
		XFT	$p_T \geq 4.09$ GeV/c
			COT layers ≥ 4
2	L2_CMX6_PT8_TRK5_3D	muon	CMX
		XFT track 1	$p_T \geq 8.34$ GeV/c
			stereo confirmed
		XFT track 2	$p_T \geq 5.19$ GeV/c
			stereo confirmed
		MAX_PRESCALE	20
		MIN_PRESCALE	1
3	L3_CMX8_TRACK5_ISO	muon	CMX
			$p_T \geq 8$ GeV/c
			$\Delta x_{CMX} \leq 30$ cm
		track	$\lvert\eta\rvert \leq 1.5$
			$p_T \geq 5$ GeV/c
			isolation (Table A.3)
			$\Delta R_{e-track} \geq 0.175$
			$\lvert\Delta Z_{e-track}\rvert \leq 15$ cm

Table A.6: Trigger requirements for the TAU_CMX8_TRACK5_ISO_DPS path, tag 4.

Trigger Level	Path	Object	Requirement
1	L1_JET5_PS100	CAL tower	$E_T \geq 5$ GeV
		PRESCALE	100
2	L2_JET20_PS50	CAL cluster	$E_T \geq 20$ GeV
			$\lvert\eta\rvert \leq 3.6$
		PRESCALE	50
2	L3_JET20	Jet Cone $\Delta R = 0.7$	$E_T \geq 20$ GeV

Table A.7: Trigger requirements for JET_20 trigger path, tag 20.

Trigger Level	Path	Object	Requirement
1	L1_JET5_PS100	CAL tower	$E_T \geq 5$ GeV
		PRESCALE	100
2	L2_JET40	CAL cluster	$E_T \geq 40$ GeV
			$\|\eta\| \leq 3.6$
2	L3_JET50	Jet Cone $\Delta R = 0.7$	$E_T \geq 50$ GeV

Table A.8: Trigger requirements for JET_50 trigger path, tag 13.

Trigger Level	Path	Object	Requirement
1	L1_JET10_PS8	CAL tower	$E_T \geq 10$ GeV
		PRESCALE	8
2	L2_JET60	CAL cluster	$E_T \geq 60$ GeV
			$\|\eta\| \leq 3.6$
2	L3_JET70	Jet Cone $\Delta R = 0.7$	$E_T \geq 70$ GeV

Table A.9: Trigger requirements for JET_70 trigger path, tag 11.

Trigger Level	Path	Object	Requirement
1	L1_JET20	CAL tower	$E_T \geq 20$ GeV
2	L2_JET90	CAL cluster	$E_T \geq 90$ GeV
			$\|\eta\| \leq 3.6$
2	L3_JET100	Jet Cone $\Delta R = 0.7$	$E_T \geq 100$ GeV

Table A.10: Trigger requirements for JET_100 trigger path, tag 10.

Trigger Level	Path	Object	Requirement
1	L1_CEM8_PT8	CAL cluster	$E_T \geq 8$ GeV
			$E_{HAD}/E_{EM} \leq 0.125$
		XFT track	COT layers ≥ 4
			$p_T \geq 8.34$ GeV/c
2	L2_CEM18_PT8	CAL cluster	$\|\eta\| \leq 1.317$
			$E_T \geq 18$ GeV
			$E_{HAD}/E_{EM} \leq 0.125$
		XFT track	COT layers ≥ 4
			$p_T \geq 8$ GeV/c
3	L3_CEM8_TRACK5_ISO	electron	central
			$L_{shr} \leq 0.4$
			$\|\Delta Z_{CES}\| \leq 8$ cm
			$E_T \geq 18$ GeV
			$p_T \geq 9$ GeV/c
			$E_{HAD}/E_{EM} \leq 0.125$

Table A.11: Trigger requirements for the ELECTRON_CENTRAL_18 path, tag 13.

Trigger Level	Path	Object	Requirement
1	L1_CMUP6_PT4	CMU stub	$p_T \geq 6$ GeV/c
			CMP hit
		XFT	$p_T \geq 4.09$ GeV/c
2	L2_TRK8_L1_CMUP6_PT4	muon	CMUP
		XFT track 1	$p_T \geq 14.77$ GeV/c
			COT layers ≥ 4
			stereo confirmed
3	L3_MUON_CMUP_18	muon	CMUP
			$p_T \geq 18$ GeV/c
			$\Delta x_{CMP} \leq 20$ cm
			$\Delta x_{CMU} \leq 10$ cm

Table A.12: Trigger requirements for the MUON_CMUP18 path, tag 11.

Trigger Level	Path	Object	Requirement
1	L1_CEM8_PT8	CAL cluster	$E_T \geq 8$ GeV
			$E_{HAD}/E_{EM} \leq 0.125$
		XFT track	COT layers ≥ 4
			$p_T \geq 8.34$ GeV/c
2	L2_CEM8_PT8_CES3_DPS	CES cluster	$E_T \geq 3$ GeV
		CAL cluster	$E_T \geq 8$ GeV
			$E_{HAD}/E_{EM} \leq 0.125$
		XFT track	$p_T \geq 8.34$ GeV/c
		MAX_PRESCALE	200
		MIN_PRESCALE	3
3	L3_ELECTRON_CENTRAL_8_PT8	electron	central
			$L_{shr} \leq 0.2$
			$\|\Delta Z_{CES}\| \leq 5$ cm
			$\|\Delta X_{CES}\| \leq 3$ cm
			$E_T \geq 8$ GeV
			$p_T \geq 8$ GeV/c
			$E_{HAD}/E_{EM} \leq 0.055$

Table A.13: Trigger requirements for the ELECTRON_CENTRAL_8_L2_DPS path, tag 8.

Trigger Level	Path	Object	Requirement
1	L1_CMUP6_PT4	CMU stub	$p_T \geq 6$ GeV/c
			CMP hit
		XFT	$p_T \geq 4.09$ GeV/c
2	L2_CMUP6_PT8_DPS	muon	CMUP
		XFT track 1	$p_T \geq 8.34$ GeV/c
			COT layers ≥ 4
		MAX_PRESCALE	80
		MIN_PRESCALE	1
3	L3_MUON_CMUP_8	muon	CMUP
			$p_T \geq 8$ GeV/c
			$\Delta x_{CMP} \leq 20$ cm
			$\Delta x_{CMU} \leq 15$ cm

Table A.14: Trigger requirements for the MUON_CMUP8_DPS path, tag 5.

Trigger Level	Path	Object	Requirement
1	L1_CMX6_PT4	CMX stub	$p_T \geq 6$ GeV/c
			CSX hit
		XFT	$p_T \geq 4.09$ GeV/c
			COT layers ≥ 4
2	L2_CMX6_PT8_TRK5_3D	muon	CMX
		XFT track 1	$p_T \geq 8.34$ GeV/c
			stereo confirmed
		XFT track 2	$p_T \geq 5.19$ GeV/c
			stereo confirmed
		MAX_PRESCALE	15
		MIN_PRESCALE	1
3	L3_CMX8_TRACK5_ISO	muon	CMX
			$p_T \geq 8$ GeV/c
			$\Delta x_{CMX} \leq 50$ cm
		track	$\lvert\eta\rvert \leq 1.$
			$p_T \geq 8$ GeV/c

Table A.15: Trigger requirements for the TAU_CMX8_TRACK5_ISO_DPS path, tag 6.

Appendix B

Tau Fake Rate

We tested our method to estimate the number of events with fake taus decaying in hadrons. The validation plots of the method are collected in this appendix.

We want to remind that the events with fake taus are evaluated by the use of the probability of tau-like jets to be misidentified as tau candidates (measured with the methods explained in Section 5.4). This probability, called the tau fake rate, has been estimate as the average of the probability of the leading jets and the subleading jets to fake taus.

We use three samples for our estimate of events with fakes: the "calibration electron" for the top pair decay channels with an electron; the "calibration muon" or "lepton plus track" for the top pair decay channels with a CMUP or CMX muon respectively. The events in data samples are required to contain one electron or one muon candidate plus at least a tau-like jet. Then the events are required to pass the kinematic selection and each couple formed by a tau-like jet and the other lepton (electron or muon) are accounted with the weight represented by the tau fake rate.

We show in this appendix that the result obtained with the leading and the subleading jets are correctly overestimating and underestimating the events selected in data. It demonstrates that our systematic boundaries of the fake rate are correctly reflected in the evaluation of the number of fake events in data.

To test our estimate of the fake rate we used two control regions defined by kinematic requirements, which in one case select QCD multi-jet events and in the other case W plus jets events. These two class of processes are our biggest contribution to the background in our signal sample without b tag requirement. These two control regions are usefull to test the fake rate in two different lepton transverse momentum regimes: one group of events is enriched by high p_T real leptons and the other by low p_T fake leptons. These control regions contain on purpose only small fraction of the events passing our final selection.

B.1 Acceptance Correction for the Electron Sample

The sample "calibration electron" is selected with the trigger requirements described in Section A.5.1. The trigger Level 3 requirement $E_{HAD}/E_{EM} \leq 0.055$ is tighter than the standard requirement contained in the electron identification ($E_{HAD}/E_{EM} \leq (0.055 + 0.00045 \times E)$). For this reason we evaluated a correction factor to account for the lower acceptance of the trigger selection.

We selected an inclusive sample of events with one electron candidate from the sample "electron plus track". This sample is selected with a class of triggers which requires an electron of $E_T \geq 8$ GeV and a track of $p_T \geq 8$ GeV. The trigger requirements on the electron are similar to ones in the "electron plus isolated track" trigger, used for the signal extraction.

The denominator is represented by the number of events which have the electron candidates passing the requirement $E_{HAD}/E_{EM} \leq 0.055$; while the numerator is the total number of events. We obtained three measurements corresponding to data periods 4, 11 and 16:

- period 4, 1.042 ± 0.003;
- period 11, 1.041 ± 0.002;
- period 16, 1.041 ± 0.003.

The measurements are statistically in agreement.

This result represents an average of all the electron candidates, indipendently from their calorimeter energy. Since the requirement on the electromagnetic fraction scales with the energy of the electron, the corrections could be different for high and low E_T electrons. For this reason we use a conservative uncertainty on this measurement, equal to half of the difference from the unitary value: 1.04 ± 0.02.

B.2 Events with Fake Taus in QCD Enriched Control Region

The events in this control region are selected with the following requirements:

- 1 fakable tau object;
- 1 electron or 1 muon candidate;
- at least 2 jets;
- missing transverse energy $\not\!\!E_T \leq 20$ GeV.

The fakable tau object is defined in Section 5.4.2; the electron or muon identification is defined in Chapter 4, and the two jets are such that the leading one has $E_T \geq 20$ GeV and the subleading ones $E_T \geq 15$ GeV.

Some of the most important kinematic distributions of the events are represented in Figure B.1 and Figure B.2. The first figure report the distribution of events with fakes using the leading jet fake rate, the second figure using the subleading jet fake rate. It is possible to notice that the two different expectations well contain the number of events selected.

B.3 Events with Fake Taus in W plus Jets Enriched Control Region

The events in this control region are selected with the following requirements:

- 1 fakable tau object;
- 1 electron or 1 muon candidate;
- at least 2 jets;
- missing transverse energy $\not\!\!E_T \geq 20$ GeV;
- $M_T(\ell,\not\!\!E_T) \geq 40$ GeV;
- $Ht < 200(205)$ GeV.

The fakable tau object is defined in Section 5.4.2; the electron or muon identification is defined in Chapter 4; the two jets are such that the leading one has $E_T \geq 20$ GeV and the subleading ones $E_T \geq 15$ GeV; $M_T(\ell,\not\!\!E_T)$ represents the transverse mass of the system composed by the electron or muon, and the $\not\!\!E_T$; Ht is the variable defined in Section 6.2.

Some of the most important kinematic distributions of the events are represented in Figure B.3 and Figure B.4. As already showed in the previous section, the first figure is obtained estimating the distribution of events with the use of the leading jet fake rate, the second figure with the use of the subleading jet fake rate. Some data points exceed the evaluation done with the high value of the fake rate, but on the overall the expectations are compatible with the selected data events.

B.4 Concluding Remarks

We have showed in this appendix that we correctly estimate the events with fakes and the sistematic uncertainty on the fake rate allow to correctly estimate the uncertainty of our evaluation of this background.

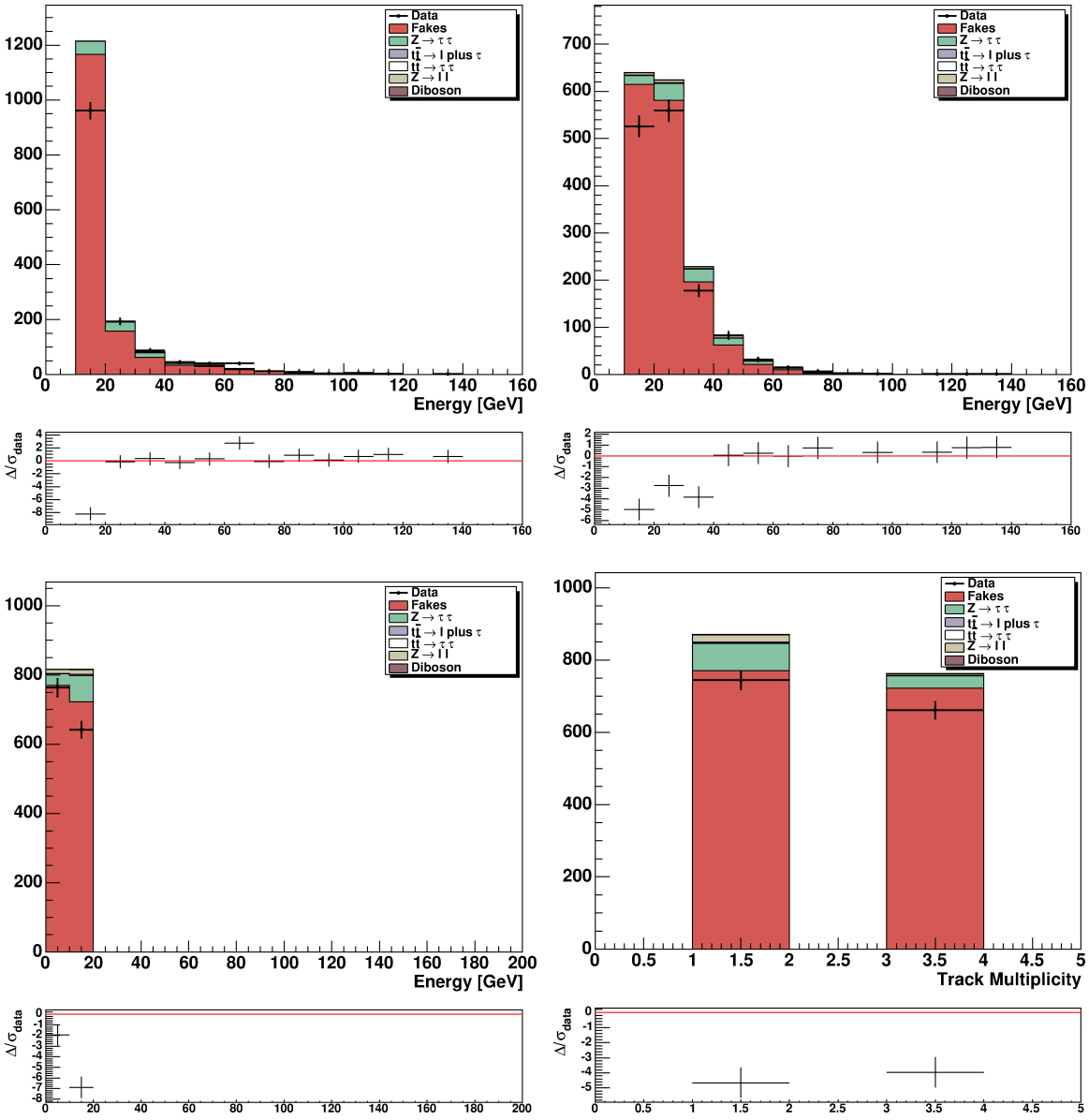

Figure B.1: Distribution of electron or muon p_T (left up), of tau cluster E_T (right up), $\not\!\!E_T$ (left down), and track multiplicity of tau induced jet (right down). Result obtained in the QCD control region with the use of the leading jet fake rate.

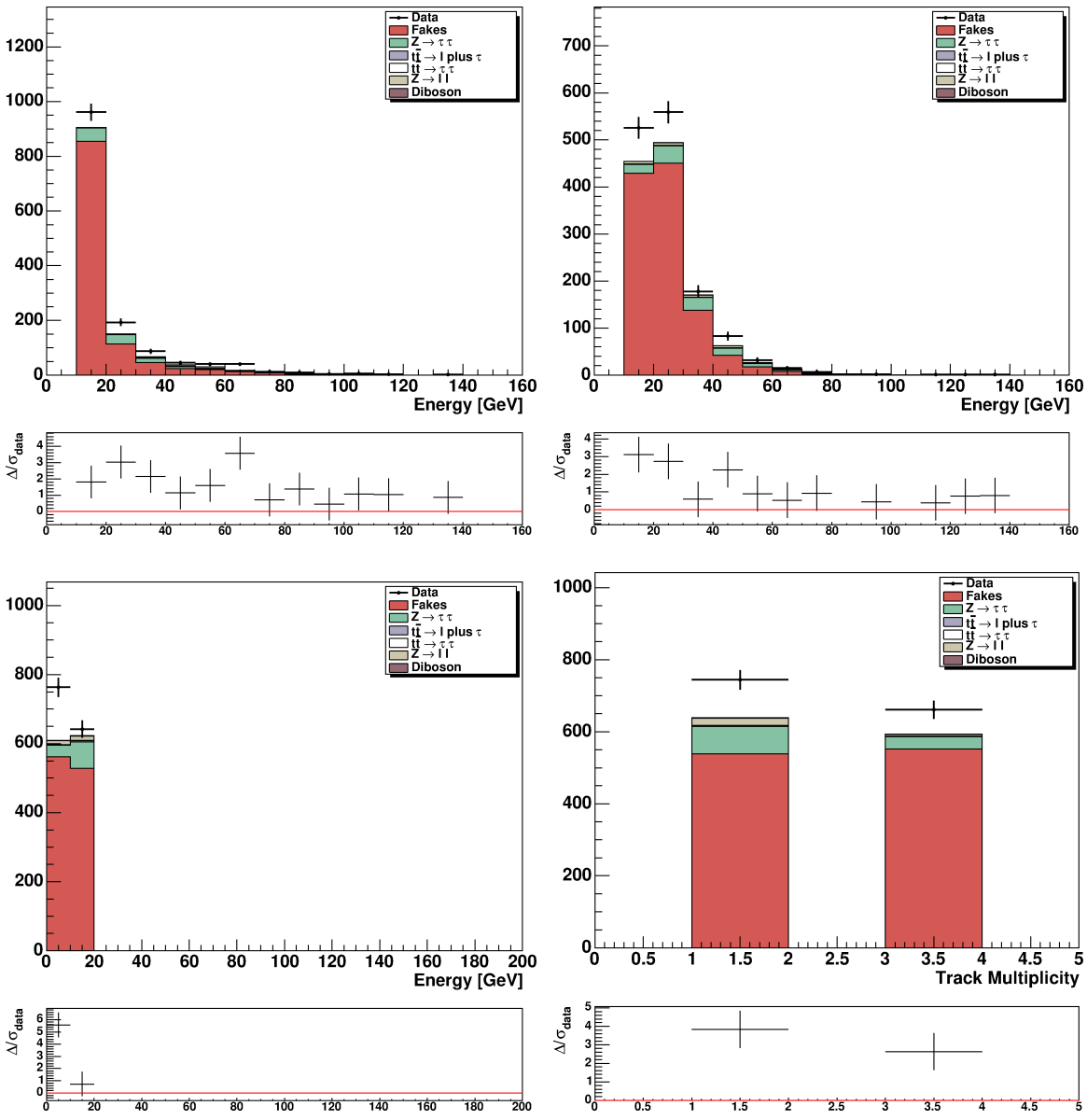

Figure B.2: Distribution of electron or muon p_T (left up), of tau cluster E_T (right up), $\not{E}_T$ (left down), and track multiplicity of tau induced jet (right down). Result obtained in the QCD control region with the use of the subleading jet fake rate.

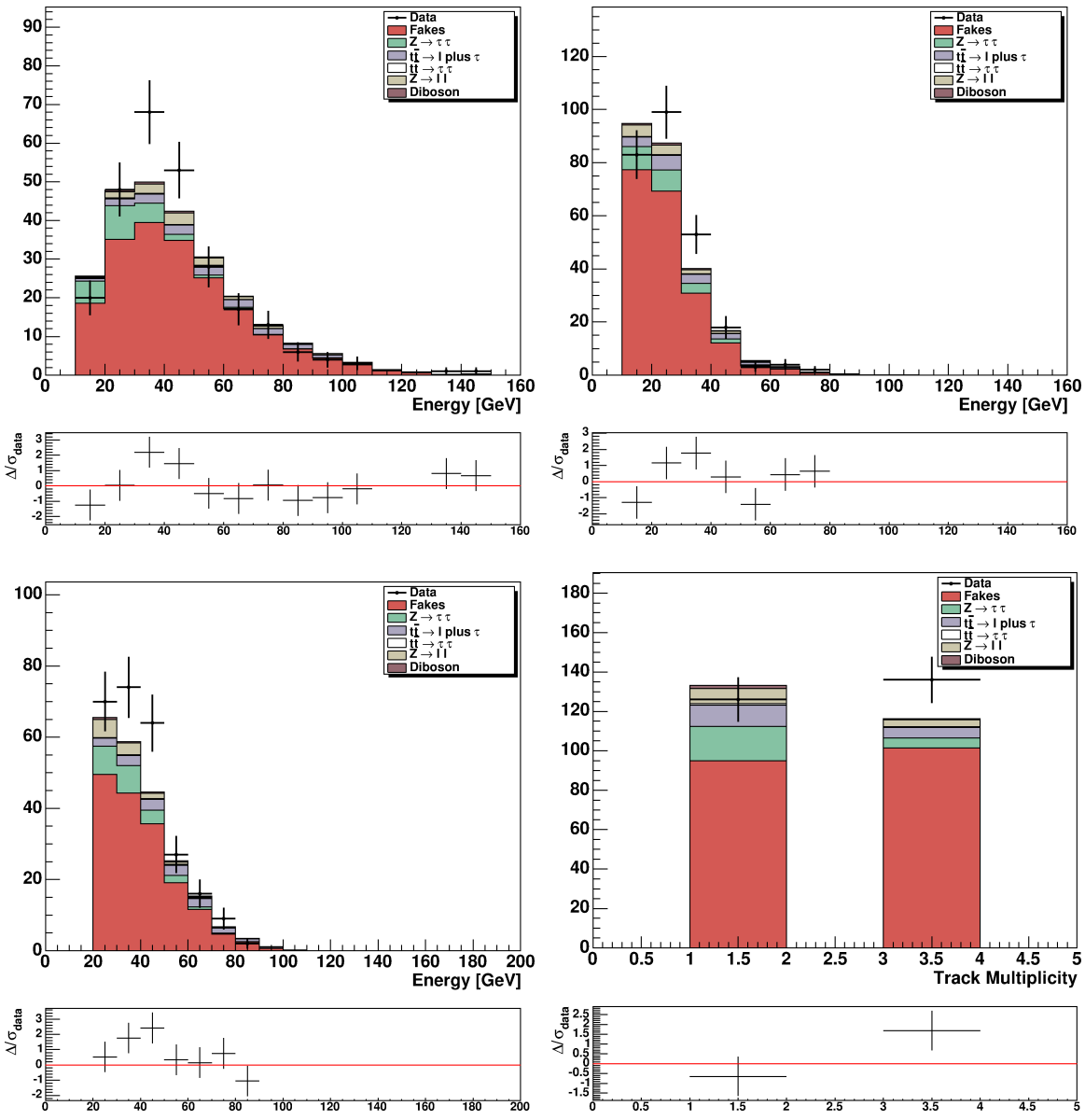

Figure B.3: Distribution of electron or muon p_T (left up), of tau cluster E_T (right up), $\not{E}_T$ (left down), and track multiplicity of tau induced jet (right down). Result obtained in the W plus jets control region with the use of the leading jet fake rate.

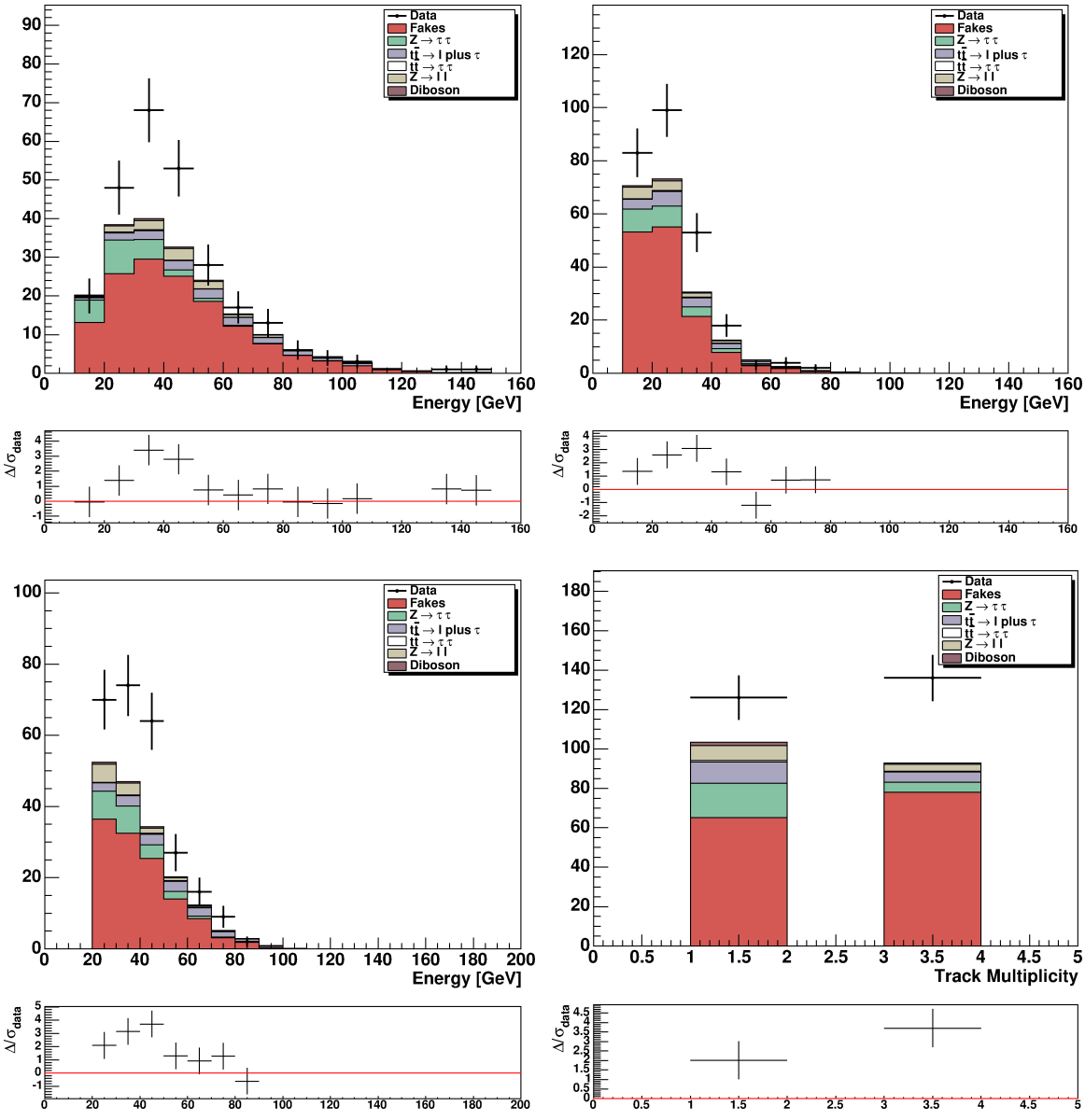

Figure B.4: Distribution of electron or muon p_T (left up), of tau cluster E_T (right up), $\not{E}_T$ (left down), and track multiplicity of tau induced jet (right down). Result obtained in the W plus jets control region with the use of the subleading jet fake rate.

Bibliography

[1] F. Halzen, A. D. Martin, "Quark & Leptons: An Introductory Course In Modern Particle Physics", Wiley and Sons (1984)

[2] F. J. Hasert et al., Phys. Lett. **B46**, 138 (1973).

[3] M. Holder et al., Phys. Lett. **B71**, 222 (1977).

[4] UA1 Collaboration, G. Arnison et al., Phys. Lett. **B122**, 102 (1983).

[5] UA2 Collaboration, M. Banner et al., Phys. Lett. **B122**, 476 (1983).

[6] P. W. Higgs, Phys. Lett. **12**, 132 (1964).

[7] K. Nakamura et al. (Particle Data Group), J. Phys. G 37, 075021 (2010).

[8] N. Cabibbo, Phys. Rev. Lett. **10**, 531 (1963)

[9] M. Kobayashi and T. Maskawa, Prog. Theor. Phys. **49**, 652 (1973)

[10] S. Glashow and S. Weinberg, Phys. Rev. **D15**, 1958 (1977).

[11] J. F. Gunion et al., "The Higgs Hunter's Guide", Frontiers in Physics Series (Vol. No. 80), Addison-Wesley Publishing Company (1990).

[12] J. S. Lee et al., "CPsuperH: a Computational Tool for Higgs Phenomenology in the Minimal Supersymmetric Standard Model with Explicit CP Violation", Comput. Phys. Commun. **156** 283 (2004).

[13] R. Eusebi, PhD Thesis, "Search for Charged Higgs in ttbar Decay Products from Proton-Antiproton Collisions at s**(1/2) = 1.96 TeV", FERMILAB-THESIS-2005-33.

[14] G. Aubrecht , "A Teachers Guide To The Nuclear Science Wall Chart", Contemporary Physics Education Project (2003),

[15] F. B. Division, "The Linac Rookie Book, 2006", available at `http://www-bdnew.fnal.gov/operations/rookie_books/LINAC_v2.pdf`.

[16] F.B. Division, "The Booster Rookie Book, 2009", available at http://www-bdnew.fnal.gov/operations/rookie_books/Booster_v4.1.pdf.

[17] F.B. Division, "The Main Injector Rookie Book, 2010", available at http://www-bdnew.fnal.gov/operations/rookie_books/Main_Injector_v1.1.pdf.

[18] F.B. Division, "The Antiproton Source Rookie Book, 2009", available at http://www-bdnew.fnal.gov/operations/rookie_books/Pbar_v2.pdf.

[19] D. Mohl et al., Phys. Reports **58**, 73–102 (1980).

[20] S. Nagaitsev et al., Phys. Rev. Lett. **96**, 044801 (2006).

[21] F.B. Division, "The Recycler Rookie Book, 2010", available at http://www-bdnew.fnal.gov/operations/rookie_books/Recycler_v1.141.pdf.

[22] CDF Collaboration, "The CDF II Detector Technical Design Report", FERMILAB-PUB-96/390-E (1996).

[23] N. Timothy, "The CDF L00 Detector", CDF Public Note 5780 (2001).

[24] A. Sill, "CDF Run II Silicon Tracking Project", Nucl. Instrum. Meth. **A447**, 1 (2000).

[25] A. Affolder et al., "Status Report of the Intermediate Silicon Layer Detector at CDF II", Nucl. Instrum. Meth. **A485**, 178-182 (2002).

[26] C. M. Ginsburg at al., "CDF Run II Muon System", Eur. Phys. J. **C33**, S1002 (2004).

[27] C. Avila et al., "A Measurement of the Proton-Antiproton Total Cross Section at $\sqrt{s} = 1.8$ TeV, Phys. Lett. **B 445**, 419 (2002).

[28] D. Acosta et al., "The Performance of the CDF Luminosity Monitor", Nucl. Instrum. Methods **494** (2002).

[29] E.J.Thomson et al., "Online Track Processor for the CDF Upgrade", IEEE Trans.Nucl.Sci. **49**, 1063–1070 (2002).

[30] A.Abulencia et al., "The CDF II Level 1 Track Trigger Upgrade", IEEE Trans.Nucl.Sci. **55**, 126–132 (2008).

[31] A. Bhatti et al., "Level-2 Calorimeter Trigger Upgrade at CDF", IEEE Trans.Nucl.Sci., **56**, 1685–1689 (2009).

[32] A.Abulencia et al., "The CDF II 3D-Track Level 2 Trigger Upgrade", In Real-Time Conference, 15th IEEE-NPSS, 1–5 (2007).

[33] M. S. Carena et al., "Physics at Run II: Supersymmetry / Higgs Workshop", Fermilab Publication FERMILAB-PUB-00-349 and FERMILAB-PUB-00-349-1

[34] A. Anastassov et al., "Selection of Tau Leptons with the CDF Run 2 Trigger System", CDF Note CDF/PUB/TRIGGER/PUBLIC/6499

[35] M. Chertok et al., "Lepton + Track Trigger in Run II: A New Approach for Triggering on Dileptons - Electron Case", CDF Note CDF/MEMO/TRIGGER/CDFR/4807

[36] M. Garcia-Sciveres et al., "The SVX3D Integrated Circuit for Deadtimeless Silicon Strip Readout", Nucl. Instr. and Meth. **A435** 58 (1999).

[37] S. Belforte et al., Silicon Vertex Tracker Technical Design Report, Public CDF Note 3108

[38] R.J. Tesarek et al., Nucl. Inst. and Meth. **A514** (2003) 188.

[39] P. Dong et al., CDF internal note 8219, 2006.

[40] M. Swartz et al., Observation, modeling, and temperature dependence of doubly peaked electric fields in irradiated silicon pixel sensors, Nucl. Instrum. Methods **A565**, 212-220 (2006).

[41] G. Lindström, M. Moll and E. Fretwurst, Nucl. Instr. and Meth. **A426** (1999) 1.

[42] Nucl. Phys. **B 61** Proceedings Supplements, 360-365, (1998).

[43] M. Bishai et al., "Dense Optical Interface Module for the CDF Run II Silicon Tracking System", CDF Internal Note 6497.

[44] A. Anastassov et al., "Muon Trigger Efficiencies for v5.3 Tau Data", CDF internal note, CDF/ANAL/EXOTIC/CDFR/7837 (2005).

[45] S. Dube et al., "Searches for Chargino-Neutralino Production in mSUGRA model in a Di-electron + Track Channel", CDF internal note, CDF/DOC/EXOTIC/CDFR/8445 (2006).

[46] C. Cuenca Almenar, "Search for the Neutral MSSM Higgs Bosons in the Tau-Tau Decay Channels at CDF Run II", PhD Thesis, Universitat de Valencia (2008).

[47] A. Anastassov et al., "Search for Neutral MSSM Higgs Boson(s) in the Tau Tau Decay Channel", CDF internal note, CDF/PHYS/EXOTIC/CDFR/8972 (2007).

[48] CDF Collaboration, "Search for Neutral MSSM Higgs Bosons Decaying to Tau Pairs with 1.8 fb^{-1} of Data", CDF public note, CDF/PHYS/EXOTIC/PUBLIC/9071 (2007)

[49] P. Murat, Y. Tu, "Monte Carlo modelling of the jet $\rightarrow$ tau_h fake rates", CDF/DOC/ELECTROWEAK/CDFR/8809 (2007).

[50] P.Skands, T.Sjosrand, S.Mrenna, "PYTHIA 6.4 Physics and Manual", Jour. High. Ener. Phys. **0605**, 26 (2006).

[51] S.Jadach et al., "The tau decay library TAUOLA: Version 2.4", Comput. Phys. Commun., **76**, 361–380 (1993).

[52] A. Bhatti et al., "Determination of the Jet Energy Scale at the Collider Detector at Fermilab", arXiv:hep-ex/0510047v1.

[53] CDF Collaboration, "Measurement of the $t\bar{t}$ production cross section in $p\bar{p}$ collisions at $\sqrt{s} = 1.96$ TeV using lepton + jets events with secondary vertex b-tagging", Phys. Rev. **D71**, 052003 (2005)

[54] C. Neu, "CDF b-tagging: Measuring Efficiency and False Positive Rate", Published Proceedings TOP 2006, International Workshop on Top Quark Physics, Coimbra, Portugal (2006).

[55] G. C. Blazey et al. "Run II jet physics", arXiv:hep-ex/0005012 (2000).

[56] M. Mangano et al., "Alpgen a generator for hard multiparton process in hadronic collisions", Jour. High. Ener. Phys. **0307**, 1 (2003).

[57] G. Corcella et al., "HERWIG 6: an event generator for Hadron Emission Reactions With Interfeiring Gluons (including supersummetric processes)", JHEP 0101 010 (2001).

[58] CTEQ Collaboration, H.L. Lai et al., Eur. Phys. J. **C12**, 375 (2000).

[59] T. Sjostrand, Nucl. Phys. 248, 469 (1984).

[60] R.Brun et al., "GEANT: Simulation Program for Particle Physics Experiments", User Guide and Reference Manual, (1978), CERN-DD-78-2-REV.

[61] D. Stuart, "Effects of Material in the CDF-II Silicon Detectors", CDF note CDF/DOC/TRACKING/PUBLIC/5268.

[62] S. Rolli et al., "Electron id efficiencies and scale factors for periods 9 to 12", CDF/DOC/ELECTRON/CDFR/9148 (2007).

[63] X.Zhang et al., "High-pT muons reccommended cuts and efficiencies for summer 2006", CDF/ANAL/TOP/CDFR/8262 (2006).

[64] S. Camarda et al., "Measurement of $Z/\gamma^* \to e^+e^-$ + jets Production Cross Section", CDF/PHYS/JET/PUBLIC/10394 (2011).

[65] A. Anastassov et al., "Search for Neutral MSSM Higgs Boson(s) in the Tau Tau Decay Channel", CDF/ANAL/EXOTIC/CDFR/7622 (2005).

[66] R. Field, C. R. Group, "Pythia Tune A, Herwig, and Jimmy in Run 2 at CDF", arXiv:hep-ph/0510198v1.

[67] A. Buckley et al., "Systematic event generator tuning for the LHC", arXiv:0907.2973v1

[68] J. Campbell and K. Ellis, "Monte Carlo for FeMtobarn processes", shttp://mcfm.fnal.gov.

[69] J. Campbell and K. Ellis, "Update on vector boson pair production at hadron colliders", Phys. Rev. **D60**, 113006 (1999).

[70] CDF Collaboration, "Combination of CDF top quark pair production cross section measurements with up to 4.6 fb^{-1}", CDF Conference note 9913 (2009).

[71] D0 Collaboration, "Measurement of the $t\bar{t}$ production cross section using dilepton events in $p\bar{p}$ collisions", Phys. Lett. **B**, 704, 403-410 (2011).

[72] ATLAS Collaboration, "Observation of an Excess of Events in the Search for the Standard Model Higgs Boson with the ATLAS Detector at the LHC", Conference Note ATLAS-CONF-2012-093.

[73] CMS Collaboration, "Observation of a new boson with a mass near 125 GeV", Conference Note CMS-PAS-HIG-12-020.

[74] CDF and D0 Collaboration, "Updated Combination of CDF and DØ Searches for Standard Model Higgs Boson Production with up to 10.0 fb^{-1} of Data", arXiv:1207.0449v2 (2012).

[75] CDF Collaboration, "Search for the top $\rightarrow \tau\nu q$ channel in top dilepton", CDF Conference note 8376 (2006).

[76] DØ Collaboration, "Measurement of $t\bar{t}$ Production Cross Section in the Lepton + Tau + b-jet(s) + $\not\!\!E_T$ Channel Using 1.2 fb^{-1} of Run IIb Data", D0 Conference note 5607 (2008)

[77] CDF Collaboration, "Measurements of Top Quark Properties in the τ + jets decay channel at CDF", CDF/PUB/TOP/PUBLIC/10562 (2011).

[78] DØ Collaboration, "Measurement of the $t\bar{t}$ production in the τ + jets topology using $p\bar{p}$ collisions at $\sqrt{s} = 1.96$ TeV, Phys. Rev. **D82**, 071102 (2001).

[79] CMS Collaboration, "Measurement of the $t\bar{t}$ production cross section in pp collisions at $\sqrt{s} = 7$ TeV in dilepton final states containing a τ" , arXiv:1203.6810v1.

[80] ATLAS Collaboration, "Measurement of the $t\bar{t}$ production cross section in the final state with a hadronically decaying tau lepton and jets using the ATLAS detector", ATLAS-CONF-2012-032.

[81] N. Kidonakis, "Next-to-next-to-leading soft-gluon corrections for the top quark cross section and transverse momentum distribution", Phys. Rev. **D82**, 114030 (2010).

[82] T. Junk, "Sensitivity, Exclusion and Discovery with Small Signals, Large Backgrounds, and Large Systematic Uncertainties", CDF note CDF/DOC/STATISTICS/PUBLIC/8128.

[83] CDF Collaboration, "Search for Charged Higgs Bosons from Top Quark Decays in $p\bar{p}$ Collisions at $\sqrt{s} = 1.96$ TeV, Phys. Rev. Lett. **96**, 042003 (2006).

[84] DØ Collaboration, "Search for charged Higgs boson in the top quark decays", arXiv:0908.1811v2 (2009).

[85] Tom Junk, "Sensitivity, Exclusion and Discovery with Small Signals, Large Backgrounds, and Large Systematics", CDF Public Note 8128.

[86] DØ Collaboration, "Measurement of the $t\bar{t}$ production cross section and top quark mass extraction using dilepton events in $p\bar{p}$ collisions", arXiv:0901.2137 (2009).

[87] ATLAS Collaboration, "Search for the charged Higgs bosons decaying via $H^{\pm} \to \tau\nu$ in $t\bar{t}$ events using pp collision data at $\sqrt{s} = 7$ TeV with the ATLAS detector", arXiv:1204.2760v1 (2012).

[88] CMS Collaboration, "Search for the light charged Higgs boson in the top quark decays in pp collisions at $\sqrt{s} = 7$ TeV", CMS analysis CMS-HIG-11-019 (2012).